ENGINEERING MECHANICS 2026

32nd INTERNATIONAL CONFERENCE

MAY 11 – 13, 2026, MEDLOV, CZECH REPUBLIC

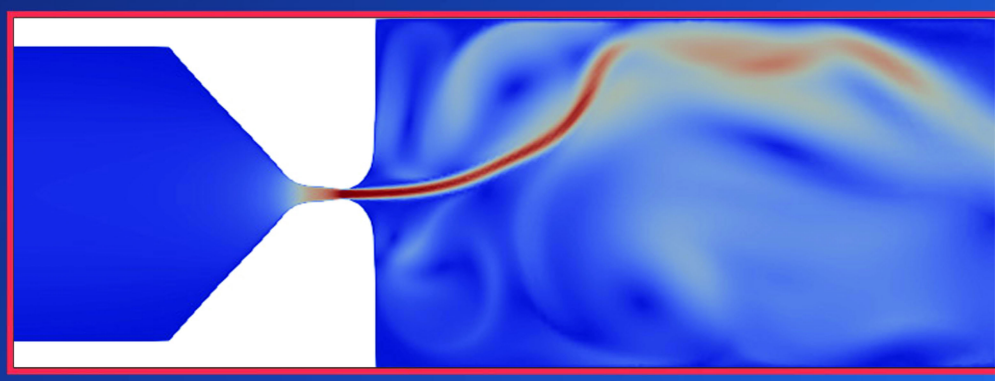

BOOK OF FULL TEXTS

Editors: Vojtěch RADOLF
Igor ZOLOTAREV

ENGINEERING MECHANICS 2026

32nd INTERNATIONAL CONFERENCE

MAY 11 – 13, 2026, MEDLOV, CZECH REPUBLIC

BOOK OF FULL TEXTS

Editors: **Vojtěch Radolf**
Igor Zolotarev

Institute of Thermomechanics
of the Czech Academy of Sciences

Institute of Solid Mechanics, Mechatronics and Biomechanics,
Faculty of Mechanical Engineering, Brno University of Technology

Institute of Theoretical and Applied Mechanics
of the Czech Academy of Sciences

ŽĎAS, a.s., Žďár nad Sázavou

IFToMM Member Committee of the Czech Republic

Czech Society for Mechanics

All papers were reviewed by members of the scientific committee.

First edition, 2026

Cover figure: Velocity magnitude during a soft-voice phonation.
(Karel Vacek – Department of Technical Mathematics, CTU)

ISBN 978-80-87012-94-9 (electronic)

ISSN 1805-8256 (electronic)

DOI 10.21495/em2026

The Conference is hosted by the Hotel Medlov, Fryšava pod Žákovou horou 143, CZ.

SCIENTIFIC COMMITTEE

Vojtěch Radolf, PhD. (chairman)	Institute of Thermomechanics CAS, Prague, CZ
Igor Zolotarev, PhD. (co-chairman)	Institute of Thermomechanics CAS, Prague, CZ
Prof. Ivan Baláž, PhD.	Slovak University of Technology in Bratislava, SK
Prof. Dr. Pavol Bauer	Delft University of Technology, NL
Prof. Matej Daniel, PhD.	Czech Technical University in Prague, CZ
Prof. Ľudovít Fillo, PhD.	Slovak University of Technology in Bratislava, SK
Cyril Fischer, PhD.	ITAM CAS, Prague, CZ
Prof. Paola Forte	University of Pisa, IT
Assoc. Prof. Vladimír Fuis, PhD.	Institute of Thermomechanics CAS, Brno, CZ
Jaromír Horáček, DSc.	Institute of Thermomechanics CAS, Prague, CZ
Assoc. Prof. Lidia Ilieva-Mitutsova, PhD.	Bulgarian Academy of Sciences, Sofia, BG
Prof. Zbyněk Jaňour, DSc.	Institute of Thermomechanics CAS, Prague, CZ
Assoc. Prof. Tomasz Kałaczyński, PhD.	Bydgoszcz University of Sciences and Technology, PL
Prof. Anne-Maria Laukkanen, PhD.	University of Tampere, FI
Prof. František Maršík, DSc.	Institute of Thermomechanics CAS, Prague, CZ
Assoc. Prof. Adam Mazurkiewicz, PhD.	Bydgoszcz University of Sciences and Technology, PL
Prof. Arkadiusz Mężyk	Silesian University of Technology, Gliwice, PL
Prof. Dr. Damijan Miljavec	University of Ljubljana, Ljubljana, SI
Jiří Náprstek, DSc.	ITAM CAS, Prague, CZ
Prof. Dr. Paolo Pennacchi	Politecnico di Milano, Milan, IT
Prof. Jindřich Petruška, PhD.	Brno University of Technology, CZ
Jiří Plešek, PhD.	Institute of Thermomechanics CAS, Prague, CZ
Prof. Dr. Eduard Rohan, DSc.	University of West Bohemia in Pilsen, CZ
Assoc. Prof. Zdenka Sant, PhD.	University of Malta, MT
Prof. Ing. Milan Sokol, PhD.	Slovak University of Technology, Bratislava, SK
Prof. Václav Uruba, PhD.	Institute of Thermomechanics CAS, Prague, CZ
Assoc. Prof. Stanislav Věchet, Ph.D	Brno University of Technology, Brno, CZ
Prof. Pavel Vlasák, DSc.	Institute of Hydrology CAS, Prague, CZ
Prof. Jaroslav Zapoměl, DSc.	Institute of Thermomechanics CAS, Ostrava, CZ

HONORARY COMMITTEE

Ing. Pavel Cesnek — **Managing Director of the ŽĎAS, Inc.**

ORGANIZING COMMITTEE

Vojtěch Radolf	**Institute of Thermomechanics CAS, Prague, CZ**
Igor Zolotarev	**Institute of Thermomechanics CAS, Prague, CZ**
Michael Formánek	**ŽĎAS a.s., Žďár nad Sázavou, CZ**

LIST OF SECTIONS

KEY	**Keynote Lectures**
BIO	**Biomechanics**
DYN	**Dynamics**
FLU	**Fluid Mechanics**
FRA	**Fracture Mechanics**
MCT	**Mechatronics**
REL	**Reliability**
SOL	**Mechanics of Solids**
TEC	**Technological Processes**

32nd International Conference
ENGINEERING MECHANICS 2026
Medlov, Czech Republic, May 11 – 13, 2026

PEER REVIEW STATEMENT

Radolf V.[1]

Abstract: *This statement is provided in accordance with formal publication standards and administrative requirements. All papers included in the proceedings of the 32nd International Conference on Engineering Mechanics (EM2026) underwent blind peer review by members of the Scientific Committee, comprising 29 experts across multiple disciplines. The conference is further characterized by open discussion, active exchange of ideas, and a collaborative environment that supports high-quality scientific contributions.*

All papers included in the proceedings of the 32nd International Conference on Engineering Mechanics (EM2026) have undergone a rigorous peer-review process to ensure their quality, relevance, and scientific integrity.

A total of 39 submissions were received. Each manuscript was evaluated through a blind peer-review process conducted by members of the Scientific Committee, comprising 29 distinguished researchers and experts from various fields of mechanics. The reviews focused on originality, methodological soundness, scientific contribution, and clarity of presentation. Based on the reviewers' evaluations and the committee's recommendations, 37 papers were accepted for publication.

The conference program therefore features 37 oral and poster presentations, covering a broad range of topics, including solid and fluid mechanics, biomechanics, mechatronics, and fracture mechanics.

We gratefully acknowledge the reviewers for their careful evaluations and constructive feedback, which have significantly contributed to the overall quality of this volume.

Contact person for queries:

Name: Vojtěch Radolf
Email: radolf@it.cas.cz
Affiliation: Institute of Thermomechanics of the Czech Academy of Sciences

[1] Ing. Vojtěch Radolf, PhD.: Institute of Thermomechanics of the Czech Academy of Sciences, Dolejškova 1402/5, 182 00 Prague, CZ, radolf@it.cas.cz

ISSN: 1805-8256, doi: 10.21495/em2026-v

32nd International Conference
ENGINEERING MECHANICS 2026
Medlov, Czech Republic, May 11 – 13, 2026

GENERALIZED STANDARD MATERIALS FRAMEWORK AND ITS APPLICATION IN CONSTITUTIVE MODELING OF SHAPE MEMORY ALLOYS

Frost M.[1]

Abstract: *Advances in modern materials and manufacturing provide engineers with opportunities to pioneer innovative applications and redesign conventional concepts. Central to such an endeavor is a sound understanding of complex (thermo)mechanical behavior, which must be translated into reliable constitutive models for high-fidelity computational simulations. This work highlights the advantages of the Generalized Standard Materials framework—a systematic methodology that ensures a priori thermodynamic consistency and mathematical coherence, thereby offering a robust foundation for modeling advanced materials, where ad hoc approaches often prove inadequate.*

Keywords: **Generalized standard materials, Internal variables, Dissipation potential, Shape memory alloys**

1. Introduction

As materials science and technology provide engineers with novel materials — such as high-performance composites, additive-manufactured or functionally graded alloys, and architected metamaterials — the demand for sophisticated material modeling increases. By accurately capturing non-linearities, temporal dependencies, and multiphysical couplings, such modeling enables the design of optimized, resilient applications that push the boundaries of safety, efficiency, and innovation across a wide range of industries, from aerospace to biomedical.

Constitutive laws provide the backbone of efficient computational models. Within the general concept of continuum mechanics, the balance laws and side conditions (boundary, initial) are complemented by constitutive equations, which characterize the response of a material to imposed stimuli, so that the response of a solid body to external fields can be determined. The constitutive laws often account for inelastic deformation, which is related to microstructural changes in the material and is associated with energy dissipation, e.g., viscoelasticity, plasticity, damage, delamination, etc. Methods for developing constitutive laws in the form of mathematical equations range from purely phenomenological approaches based on simple observations to sophisticated frameworks anchored in thermodynamics. The latter approaches yield special classes of constitutive laws, see, e.g., (Truesdell and Noll, 1965; Coleman and Gurtin, 1967; Lubliner, 1969), and their advantage is that thermodynamical and mathematical properties of models in a particular class have already been investigated in a general manner, hence, they are known *a priori* for any newly developed member.

In this contribution, we briefly summarize the Generalized Standard Materials framework, introduced by Halphen and Nguyen (1975), which provides a rigorous basis for constructing a rich family of constitutive models. Standard in this context means that the entire thermomechanical behavior—both reversible and irreversible—can be derived from just two scalar potentials, and, under certain conditions, it is automatically consistent with the laws of thermodynamics. We also highlight the framework's benefits and provide illustrative examples with a particular focus on shape memory alloys.

[1] RNDr. Miroslav Frost, Ph.D.: Institute of Thermomechanics, Czech Academy of Sciences, Dolejškova 1402/5; 182 00, Prague; CZ, mfrost@it.cas.cz

ISSN: 1805-8256, doi: 10.21495/em2026-1

2. Thermodynamics preliminaries

In continuum theory, a material point is a small enough elementary particle of a solid or fluid, whose state represents the local state of the material. The local equilibrium thermodynamics then assumes that "the system is composed of infinitesimal subsystems in slow evolution such that each subsystem can always be considered as almost in thermodynamic equilibrium at any time" (Nguyen, 2000). Any material point is then understood to be composed of one of these infinitesimal subsystems, and the state of a material point in equilibrium can be characterized by the present value of a set of variables called state variables. The set of state variables includes the temperature, T, and other physical variables suitable for the investigated system.[2]

The mechanical response of an inelastically deforming material is linked to changes in its microstructure. Within the concept pioneered in (Coleman and Gurtin, 1967), the microstructure of the material (at the continuum level) can be fully described by a set of additional parameters called *internal state variables*, also termed just as internal variables, and "the present state of a material point depends only on the present values of macroscopic state variables and a set of internal variables" (Horstemeyer and Bammann, 2010).The macroscopic response of the material is then linked to the time evolution of the internal variables (Maugin and Muschik, 1994a).

Adopting the small strain setting for simplicity, we can choose temperature, T, and the small strain tensor, $\boldsymbol{\varepsilon}$, as state variables and denote the vector of all internal variables as $\boldsymbol{\alpha}$. Hence, internal energy, $u(T, \boldsymbol{\varepsilon}, \boldsymbol{\alpha})$, entropy, $s(T, \boldsymbol{\varepsilon}, \boldsymbol{\alpha})$, heat flux $\mathbf{q}(T, \boldsymbol{\varepsilon}, \boldsymbol{\alpha})$, and the Cauchy stress, $\boldsymbol{\sigma}(T, \boldsymbol{\varepsilon}, \boldsymbol{\alpha})$, are all considered functions of the state and internal variables.

Combining the local versions of the first and second laws of thermodynamics leads to the Clausius-Duhem inequality (being thus an equivalent form of the second law) in the form

$$\boldsymbol{\sigma} : \dot{\boldsymbol{\varepsilon}} - (\dot{f} + s\dot{T}) - \mathbf{q} \cdot \frac{\nabla T}{T} \geq 0 \tag{1}$$

where the Helmholtz free energy, $f(T, \boldsymbol{\varepsilon}, \boldsymbol{\alpha})$, is defined as a Legendre-Fenchel transformation of internal energy, $f = u - sT$, as a more convenient form for continuum mechanics of solids. The term

$$\mathcal{D}_{\text{mech}} := \boldsymbol{\sigma} : \dot{\boldsymbol{\varepsilon}} - \dot{f} - s\dot{T} \tag{2}$$

is called a *mechanical dissipation*, whereas the last term on the left-hand side of (1) is often called a *thermal dissipation* (Houlsby and Puzrin, 2000; Nguyen, 2000). It is usually reasonable to adopt the Fourier law for the heat conduction, i.e., to assume the heat flux density, $\mathbf{q}$, is proportional to a negative gradient of temperature, $-\nabla T$, with an appropriate proportionality coefficient so that the thermal dissipation is always non-negative. Requiring the mechanical dissipation itself to be non-negative

$$\mathcal{D}_{\text{mech}} \geq 0 \tag{3}$$

is then a slightly more stringent condition than the Clausius-Duhem inequality itself. However, it is a widely accepted assumption that provides sufficient space for advanced constitutive modeling.

Expanding (2) and inserting into (3) leads to

$$\boldsymbol{\sigma} : \dot{\boldsymbol{\varepsilon}} - \frac{\partial f}{\partial \boldsymbol{\varepsilon}} : \dot{\boldsymbol{\varepsilon}} - \frac{\partial f}{\partial T}\dot{T} - \frac{\partial f}{\partial \boldsymbol{\alpha}} \cdot \dot{\boldsymbol{\alpha}} - s\dot{T} \geq 0 \tag{4}$$

Applying a strategy known as the Coleman-Noll procedure (Coleman and Gurtin, 1967), one gets the system:

$$\boldsymbol{\sigma} - \frac{\partial f}{\partial \boldsymbol{\varepsilon}} = \mathbf{0}, \tag{5}$$

$$s + \frac{\partial f}{\partial T} = 0, \tag{6}$$

$$-\frac{\partial f}{\partial \boldsymbol{\alpha}} \cdot \dot{\boldsymbol{\alpha}} \geq 0. \tag{7}$$

[2] The above postulate allows us to introduce the entropy and thermodynamic potentials locally as functions of state variables, even when the system as a whole is not necessarily in equilibrium.

Equation (3) may be understood as a restriction imposed by the second law of thermodynamics on the time evolution of state variables, including the formally introduced additional internal variables. System (5)–(7) may then be viewed as a set of sufficient conditions for satisfying that restriction, useful for the construction of constitutive models.

Defining a vector of *generalized forces*

$$\boldsymbol{A} := -\frac{\partial f}{\partial \boldsymbol{\alpha}}, \tag{8}$$

the entropy production inequality (7) takes the form

$$\boldsymbol{A} \cdot \dot{\boldsymbol{\alpha}} \geq 0. \tag{9}$$

Let us note that $\dot{\boldsymbol{\alpha}}$ is termed as *generalized flux* or *generalized velocity* and A serves as a "driving force" for microstructural processes captured by $\dot{\boldsymbol{\alpha}}$ in this context.

The formulation of the constitutive equations now boils down to establishing the relation between A and $\dot{\boldsymbol{\alpha}}$. In addition to the ad hoc approach, systematic methods have been reported in the literature. They are often based on an extremum principle applied to a physical quantity related to entropy production (Fischer et al., 2014). Among the most well-known are the maximum entropy production principle (also known as the principle of maximum dissipation rate), whose roots can be traced back to Onsager, the minimum principle for the dissipation potential, the modern GENERIC framework, and others. In what follows, we focus on the approach widely used in the engineering mechanics of solids.

3. Generalized Standard Materials framework

Within the Generalized Standard Materials (GSM) methodology, the relation between A and $\dot{\boldsymbol{\alpha}}$ is resolved via defining an additional constitutive function, d, called *dissipation potential*[3] and the "normality rule", which states that the generalized force $\boldsymbol{A}$ belongs to the *subdifferential*[4] of the dissipation potential:

$$\boldsymbol{A} \in \partial d_{\dot{\boldsymbol{\alpha}}}(\boldsymbol{\chi}, \boldsymbol{\alpha}, \dot{\boldsymbol{\alpha}}), \tag{10}$$

where $\boldsymbol{\chi}$ represents a set of state variables, i.e. $\{\boldsymbol{\varepsilon}, T\}$ in the situation at hand. In the differentiable case, this simplifies to

$$\boldsymbol{A} = \frac{\partial d(\boldsymbol{\chi}, \boldsymbol{\alpha}, \dot{\boldsymbol{\alpha}})}{\partial \dot{\boldsymbol{\alpha}}}. \tag{11}$$

The function $d(\boldsymbol{\chi}, \boldsymbol{\alpha}, \dot{\boldsymbol{\alpha}})$ hence describes the kinetics of the irreversible processes. To fullfill (9), it is assumed to satisfy:

(A1) **Convexity:** $d(\boldsymbol{\chi}, \boldsymbol{\alpha}, \dot{\boldsymbol{\alpha}})$ is convex in the rate(s) $\dot{\boldsymbol{\alpha}}$,

(A2) **Non-negativity:** $d(\boldsymbol{\chi}, \boldsymbol{\alpha}, \dot{\boldsymbol{\alpha}}) \geq 0$,

(A3) **Vanishing for zero rate(s):** $d(\boldsymbol{\chi}, \boldsymbol{\alpha}, \boldsymbol{0}) = 0$.

Indeed, then clearly

$$\boldsymbol{A} \cdot \dot{\boldsymbol{\alpha}} \overset{(\mathrm{A1})}{\geq} d(\boldsymbol{\chi}, \boldsymbol{\alpha}, \dot{\boldsymbol{\alpha}}) - d(\boldsymbol{\chi}, \boldsymbol{\alpha}, \boldsymbol{0}) \overset{(\mathrm{A3})}{=} d(\boldsymbol{\chi}, \boldsymbol{\alpha}, \dot{\boldsymbol{\alpha}}) \overset{(\mathrm{A2})}{\geq} 0. \tag{12}$$

Thus, the Clausius-Duhem inequality is satisfied *by construction*, namely by virtue of satisfying (5)–(7).

The GSM [5] framework developed originally by Halphen and Nguyen (1975) hence allows for the construction of a rich family of constitutive models satisfying the Clausius-Duhem inequality. The key points for

[3] Alternative terms *dissipation functional*, *dissipation (rate) function*, *generalized stress potential*, *force potential*, etc. can be found depending on the author and context.

[4] Loosely speaking, subdifferential is a generalization of the gradient for non-smooth functions, i.e. the set of all possible slopes of tangent planes at a point on a convex function; see (Rockafellar, 1970) for details.

[5] Alternative terminology can also be found in the literature, e.g. *generalized standard models* (Germain et al., 1983) or *standard media* (Junker et al., 2014), *hyperplasticity* (Houlsby and Puzrin, 2000), etc.

establishing a model within GSM are: i) parametrization of dissipative processes by internal variables, $\boldsymbol{\alpha}$, and ii) specification of two scalar constitutive functions: one for energy storage, $f(\boldsymbol{\chi}, \boldsymbol{\alpha})$, and the other for energy dissipation, $d(\boldsymbol{\chi}, \boldsymbol{\alpha}, \dot{\boldsymbol{\alpha}})$, which must satisfy the properties (A1)–(A3). Both functions may depend on state and internal variables. As pointed out by Nguyen (2000), a good understanding of the microstructural mechanisms operating within the considered material is essential for constructing a physically relevant model.

4. Benefits of GSM framework

Models constructed within the GSM framework constitute only a subclass of all possible material models. However, the framework appears to be highly useful and powerful, at least from the following perspectives.

4.1. Thermodynamics

As shown above, the requirements on the dissipation function (A1)–(A3) automatically ensure the consistency of any GSM model with the fundamental laws of thermodynamics. In fact, this general consistency was the natural motivation for the development of the concept. Moreover, in many common situations,[6] the relation (10) may be derived from so-called thermodynamic extremal principles, e.g., the minimum principle for the dissipation potential

$$\min_{\dot{\alpha}} \{\dot{f} + d\}, \tag{13}$$

with the dot denoting the time derivative, see (Hackl and Fischer, 2008; Fischer et al., 2014) for details.

Example. The dissipation potential of a rate independent process (e.g. elasto-plasticity) is a positive one-homogenous function[7], its dual has a specific form, cf. (Houlsby and Puzrin, 2000), and it holds

$$\boldsymbol{A} \cdot \dot{\boldsymbol{\alpha}} = d(\boldsymbol{\chi}, \boldsymbol{\alpha}, \dot{\boldsymbol{\alpha}}). \tag{14}$$

Hence, equation (2) implies

$$d = \mathcal{D}_{\mathrm{mech}}, \tag{15}$$

i.e., the value of the prescribed potential, d, is equal to the mechanical part of the dissipation. This provides a clue for relating the hysteresis in the response to the dissipation potential.

4.2. Experimental physics

Internal state variables are often introduced with a specific motivation, i.e., they are related to some real parameters of the microstructure. Recent advances in materials characterization techniques extend the capabilities of direct imaging; hence, these techniques enable validation of model predictions not only in terms of macroscopic response but also of microstructural information.

Example. In (Frost et al., 2018, 2020), the computed evolution of the internal variable representing volume fractions of phases in a GSM model was directly compared with their experimental counterparts obtained with advanced in-situ three-dimensional X-ray tomographic techniques.

4.3. Applied mathematics and computations

The GSM framework unifies diverse physical behaviors under a single mathematical "roof". Thanks to the aforementioned relation to extremal principles, the mathematical structure of the evolutionary system is well-defined and allows for rigorous analysis within a suitable solution concept, e.g., (Mielke and Roubíček, 2015) for non-smooth d. The analysis can also provide a hint for a tailored numerical discretization scheme.

Example. Since the GSM framework complies well with variational formulations, the developed models can be implemented using optimization techniques. The starting point is the incremental energy functional J for a time step Δt evaluated at time increment $n+1$, i.e.

$$J(\Delta\boldsymbol{\alpha}) = f(\boldsymbol{\chi}_{n+1}, \boldsymbol{\alpha}_n + \Delta\boldsymbol{\alpha}) - f(\boldsymbol{\chi}_n, \boldsymbol{\alpha}_n) + d\left(\boldsymbol{\chi}_{n+1}, \boldsymbol{\alpha}_n, \frac{\Delta\boldsymbol{\alpha}}{\Delta t}\right)\Delta t. \tag{16}$$

[6] For instance, if f is convex and d is homogeneous (see also the next footnote).

[7] A function $g(x)$ is called *positive k-homogenous* with k being integer, if for any real $\lambda > 0$ and any x it holds $g(\lambda x) = \lambda^k g(x)$.

Tab. 1: GSM formulations for some simplified mechanical behaviors of solids in a one-dimensional material point. $\mathcal{I}_{\mathbb{R}_0^+}(\cdot)$ denotes the indicator function of non-negative reals (in the sense of convex analysis). Characters other than ε, T, and those marked as internal variables denote material parameters.

Material Model	**Int. Var. $\boldsymbol{\alpha}$**	**Free Energy f**	**Dissipation Potential d**
Linear Elasticity	–	$\frac{1}{2}E\varepsilon^2$	–
Perfect Elastoplasticity	$\varepsilon_{\mathrm{pl}}$	$\frac{1}{2}E(\varepsilon-\varepsilon_{\mathrm{pl}})^2$	$Y_{\mathrm{p}}\lvert\dot{\varepsilon}_{\mathrm{pl}}\rvert$
EP with Kinematic Hardening	$\varepsilon_{\mathrm{pl}}$	$\frac{1}{2}E(\varepsilon-\varepsilon_{\mathrm{pl}})^2+\frac{1}{2}\kappa\varepsilon_{\mathrm{pl}}^2$	$Y_{\mathrm{p}}\lvert\dot{\varepsilon}_{\mathrm{pl}}\rvert$
EP with Isotropic Hardening	$\varepsilon_{\mathrm{pl}}$	$\frac{1}{2}E(\varepsilon-\varepsilon_{\mathrm{pl}})^2$	$(Y_{\mathrm{p}}+\zeta\varepsilon_{\mathrm{pl}})\lvert\dot{\varepsilon}_{\mathrm{pl}}\rvert$
Brittle Damage	$\omega\in[0,1]$	$\frac{1}{2}E(1-\omega)\varepsilon^2$	$(Y_{\mathrm{d}}+\chi\omega)\dot{\omega}+\mathcal{I}_{\mathbb{R}_0^+}(\dot{\omega})$
Perfect Superelasticity	$\xi\in[0,1]$	$\frac{1}{2}E(\varepsilon-\xi\epsilon)^2+\upsilon(T-T_0)$	$Y_{\mathrm{pt}}\lvert\dot{\xi}\rvert$
Kelvin-Voigt Viscoelasticity	$\varepsilon_{\mathrm{vis}}$	$\frac{1}{2}E(\varepsilon-\varepsilon_{\mathrm{vis}})^2$	$\frac{1}{2}\eta\dot{\varepsilon}_{\mathrm{vis}}^2$

The state update is then obtained as $\boldsymbol{\alpha}_{n+1}-\boldsymbol{\alpha}_n=\Delta\boldsymbol{\alpha}=\arg\min J$, thereby transforming the relation (10) to a minimization problem (16). Advantageously, this can be further combined with the principle of minimum potential energy, yielding a compact, discrete variational formulation of the evolutionary boundary value problem (Hackl and Fischer, 2008) that is solvable, e.g., using the finite element method with a suitable numerical strategy, cf. (Frost and Valdman, 2022).

4.4. Continuum mechanics

Many common material models can be reformulated to fit the GSM framework, see Tab. 1 and (Maugin and Muschik, 1994b; Houlsby and Puzrin, 2000, 2002) for instance. More importantly, the variational approach of GSM provides a *systematic way* for the derivation of evolution equations for internal variables and, thus, "can also be applied to rather complex systems, for which the classical approach involving application of phenomenological equations fails" (Fischer et al., 2014). This is particularly the case of multiple, strongly coupled dissipation processes (Einav et al., 2007).

The mathematical theory of convex functions provides useful relations between formulations in terms of generalized forces and fluxes, which are beneficial for recasting the physical understanding of the system into concrete constitutive equations. Under relatively mild mathematical conditions[8] on d, relation (10) is equivalent to the *dual formulation*

$$\dot{\boldsymbol{\alpha}}\in\partial_{\boldsymbol{A}}d^*(\boldsymbol{\chi},\boldsymbol{\alpha},\boldsymbol{A}), \tag{17}$$

where the *dual dissipation potential*, d^*, is given by the Legendre-Fenchel transform of d as follows

$$d^*(\boldsymbol{\chi},\boldsymbol{\alpha},\boldsymbol{A}):=\sup_{\dot{\boldsymbol{\alpha}}}\{\boldsymbol{A}\cdot\dot{\boldsymbol{\alpha}}-d(\boldsymbol{\chi},\boldsymbol{\alpha},\dot{\boldsymbol{\alpha}})\}. \tag{18}$$

Moreover,

$$d(\boldsymbol{\chi},\boldsymbol{\alpha},\dot{\boldsymbol{\alpha}})+d^*(\boldsymbol{\chi},\boldsymbol{\alpha},\boldsymbol{A})=\boldsymbol{A}\cdot\dot{\boldsymbol{\alpha}}. \tag{19}$$

More details can be found in (Rockafellar, 1970).

Example. To illustrate the above relations and the way they can be used in developing constitutive laws, let us find a dissipation potential for a microstructurally transforming material inspired by (Richards et al., 2013). Let α be a scalar representing the volume fraction of a new constituent and A be the thermodynamic generalized force controlling the process. For material parameters $A_0\geq 0, c>0$, the kinetics of the process is prescribed by the following relation

$$\dot{\alpha}=\begin{cases} c(A-A_0) & \text{if} \quad A\geq A_0,\\ 0 & \text{if } -A_0<A<A_0,\\ c(A+A_0) & \text{if} \quad A\leq -A_0. \end{cases} \tag{20}$$

[8] For functions satisfying (A1)-(A3), it is additionally the weak lower semi-continuity.

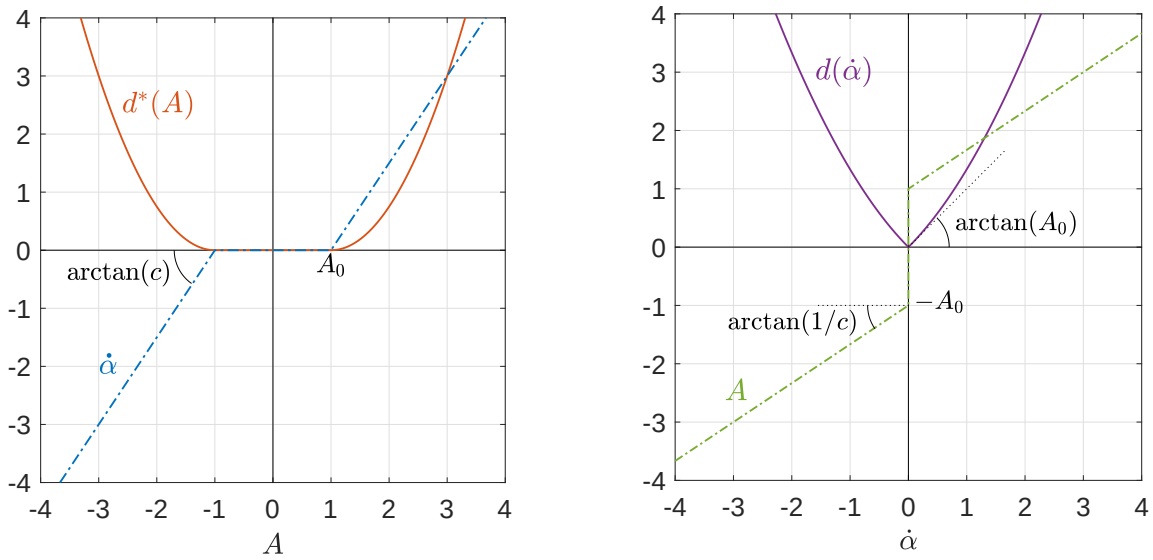

Fig. 1: Visualization of the kinetic relations and dissipation potentials treated in the example in subsection 4.4. with material parameters fixed to $A_0 = 1$ and $c = 1.5$.

Clearly, $A\dot\alpha \geq 0$ as required by (9). First, the dual form (i.e., the dissipation potential in terms of the generalized force) is for the fixed state variables resolved by applying (17) and employing (19), so one gets

$$d^*(A) = \begin{cases} \frac{c}{2}(A - A_0)^2 & \text{if} \quad A \geq A_0, \\ 0 & \text{if} \; -A_0 < A < A_0, \\ \frac{c}{2}(A + A_0)^2 & \text{if} \quad A \leq -A_0. \end{cases} \tag{21}$$

Then, (18) allows to recover the dissipation potential as

$$d(\dot\alpha) = A_0|\dot\alpha| + \frac{1}{2c}\dot\alpha^2. \tag{22}$$

Finally, the force-flux relation (10) takes the form

$$\begin{array}{ll} A = A_0 \frac{\dot\alpha}{|\dot\alpha|} + \frac{1}{c}\dot\alpha & \text{if} \;\; \dot\alpha \neq 0, \\ A \in [-A_0, A_0] & \text{if} \;\; \dot\alpha = 0. \end{array} \tag{23}$$

Note that a closed interval of values is admissible for the zero rate, see the second line. Such a response corresponds to an activated system with rate-dependent kinetics (i.e., of a visco-plastic type): the constant A_0 determines the critical force for activation of the process, and $1/c$ is the kinetics rate coefficient. Fig. 1 illustrates the derived relations. Let us note that for $A_0 = 0$, the process occurs even for an infinitesimal value of the driving force (i.e., becoming of a purely viscous type), which results in a completely smooth $d(\dot{\boldsymbol{\alpha}})$.

5. Modeling the thermomechanical response of shape memory alloys using GSM

Shape memory alloys (SMAs) are metallic materials that undergo a reversible solid-to-solid phase transformation between a high-temperature phase and a low-temperature phase. In addition to temperature changes, the transformation may be induced by applying stress to the high-temperature phase. The most common and widely used examples are alloys with nickel and titanium as the dominant constituents, known as NiTi-based SMAs, in which the two dominant phases are termed austenite and martensite, respectively.

From a mechanical standpoint, NiTi polycrystals exhibit exceptional features (Otsuka and Wayman, 1998). They can be strained up to several percent deformation and, upon unloading, fully recover their original shape; this is termed *superelasticity* and typically occurs at higher temperatures, where austenite is stable. If the material is deformed at low temperatures and its shape change is constrained, it generates a high recovery force against that constraint. Finally, loaded SMA structures can perform mechanical work when

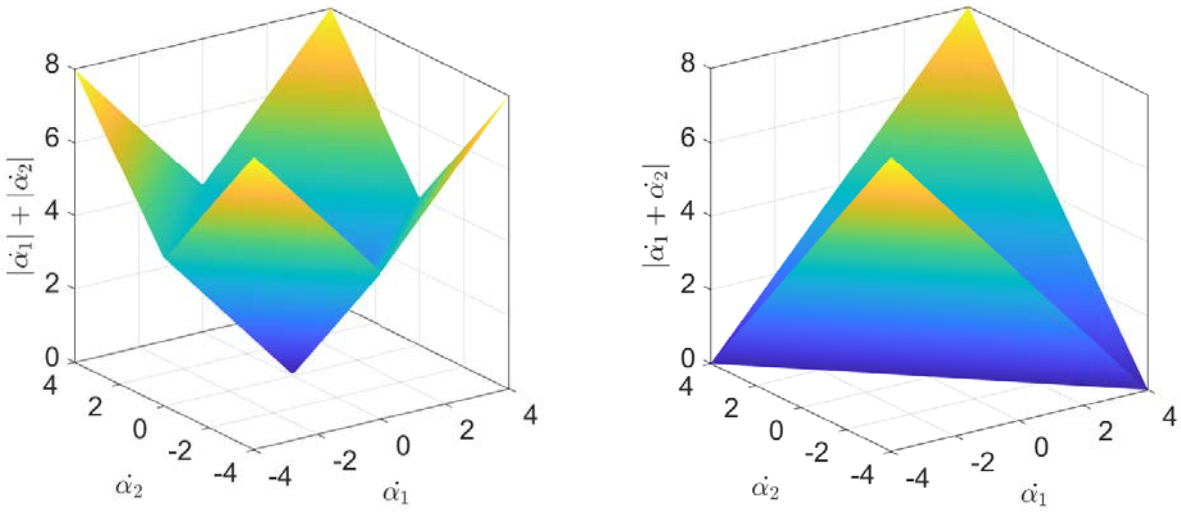

Fig. 2: The difference between the decoupled (left) and coupled (right) functions of the type used in the dissipation potential for SMAs is illustrated for a simpler situation with two scalar internal variables α_1, α_2 and functions $|\dot{\alpha}_1| + |\dot{\alpha}_2|$ and $|\dot{\alpha}_1 + \dot{\alpha}_2|$.

cycled between high and low temperatures. All these features have led to numerous smart and useful applications (Mohd Jani et al., 2014).

The mechanical response of NiTi exhibits many peculiarities, e.g., the pronounced asymmetry of the response in tension and compression, phase-dependency and anisotropy of properties, or a tendency towards strain localization. However, the fundamental challenge in constructing a robust and comprehensive constitutive model lies in the coupling among multiple dissipative processes associated with microstructural changes (phase transformation, (de)twinning, plasticity).

Based on the analysis of the hysteretic behavior and inspired by previous experimental findings, a particular form of the dissipation potential for the *fully reversible* behavior of NiTi SMAs was suggested in (Sedlák et al., 2012; Frost et al., 2016).[9] The vector of internal variables consists of two members: one scalar, ξ capturing the phase transformation, and the other tensorial, $\boldsymbol{\varepsilon}^{\mathbf{tr}}$, describing the martensitic microstructure reconfiguration (detwinning).[10] The dissipation potential takes the form

$$d_{\mathrm{SMA}}(T, \xi, \boldsymbol{\varepsilon}^{\mathrm{tr}}, \dot{\xi}, \dot{\boldsymbol{\varepsilon}}^{\mathrm{tr}}) = \begin{cases} c^{\mathrm{f}}(\xi)|\dot{\xi}| + k^{\mathrm{f}}(T)\|\dot{\xi}\boldsymbol{\varepsilon}^{\mathrm{tr}} + \xi\dot{\boldsymbol{\varepsilon}}^{\mathrm{tr}}\|, & \text{if } \dot{\xi} \geq 0, \quad (24) \\ c^{\mathrm{r}}(\xi)|\dot{\xi}| + k^{\mathrm{r}}(T)\left(\|\dot{\xi}\boldsymbol{\varepsilon}^{\mathrm{tr}}\| + \|\xi\dot{\boldsymbol{\varepsilon}}^{\mathrm{tr}}\|\right) & \text{if } \dot{\xi} < 0. \quad (25) \end{cases}$$

where $\|\cdot\|$ is (Frobenius) tensor norm. Material functions $c^{\mathrm{f}}(\xi), c^{\mathrm{r}}(\xi)$ and $k^{\mathrm{f}}(T), k^{\mathrm{r}}(T)$ are linear in their variables and all are chosen to ensure (A1)-(A3), cf. (Frost et al., 2025).

It is worth noting that the function d_{SMA} is 1-homogeneous in rates of internal variables, which corresponds to the rate-independent nature of both processes. The function depends on the "direction" of one process – the sign of $\dot{\xi}$ distinguishes the forward transformation (24) from the reverse one (25), and it is clearly *asymmetric* with respect to this. Moreover, due to the coupling of internal variables in the second term in (24), it is not possible to split the dissipation potential into two additive terms corresponding to the time evolution of the respective variables. This is in sharp contrast to the separation of processes that is common in uncoupled or weakly-coupled models, cf. (Einav et al., 2007). On the other hand, the separation of processes as in (25) allows for capturing the so-called mechanical stabilization effect in SMAs (Frost and Valdman, 2022).

The difference between the terms that combine both processes in d_{SMA} is illustrated in a much simpler setting in Fig. 2. Whereas the decoupled formula (left) is non-smooth only in situations where at least one flux vanishes, the coupled formula (right) is non-smooth even if both processes are active. Tackling non-

[9] An extension towards incorporating also the irreversible processes, namely plasticity, was suggested in (Sedlák et al., 2022).

[10] Let us also note that $\xi \in [0, 1]$ and $\boldsymbol{\varepsilon}^{\mathbf{tr}}$ is bounded to a convex set.

smoothness is crucial for the numerical implementation of such models, especially in methods that require gradients of the dissipation potential.

6. Conclusions

The GSM framework is a powerful tool for developing constitutive equations for materials behavior, particularly those with multiple interacting dissipative processes. The resulting models are thermodynamically consistent and mathematically rigorous; hence, they can be theoretically investigated using a priori developed methodologies and implemented in computational and simulation tools, thereby enabling sophisticated materials engineering and product design.

Nevertheless, as a "mere" tool, the GSM framework encourages researchers to draw on their creativity and materials-science insight to identify appropriate descriptors for the investigated material phenomena and to define the specific forms of the two constitutive functions. Consequently, this stimulates further enhancements, e.g., incorporation of (non-local) gradient theories (Nguyen, 2021) or analysis of GSM systems with two competing dissipative mechanisms (Mielke et al., 2025).

Acknowledgments

This work has been financially supported by the Czech Science Foundation [Project No. 24-10366S] and by the Operational Programme Johannes Amos Comenius of the Ministry of Education, Youth and Sport of the Czech Republic, within the frame of the project Ferroic Multifunctionalities (FerrMion) [Project No. CZ.02.01.01/00/22_008/0004591], co-funded by the European Union.

References

Coleman, B. D. and Gurtin, M. E. (1967) Thermodynamics with internal state variables. *J. Chem. Phys.*, 47, pp. 597–613.

Einav, I., Houlsby, G. T., and Nguyen, G. D. (2007) Coupled damage and plasticity models derived from energy and dissipation potentials. *Int. J. Solids Struct.*, 44, pp. 2487–2508.

Fischer, F. D., Svoboda, J., and Petryk, H. (2014) Thermodynamic extremal principles for irreversible processes in materials science. *Acta Mater.*, 67, pp. 1–20.

Frost, M., Benešová, B., and Sedlák, P. (2016) A microscopically motivated constitutive model for shape memory alloys: formulation, analysis and computations. *Math. Mech. Solids*, 21, 3, pp. 358–382.

Frost, M., Moskovka, A., and Knapek, M. (2025) Modeling the hysteresis of the thermomechanical response of superelastic β-titanium alloys. In Adámek, V., Jonášová, A., and Plánička, S., eds, *Proceedings of Computational Mechanics 2025*. West Bohemian University, Plzeň, pp. 35–38.

Frost, M., Sedlák, P., Heller, L., Kadeřávek, L., and Šittner, P. (2018) Experimental and computational study on phase transformations in superelastic NiTi snake-like spring. *Smart Mater. Struct.*, 27, pp. 095005.

Frost, M. and Valdman, J. (2022) Vectorized MATLAB implementation of the incremental minimization principle for rate-independent dissipative solids using FEM: A constitutive model of shape memory alloys. *Mathematics*, 10, 23, pp. 4412.

Frost, M., Ševčík, M., Kadeřávek, L., Šittner, P., and Sedlák, P. (2020) Reconstruction of phase distributions in NiTi helical spring: comparison of diffraction/scattering computed tomography and computational modeling. *Smart Mater. Struct.*, 29, pp. 075036.

Germain, P., Nguyen, Q. S., and Suquet, P. (1983) Continuum thermodynamics. *J Appl Mechanics*, 50, pp. 1010–1020.

Hackl, K. and Fischer, F. D. (2008) On the relation between the principle of maximum dissipation and inelastic evolution given by dissipation potentials. *Proc. R. Soc. London, Ser. A*, 464, pp. 117–132.

Halphen, B. and Nguyen, Q. S. (1975) Sur les matériaux standard généralisés. *J. Mecanique*, 14, pp. 39–63.

Horstemeyer, M. F. and Bammann, D. J. (2010) Historical review of internal state variable theory for inelasticity. *Int. J. Plasticity*, 26, pp. 1310–1334.

Houlsby, G. T. and Puzrin, A. M. (2000) A thermomechanical framework for constitutive models for rate-independent dissipative materials. *Int. J. Plasticity*, 16, pp. 1017–47.

Houlsby, G. T. and Puzrin, A. M. (2002) Rate-dependent plasticity models derived from potential functions. *J. Rheol.*, 46, pp. 113–126.

Junker, P., Makowski, J., and Hackl, K. (2014) The principle of the minimum of the dissipation potential for non-isothermal processes. *Continuum Mech. Thermodyn.*, 26, pp. 259–268.

Lubliner, J. (1969) On fading memory in materials of evolutionary type. *Acta Mechanica*, 8, pp. 75–81.

Maugin, G. A. and Muschik, W. (1994a) Thermodynamics with internal variables. Part I. General concepts. *J. Non-Equilib. Thermodyn.*, 19, pp. 217–249.

Maugin, G. A. and Muschik, W. (1994b) Thermodynamics with internal variables. Part II. Applications. *J. Non-Equilib. Thermodyn.*, 19, pp. 250–289.

Mielke, A., Rossi, R., and Stephan, A. (2025) On time-splitting methods for gradient flows with two dissipation mechanisms. *Calc. Var.*, 64, pp. 63.

Mielke, A. and Roubíček, T. (2015) *Rate-Independent Systems: Theory and Application*. Applied Mathematical Sciences. Springer New York.

Mohd Jani, J., Leary, M., Subic, A., and Gibson, M. A. (2014) A review of shape memory alloy research, applications and opportunities. *Mater. Design*, 56, pp. 1078–1113.

Nguyen, Q. S. (2000) *Stability and Nonlinear Solid Mechanics*. John Wiley & Sons, New York.

Nguyen, Q. S. (2021) On standard gradient plasticity and visco-plasticity. *Int. J. Solids Struct.*, 225, pp. 111038.

Otsuka, K. and Wayman, C. M. (1998) *Shape Memory Materials*. Cambridge University Press.

Richards, A. W., Lebensohn, R. A., and Bhattacharya, K. (2013) Interplay of martensitic phase transformation and plastic slip in polycrystals. *Acta Mater.*, 61, 12, pp. 4384–4397.

Rockafellar, R. T. (1970) *Convex analysis*. Princeton University Press.

Sedlák, P., Frost, M., Benešová, B., Šittner, P., and Ben Zineb, T. (2012) Thermomechanical model for NiTi-based shape memory alloys including R-phase and material anisotropy under multi-axial loadings. *Int. J. Plasticity*, 39, pp. 132–151.

Sedlák, P., Frost, M., Seiner, H., Heller, L., and Šittner, P. (2022) Thermodynamical model of NiTi shape memory alloys including plastic deformation mechanisms. In *SMST 2022: Extended Abstracts from the International Conference on Shape Memory and Superelastic Technologies*, Carlsbad: USA. ASM International, pp. 65–66.

Truesdell, C. and Noll, W. (1965) *The Non-Linear Field Theories of Mechanics*. Springer, Berlin.

32nd International Conference
ENGINEERING MECHANICS 2026
Medlov, Czech Republic, May 11 – 13, 2026

QUA VADIS MECHANICS
Subjective Point of View

Valášek M.[1]

Abstract: *The paper deals with the subjective point of view on the recent and current development in the area of engineering mechanics. It starts new technologies that have significantly influenced engineering mechanics. Then it discusses the area of structural mechanics in micro, mezzo, macro scale. Then it deals with embedded systems that is basis for mechatronic and controlled mechanical systems. The essential is the control challenges dealing with vibration, motion, control distribution and influence of nonlinearities. It continues with new ways of simulation techniques. Finally, it ends with design challenges and design principles applied to mechanical systems.*

Keywords: Mechanical system, new technologies, structural mechanics, embedded systems, control, simulation, design principles

1. Introduction

This paper deals with subjective point of view on the recent and current developments of mechanics as the basis of design of machines and mechanical engineering generally. This paper provides an overview of innovative concepts of mechanics on which the author participated – this is especially the subjective point of view. Despite of that the described innovative concepts represent results that have been investigated for various applications. This paper in its limited size is just an overview of topics.

2. New technologies

The key development impulses are besides the creativity of human designers and researchers the new technologies that open new possibilities. In mechanics they can be summarized into

- New materials, recently it was carbon fibers leading to composite materials
- 3D printing as a new manufacturing technology
- Embedded systems in general, not only embedded control systems as the basis of mechatronics
- New computing approaches – after recursive formulation of equations, it is parallel computing, AI as LLM models dealing with time series, quantum computing.

To the computing approaches it can be added the creativity as a new computing power. Creativity lies in our subconscious. The subconscious solves everything, and only the subconscious can provide new innovative solutions. Creativity lies in discussion, in dialogue. The key is to ask the right questions; the answers are already there (in the subconscious).

The new technologies always open the question whether machine components and entire machines with significantly improved mechanical properties can be achieved.

[1] Prof. Ing. Michael Valášek, DrSc.: Czech Technical University in Prague, Faculty of Mechanical Engineering, Center of Aviation and Space Research, Technická 4; 16000 Prague; CZ

ISSN: 1805-8256, doi: 10.21495/em2026-11

3. Structural mechanics

The structures are the visible applications of new concepts initiated by the application of new technologies. They can be classified into micro, mezzo and macro level. On the micro or mezzo level it is the creation of new materials with deterministic structure. Historically it was composite materials, currently it is metamaterials. These approaches use artificial cell structure creating new materiál with desired properties. A new approach on macro level is the combination of materials (Fig.1). A clamped beam with prescribed stiffness can be manufactured for example from dural only with some weight or from steel only with another weigth. If both materials are combined (1 is dural, 2 is steel) then the resulting structure has lower weight by 5+% than any of previous standalone material choices.

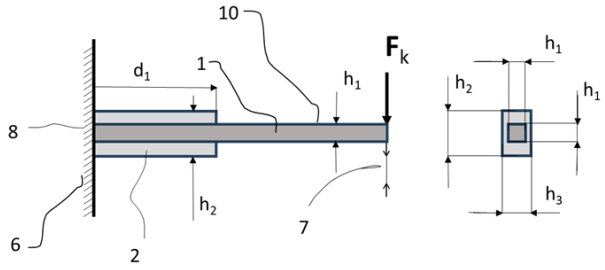

Fig. 1: Combination of materials.

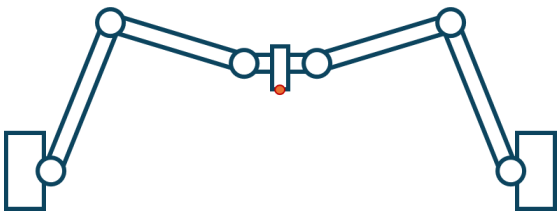

Fig. 2: Vault principle in connected robots.

Very remarkable it is the usage of nonlinearities. The nonlinearity is usually supposed as undesirable property, but it opens new areas of overcoming the limitations derived from linear world. Either the linear extension of influence is limited or the superposition is not happening. Example is the vault principle in Fig. 2. It was expected the addition of stiffness of two robots, but the resulting stiffness of 3.5 times of single robot is the consequence of vault principle. However, the nonlinearity in dynamics and control has larger and more significant influence.

This example of physically connected robots is an example of interconnected subsystems. To these interconnected systems it belongs various systems. They are the parallel kinematice machines, vault structures, mechatronic systems, collaborative robots, redundant measurement and nonlinear structural elements. The transition from serial kinematics of traditional robots through usual parallel kinematice machines to the redundantly actuated parallel kinematics machines is in Fig. 3 where the red arrows are drives. The redundant actuation means that the number of drives is larger than the number of DOFs. The advantage of parallel kinematics is that the drives are placed at the frame only. However, parallel kinematics suffers from singularities.

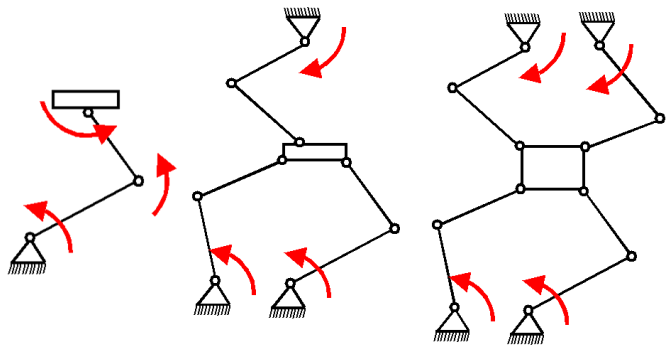

Fig. 3: Serial, parallel and redundant parallel kinematics.

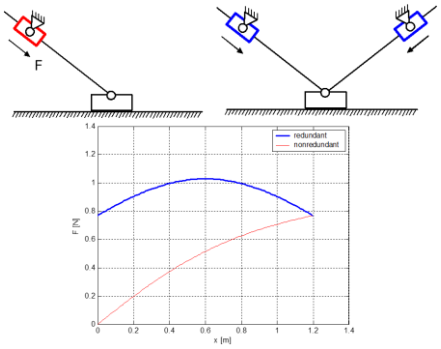

Fig. 4: Singularity removal by redundant actuation.

An example is in Fig. 4 where the actuator with force F moves the horizontal carriage in x direction. If the actuator and the carriage are one above the other then the actuator cannot transmit the force on the carriage. If there are two such drives, then the transmitted force from actuator is always nonzero and is almost uniform as i tis visible from the graph. The examples of redundantly actuated parallel kinematice machines are in Fig. 5. The left one (Sliding Star) has the potential to achieve three times increase of stiffness, eigenfrequencies and dynamics compared to seriál arm structure. The middle one (HexaSphere) enables to achieve +/- 100 degrees orientation capability that is for parallel kinematics exceptional. The right one (DoubleSphere) has the same orientation capability but achieved only with three drives.

The redundantly actuated parallel kinematics are the basis of cable driven robots and machines. Cable driven mechanisms require at least one additional force to the cable forces corresponding to the number of DOFs. Remarkable examples are in Fig. 6. In the figure left it is cable driven HexaSphere. In the middle the cable based mechatronic stiffness for gantry structures of machine tools is depicted. This can be passive as well as active structure. In the right it is the concept of multi-link cable driven robot with mechatronic stiffness. The traditional joints are stiffer (mass/stiffness ratio) than tensegrity structures. The cable based drives are lighter. The cable based mechatronic stiffness is multiplying the mass/stiffness ratio.

A specific redundantly actuated drive is the concept motor-on-motor (Fig. 13) that is capable to remove the dynamic part from the reaction forces in mechanisms.

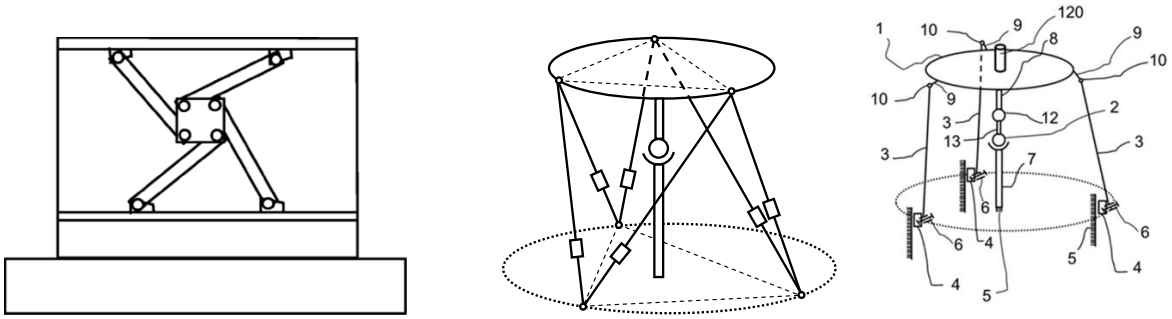

Fig. 5: Concepts of redundantly actuated parallel kinematics: Sliding Star, HexaSphere, Double Sphere.

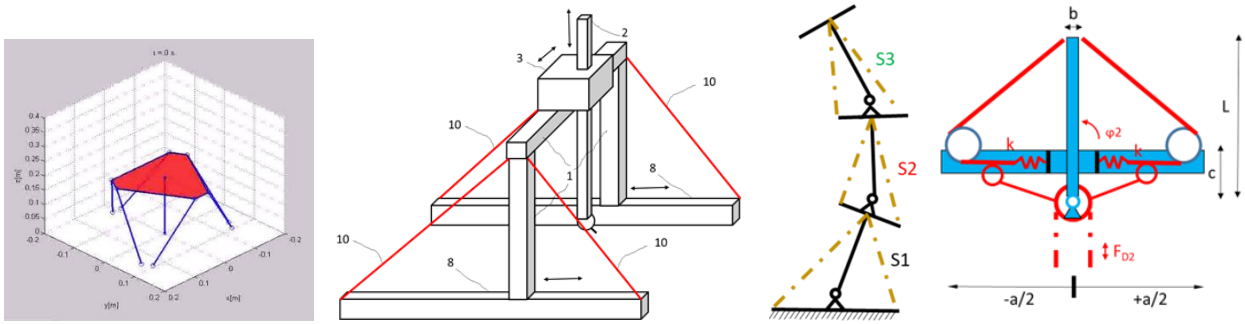

Fig. 6: Cable driven robots and machines.

The vault structures have been detected at connection of two robotic arms, example in Fig. 2. The composition of stiffness of the arms is super-linear.

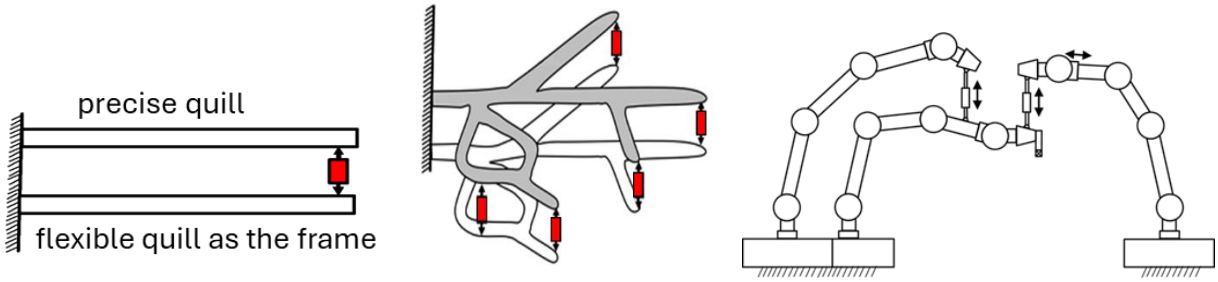

Fig. 7: Mechatronic stiffness.

The concept of mechatronic stiffness is the combination of interconnected substructures and mechatronics (active control). The concept and example are depicted in Fig. 7. Mechanical construction/structure is equipped with concurrent auxiliery structure and both structures are connected in connecting points by one or more actuators that are controlled based on deformation/motion of connecting points. The ratio of disturbance and actuator force is 1 and less. The basis with one actuator is in left figure. The middle figure describes multiple actuators and the right figure is robotic application. Another example of mechatronic system is the active spherical joint for +/- 160 degrees movability. It contains four DOFs from which always one axis must be blocked.

The examples of cooperating (collaborative) robots are in Fig. 2 and Fig. 9. In Fig. 9 left it is the application of connected kinematically redundant robot arms using the vault principle for operating within a cavity with increased stiffness. In Fig. 9 right it is a concept of manipulation with pliable objects, in particular the way how to push a pliable object through a hole. It always requires to use multiple robots.

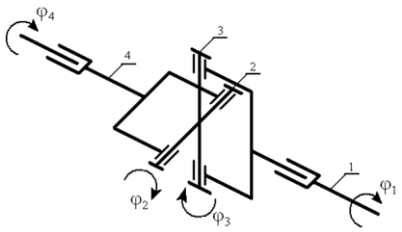

Fig. 8: Active spherical joint.

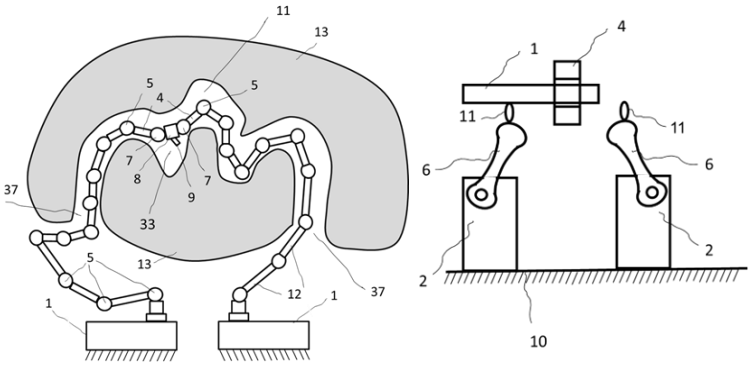

Fig. 9: Cooperating (collaborative) robots.

The consequence of redundant actuation is the redundant measurement. Its principle is in Fig. 10 left upper where instead of repetitive measurement in time the redundant measurements are carried out in the same time instant from various places in the space. The redundant measurement brings the phenomena of self-calibration and avoidance of uncertainty adding by increase of measurement accuracy. The application of this approach as a standalone redundant calibration and measuring machine (ReDCaM) for machine tools or robots is in Fig. 10 right upper. It has been used for mechanical ReDCaM with limited workspace in Fig. 10 left bottom. It has been extended into optical ReDCaM with large workspace in Fig. 10 middle left bottom. Another mechanical ReDCaM with extended workspace is in Fig. 10 right bottom. It has demonstrated the importance of angle measurements. The application of redundant measurement inside parallel kinematics machine (Sliding Star) is in Fig. 10 right bottom. In all cases the increase of accuracy is significant.

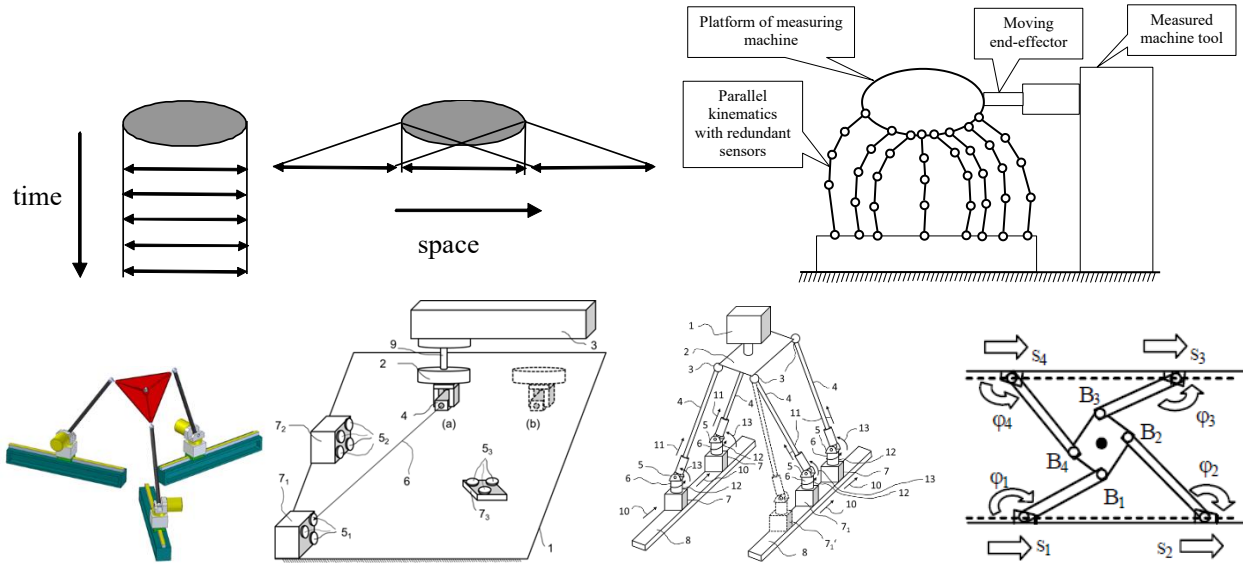

Fig. 10: Redundant measurement.

The development of suitable structural nonlinear elements for mechanical structures and machines is current research topic. Some examples are in Fig. 2, Fig. 6, Fig. 10.

The majority of machines benefits from possibility to modify their structure and parameters according to their state in which they operate. It is achieved by morphing their structure. The application of morphing forces in order to minimize the morphing effort is a challenge of movable structural mechanics. The concept of mechatronic stiffness is leading to favorable demand on the actuator's capacity. Examples of morphing mechanisms for aircraft wings are in Fig. 11.

The new technology of 3D printing enables to manufacture metamaterials, embedded functional structures and other embedded systems described in next section. The progress of mechanics by 3D printing will be in structures that are otherwise unmanufacturable by traditional technologies. An example of such embedded functional structure is in Fig. 12. It is acoustic barrier with surfaces with both finite curvatures. Another example is heat exchanger.

4. Embedded systems

Embedded systems were traditionally the electronics for control in mechatronic systems. 3D printing can manufacture general embedded systems. The usage of this approach is for manufacture of distributed actuators depicted in Fig. 14. There are four research problems: how to manufacture distributed actuators in material of machines, how to supply them by energy, how to control them and for which purpose use them.

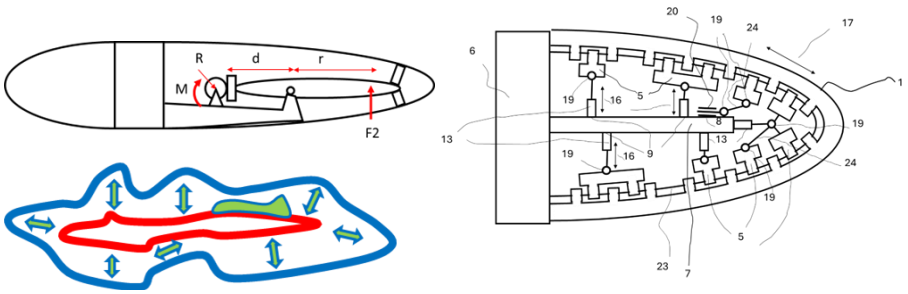

Fig. 11: Morphing of mechanical systems.

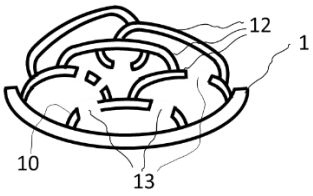

Fig. 12: Acoustic barrier.

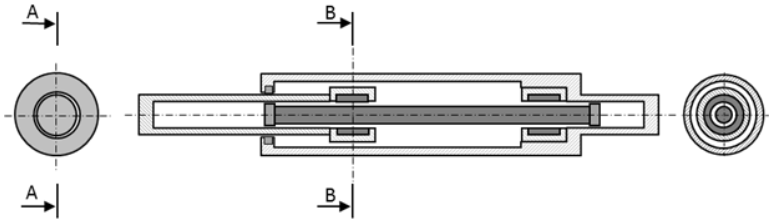

Fig. 13: Concept of motor on motor.

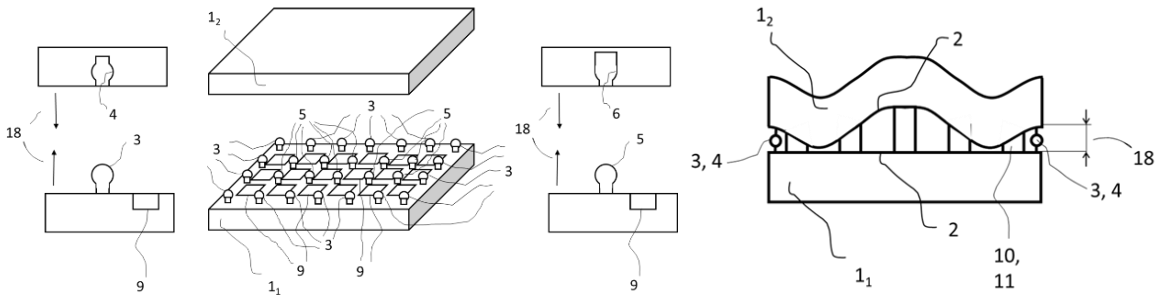

Fig. 14: Distributed actuators.

5. Control challenges

Control is through mechatronics today an important part of mechanical systems. However, the advanced application of control has many challenges. They are related to the stability and the need to know the system model. They are noncollocated vibration suppression – stable and model-free, the control of redundant drives that being deviation-based control leads to inaccuracy and instability, distributed control – stable and model-free, nonlinearity – what is it useful for?

The noncollocated vibration suppression means that the disturbance force Fk, Mk is applied in the place A, its influence is suppressed in the place B and the control actuation is available in the place C (Fig. 15). Interesting possibility to cope with that is the usage of vibration absorber with external control (Fig. 16) that enables to decouple the feedback influence on mechanical system. Another interesting possibility to

cope with that is the usage of Wave Based Control (Fig. 17) that is an exceptional control approach without model knowledge.

The control of redundant drives if it is based on deviation feedback suffers from potential instability and inaccuracy. This can be solved by application of Sliding Mode Control (SMC) that does not depend on deviations. Another question is how the redundant measurement can create the system model online.

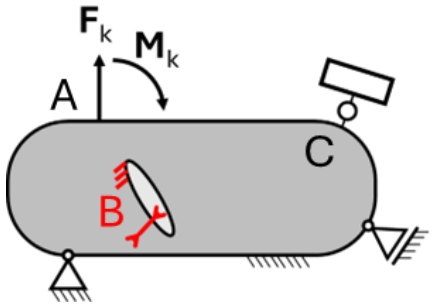

Fig. 15: Noncollocated vibration suppression.

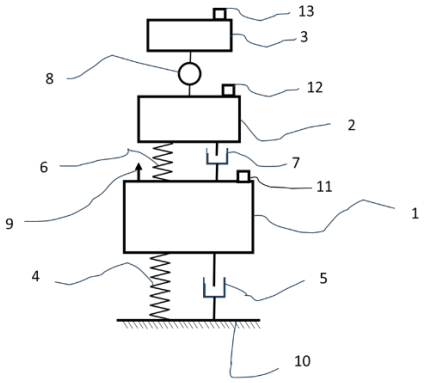

Fig. 16: Vibration absorber with external control.

Relatively new challenge in control of mechanical systems is their distributed control, its stability and requirement on knowledge of their model. A promising approach is the Wave Based Control (WBC) in Fig. 17 that offer stability without knowledge of the model. The difficult challenge in control of mechanical systems is the usage of appropriate nonlinearities. It can be the way how to overcome the limitation of their performance given in Bode sensitivity integral. Another fact is that nonlinearity is essential for the control of underactuated systems.

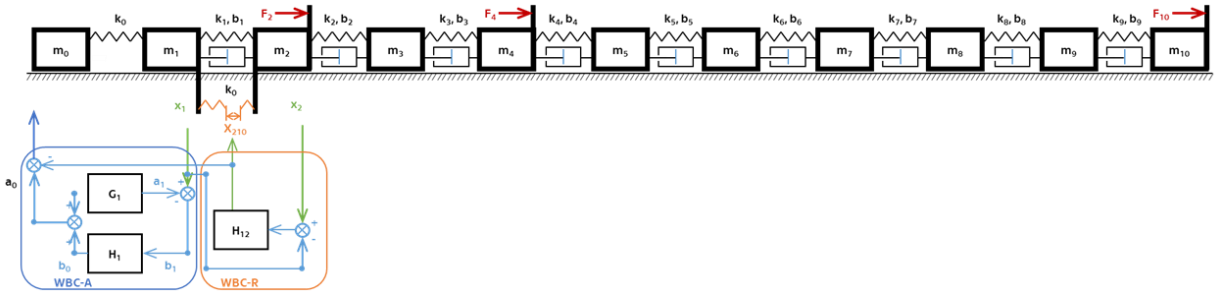

Fig. 17: Wave Based Control.

6. Simulation challenges

The design of mechanical systems requires their effective simulations. There have been developed the recursive algorithms for single computers. The new developments are expected using parallel computers, AI tools and quantum computing. Each of these areas are separate broader areas of interest and results.

7. Design challenges

The mechanical systems that use the above mentioned concepts must be designed into real machines. The design challenge is how to apply these new concepts and/or principles in design practice. The discussed principles are mechatronic stiffness, redundantly driven systems, redundant drives in parallel configuration, redundant measurement, motor-on-motor, externally controlled vibration absorber, nonlinearities.

8. Conclusions

New explored and yet not explored concepts in mechanics as well as the origins of new developments of these concepts have been briefly described. The references can be found at publications on webpage https://fs.cvut.cz/ustavy/sekce-ustav-mechaniky-biomechaniky-a-mechatroniky/ustav-mechaniky-biomechaniky-a-mechatroniky-12105/ustav-12105/lide-12105/?people=20462.

32nd International Conference
ENGINEERING MECHANICS 2026
Medlov, Czech Republic, May 11 – 13, 2026

PORTABLE SOLUTIONS FOR MEASURING DYNAMIC STRESS AND CURVATURE OF BUILDING STRUCTURES

Bayer J.[1], Urushadze S.[2], Černý M.[3]

Abstract: *For ambient vibration measurements on building structures, a strain gauge displacement sensor has been developed alongside two accessories that enable local relative deformations and/or curvatures of a structure to be measured at very low levels. With a resolution below 0.01 microns, the sensor has been tested in the 0–100 Hz frequency range, making it suitable for frequency measurements as well. The sensor can be mounted on the structure using magnets quickly and easily. This article presents two application examples that demonstrate the device's advantages and sensitivity. The device is intended for diagnosing damage in building structures, as relative deformations and curvatures directly reflect stresses within the structure.*

Keywords: Dynamic measurements, Strains, Curvatures, Portable transducer, SHM

1. Introduction

Ambient vibrations of building structures are typically measured using accelerometers or geophones. If we do not want to wait for windy conditions or other sources of external excitation, sensitive sensors are required. However, measured accelerations and velocities are not directly related to stresses in structures. In the case of low frequencies (i.e. under 1 Hz), the conditions for applying accelerometers are even less favourable (Ewins, 1984).

Although displacement and strain measurements are more convenient for assessing low frequencies, the sensitivity of conventional strain gauges is insufficient for measuring stresses caused by ambient vibrations. Furthermore, strain gauges cannot compete with accelerometers in terms of durability and ease of mounting (Rytter, 1993). Additionally, strain and curvature measurements are of interest as they have been proven to be good indicators of local damage (Padney, 1995; Maeck, 1999; Reynders, 2010).

When it comes to assessing or monitoring the condition of large building structures, measuring ambient vibrations is often the most widely used and cost-effective solution (An, 2019). In this context, the relationship between stresses and deformations is crucial, but requires the measurement of both ambient deformations and corresponding strains. New technologies, such as the interrogation units of fibre Bragg grating (FBG) sensors, which offer similar parameters (Anastasopoulos, 2025), are relatively costly.

Recently, the need to measure local deformations in the vicinity of impact loads has led to the displacement sensor being adapted for measuring curvatures, too. The remarkable properties of the device are demonstrated by practical examples of both applications of the sensor, taken from measurements.

[1] Ing. Jan Bayer, CSc.: Institute of Theoretical and Applied Mechanics of the CAS, Prosecká 809/76; 190 00, Prague 9; CZ, bayer@itam.cas.cz

[2] Ing. Shota Urushadze, CSc.: Institute of Theoretical and Applied Mechanics of the CAS, Prosecká 809/76; 190 00, Prague 9; CZ, urushadze@itam.cas.cz

[3] Ing. Miloš Černý: Institute of Theoretical and Applied Mechanics of the CAS, Prosecká 809/76; 190 00, Prague 9; CZ, mil@itam.cas.cz

ISSN: 1805-8256, doi: 10.21495/em2026-17

2. Displacement Transducer and Accessories

The sensor operates using standard Wheatstone bridge amplifiers. Its sensitive component is a clamped steel frame, in which horizontal displacement is linearly proportional to stress near the clamped supports, which are equipped with strain gauges. The forces required to displace the sensitive upper part of the frame are negligible compared to those acting due to vibrations in massive building structures. Therefore, the stresses measured at the clamped end are proportional to the displacements at the sensor's touch point. However, the transducer exhibits slight nonlinearity due to various factors, including the applied semiconductor strain gauges. When measuring at lower levels, it is recommended that the sensor is calibrated near the zero position to allow for a higher resolution, where the nonlinearity is negligible. The transducer was calibrated using an Instron Extensometer Calibrator with a resolution of 1 µm. Another possibility for calibration could be the use of a sine wave shaker.

The sensor is easy to apply due to its neodymium magnetic connections. Using magnets at the touch point also means that the measuring frame does not need to be pre-stressed in order to measure both negative and positive displacements. The gauge can be fixed to the structure quickly and easily.

The displacement transducer has a measurement range of ±0.5 mm, which corresponds to stresses of approximately ±200 MPa at the inner sensing part that is equipped with strain gauges. The characteristic relationship between internal strain and measured displacement is 1.9 m^{-1}. Both arrangements were tested in the 0–100 Hz frequency range. The accessories have a measurement base of 20 cm, with the option of a 10 cm base for strain measurements.

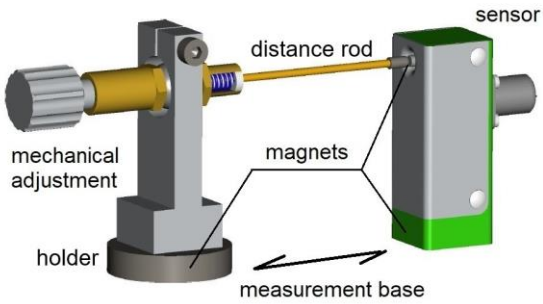

Fig. 1: Measuring arrangement for strain measurements (portable strain gauge)

When measuring strains (see Fig. 1), a reference part with fine adjustment is connected to the sensor via a distance rod. This setup enables the measurement of strains (i.e. relative displacements between the holder and the sensor divided by the measuring base length) in parallel with the connecting rod (i.e. the distance element).

Another accessory allows for measuring curvatures, with the transducer being mounted on an aluminium beam that has an opening at its centre, allowing the sensor to be connected to the structure using a connecting rod that is perpendicular to the surface of the structure. With this setup, the difference in vertical displacement is measured between the supports of the aluminium beam and the midpoint between them. This measurement setup allows for the detection of very low stresses in building structures caused by ambient vibrations, which will be demonstrated in the next section.

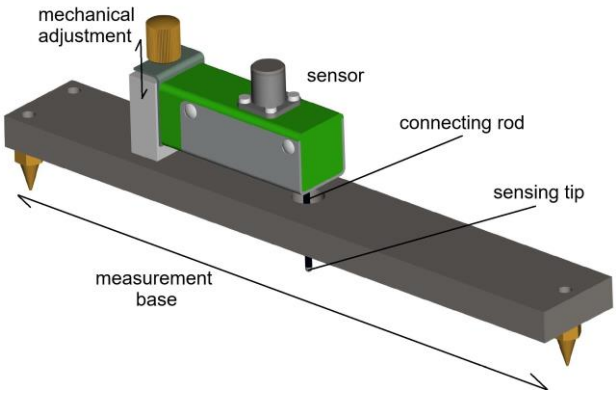

Fig. 2: Measuring arrangement for curvature measurements (deformeter)

This equipment was designed to measure dynamic stresses because a temperature change of 1°C can cause a relative displacement of 2.4 µm at the 20 cm base of common materials. Therefore, the transducer's sensitivity can only be used for static applications during very short measurements or when compensating for natural temperature drift. In dynamic applications, the pseudo-static part caused by temperature drift can easily be filtered out using a high-pass filter.

3. Experiments

3.1. Measuring the vibrations of the Cukrák Tower at its foundation

An experiment was conducted at the 195-metre-high Cukrák TV Tower, which is made of steel and has a 6-millimetre-thick outer coating and hollow vertical ribs. The tower's diameter at its base is 16 metres, and its first natural frequency is 0.29 Hz.

It should be noted that vibrations cannot be measured at the top of the tower due to the strong electromagnetic field surrounding it. However, accelerations can be measured without issue up to approximately half the tower's height using standard equipment.

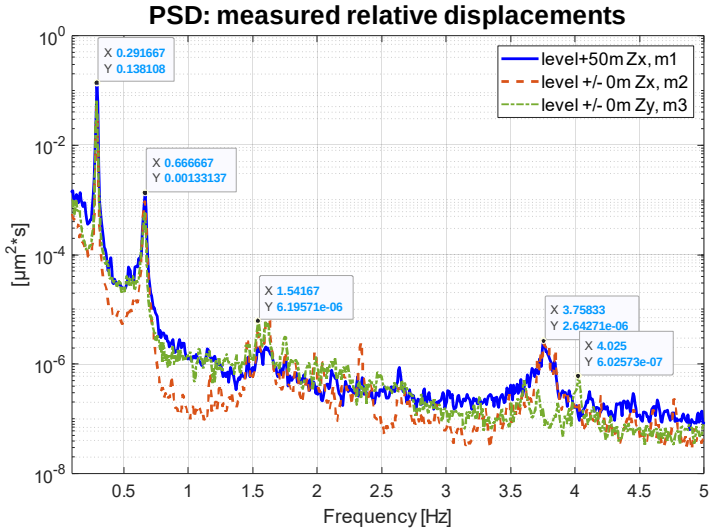

Fig. 3: Measured relative displacements using arrangement from Fig.1

Measurements were taken at two levels: +50 m and ±0 m on the ground floor. Mounting the sensor vertically to measure the dominant stresses on the steel ribs, along with the necessary mechanical and electrical adjustments, took no more than five minutes using a 20 cm measurement base. The sensor was successively placed on both levels (+50 m in the Zx plane and ±0 m in the Zx and Zy planes). To validate the measurements, a pair of sensitive accelerometers (Wilcoxon Research Model 731A) were used horizontally at the +50 m level. The signals were recorded using a DEWETRON measurement rack.

The new sensor provided a clear signal at both levels (see Fig. 4). The power spectral density (PSD) displacement spectra from the basement show that there is sufficient resolution and a clear signal even below 10^{-9} m using approximately 60 averages over one hour with a resolution of under 0.1 Hz. For instance, at a frequency of 4 Hz, an RMS strain of $3.9 \cdot 10^{-3}$ µε was measured, which corresponds to a stress of 0.8 kPa. Comparing with measured acceleration spectra confirmed the same position of dominant frequency peaks.

3.2. Measuring impact-induced local deformations on a steel beam

In connection with research on moving impact loads, it was necessary to measure the local response to a force impulse on a 4 m long, simply supported steel U-profile beam (210x50x5 mm). For this purpose, the curvature accessory was used. The impulse was applied using a 0.5 kg Brüel & Kjær impact hammer (type 8202).

Figure 4 shows the measured responses close to the midpoint (2.08 m) and near the support (3.74 m). Note that the double amplitude measured one second after impact was 0.054 µm (corresponding to a curvature of 5.4*10-10), and after 20 seconds the decay was still 0.007 µm, demonstrating a remarkable signal-to-noise ratio.

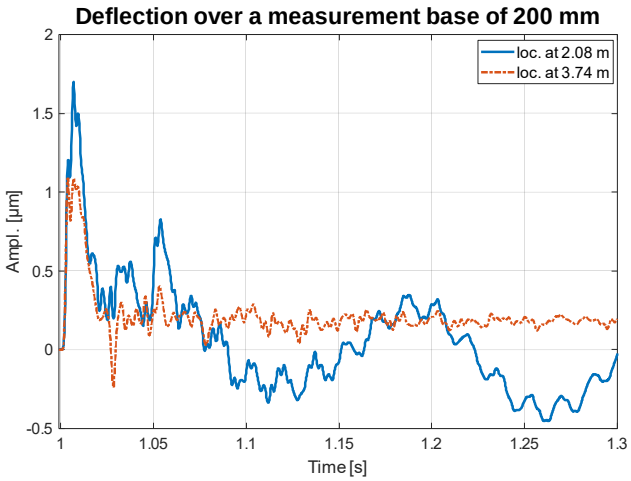

Fig. 4: Measured deflection over a meas. base of 200 mm due to impulse loading

4. Conclusions

A prototype of a new, portable relative displacement sensor has been introduced, along with two accessories. The sensor can be quickly and easily mounted on a structure. The sensor can measure dynamic displacements, as well as dynamic strains and curvatures, at ambient vibration levels. This cost-effective solution offers extremely high sensitivity, making it ideal for measuring natural frequencies and stress amplitudes.

The measurement approach presented here can be used to investigate wind-induced vibrations in tall, slender structures, where low-frequency responses and stress-related quantities play a dominant role. Notably, the capacity to measure dynamic strains and curvatures at ambient vibration levels establishes a robust foundation for the experimental analysis of aeroelastic phenomena, including galloping, flutter, and vortex-induced vibrations. The proposed measurement concept enables detailed observation of the structural response, which is often impossible with conventional acceleration-based measurements due to insufficient sensitivity. Therefore, the developed measurement methodology represents a promising experimental tool for future research focused on the interaction of wind-excited slender structures.

Further applications are anticipated, such as measuring crack activity in ageing historic structures and assessing the condition of civil engineering structures.

Acknowledgement

This research was partially funded by the Czech Scientific Foundation (project no. 24-13061S) and cofounded by the European Union under the INODIN project no. CZ.02.01.01/00/23_020/0008487. The financial support is gratefully acknowledged.

References

An Y., Chatzi E., Sim S-H., Laflamme S., Blachowski B., Ou J. (2019) Recent progress and future trends on damage identification methods for bridge structures. *Struct Control Health Monit., July 2019*, *26*: e2416,

Anastasopoulos D., Reynders E.P.B. (2025) Dynamic strain‐based monitoring of a historical Vierendeel truss bridge under changing environmental and support conditions. *Journal of Civil SHM 15,* 1465–1492, https://doi.org/10.1007/s13349-024-00888-5

Ewins, D.J. (1984), Modal Testing: Theory and Practice. *Mechanical Engineering Research Studies: Engineering Dynamics Series*, 2nd Edition, ISBN-10: 0863802184.

Maeck, J., De Roeck, G. (1999) Dynamic bending and torsion stiffness derivation from modal curvatures and torsion rates. *Journal of Sound and Vibration 225(1),* p.153–170

Pandey, A. K., Biswas, M. (1995), Experimental Verification of Flexibility Difference Method for Locating Damage in Structures. *Journal of Sound and Vibration 184(2)*, p. 311–328

Reynders E., De Roeck G.A. (2010) A local flexibility method for vibration-based damage localization and quantification. *Journal of Sound and Vibration 329, 2367–2383*, https://doi.org/10.1016/j.jsv.2009.04.026

Rytter, A. (1993) Vibration Based Inspection of Civil Engineering Structures. *PhD Thesis, Aalborg University, Denmark*

32nd International Conference
ENGINEERING MECHANICS 2026
Medlov, Czech Republic, May 11 – 13, 2026

INFLUENCE OF PIPING SYSTEM PARAMETERS ON WATER HAMMER USING 1D CFD APPROACH

Burda R.[1], Vondál J.[2], Sedlář M. [3], Abrahámek P. [4]

Abstract: *Water hammer poses a significant risk to the integrity of piping systems and pumps, particularly in critical applications such as nuclear power plants. This transient phenomenon is characterized by rapid changes in pressure and flow, often resulting from pump shutdowns or valve closures. This paper presents a detailed computational analysis of water hammer using the 1D CFD software Flownex. The study investigates the impact of various system parameters on the pressure response, specifically focusing on the influence of pump characteristics, the number of hydraulic accumulators, the gas-to-liquid ratio within those accumulators, and the presence of non-condensable air in the water. Results indicate that additional accumulators and optimized gas ratios mitigate pressure peaks. Also, the presence of non-condensable gas plays a crucial role in damping pressure fluctuations through the alteration of the fluid's bulk modulus.*

Keywords: Water hammer, Flownex, Accumulator, Air content, Mitigation of pressure pulsations

1. Introduction

The accurate prediction and mitigation of water hammer are critical for ensuring the safety and longevity of hydraulic systems, as the resulting rapid pressure fluctuations can lead to catastrophic structural failures, cavitation-induced fatigue, and severe damage to pumping components (Ghidaoui et al., 2005; Bergant et al., 2006). To model these transient events efficiently across complex pipe networks, one-dimensional (1D) Computational Fluid Dynamics (CFD) solvers are employed, offering a necessary balance between computational speed and the ability to capture essential flow characteristics averaged over the pipe cross-section (Himr, 2013). These simulations are indispensable for the sizing and optimization of protective devices such as hydraulic accumulators, which act as local energy reservoirs to absorb pressure surges and prevent column separation.

2. Method

The Flownex software is used in the analysis, which is based on the numerical solution of the equations of motion and heat transfer. A 1D CFD approach to simulate fluid flow in piping systems is used, which takes into account the flow parameters averaged over the pipe cross-section. Fluid compressibility and pipe wall flexibility are also included and the adaptive time stepping algorithm is used to adjust the time step based on the rate of change in flow. Single-phase water is used, and the algorithm can drop to negative values of pressure, while not going into cavitation. Therefore, regions of negative pressure only indicate the phase change in real application.

The piping system contains 2 outlet branches with up to 6 pumps and 5 accumulators (see Fig. 1). The 3 and 3 pumps are connected with the connecting valve and all the pumps have their own check valve to protect from water hammer during system failure. With the connecting valve the most dangerous scenario

[1] Ing. Radim Burda, PhD.: SVS FEM s.r.o., rburda@svsfem.cz
[2] Ing. Jiří Vondál, PhD.: SVS FEM s.r.o., jvondal@svsfem.cz
[3] RNDr. Milan Sedlář, CSc.: CENTRE OF HYDRAULIC RESEARCH, m.sedlar@sigma.cz
[4] Ing. Petr Abrahámek.: CENTRE OF HYDRAULIC RESEARCH, p.abrahamek@sigma.cz

ISSN: 1805-8256, doi: 10.21495/em2026-21

of 6 pumps into 1 outlet piping branch is possible but is never operational. The inlet and outlet share the same boundary conditions of atmospheric pressure and 20 °C temperature. The maximum volume of accumulators is 30 m^3 with 10 m^3 of initial gas with reference pressure of 1.5 MPa.

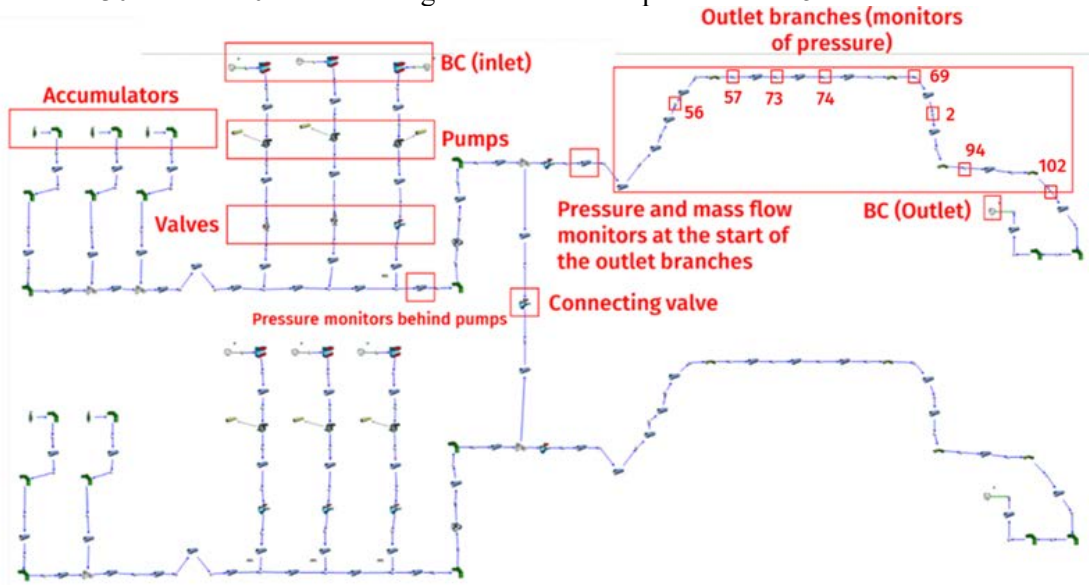

Fig. 1: Piping system of the pumping station.

The length as well as the elevation of the outlet branches can be seen in Fig. 2. The important nodes of the outlet branches are labelled with numbers that are then used for pressure monitoring. In Fig. 2 you can also see the characteristics of the closure of the check valve. The closing time as well as the valve flow coefficient can have a large impact on the final pressure course in the piping system during the water hammer mitigation. The characteristics of the pumps for various rotational speeds and even for negative flow rates need to be included as the flow can change direction during the shut-down of the pump. This is especially important when properly assessing the decreasing rotational speed during the shutdown. During the assessment of various parameters, different numbers of accumulators (ACC), pumps (C) and outlet branches (V) are assessed. The initial state of the piping system is the steady state operation of the pump station. During the first timestep the shut-down of the pump happens which replicates the power outage.

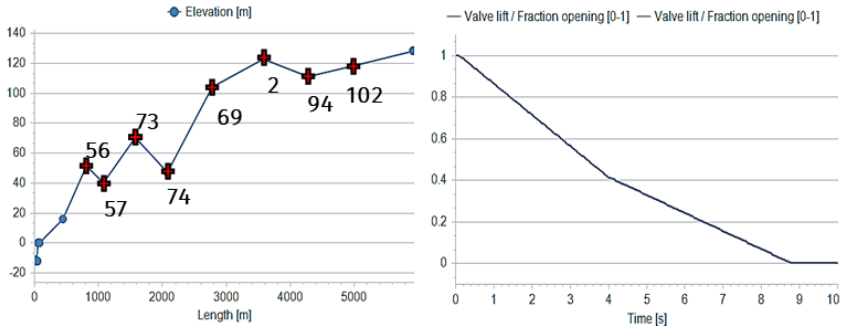

Fig. 2: Elevation of the nodes used for monitoring (left), characteristics of the check valve closure (right).

3. Results

This chapter is devoted to the effect of various system parameters on the resulting pressure waves during the water hammer phenomenon. The results are showcased as the pressure course as a function of time for all important nodes of the outlet branches. The simulation can also track the pressure behind the pump, the change of the gas/liquid content in accumulators and rotational speed and torque of the pump. Typically, there is a limit for the minimum and maximum pressure in the system. The minimum is usually connected to either saturation pressure when cavitation occurs and the atmospheric pressure when pipes start to deform inwards. The maximum pressure is connected to the potential of deforming outwards but is usually less problematic than the minimum pressure of the travelling wave. The minimum pressure typically occurs in the highest elevation point of the system whereas the maximum pressure occurs right after the connection of the pumps. The overall protection might mean increasing the accumulators in the

system, prohibiting the scenario all together or locally resolving the nodes of low pressure with air valve, which sucks air into the system a thus does not allow for the pressure to drop below atmospheric pressure.

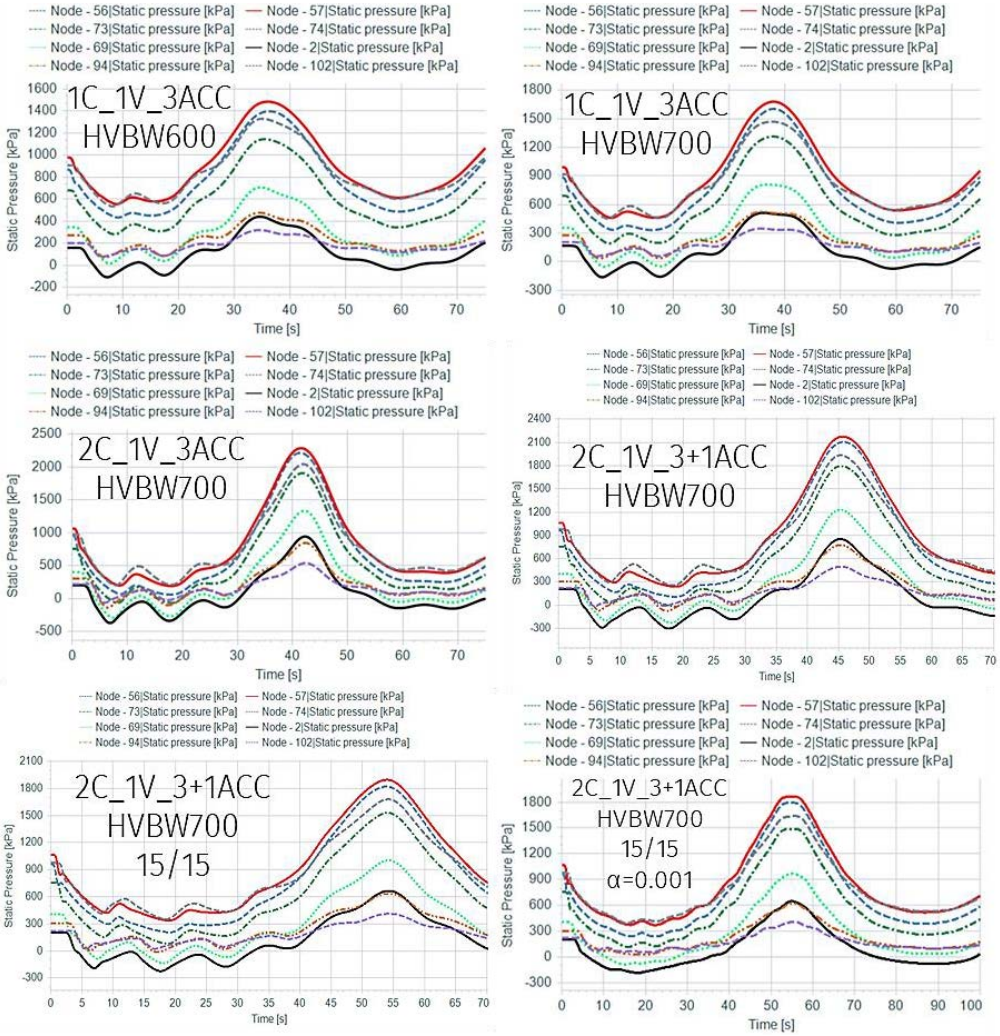

Fig. 3: Influence of various parameters of the pumping station on the pressure course in important nodes.

The first two images of Fig. 3 showcase the difference between pump HVBW600 and HVBW700, which is a change proposed by the customer to ensure sufficient water supply. We can see that both the pressure maximum and minimum for the same scenarios as pump 600 HVBW exceed the original values. The pump 700 HVBW allows for higher flowrate with the same pressure drop which results in stronger water hammer phenomenon. Based on these simulation results we can see that even with just 1 pump the pressure in nodes 69, 2, 94 and 102 goes into negative values, which indicates cavitation. The third image shows inclusion of the secondary pump to the previous scenario with HVBW700. We can clearly see that 2 pumps result in higher maxima and minima of pressure in the system, which is once again connected to the higher flowrate in the regular operation state. The saturation pressure is reached even for node 56 and 73. The fourth image shows introduction of additional accumulator. We can see that the introduction of just 1 accumulator almost resolved the node 56 and 102 but the rest of the nodes are still problematic. Introducing additional accumulators can be costly and therefore solving each piping system by introducing as many accumulators as possible is not ideal. The next chart shows the influence of the different ratio of gas/liquid in the accumulator at the start of the simulation. The ratio is changed to 15/15 m^3 from the original 10/20 m^3 gas/liquid content. The change results in the decrease of maximum pressure behind the pumps from 2800 kPa to 2550 kPa. The pressure minimum was also slightly affected (raising the pressure above 0 Pa for nodes 94 and 102). Therefore, the change is beneficial but does not resolve the potential of cavitation. The last image shows the introduction of air content which effects the bulk modulus of the water and thus damp the pressure fluctuations. The water is taken from the system which is estimated to have between 0.005 and 0.001 air volume fraction ($\alpha = 0.001$ is used). The change of the bulk modulus based on the air content implemented here can be found in Adamec (2010). From the image, it is clear that the region of lower pressure is influenced more, whereas the pressure peak

maximum does not change. This is in agreement with the Adamec (2010), where we can find constant value of bulk modulus for region of high pressure.

The simulations with all included factors were conducted for all operation scenarios (see Fig. 4). We can see that nodes 69 and 2 are still dangerous for all the simulated variants which are in accordance with the actual state of the physical piping system, which was supplemented with the air valves, which should also improve the nodes 94 and 102. The scenario 3C_1V_4Acc (3 pumps into 1 outlet branch) was restricted. This was mainly due to highest pressure peak behind the pumps.

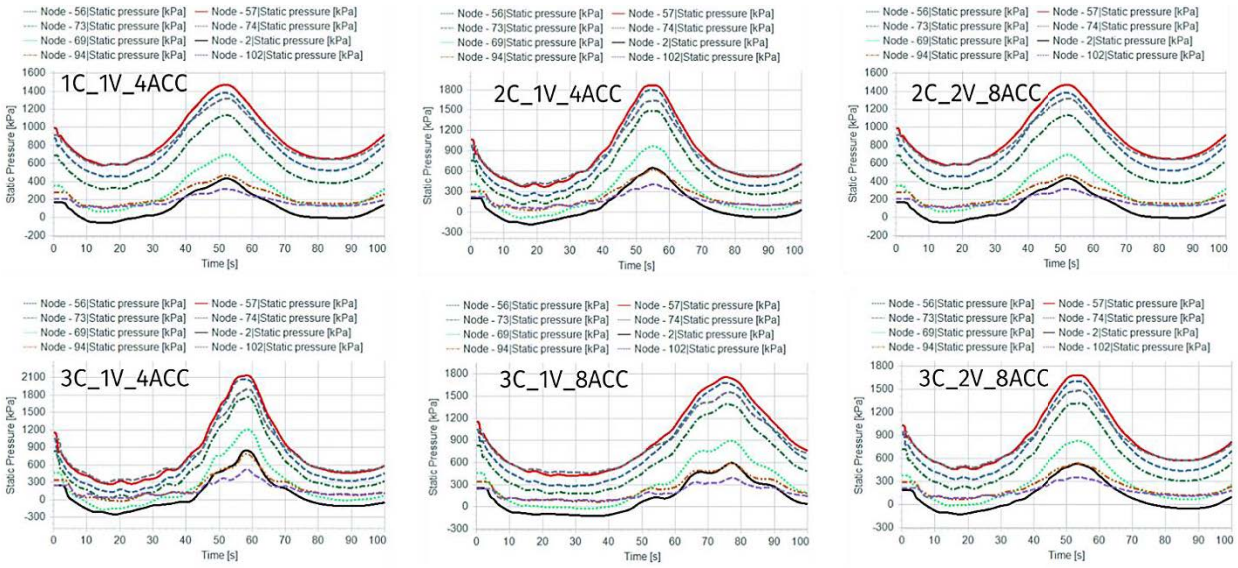

Fig. 4: The pressure in the important nodes of the outlet branches for all operation scenarios (HVBW700, gas/liquid ratio 15/15 m^3, $\alpha = 0.001$).

4. Conclusions

In this study the water hammer effects in a pumping station were analysed using 1D CFD simulations to evaluate system response during a power outage. It was found that while increasing the number of hydraulic accumulators and optimizing gas-to-liquid ratios effectively lowered maximum pressure peaks, these measures alone could not prevent cavitation at high-elevation nodes. The inclusion of non-condensable air content proved vital, as it lowered the fluid's bulk modulus and provided significant damping of pressure fluctuations. To ensure system integrity, strategic air valve placement was implemented at critical nodes to mitigate vacuum pressures. Future work will focus on the direct numerical inclusion of these air valves within the simulation environment to further refine the mitigation strategy.

References

Ghidaoui, M. S., Zhao, M., McInnis, D. A., & Axworthy, D. H. (2005). A review of water hammer theory and practice. *Appl. Mech. Rev.*, *58*(1), 49-76.

Bergant, A., Simpson, A. R., & Tijsseling, A. S. (2006). Water hammer with column separation: A historical review. *Journal of fluids and structures*, *22*(2), 135-171.

Himr, D. (2013). Numerical simulation of water hammer in low pressurized pipe: comparison of SimHydraulics and Lax-Wendroff method with experiment. In *EPJ Web of Conferences* (Vol. 45, p. 01037). EDP Sciences.

Adamec, R. (2010). *Vliv obsahu vzduchu na hydraulický ráz* [Influence of air content on water hammer] [Bachelor's thesis, VŠB – Technical University of Ostrava]. DSpace at VŠB-TUO. https://dspace.vsb.cz/handle/10084/81309

32nd International Conference
ENGINEERING MECHANICS 2026
Medlov, Czech Republic, May 11 – 13, 2026

DESIGN AND ENERGY MANAGEMENT OF ELECTRIC FAN MOTORIZED (EDF) VTOL UNMANNED AERIAL VEHICLE

Celik H.F.[1], Vatandas O.E.[2]

Abstract: *In this study, the design, production and some tests of an unmanned aerial vehicle (UAV) equipped with an electric ducted fan (EDF) propulsion system and vertical take-off and landing (VTOL) capability have been carried out. A tilt-based thrust vectoring system was employed to enable transitions between different flight regimes. During the design process, initial requirements were defined, and a conceptual design was created based on these parameters. The formulas used in the design calculations were transferred to Microsoft Excel, and various technical data-driven tables and graphs were generated to determine the most suitable design values. The UAV's overall dimensions and basic performance parameters were established. A preliminary study for production was completed, and the CAD drawings were adapted to be manufacturing-ready. As part of the production phase, mold designs were prepared for the outer body components of the aircraft, and these parts were successfully manufactured using carbon fiber reinforced composite material. This project was awarded first place in the inaugural year of the "Hangar Campus Innovation Program" organized by Turkish Aerospace Industries (TUSAŞ).*

Keywords: UAV conceptual design, Vertical Take-Off and Landing (VTOL), Electric fan motor, Tilt mechanism, Carbon fiber

1. Introduction

Today, unmanned aerial vehicles (UAVs) are widely used in military, civilian, agricultural, and security applications. While rapid advancements in hardware and software have produced new solutions, widespread use has revealed some operational and structural limitations. UAVs are primarily classified as fixed-wing and rotary-wing systems (Austin, 2010). Fixed-wing UAVs offer advantages such as high speed, long flight duration, and higher payload capacity, but are limited in rugged terrain and confined areas due to runway requirements. Although rotary-wing systems have vertical take-off and landing capabilities, eliminating the need for a runway, they are at a disadvantage in terms of range, speed, and payload capacity. (Bouabdallah, 2007; Austin, 2010).

To balance these contrasting characteristics, VTOL (Vertical Take-Off and Landing) fixed-wing UAVs have rapidly gained popularity in recent years, combining the flexibility of vertical take-off/landing with the efficiency of a fixed wing in horizontal flight (Ozdemir et al., 2014; Dündar et al., 2020; Tyan et al., 2017). However, a significant portion of existing VTOL designs are based on similar architectures; the use of different engines for vertical and horizontal flight on many platforms increases weight and cost, and also results in relatively low cruising speeds. This study presents a unique and high-performance VTOL UAV architecture that aims to reduce these limitations.

2. Design Approach

The UAV has 4 engines. Two of these engines will be located in sections integrated into the leading edges of the wings, while the other two will be positioned on the right and left sides of the vertical tail stabilizer.

[1] Huseyin Furkan Çelik , M.Sc .: Istanbul Gelisim University; Istanbul; TR, hfcelik@gelisim.edu.tr

[2] Prof. O. Erguven Vatandas, PhD.: Czech Technical University, Prague, CZ, osman.erguven@cvut.cz; Istanbul Gelisim University, Istanbul;TR

ISSN: 1805-8256, doi: 10.21495/em2026-25

Each engine is designed to be positioned at three different angles using a tilt mechanism:

- 0°: For forward thrust in horizontal flight mode,
- Approximately 65°: For stabilizing thrust during the transition phase,
- 90°: For vertical takeoff and landing, perpendicular to the ground.

The engine placement configuration has been optimized to allow the UAV to both perform VTOL (Vertical Take-Off and Landing) manoeuvres and improve aerodynamic efficiency during horizontal flight (Ozdemir et al., 2014; Tyan et al., 2017).

Stall speed is the lowest horizontal flight speed at which an aircraft's wings can no longer generate sufficient lift, causing the aircraft to lose altitude and cease to stay airborne. Technically, it occurs when the airflow over the wing separates from the surface as the angle of attack increases, resulting in a sudden decrease in lift (Austin, 2010). In this study, the approximate pitching moment slope value for the EDF-powered VTOL unmanned aerial vehicle was obtained through calculations based on Raymer's methods (Raymer, 2012), considering the wing and tail geometry, center of gravity position, and tail volume coefficient. (Table 1)

$$\frac{dC_m}{d\alpha} = -0.1473\ rad^{-1}$$

This value clearly demonstrates that the aircraft is statically stable in the longitudinal direction. The resulting stability margin not only ensures stability but also allows for aerodynamically stable flight performance. This result indicates a reduction in the need for control input, particularly for cruising flights in the fixed-wing segment. (Fig.1)

Tab. 1: Main design parameters of the UAV.

MTOW:	*40 kg*
Wing Area:	*1.045 m²*
Wingspan:	*1.9 m*
Wing Airfoil:	*NACA 4412*
Length:	*2.28 m*
Aspect Ratio:	*3.45*
Taper Ratio:	*0.466*
Cruise Speed:	*22.6 m/s*
Stall Speed:	*16.75 m/s*

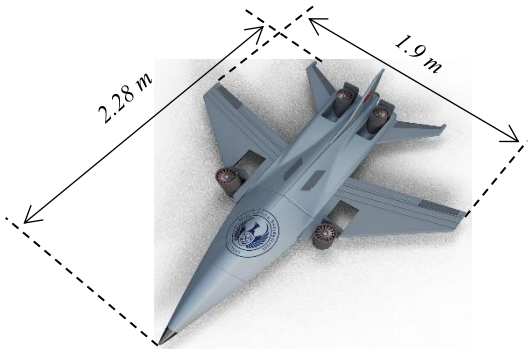

Fig. 1: The sketch of the UAV.

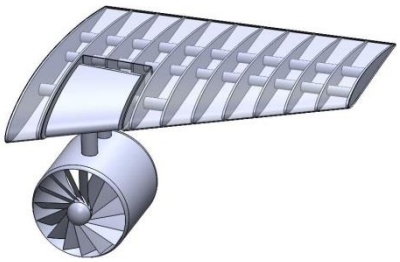

Fig. 2: The second revised wing/engine design.

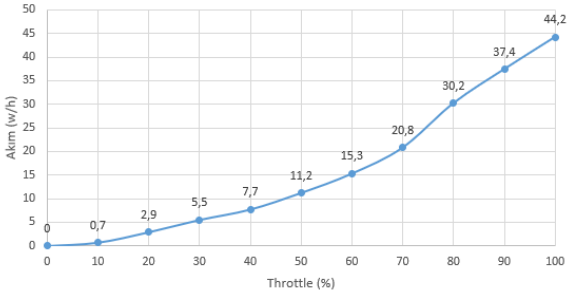

Fig. 3: Throttle adjustment – Electric Current graph.

3. Avionics Equipment

In this study, the Pixhawk Cube Orange+ (IMU V8) ADS-B Carrier Board was used as the flight control unit. The aim was to provide high data processing capacity and safety against sensor failures with a 480 MHz STM32H7 processor and a triple-redundant IMU architecture. The integrated ADS-B capability provides the infrastructure for collision avoidance approaches by detecting surrounding air

traffic. The system is configured with ArduPilot in a QuadPlane architecture (CubePilot, 2023; ProfiCNC & Hex Technology, 2022); the switching logic is designed through VTOL parameters (e.g., Q_TILT_* and related VTOL activation/assist parameters) such as motor-servo switching synchronization (ArduPilot Documentation, n.d.).

The integration includes: 4 x Dr. Mad Thrust 120 mm 12-blade EDF (650 kV) motors, 4 x high-torque servos (tilt), 2 x 12S 44.4V 16000 mAh Li-Po batteries, high-current ESCs, PDB, and sensor modules. The ESCs for the EDF motors are connected to the flight computer's MAIN OUT 1–4 lines, and the tilt servos are connected to the PWM OUT 5–8 range; the servos are powered by a 6V BEC. Power distribution is done via the PDB, and the flight computer is powered by an HV power module, incorporating voltage/current monitoring capability into the system (ProfiCNC & Hex Tech., 2022).

RF communication architecture is designed around three channels:

1. RC control: Low latency and long range connection via TBS Crossfire (868 MHz, CRSF),
2. Telemetry: Bidirectional data transfer (TELEM1/UART) with RFD900X (915 MHz) modules, robustness with FHSS/GFSK,
3. Video: 1080p video transmission with low latency (≈40 ms) via DJI FPV HD Air Unit (5.8 GHz). Antenna placements are physically isolated; shielded cabling and ferrite applications are planned for RF/GPS lines to protect against EMI risk from EDF sources (Spitzer, 2007).

4. Engine Energy Management and Battery Evaluation

The EDF motors used were designed for a 12S (44.4V) system with a power consumption of approximately 6.3 kW at around 120A and a static thrust range of 8–10 kg. Due to the limited availability of the manufacturer's datasheet, the motor's energy profile was determined by testing it with a 6S 22.2V 5000 mAh 45C Li-Po battery at different gas levels using a UNI-T UT221 ammeter for current/power measurements; the resulting characteristics were used as a basis for more reliably predicting the requirements of the 12S system (Fig.3).

To determine the power consumption behavior of the Dr. Mad Thrust 120 mm 12-Blade EDF 650kV motor under vertical take-off conditions, an experiment was conducted (Fig.4) with a fully charged Gens Ace 22.2V 5000mAh 45C 6S Li-Po battery at 100% throttle. This test aimed to investigate the system's energy consumption and thermal behavior when the motor produces maximum thrust. The experiment showed that the motor could operate continuously for approximately 7.1 minutes at 100% throttle. During the experiment, the motor, ESC, and battery temperatures were monitored at regular intervals, and no overheating that would pose a safety risk was observed. This test provided important data for evaluating the system's energy requirements during the vertical take-off phase and determining the appropriate battery configuration.

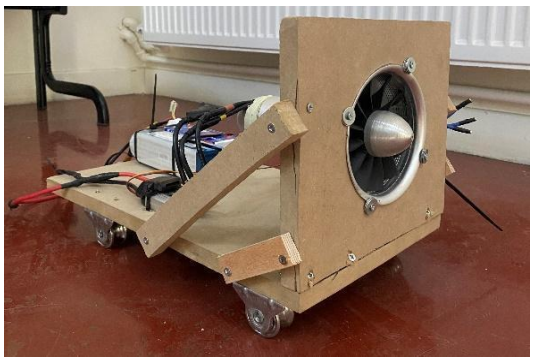

Fig. 4: EDF motor test setup.

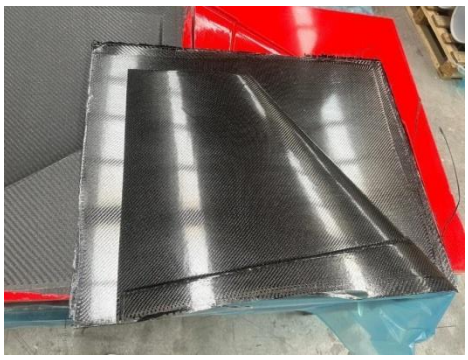

Fig. 5: Carbon fiber vertical tail fin fuselage.

5. Mold designs and production methods

In the design, a square-section carbon fiber tube extending along the fuselage is positioned as the main backbone element; it is structured to carry axial loads and bending moments. Bulkhead profiles are used at different stations to maintain the fuselage geometry and create the interfaces to which the composite outer surface is attached. These bulkheads are planned to be manufactured from laser-cut plywood

due to the advantages of rapid prototyping and machinability. Instead of traditional longeron elements, 3D-printed plastic stringer elements are preferred to reduce buckling of the outer covering and contribute to load distribution. Stringer placements are positioned according to load densities along the fuselage and mounted to the composite inner surface by gluing. This method provides low-cost and customizable production while also increasing assembly flexibility (Fig.5). In this study, assembly and integration are planned as the final stage aimed at bringing together the structural, mechanical, and electronic subsystems to make the aircraft flight-ready. The process includes not only physical assembly but also mechanical and electronic arrangements to ensure the compatible operation of the subsystems.

6. Conclusions

This study aimed to achieve vertical take-off/landing capability using four tiltable EDF motors and high lift performance at low stall speeds by using the NACA 4412 airfoil. Flight performance analyses were carried out using Raymer methods (take-off, cruising, range, climb rate, and landing), and parameter optimization was performed using some computational tools. Carbon fiber composite was chosen for the fuselage design to combine lightness and structural strength. During the production phase, the fuselage mold was prepared, the carbon fiber parts were produced using the vacuum infusion method, and the internal frame components were designed and made ready for production before assembly.

The platform's modular structure offers multi-purpose use potential in both the defense industry and civilian sectors. The system is adaptable to reconnaissance and surveillance, disaster relief, environmental monitoring, payload transport, and advanced autonomous mission profiles. In this respect, the study is not only an academic design work but also presents a VTOL UAV platform with commercial potential.

Suggestions:

i. For high-speed missions, the operational range and speed can be increased by developing a gas turbine-powered Version 2.
ii. Prior to flight tests, advanced simulations and control system validation tests should be performed, particularly due to the sensitivities of the center of gravity and stability.
iii. Mission duration and range can be improved by evaluating hybrid propulsion or new generation battery technologies in energy management.

In conclusion, this study has comprehensively presented the design, analysis, and manufacturing steps for an EDF-based VTOL fixed-wing UAV; a feasible and original platform has been developed.

Acknowledgement

The authors would like to express their sincere gratitude to all organizations and grant agencies especially Technology Transfer Office of Istanbul Gelisim University who have sponsored the successful completion of this work.

References

ArduPilot Documentation. “QuadPlane Support.” https://ardupilot.org/plane/docs/quadplane-overview.html

Austin, R. (2010). Unmanned Aircraft Systems: UAVS Design, Development and Deployment. Wiley.

Bouabdallah, S. (2007). "Design and control of quadrotors with application to autonomous flying". PhD Thesis, École Polytechnique Fédérale de Lausanne

CubePilot. (2023). Cube Orange+ Technical Reference Manual.

Dündar, Ö., Bilici, M., & Ünler, T. (2020). Design and performance analyses of a fixed wing battery VTOL UAV. Engineering Science and Technology, an International Journal, 23(5), 1182-1193.

Ozdemir, U., Aktas, YO, Vuruskan, A., Dereli, Y., Tarhan, AF, Demirbag, K., ... & Inalhan, G. (2014). Design of a commercial hybrid VTOL UAV system. Journal of Intelligent & Robotic Systems, 74(1), 371-393.

ProfiCNC & Hex Technology. (2022). Cube Orange+ Technical Reference Manual. CubePilot Documentation.

Raymer, D. (2012). Aircraft design: a conceptual approach. American Institute of Aeronautics & Astronautics, Inc..

Saengphet, W., & Thumthae, C. (2016, December). Conceptual design of fixed wing-VTOL UAV for AED transport. In The 7th TSME International Conference on Mechanical Engineering.

Spitzer, C. R. (2007). Digital Avionics Handbook. CRC Press.

Tyan, M., Van Nguyen, N., Kim, S., & Lee, J. W. (2017). Comprehensive preliminary sizing/resizing method for a fixed wing–VTOL electric UAV. Aerospace

32nd International Conference
ENGINEERING MECHANICS 2026
Medlov, Czech Republic, May 11 – 13, 2026

EXPERIMENTAL INVESTIGATION OF PROPELLER AERODYNAMIC DERIVATIVES

Čečrdle J.[1]

Abstract: *Whirl flutter is a specific type of flutter instability, for which the experimental validation of the analytical results is required. One of the key issues is the solution of propeller aerodynamic forces for which aerodynamic derivatives are used. Paper describes the mechanical concept of the used demonstrator that represents a sting-mounted nacelle with a motor and propeller and the methodology of the assessment of the derivatives. The main focus is paid on the wind tunnel test including the list of the tested variants, methodology of testing and the data assessment. Finally, the examples of the results are provided.*

Keywords: Whirl Flutter, Propeller Aerodynamic Derivative, W-STING Demonstrator

1. Introduction

Whirl flutter is a specific kind of aeroelastic flutter instability, which may appear on turboprop aircraft owing to the effect of rotating parts. It is driven by motion-induced unsteady aerodynamic propeller forces and moments acting in the propeller plane. It may cause unstable vibration, which can lead to a failure of an engine installation or a whole wing. Due to the unreliable analytical solution of propeller aerodynamic forces that are based on a propeller aerodynamic derivatives, experimental investigation is required. This paper takes up the previous work on the subject by the author (Čečrdle, 2023).

2. Theoretical Background

The principle of whirl flutter phenomenon is described on the simple mechanical system with two degrees-of-freedom with a flexible engine mounting and a rigid propeller (see figure 1). This system has two independent mode shapes. Considering propeller rotation, the gyroscopic effect causes both independent mode shapes to merge into the whirl motion. A propeller axis shows an elliptical movement. The orientation is backward relative to the propeller rotation for the mode with the lower frequency (backward whirl mode) and forward relative to the propeller rotation for the mode with the higher frequency (forward whirl mode). The gyroscopic motion results in unsteady aerodynamic forces, which may under specific conditions induce whirl flutter instability. Considering small angles, the equations of motion become:

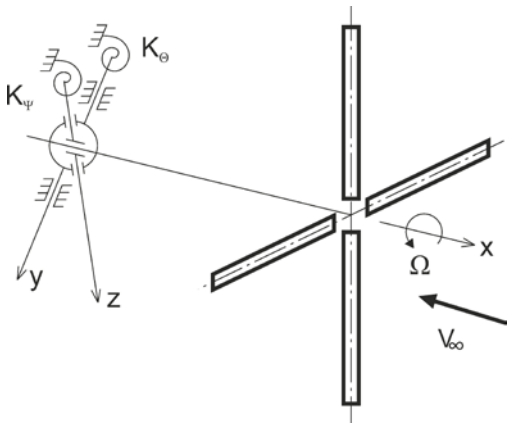

Fig. 1: Gyroscopic system with propeller

$$J_Y\ddot{\Theta} + \left(K_\Theta\gamma_\Theta/\omega\right)\dot{\Theta} + J_X\Omega\dot{\Psi} + K_\Theta\Theta = M_{YP} - aP_Z$$

[1] Ing. Jiří Čečrdle, Ph.D.: VZLU AEROSPACE (Czech Aerospace Research Centre), Beranových 130; 199 05, Prague; CZ, cecrdle@vzlu.cz

ISSN: 1805-8256, doi: 10.21495/em2026-29

$$J_Z\ddot{\Psi} + (K_\Psi\gamma_\Psi/\omega)\dot{\Psi} + J_X\Omega\dot{\Theta} + K_\Psi\Psi = M_{ZP} + aP_Y \quad (1)$$

Propeller aerodynamic forces and moments (right-hand side of eqn. 1) are determined using aerodynamic derivatives. Neglecting the aerodynamic inertia terms, the equations for the propeller's dimensionless forces and moments may be expressed as follows:

$$P_Y = qS\left(c_{y\Psi}\Psi^* + c_{y\Theta}\Theta^* + c_{yq}\left(\dot{\Theta}^*D/2V\right)\right) \quad P_Z = qS\left(c_{z\Psi}\Psi^* + c_{z\Theta}\Theta^* + c_{zr}\left(\dot{\Psi}^*D/2V\right)\right)$$

$$M_{YP} = qSD\left(c_{m\Psi}\Psi^* + c_{mq}\left(\dot{\Theta}^*D/2V\right)\right) \quad M_{ZP} = qSD\left(c_{n\Theta}\Theta^* + c_{nr}\left(\dot{\Psi}^*D/2V\right)\right) \quad (2)$$

Where q is a dynamic pressure, S is a propeller disc area, D is a propeller diameter, Θ^* and Ψ^* are effective pitch and yaw angles, respectively. The aerodynamic derivatives (c-terms) are the following:

$$c_{y\Theta} = \partial c_y/\partial\Theta^* \quad c_{y\Psi} = \partial c_y/\partial\Psi^* \quad c_{yq} = \partial c_y/\partial\left(\dot{\Theta}D/2V\right) \quad c_{yr} = \partial c_y/\partial\left(\dot{\Psi}D/2V\right)$$

$$c_{z\Theta} = \partial c_z/\partial\Theta^* \quad c_{z\Psi} = \partial c_z/\partial\Psi^* \quad c_{zq} = \partial c_z/\partial\left(\dot{\Theta}D/2V\right) \quad c_{zr} = \partial c_z/\partial\left(\dot{\Psi}D/2V\right)$$

$$c_{m\Theta} = \partial c_m/\partial\Theta^* \quad c_{m\Psi} = \partial c_m/\partial\Psi^* \quad c_{mq} = \partial c_m/\partial\left(\dot{\Theta}D/2V\right) \quad c_{mr} = \partial c_m/\partial\left(\dot{\Psi}D/2V\right)$$

$$c_{n\Theta} = \partial c_n/\partial\Theta^* \quad c_{n\Psi} = \partial c_n/\partial\Psi^* \quad c_{nq} = \partial c_n/\partial\left(\dot{\Theta}D/2V\right) \quad c_{nr} = \partial c_n/\partial\left(\dot{\Psi}D/2V\right) \quad (3)$$

Considering the symmetry (or antisymmetry), we can reduce the number of derivatives as follows:

$$c_{z\Psi} = c_{y\Theta}\,;\, c_{m\Psi} = -c_{n\Theta}\,;\, c_{mq} = c_{nr}\,;\, c_{zr} = c_{yq}\,;\, c_{z\Theta} = -c_{y\Psi}\,;\, c_{n\Psi} = c_{m\Theta}\,;\, c_{mr} = -c_{nq}\,;\, c_{yr} = -c_{zq} \quad (4)$$

In addition, we can neglect the negligible derivatives: $c_{mr} = -c_{nq} = 0$ and $c_{yr} = -c_{zq} = 0$. Finally, we obtain six independent derivatives: $c_{z\Theta}$, $c_{m\Theta}$, $c_{z\Psi}$, $c_{m\Psi}$, c_{mq} and c_{zr}. The first four ones may be investigated experimentally. The explanation of subscripts and other quantities can be found in sections 3 and 4.

3. Demonstrator Concept and Methodology of Measurement

Aeroelastic demonstrator for investigation of a propeller aerodynamic derivatives represents a sting-mounted nacelle with a motor and propeller. The demonstrator includes two degrees-of-freedom (engine pitch and yaw). Both pivots can be independently moved in the direction of the propeller axis. For the measurement, just a single degree-of-freedom is used while the other one is mechanically blocked. The propeller is powered by an electric motor with a nominal power of 15 kW. The power is sufficient to provide the measurement with the propeller in the thrust mode. The demonstrator sensor instrumentation includes measurements of both pitch (Θ) and yaw (Ψ) deformation angles using strain-gauge sensors and the measurement of both pitch ($K_\Theta\Theta$) and yaw ($K_\Psi\Psi$) pivot moments using a balance cell. Propeller and motor-related quantities include the propeller Ω, torque (M_k) and the immediate power (P) that are evaluated by a servo amplifier. The propeller thrust (T) is measured by a single component balance cell. Wind-tunnel related quantities include the angle of manipulator (Θ_m), airflow velocity (V) and dynamic pressure (q).

The static equations for the engine and propeller pitch and yaw deflection may be (from eqn. 1) expressed using the total moment-related derivatives (denoted by *) as:

$$k^2\Theta = \kappa(c^*_{m\Theta}\Theta + c^*_{m\Psi}\Psi) \qquad k^2\Psi = \kappa(c^*_{n\Psi}\Psi + c^*_{n\Theta}\Theta) \quad (5)$$

Note that the relations $c^*_{m\Theta} = c^*_{n\Psi}$ and $c^*_{m\Psi} = -c^*_{n\Theta}$ given by eqn. 4 were used in the latter equation.

For determination of $c_{m\Theta}$ and $c_{z\Theta}$ derivatives, the pitch-only arrangement of the demonstrator is used. Hence, for $\Psi = 0$, the total pitching moment coefficient (c^*_m) may be expressed as:

$$c^*_m = (K_\Theta\Theta/qSD) \quad (6)$$

Where $K_\Theta\Theta$ is the measured pitch pivot moment. The measurement is performed varying the pitch angle by the wind tunnel manipulator and the moment is evaluated with respect to the pitch angle (Θ). The slope of the measured curves is the reference pitch moment due to the pitch angle derivative ($c^*_{m\Theta}$). To separate the force and moment contributions to the total pitch moment, two configurations varying the distance between the gimbal axis and the propeller plane (a) are measured. The equations are:

$$c^*_{m\Theta 1} = c_{m\Theta} - (a_1/D)c_{z\Theta} \qquad c^*_{m\Theta 2} = c_{m\Theta} - (a_2/D)c_{z\Theta} \quad (7)$$

And the final expressions for aerodynamic derivatives become:

$$c_{m\Theta} = \big(1/(a_2 - a_1)\big)(a_2 c^*_{m\Theta 1} - a_1 c^*_{m\Theta 2}) \qquad c_{z\Theta} = \big(D/(a_2 - a_1)\big)(c^*_{m\Theta 1} - c^*_{m\Theta 2}) \tag{8}$$

For determination of $c_{m\Psi}$ and $c_{z\Psi}$ derivatives, the yaw-only arrangement of the demonstrator is used. Hence, the total yawing moment coefficient (c_n^{**}) may be expressed as:

$$c_n^{**} = (K_\Psi \Psi / qSD) = (c^*_{n\Psi}\Psi + c^*_{n\Theta}\Theta) \tag{9}$$

Where $K_\Psi\Psi$ is the measured yaw pivot moment. The measurement is performed varying the pitch angle by the wind tunnel manipulator and the moment is evaluated with respect to this pitch angle (Θ). The slope of the measured curves ($c^{**}_{n\Theta}$) and eqn. (9) are used to obtain the reference yaw moment due to pitch angle derivative ($c^*_{n\Theta}$) that is:

$$c^*_{n\Theta} = \big(c^{**}_{n\Theta} - c^*_{n\Psi}(\Psi/\Theta)\big) \tag{10}$$

The yaw-to-pitch angle ratio (Ψ/Θ) is constant just for a given blade angle and dynamic pressure. The reference yaw moment due to yaw angle derivative ($c^*_{n\Psi}$) is obtained using the antisymmetry (eqn. (4)) as $c^*_{n\Psi} = c^*_{m\Theta}$. Similarly, we use $c^*_{n\Theta} = -c^*_{m\Psi}$ to obtain the reference pitch moment due to yaw angle derivative ($c^*_{m\Psi}$). Separation of ($c^*_{m\Psi}$) to its components ($c_{m\Psi}$) and ($c_{z\Psi}$), i.e., the separation of force and moment contributions is carried out similarly as is mentioned above. The final expressions for aerodynamic derivatives are:

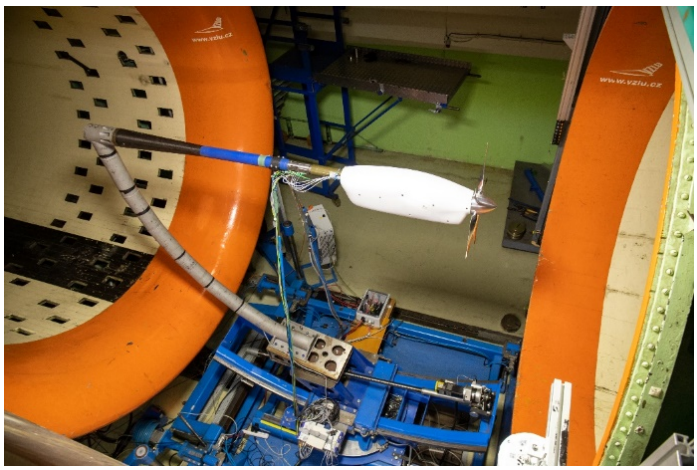

Fig. 2: Wind tunnel test arrangement.

$$c_{m\Psi} = \big(1/(a_2 - a_1)\big)(a_1 c^*_{n\Theta 2} - a_2 c^*_{n\Theta 1}) \qquad c_{z\Psi} = \big(D/(a_2 - a_1)\big)(c^*_{n\Theta 2} - c^*_{n\Theta 1}) \tag{11}$$

4. Test Arrangement, Measured Configurations and Results

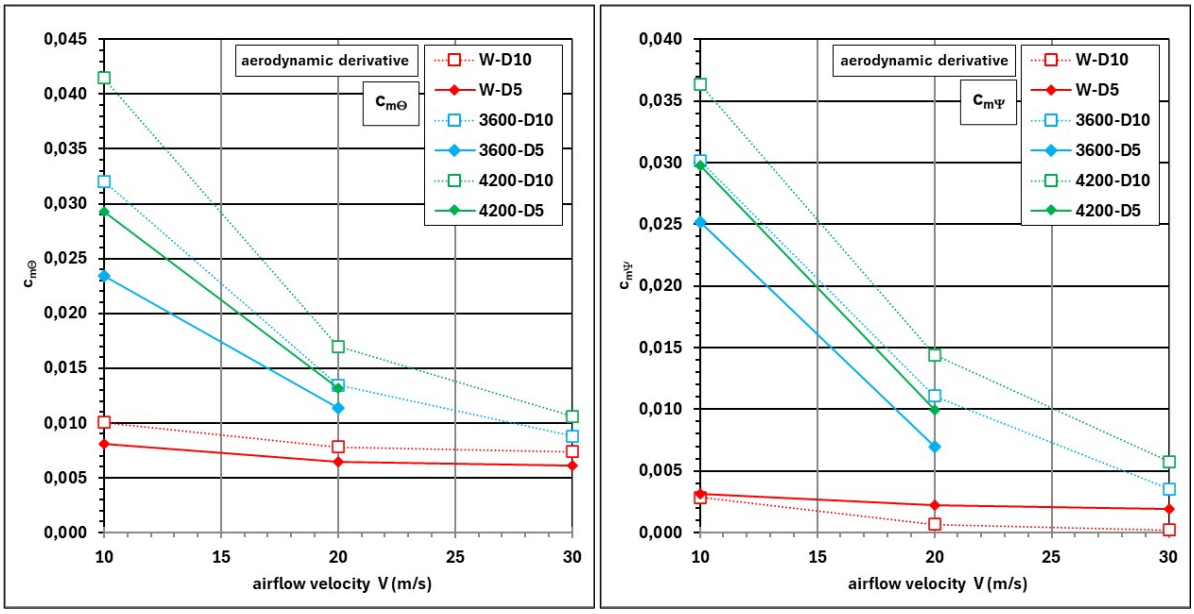

Fig. 3: Evaluated aerodynamic derivatives $c_{m\Theta}$ (a) and $c_{m\Psi}$ (b).

With respect to the above-described methodology of aerodynamic derivatives assessment, the test plan included four basic groups of measurements: 1) Pitch degree-of-freedom active, front pivot station, 2) Yaw degree-of-freedom active, front pivot station, 3) Pitch degree-of-freedom active, rear pivot station and 4) Yaw degree-of-freedom active, rear pivot station. In the above-mentioned four groups, changes of

secondary parameters were realized. The tested variants included a single choice of both yaw and pitch stiffness, a single choice of propeller's blade, two choices of blades' angle-of-attack, three choices of the propeller revolutions and 3 airflow velocities. The choices of parameters described form 54 variants in total. The wind tunnel test arrangement is documented in figure 2.

The final results include the following aerodynamic derivatives: 1) Pitch force due to pitch angle ($c_{z\Theta}$) and yaw force due to yaw angle ($-c_{y\Psi}$), 2) Pitch moment due to pitch angle ($c_{m\Theta}$) and yaw moment due to yaw angle ($c_{n\Psi}$), 3) Pitch force due to yaw angle ($c_{z\Psi}$) and yaw force due to pitch angle ($c_{y\Theta}$) and 4) Pitch moment due to yaw angle ($c_{m\Psi}$) and yaw moment due to pitch angle ($-c_{n\Theta}$).

As an example, $c_{m\Theta}$ and $c_{m\Psi}$ derivatives are presented in figure 3. The curves represent the measured variants in terms of the propeller revolutions (windmilling, 3600 rpm and 4200 rpm) and the blades' angle of attack (5 and 10 deg.).

Figure 4 demonstrate the evaluation of derivatives using the slopes of the pitch or yaw moment coefficients. The presented curves represent the blade angle of attack of 5 and 10 deg. and the states of front and rear hinge station and the pitch and yaw degree-of-freedom active (FP, RP, FY, RY).

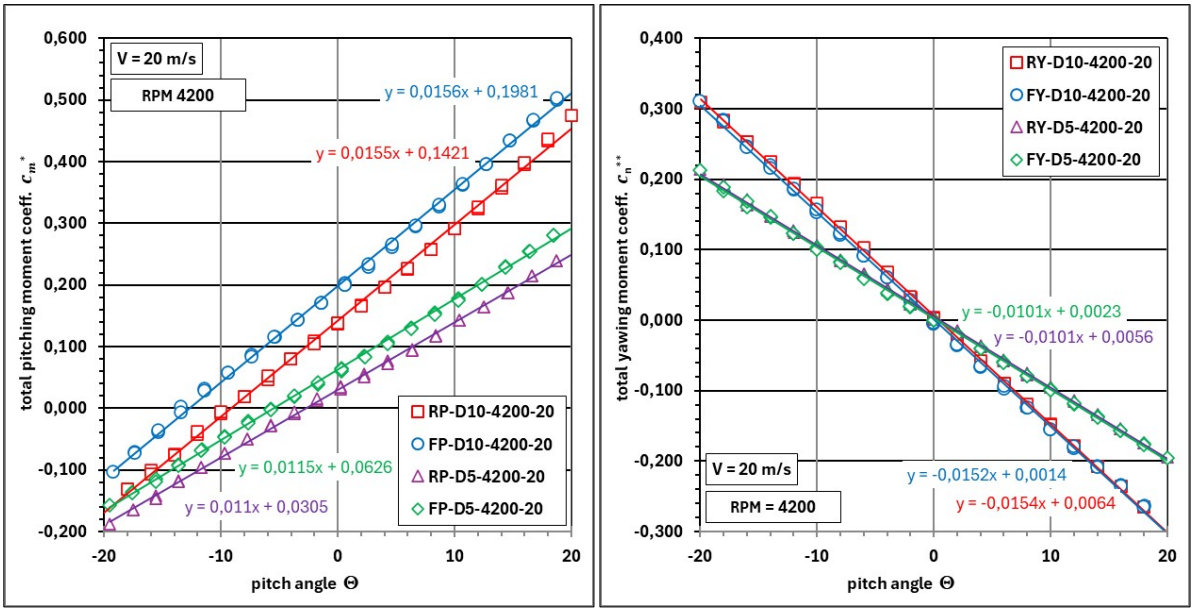

Fig. 4: Measured total pitching (a) and yawing (b) moment coefficient over pitch angle.

5. Conclusion

The paper deals with the experimental assessment of a propeller aerodynamic derivatives. A broad testing campaign in the 3m-diameter wind tunnel was accomplished. In general, the test results are in accordance with the expectations. In the future, the experimental results will be compared to the analytical results given by various analytical models and computational tools, and the experimental data will be utilised for verification and update of these tools.

Acknowledgement: Program and topic: HORIZON-JU-CLEAN-AVIATION-2022-01-SMR-01, Ultra Efficient Propulsion Systems for Short and Short-Medium Range Aircraft. Project nr. and title: 101102011, Open Fan for Environmental Low Impact of Aviation (OFELIA).

Disclaimer: Funded by the European Union. Views and opinions expressed are however those of the author(s) only and do not necessarily reflect those of the European Union or the Clean Aviation Joint Undertaking. Neither the European Union nor the granting authority can be held responsible for them.

References

Čečrdle, J. (2023) Mechanical Concept of Aeroelastic Demonstrator and Methodology for Experimental Investigation of Propeller Aerodynamic Derivatives, *Proc. 29th Conference Engineering Mechanics*, Milovy, pp. 55-58.

32nd International Conference
ENGINEERING MECHANICS 2026
Medlov, Czech Republic, May 11 – 13, 2026

ABSOLUTE POSITION SENSING IN AIRCRAFT CONTROL SYSTEMS USING 3D MAGNETIC SENSORS

Červenka M.[1], Koštial R.[2]

Abstract: *This paper proposes an absolute position sensing methodology for aircraft electromechanical actuators using 3D Hall effect sensors as a replacement for traditional, complex LVDT systems. While traditional sensing technologies often face limitations regarding mechanical wear, electromagnetic interference, and system complexity, the proposed approach leverages multi-axial magnetic field mapping to determine position as a proportional angular vector. Experimental validation across wide temperature range demonstrates reliable performance under extreme environmental conditions, establishing this non-contact method as a durable and viable alternative for short-stroke actuator applications*

Keywords: Absolute position estimation, Hall sensors, 3D magnetic sensors, Electromechanical actuator

1. Introduction

The primary objective of this project was to modernize an electromechanical actuator by replacing a brushed DC motor drive with BLDC (brushless DC) and appropriate motor control. Furthermore, the project necessitated replacing potentiometer-based measurement with LVDT (linear variable differential transformer) position sensing and a suitable LVDT driver and other signal conditioning circuitry. Although this still represents an ongoing project, work on an alternative sub-project has been initiated.

Its primary goal is to consequently also replace the LVDT position sensing utilising high-frequency analog signals and complex processing circuitry (both prone to future EMI/EMC (electromagnetic interference/compatibility) problems) by a feasible alternative based on magnetic field mapping of a displaced neodymium permanent magnet. Additionally, practical objective is also to reduce spatial footprint and manufacturing costs of the entire device.

Hence, the merit of this contribution is to evaluate how precise the absolute position estimation for a given electromechanical actuator could be, considering the range of environmental conditions in which the device must be capable of reliable operation.

2. Overview of position sensing in electromechanical actuators

The use of the Hall effect for position detection currently represents an established and well-documented method. The principle itself was discovered as early as 1879 by physicist Edwin Hall. A key milestone for the widespread adoption of Hall sensors was the development of semiconductor technologies and their integration onto silicon chips in 1960s and 1970s, which enabled deployment in the fields of automation, computing, and the automotive industry as stated in work of Ramsden (2001).

Compared to conventional technologies, such as electromagnetic resolvers or potentiometers, Hall effect-based sensors offer a number of critical advantages. Among the most significant is the non-contact nature

[1] Ing. Miroslav Červenka, PhD.: Institute of Aerospace Engineering, Brno University of Technology, Technická 2896/2, 616 69 Brno; CZ, cervenka@fme.vutbr.cz

[2] Ing. Rostislav Koštial, PhD.: Institute of Aerospace Engineering, Brno University of Technology, Technická 2896/2, 616 69 Brno; CZ, kostial@fme.vutbr.cz

ISSN: 1805-8256, doi: 10.21495/em2026-33

of the measurement, which eliminates mechanical wear and ensures high durability even in demanding operating conditions, while maintaining compact dimensions and low weight as described by Yenuganti et.al. (2025) and Crescentini et. al. (2020). These properties can be utilized when replacing standard industrial resolvers to reduce operating costs Kang et. al. (2020), or for precise spring deformation measurement of control wheel forces in internal pipe inspection devices by Jezny and Čurilla (2013). Currently, Hall effect sensors are also being intensively researched for the precise measurement of the speed and position of permanent magnet synchronous motors (PMSM) for example by Akrami et. al. (2023) or Du et al (2018).

Despite these benefits, the wider implementation of Hall sensors in the aerospace industry, especially in critical systems such as electromechanical actuators (EMA) for primary or secondary flight control remains limited. This limitation stems from stringent requirements for data integrity and electromagnetic interference (EMI) resistance. Another challenge is the influence of external conditions, where rapid temperature changes associated with the aircraft's ascent and descent can negatively affect sensor accuracy; this issue is addressed in detail by a Zhong et. al (2025) study utilizing advanced optimization models. The possibilities of integrating Hall sensors directly into the motor of an aerospace actuator (BLAC type) have already been explored in a Toman et. al. (2014) study.

3. 3D Hall Sensors Application and Idea Execution

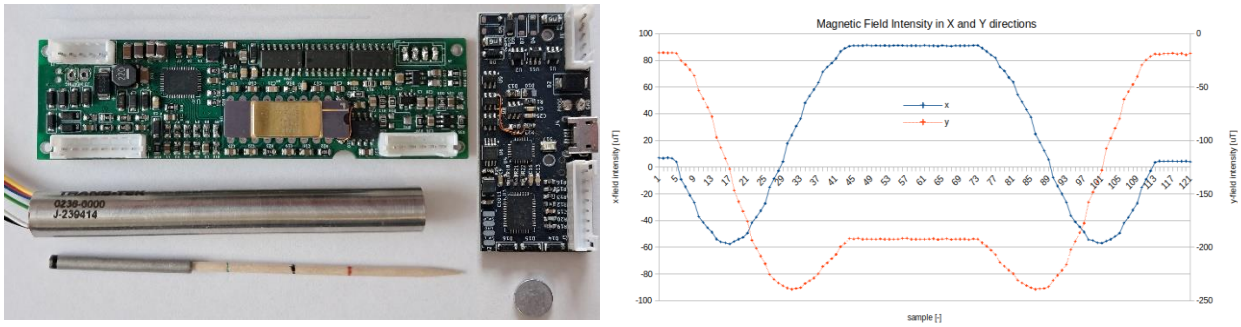

Fig.1: New and newer proposed electronics design (left), magnetic field intensity when extending and retracting the actuator's arm (right).

Fig.1 (left) shows the core and the LVDT transformer used for accurate position sensing and the developed electronics for the modernisation of the actuator (green PCB, left) while on the right there is the newly proposed solution with three 3D HALL sensors and the sensing neodymium magnet which is to be mounted onto the extendable electromechanical actuator's arm.

3.1 Absolute Position Estimation from the Magnetic Field

The principle of position estimation is the change of the magnetic field along with the extension/retraction of the arm. The measured magnetic field intensity values in X and Y axes can be seen in the Fig.1 (right). The Z-axis is omitted from this analysis because its variations are negligible (there is no movement along the Z axis and also measured magnetic field is too weak due to physical magnet orientation). This chart depicts a single extension followed by retraction of the actuating rod and shows how the intensity of the magnetic field transitions with the movement.

The absolute position is determined by calculating a two-dimensional vector rotating around a predefined center-point in the magnetic field intensity plot. The principle can be seen in Fig.2 (left). We chose a center-point *A* from which a vector in the magnetic field is calculated. Point *B* represents the initial position of the actuator's arm (retracted in this case) while its extension is represented by rotation of the vector anticlockwise over point *C* (middle/central position) up to point *E* where the arm is fully extended. Retraction of the arm then goes backwards along this C-shaped curve over the arbitrary position *D* into a fully retracted state marked by the letter *B*. Shape of this c-curve is determined by the physical geometry of the device under test while also the initial positions *B* and final position *E* are given by position of the magnet on the actuator's arm. The absolute position of the arm is then directly proportional to the angle formed by the vector with the positive direction of the X axis - the position angle φ.

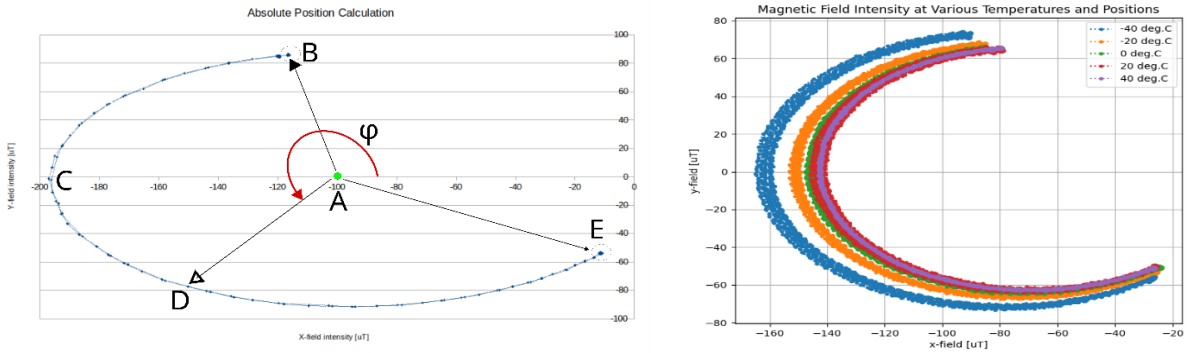

Fig.2: Principle of the position angle φ calculation (left), temperature drift of the C-curve used for position estimation (right).

3.2 Validation

As application of this project is targeted into DO-160 required temperatures range (from -55°C to +70°C), our concern was how will the evaluated magnetic sensors withstand these conditions. The following data originate from experiments conducted in a thermal chamber with focus mainly onto the lower of the temperature range (to validate reliability and survivability of the used electronic components) while tests from the higher ranges were limited due to used reference measurement equipment limitations. Hence the explored temperatures varied from -60°C to +40°C as monitored and controlled within the environmental chamber. Discrepancies are evident in the upper temperature range, resulting from inaccurate factory calibration of the magnetic sensor's thermometer subsystem.

Arrangement of this experiment was as follows: The actuator was set to its central position and remained stationary. The centre of the attached neodymium magnet which moves along with the actuator position was located in the y-axis of the hall sensor (the magnetic field in the x-axis was at its peak) while the field along the x-axis was symmetrical.

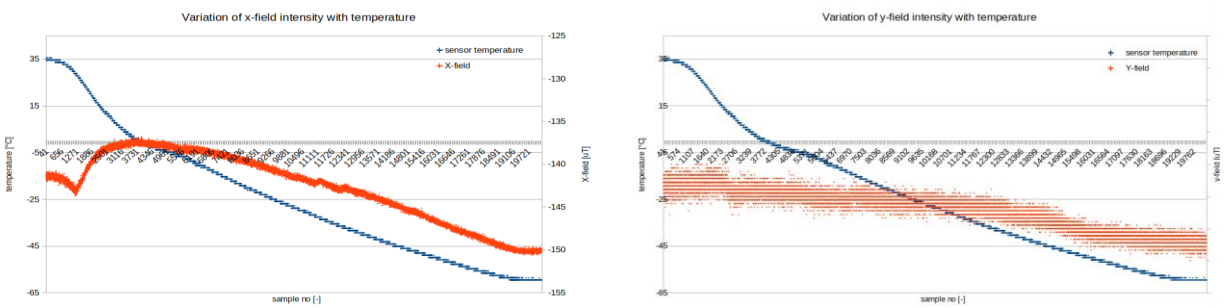

Fig.3: Temperature variation of the X and Y magnetic fields.

The charts on the Fig.2 (right) show impact of thermal drift on magnetic field intensity measurements across a broad temperature gradient. As the ambient temperature decreases, both the X and Y axes exhibit a clear negative correlation between temperature and measured intensity, indicating that the sensor's response is highly dependent on its internal thermal state. This phenomenon, often attributed to the temperature coefficient of the sensor's physical components, introduces systemic errors that may severely compromise the accuracy and repeatability of the data if not properly compensated for.

Besides the temperature variations in field measurement there is a secondary factor that might play a role in the absolute position estimation - noise of the magnetic sensor (Fig.3 and Fig. 4, red lines). While initial observations suggest high raw noise, it ultimately does not impact the position angle φ and resulting absolute arm position. Temperature drifts have the tendency to shift the arcuate trajectory in both dimensions. Estimates of the end positions (retracted (0% and extended 100%, points *A* and *E*) have moved slightly (which can eventually be compensated for) but the position angle φ along the movement track does not experience any such dramatic changes (Fig.2 right).

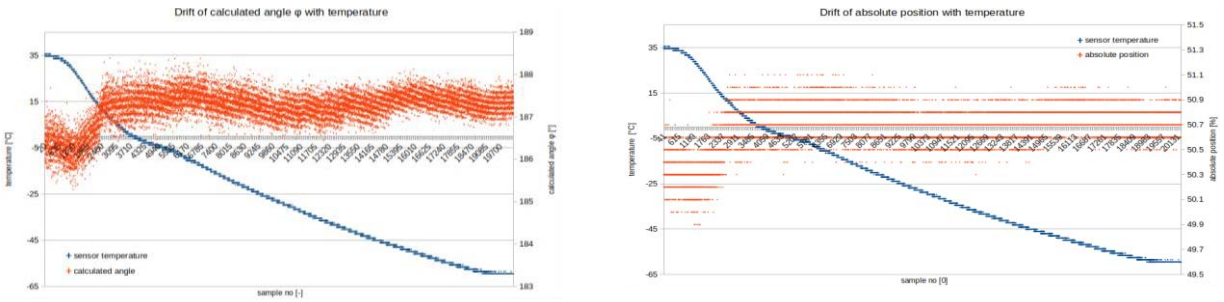

Fig.4: Drift of the calculated angle and absolute position with temperature.

3.3. Limitations

The usable magnetic field of the used neodymium magnet is limited. The specimen depicted in Fig.1 has a maximal measurable range around 2 cm. Depending on the available physical space a stronger / larger magnet could be used. If such an option is not feasible, we propose to use multiple sensors along the measuring edge (note the three identical ICs at the top edge of the black PCB) which can be switched among as needed or a specific data-fusion algorithm can be used to estimate the absolute position accurately along greater distances.

4. Conclusions

Absolute position estimation via magnetic field mapping represents a viable alternative to LVDT sensing. LVDT position sensing. Even though it encounters certain influences from temperature variations and inherent sensor noise, our proposed approach could serve as an alternative especially for short-stroke actuators. In comparison to potentiometer-based position measurement the magnetic approach offers virtually unlimited life-span for the device and less complexity and EMI problems than the LVDT approach. The limitations of short magnetic field ranges can be mitigated by utilizing multiple sensors which can be switched between or the data can be fused.

Acknowledgement

This document was created within the project TN02000009 - NaCCAS II, co-financed from the state budget by the Technology Agency of the Czech Republic within the National Centres of Competence Programme.

References

Akrami, M., Jamshidpour, E. and Frick, V. (2023) Application of Hall Position Sensor in Control and Position Estimation of PMSM - A Review. 2023 IEEE International Conference on Environment and Electrical Engineering and 2023 Industrial and Commercial Power Systems Europe (EEEIC / I&CPS Europe), pp. 1-6.

Crescentini, M., Syeda, S. F. and Gibiino, G. P. (2022) Hall-Effect Current Sensors: Principles of Operation and Implementation Techniques. IEEE Sensors Journal, 22, 11, pp. 10137-10151.

Du, S., Hu, J., Zhu, Y. and Zhang, M. (2018) A Hall Sensor-Based Position Measurement With On-Line Model Parameters Computation for Permanent Magnet Synchronous Linear Motor. IEEE Sensors Journal, 18, 13, pp. 5245-5255.

Kang, Y. G., Laborda, D. F., Fernandez, D., Reigosa, D. and Briz, F. (2020) Magnetic Resolver Using Hall-Effect Sensors. 2020 IEEE Energy Conversion Congress and Exposition (ECCE), pp. 2344-2350.

Jezný, J. and Čurilla, M. (2013) Position Measurement with Hall Effect Sensors. American Journal of Mechanical Engineering, 1, 7, pp. 231-235.

Ramsden, E. (2001) Hall-effect sensors. Advanstar Communications, pp. 1-280.

Toman, J., Singule, V. and Hadas, Z. (2014) Model of aircraft actuator with BLAC motor. 2014 16th International Power Electronics and Motion Control Conference and Exposition, pp. 197-202.

Yenuganti, S., Raju, S. S. and Settibhaktini, H. (2025) A brief review of Hall effect-based sensors. Sensor Review, ahead-of-print, ahead-of-print, pp. 1-12.

Zhong, L., Zhou, X., Jiang, W. and Liang, Q. (2025) Temperature Drift Correction of Hall-Effect Current Sensors via Harris Hawks Optimization Enhanced Surface Modeling. 2025 4th International Conference on Electronic Electrical Engineering and Automatic Control (EEEAC), pp. 272-275.

32nd International Conference
ENGINEERING MECHANICS 2026
Medlov, Czech Republic, May 11 – 13, 2026

DELAYED TURBULENCE DECAY CAUSED BY SWIRLER GRIDS

Duda D.[1], **Yanovych V.**[2], **Tomášková T.**[3] **Janský V.**[4] **Uruba V.**[5]

Abstract: *The swirler grids offer an interesting profile of turbulence decay. First, they create a lattice of aligned vortices, which behave similarly as the Two-dimensional energy condensate (vortices are parallel as in thin layer flows). Thus turbulent kinetic energy (TKE) grows downstream. Later, due to mutual interaction, the meandering grows until it destroys the vortex alignment. Once the vortices are no more parallel, their interaction switch to classical 3D direct energy cascade and the turbulence decays similarly as past a regular grid. In this contribution, we show the downstream profile of TKE measured for several swirler grids.*

Keywords: Mixing grid, Turbulent Kinetic Energy, Particle Image Velocimetry, Turbulence Decay

1. Introduction

While the grid turbulence is generally understood as the best experimentally available realization of Kolmogorov (1991)'s homogeneous and isotropic turbulence (HIT), the nature often contain very different cases: especially the geophysical flows are often effectively two-dimensional, see Izakov (2013) containing inverse energy cascade of Alexakis (2023). Similarly, the technical applications do not satisfy with HIT: the length-scales are not distributed beneficially, the turbulence decay is too steep, and the cooling or mixing efficiency is not easy to homogenize along flow path. Fractal grids developed by Valente and Vassilicos (2011); Hurst and Vassilicos (2007); Discetti et al. (2011); Gomes-Fernandes et al. (2012) solve such issues by creating larger-scale turbulent structures at the beginning followed by decay from the small scales.

In this contribution we summarize recent attempts at the University of West Bohemia in Pilsen regarding the development of *swirler grids* focusing to the downstream decay of Turbulent Kinetic Energy (TKE) measured by using Particle Image Velocimetry (this method is best described by Adrian et al. (2000)).

2. Experimental setup

This limited-length contribution does not allow the full description of the setup. The wind tunnel is described by Yanovych et al. (2019, 2021). The swirler grid is introduced by Duda and Yanovych (2024). The PIV equipment at UWB is examined by Duda et al. (2020a). The method of individual vortices is developed by Duda (2021). The measurement with model of nuclear fuel assembly is described by Duda et al. (2026).

3. Results

3.1. Downstream development of Turbulent Kinetic Energy

Figure 1 displays the decay of Turbulent kinetic energy (TKE) past various grids developed at the University of West Bohemia The solid black line represents a regular square grid by Duda et al. (2020b). The green

[1] Ass. Prof. RNDr. Daniel Duda, Ph.D.: Faculty of Mechanical Engineering, University of West Bohemia in Pilsen, Univerzitní 22; 306 14, Pilsen; CZ, dudad@fst.zcu.cz
[2] Ass. Prof. Ing. Vitalii Yanovych, DrSc.: Faculty of Mechanical Engineering, University of West Bohemia in Pilsen; Univerzitní 22; 306 14, Pilsen; CZ, yanovych@fst.zcu.cz
[3] Ing. Tetjana Tomášková, PhD.: Faculty of Education, University University of West Bohemia in Pilsen; Veleslavínova 42; 301 00, Pilsen; CZ, tomaskot@fpe.zcu.cz
[4] Ing. Vojtěch Janský: Elektrárna Dukovany II; Duhová 2; 140 00, Prague; CZ, vjansky@fst.zcu.cz
[5] Prof. Ing. Václav Uruba, CSc.: Faculty of Mechanical Engineering, University of West Bohemia in Pilsen, Univerzitní 22; 306 14, Pilsen; CZ, uruba@fst.zcu.cz

ISSN: 1805-8256, doi: 10.21495/em2026-37

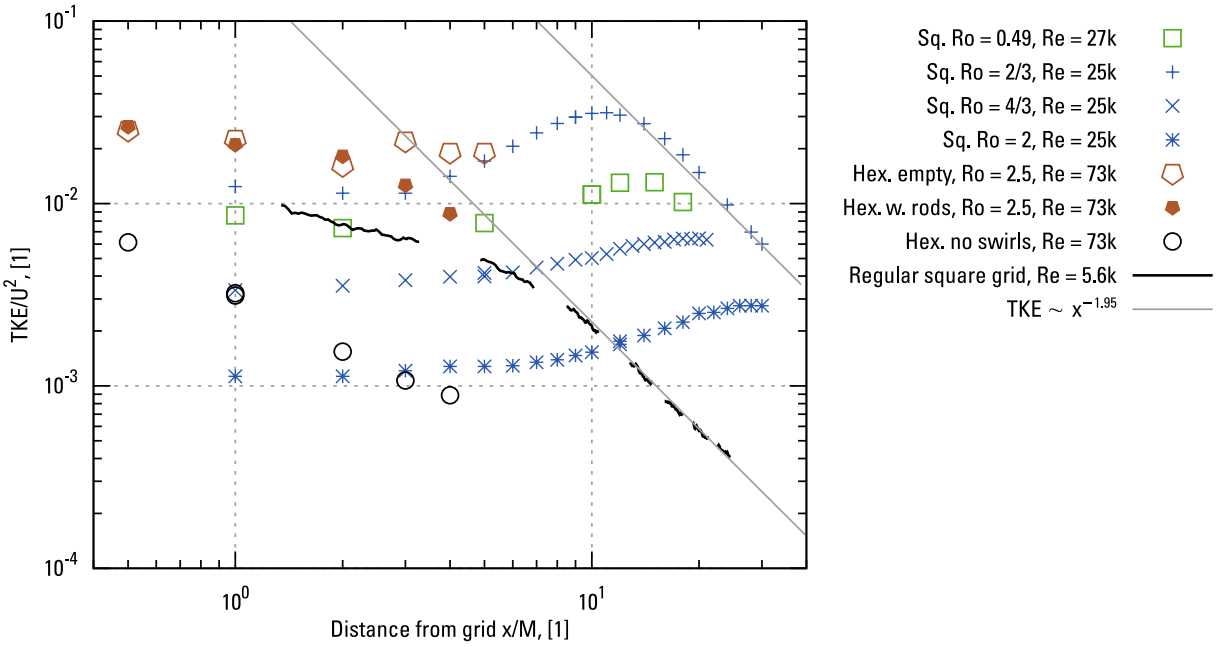

Fig. 1: Turbulent kinetic energy as a distance downstream the grid for several cases explored at the University of West Bohemia in Pilsen. The data past a regular square grid is displayed as solid black line (–). The green square (□) represents the data past a simple swirl grid described by Duda and Yanovych (2024). The blue crosses (+, ×, ✳) represent the swirler grid of sine profile, those data are not published yet. The symmetry is square and three Rossby numbers are explored. The empty reddish pentagon (⬠) is grid of hexagonal symmetry with swirling element only in every second node. This grid is designed as a mixing grid for nuclear reactor of VVER type, thus, when the fuel rods are added, the significant damping through boundary layers appear; such data are denoted by filled pentagons (⬠). A basic spacer grid for VVER reactors with fuel rods is displayed by black circles (○).

and blue symbols represent the swirler grids of square symmetry, while the reddish symbols play for grids of hexagonal symmetry developed to serve as mixing grid within the VVER nuclear reactors. The basic grid with no swirling elements (black ○) has been used by Duda et al. (2026) to explore the effect of random blockage of the spacer grid.

We see that TKE past the standard grid (black line) or past a swirler grid at large enough distances (blue times ×) decays according to power law with exponent $-1.95 \approx -2$ as observed by many classical studies, see e.g. Warhaft and Lumley (1978); Kurian and Fransson (2009); Grzelak and Wierciński (2015); Duda et al. (2020b). This decay exponent varies a little in dependence not only on the grid parameters like symmetry and blockage, but also by the methodology used for data fitting – e.g. if there is some *virtual origin* Mohamed and LaRue (1990) or not, and so on.

3.2. Observed scenario of the delayed decay

All the swirler grids display delayed decay of turbulence. The scenario is, that first some part of energy is hidden into the energy of vortices. As the vortices are located at stable positions, this energy does not contribute to the TKE (see Figure 2, where this fluctuation energy contribution is displayed at instantaneous snapshots). Later, the vortices start to *meander*, see Fig. 2(c) and the TKE signal grows. Later, the fluctuations in the vortex parameters grow exponentially; in other words, the larger the deviation, the stronger the advection of the neighboring vortex ⇒

$$\frac{\partial f}{\partial t} \sim f \Rightarrow f \sim e^t \tag{1}$$

This stage is captured in Fig.2(d). When the alignment among neighboring vortices gets lost, the vortices transit into classical 3D interactions governed by *vortex stretching* and *reconnections*. Therefore, the direct energy cascade forms and the decay process converges towards the classical decay of TKE $\sim x^{-2}$. This regime can be observed in Fig2(e).

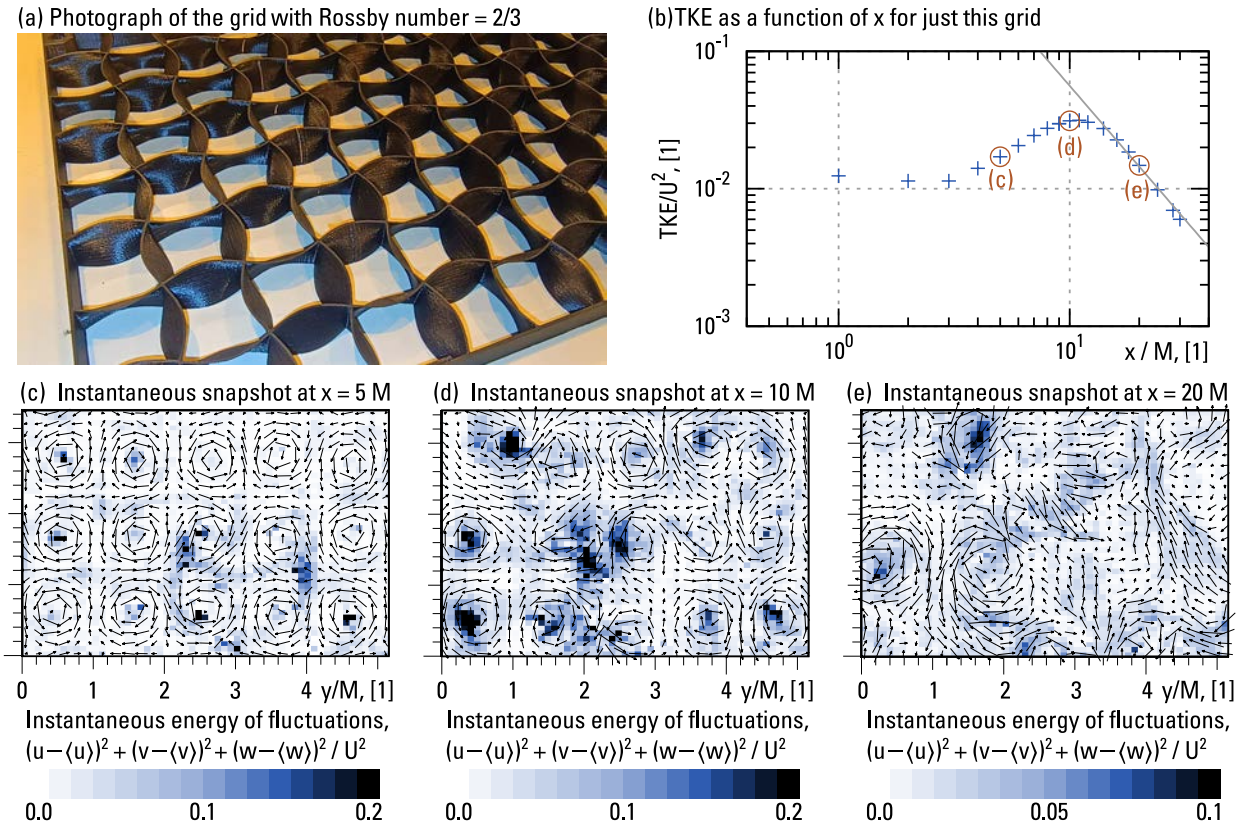

Fig. 2: A small example of the measured data at the University of West Bohemia. Panel (a) shows the swirler grid of sine profiling with $\mathrm{Ro} = 2/3$*, i.e. the smallest explored Ro (stronger initial vortices). Panel (b) displays the same data as Fig. 1, but for this grid only for sake of simplicity. The encircled points denoted (c – e) are displayed in corresponding panels (c – e) in a form of spatial map of instantaneous in-plane velocity magnitude. At (c) we see the regular grid of vortices already with deviations apparent by naked eye, panel (d) is the case with maximal TKE: the vortices are still mostly at regular grid positions, however their meandering is large*

3.3. Swirler grids for nuclear reactor fuel assembly

This behavior offers very interesting application for turbulent mixing, where we obey the quite steep decrease of mixing performance past classical grids. Instead, we can plan the position of maximal mixing and shift it downstream to an area, far from solid components. Especially, in the case of nuclear reactors, these mixing grids might homogenize the cooling performance along the fuel rods. We had tested this idea constructing the swirler-mixing grid adapted for VVER 440 geometry (Blanc (2022)), reddish pentagons ⬠ in Fig. 1.

The swirler grid for nuclear reactor has hexagonal symmetry and the swirler elements are more far from each other – the ”spacer” function of the grid has to remain, thus every odd node is circle touching fuel rods, while every even node can become swirler.

We tested the configuration of empty mixing grid (empty reddish pentagons ⬠) and the more realistic case with the fuel rods (filled). However, the rods are not heated, the flow can be considered as isothermal. In the close vicinity we observe very similar behavior in both cases – the vortices does not know about each other, neither about the fuel rods and their boundary layers. Since $x \sim 2M$ the data split into two branches: past the empty grid, TKE grows as expected from the other swirler grids, while the case with fuel rods display continuous decay, because the vortices are effectively separated by the fuel rods, thus they cannot multiply their meandering as described above. Instead, they slows down via interaction with boundary layers. Therefore, this attempt to control the mixing performance inside a nuclear reactor is a fiasco.

4. Conclusions

The swirler grids investigated in this study exhibit a characteristic delay in turbulence decay, caused by the initial formation of a stable lattice of aligned vortices. While this organized structure temporarily stores a significant portion of the fluctuation energy, the subsequent growth of vortex meandering releases this energy back into the flow and produces a downstream maximum of TKE. Once the vortex alignment collapses, the flow returns to a classical three-dimensional cascade with a decay rate comparable to that behind a regular grid. This mechanism offers a promising route for controlled positioning of enhanced mixing, although its applicability in nuclear-reactor fuel assemblies is limited: the presence of fuel rods suppresses vortex interaction and prevents the delayed-decay scenario from developing. Overall, swirler grids provide a promising tool for tailoring turbulence development in open flows, but their performance in confined geometries requires further refinement.

Acknowledgments

Special thanks go to Copilot for its invaluable assistance in writing the "Conclusion" section of this paper, ensuring a clear and effective summary of our work.

References

Adrian, R. J., Christensen, K. T., and Liu, Z.-C. (2000) Analysis and interpretation of instantaneous turbulent velocity fields. *Experiments in Fluids*, 29, 3, pp. 275–290.

Alexakis, A. (2023) Quasi-two-dimensional turbulence. *Reviews of Modern Plasma Physics*, 7, 1.

Blanc, P. (2022) Framatome vver-1000 fuel status & methodology. Technical report, Framatom.

Discetti, S., Ziskin, I. B., Adrian, R. J., and Prestridge, K. P. (2011) Piv study of fractal grid turbulence.

Duda, D. (2021) Searching of individual vortices in experimental data. In Bakırtaş, I. and Antar, N., eds, *Vortex Dynamics – From Physical to Mathematical Aspects*, IntechOpen.

Duda, D., Bém, J., Yanovych, V., Pavlíček, P., and Uruba, V. (2020a) Secondary flow of second kind in a short channel observed by piv. *European Journal of Mechanics, B/Fluids*, 79, pp. 444–453.

Duda, D., Mrázová, A., Mistre, F., Yanovych, V., Janský, V., Uruba, V., and Kovalova, K. (2026) Experimental study of the debris blockage impact on the isothermal flow through the nuclear fuel assembly model. *Nuclear Engineering and Design*, 446, pp. 114635.

Duda, D. and Yanovych, V. (2024) Interaction of stream-wise vortices generated by swirler grid. *Physics of Fluids*, 36, 5.

Duda, D., Yanovych, V., and Uruba, V. (2020b) An experimental study of turbulent mixing in channel flow past a grid. *Processes*, 8, 11, pp. 1–17.

Gomes-Fernandes, R., Ganapathisubramani, B., and Vassilicos, J. C. (2012) Particle image velocimetry study of fractal-generated turbulence. *Journal of Fluid Mechanics*, 711, pp. 306–336.

Grzelak, J. and Wierciński, Z. (2015) The decay power law in turbulence. *TRANSACTIONS OF THE INSTITUTE OF FLUID-FLOW MACHINERY*, 130, pp. 93–107.

Hurst, D. and Vassilicos, J. C. (2007) Scalings and decay of fractal-generated turbulence. *Physics of Fluids*, 19, 3.

Izakov, M. N. (2013) Large-scale quasi-two-dimensional turbulence and a inverse spectral flux of energy in the atmosphere of venus. *Sol Syst Res*, 47, pp. 170–181.

Kolmogorov, A. N. (1991) Dissipation of Energy in the Locally Isotropic Turbulence. *Proceedings of the Royal Society A: Mathematical, Physical and Engineering Sciences*, 434, 1890, pp. 15–17.

Kurian, T. and Fransson, J. H. M. (2009) Grid-generated turbulence revisited. *Fluid Dynamics Research*, 41, 2, pp. 021403.

Mohamed, M. and LaRue, J. (1990) The decay power law in grid-generated turbulence. *J. Fluid Mech.*, 219, pp. 195–214.

Valente, P. C. and Vassilicos, J. C. (2011) The decay of turbulence generated by a class of multiscale grids. *Journal of Fluid Mechanics*, 687, pp. 300–340.

Warhaft, Z. and Lumley, J. L. (1978) An experimental study of the decay of temperature fluctuations in grid generated turbulence. *J. Fluid Mech.*, 88, pp. 659–684.

Yanovych, V., Duda, D., Horáček, V., and Uruba, V. (2019) Research of a wind tunnel parameters by means of cross-section analysis of air flow profiles. *AIP Conference Proceedings*, 2189, 020024.

Yanovych, V., Duda, D., Uruba, V., and Antoš, P. (2021) Anisotropy of turbulent flow behind an asymmetric airfoil. *SN Appl. Sci.*, 3, pp. 885.

32nd International Conference
ENGINEERING MECHANICS 2026
Medlov, Czech Republic, May 11 – 13, 2026

LOW-AMPLITUDE STRESS WAVE MEASUREMENT IN SPLIT HOPKINSON BARS USING A VISCOELASTIC POLYMERIC BAR: ROLE OF PULSE SHAPING

Fíla T.[1], **Falta J.**[2]

Abstract: *The Split Hopkinson Pressure Bar (SHPB) technique is widely used for high strain-rate characterization, but its application to low-impedance materials is limited by low signal amplitudes and poor signal-to-noise ratio in conventional metallic bars. Polymeric viscoelastic bars offer improved sensitivity but introduce wave dispersion, complicating signal interpretation. This study proposes a simplified approach combining a linear elastic aluminium input bar with a viscoelastic polyamide output bar and a wave separation technique based on simultaneous strain and velocity measurements at a single location. Instead of employing complex viscoelastic models, an effective linear elastic representation of the viscoelastic bar is calibrated using void tests. The results show that the approach is only valid when the frequency bandwidth of the stress wave is sufficiently reduced. Without pulse shaping (mechanical filtering), strong dispersion leads to significant discrepancies in measured signals. By introducing a soft copper pulse shaper, high-frequency components are suppressed, enabling accurate reconstruction of force and velocity using the simplified model. The method is successfully demonstrated on a very low-impedance material, where the polymeric bar provides significantly improved signal quality compared to a conventional metallic bar.*

Keywords: Split Hopkinson bar, Viscoelastic bar, Stress waves, Pulse shaping, Low impedance materials

1. Introduction

The Split Hopkinson Pressure Bar (SHPB) is a well-established method for determining material behavior at high strain rates due to its reliability and relative simplicity. However, it is limited for low-impedance materials (Bacon, 1998), where small deformation forces produce weak signals in conventional metallic bars, resulting in poor signal-to-noise ratios and reduced measurement accuracy. Polymeric viscoelastic bars with lower Young's modulus improve sensitivity (Bacon, 1998; Zhao and Gary, 1997), but introduce dispersion and attenuation, distorting stress waves. These effects are typically corrected using viscoelastic wave propagation models based on experimental transfer functions (Bacon, 1998) or constitutive models (Zhao and Gary, 1997; Bacon, 1999). Both approaches have drawbacks: experimental calibration may overfit, while constitutive modeling is complex and uncertain. Wave separation methods mitigate dispersion but require multiple measurement locations and extensive calibration (Zhao and Gary, 1997; Bussac et al., 2002; Lundberg and Henchoz, 1977; Casem et al., 2003).

Here, a simplified approach is proposed combining a linear elastic input bar with a viscoelastic output bar. Wave separation is performed using simultaneous strain and velocity measurements at a single location on each bar (Casem et al., 2003; Fíla et al., 2025). The viscoelastic bar is approximated as an effective linear elastic medium, calibrated via void tests. Reliable results are obtained when stress wave bandwidth is limited, achieved through pulse shaping to suppress high-frequency dispersion.

[1] Tomáš Fíla: Czech Technical University in Prague, Faculty of Transportation Sciences, Konviktská 20; 110 00, Prague; CZ, fila@fd.cvut.cz
[2] Jan Falta: Czech Technical University in Prague, Faculty of Transportation Sciences, Konviktská 20; 110 00, Prague; CZ, falta@fd.cvut.cz

ISSN: 1805-8256, doi: 10.21495/em2026-41

2. Materials and Methods

2.1. Split Hopkinson Pressure Bar Setup

Experiments were conducted on a universal Split Hopkinson Bar (USHB) system in compression at DynLab, Faculty of Transportation Sciences, Czech Technical University. The setup targets low-impedance materials using a hybrid configuration with a metallic input bar and a viscoelastic polymeric output bar. The input bar was aluminium alloy EN-AW-7075 (3000 mm length, 30 mm diameter), while the output bar was polyamide PA6 (3070 mm length, 30 mm diameter). An aluminium striker bar (2700 mm length) generated the incident pulse and was accelerated by a gas gun with a 3000 mm barrel, enabling controlled impact velocities. Stress waves generated in the input bar propagated into the viscoelastic output bar, where dispersion and attenuation influenced their evolution.

2.2. Stress Wave and Velocity Measurements

Stress wave propagation was measured via simultaneous strain and particle velocity acquisition at a single location on each bar. Axial strain was recorded using HBM foil strain gauges, and particle velocity using a magnetic linear encoder (LM10, RLS, Slovenia). This enabled wave separation into forward- and backward-propagating components (Fíla et al., 2025). Signals were acquired at 1 MHz using a high-speed, low-noise system, providing sufficient temporal resolution for transient wave capture. Data were processed using the referenced wave separation algorithm to reconstruct stress wave evolution. Calibration of the viscoelastic output bar was performed using void tests, where input and output bars were in direct contact, allowing direct assessment of wave transmission and effective propagation parameters. Additional tests used low-density cork as a very low-impedance specimen to evaluate performance under realistic conditions, with two impact velocities to assess rate effects. The influence of pulse shaping on wave frequency content was investigated via void tests with and without a pulse shaper. The shaper, a $\sim$1 mm thick soft copper disk at the input bar interface, modified the incident pulse by attenuating high-frequency components. This reduced bandwidth is essential to limit Pochhammer–Chree dispersion in the viscoelastic bar, minimizing signal distortion and enabling the use of simplified wave propagation models.

2.3. Wave Correction Procedure

Correction of stress waves in the viscoelastic output bar was based on calibration from void tests. Signals from the aluminium input bar were first processed and time-shifted to the bar interface using linear elastic wave relations and known material properties, providing a reliable reference for force and particle velocity. Continuity conditions require equality of force and velocity across the interface, which was independently confirmed by high-speed imaging, showing no separation or slip. The polyamide bar response was then calibrated to match these reference signals.

An effective linear elastic model of the viscoelastic bar was introduced, with parameters - effective nominal wave speed and Young's modulus - identified by fitting polyamide signals to the interface reference. Calibration was performed with and without pulse shaping to assess bandwidth effects on the linear approximation. Both strain- and velocity-based signals were used, and their consistency verified. The resulting effective parameters are summarized in Table 1.

Tab. 1: Materials constants of linear elastic models

	Aluminum alloy EN-AW-7075	Polyamide PA6
Dynamic Young's modulus [MPa]	72000	3525
Wave propagation velocity [m/s]	5218	1670

3. Results

Void test results demonstrate the necessity of pulse shaping to control stress wave bandwidth. Comparison of force and velocity signals from the aluminium input bar and polyamide output bar shows that,

without pulse shaping, force remains relatively consistent, but velocity exhibits significant discrepancies (Fig. 1). This indicates strong dispersion in the viscoelastic bar, where broad frequency content and high-frequency components are affected by Pochhammer–Chree dispersion. Consequently, velocity signals in the polyamide bar deviate markedly from the aluminium reference, showing that a linear elastic approximation is insufficient and that accurate correction would require frequency-domain viscoelastic models with transfer functions.

With pulse shaping, high-frequency components are suppressed, reducing bandwidth and dispersion effects. Force and velocity signals from both bars then agree well (Fig. 2), validating the effective linear elastic approximation for sufficiently smooth, low-frequency waves. A key observation is the noise difference: the aluminium bar exhibits high noise due to its high stiffness and low strain amplitudes under low-force loading, reducing sensitivity. In contrast, the polyamide bar provides larger strains and a significantly improved signal-to-noise ratio, making it more suitable for low-impedance materials.

Performance is further demonstrated on low-density cork tested at two impact velocities. Force–displacement curves show that aluminium bar data are dominated by noise and unsuitable for force evaluation, though still usable for velocity and displacement. The calibrated polyamide bar yields smooth, consistent force signals (Fig. 3). Wave separation additionally enables analysis of multiple wave reflections, allowing evaluation over extended loading, including later deformation stages such as densification, especially at higher impact velocities.

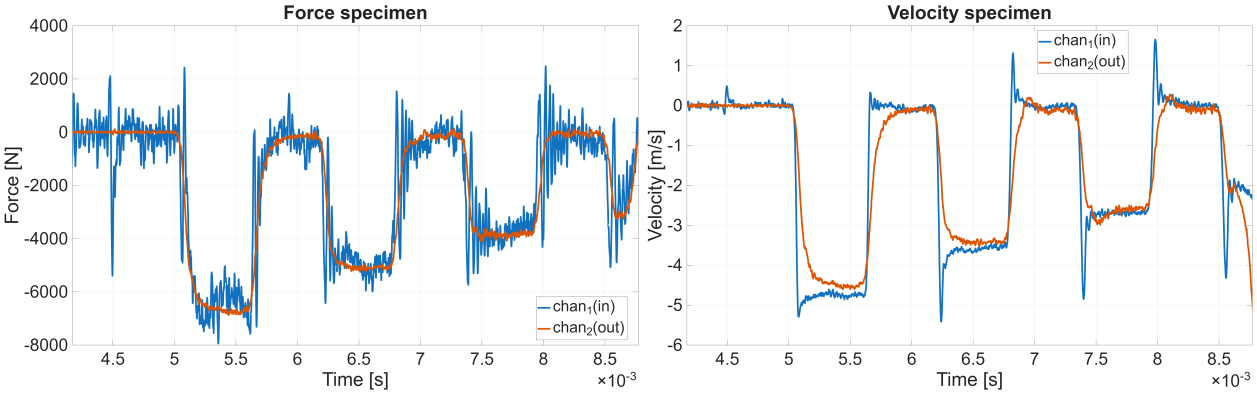

Fig. 1: Force-time (left) and velocity-time (right) diagrams showing differences of force and velocity data from input aluminum alloy bar (blue curve) and output polyamide bar (red curve) during a test without a pulse shaper.

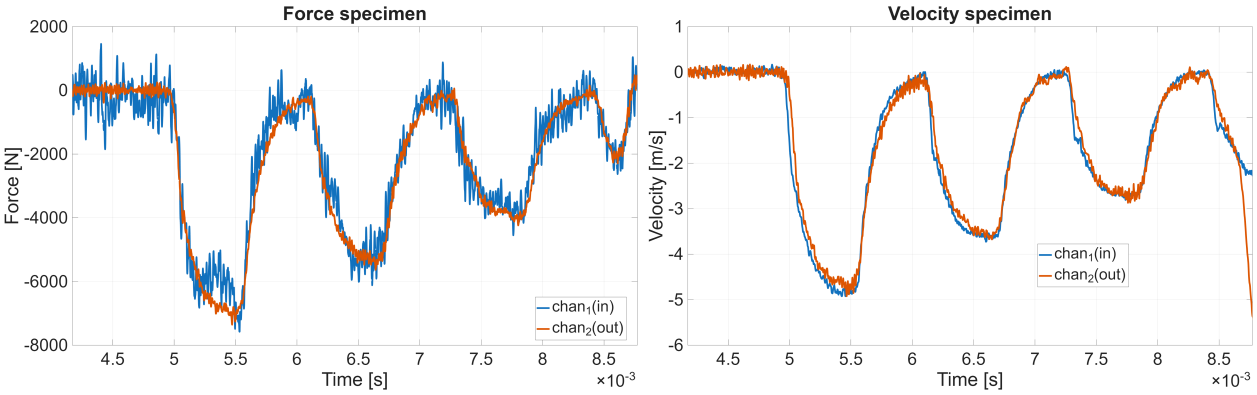

Fig. 2: Force-time (left) and velocity-time (right) diagrams showing consistency of force and velocity data from input aluminum alloy bar (blue curve) and output polyamide bar (red curve) during a test with a pulse shaper.

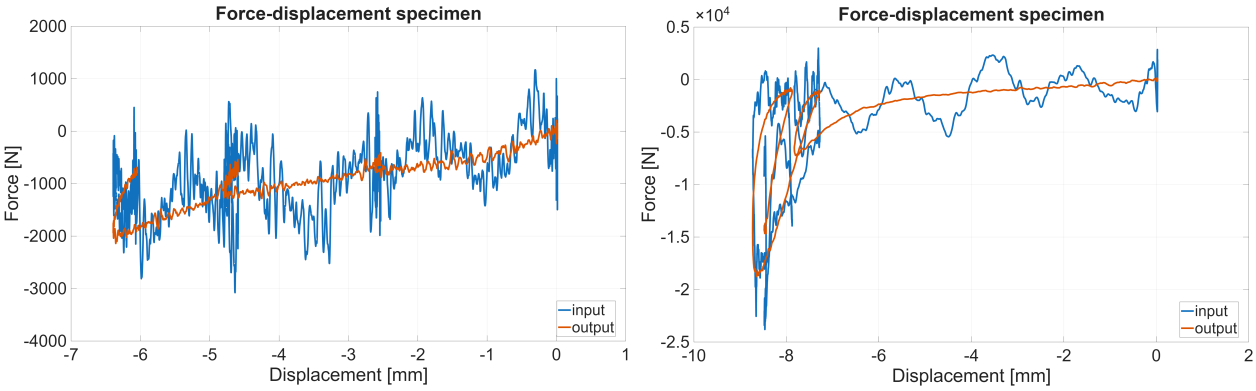

Fig. 3: Force-displacement diagram of soft cork specimen at a velocity of 5 m/s (left) and 15 m/s (right) showing extensive difference between noise in aluminum alloy bar (blue curve) and polyamide bar (red).

4. Conclusions

A hybrid Split Hopkinson bar configuration combining a linear elastic aluminium input bar and a viscoelastic polyamide output bar was shown to enable reliable measurement of low-amplitude stress waves when combined with a wave separation technique and velocity–strain measurements. The study demonstrates that a simplified effective linear elastic model of the viscoelastic bar is only valid when the frequency bandwidth of the stress wave is reduced. Without pulse shaping, wave dispersion effects are too significant and require a full viscoelastic treatment. By introducing a soft copper pulse shaper, the frequency content is sufficiently limited, allowing accurate correction using the proposed approach.

Acknowledgments

The research was supported by the Czech Science Foundation (project Junior Star no. 22-18033M).

References

Bacon, C. (1998) An experimental method for considering dispersion and attenuation in a viscoelastic Hopkinson bar. *Experimental Mechanics*, 38, 4, pp. 242–249.

Bacon, C. (1999) Separation of waves propagating in an elastic or viscoelastic Hopkinson pressure bar with three-dimensional effects. *International Journal of Impact Engineering*, 22, 1, pp. 55–69.

Bussac, M.-N., Collet, P., Gary, G., and Othman, R. (2002) An optimisation method for separating and rebuilding one-dimensional dispersive waves from multi-point measurements. Application to elastic or viscoelastic bars. *Journal of the Mechanics and Physics of Solids*, 50, 2, pp. 321–349.

Casem, D., Fourney, W., and Chang, P. (2003) Wave separation in viscoelastic pressure bars using single-point measurements of strain and velocity. *Polymer Testing*, 22, 2, pp. 155–164.

Fíla, T., Falta, J., and Dvořák, R. (2025) A simple wave separation method for split hopkinson bar experiments using linear encoders. *Results in Engineering*, 28, pp. 106980.

Lundberg, B. and Henchoz, A. (1977) Analysis of elastic waves from two-point strain measurement: Strain, particle velocity, power transmission and related quantities can be determined at an arbitrary section of a cylindrical rod from measurement of strains at two different rod sections. *Experimental Mechanics*, 17, 6, pp. 213–218.

Zhao, H. and Gary, G. (1997) A new method for the separation of waves. Application to the SHPB technique for an unlimited duration of measurement. *Journal of the Mechanics and Physics of Solids*, 45, 7, pp. 1185–1202.

32nd International Conference
ENGINEERING MECHANICS 2026
Medlov, Czech Republic, May 11 – 13, 2026

POST-CRITICAL STABILITY OF STATIONARY SOLUTIONS IN A 2DOF GENERALIZED VAN DER POL AEROELASTIC MODEL

Fischer C.[1], **Náprstek J.**[1]

Abstract: *This paper analyzes post-critical stationary solutions of a two-degree-of-freedom (2DOF) aeroelastic system modeled by a generalized van der Pol formulation. The sign of the linear damping term is shown to govern the qualitative character of instability, distinguishing cases with stable trivial equilibrium from self-excited oscillatory regimes corresponding to flutter- and galloping-type behavior. Stationary responses are derived using harmonic balance, yielding generalized modal amplitudes and multiplicative coupled solutions. The stability of trivial and nontrivial branches is examined analytically. Higher-order nonlinear damping terms of fourth and sixth degree are shown to ensure bounded post-critical motion and suppress excessive vibration growth. The linear stability boundary is related to Routh–Hurwitz conditions of the underlying 2DOF aeroelastic system, identifying flutter limits as the onset of Hopf bifurcation. The proposed framework provides a unified analytical interpretation of post-critical aeroelastic oscillations and their nonlinear saturation mechanisms.*

Keywords: Aeroelasticity, Flutter, Galloping, Van der Pol oscillator, Nonlinear damping

1. Introduction

Aeroelastic oscillations of bluff structures, such as bridge decks or slender beams in cross-flow, arise from the nonlinear interaction between structural motion and aerodynamic forces. Even within simplified two-degree-of-freedom (2DOF) models involving heave and pitch, the system exhibits a rich spectrum of stability phenomena, including flutter, divergence, and galloping-type instabilities (Strømmen, 2006).

Stability boundaries of coupled heave–pitch systems can be described using Routh–Hurwitz conditions in the frequency domain (Náprstek and Pospíšil, 2012). However, linear theory is insufficient for describing post-critical behavior, where nonlinear mechanisms determine whether oscillations grow unboundedly or settle into stable limit cycles. A convenient reduced-order representation of such is provided by generalized van der Pol–type equations. In these models, the linear damping term may change sign depending on flow velocity, while higher-order nonlinear terms provide amplitude limitation(Dowell, 2022).

In aeroelastic interpretation, regimes differing in the sign of the linear damping term correspond to physically distinct instability mechanisms. When the trivial solution loses stability due to coupled modal interaction and gyroscopic or nonconservative effects, the system undergoes flutter-type instability, characterized by oscillatory growth of coupled modes (Náprstek and Pospíšil, 2012), for nonlinear setting see (Náprstek and Fischer, 2020). In contrast, when negative aerodynamic damping dominates in a single mode, the response resembles galloping-type behavior, where nonlinear aerodynamic damping limits the oscillation amplitude to finite values (Vio et al., 2007).

Quadratic nonlinearities provide the primary saturation mechanism typical of supercritical flutter or galloping. However, if the linear damping term becomes negative—implying an unstable trivial equilibrium—additional higher-order damping terms are necessary to prevent unbounded amplitude growth and to establish a stable finite-amplitude limit cycle. Then the sixth-degree term acts as a global stabilizing contribution, ensuring bounded solutions even under strong negative linear damping (Dowell, 2022).Conversely, when the linear damping coefficient is positive, a fourth-degree nonlinear term may produce an unstable limit cycle surrounding the origin.

[1] RNDr. Cyril Fischer, Ph.D., Ing. Jiří Náprstek, DrSc., Institute of Theoretical and Applied Mechanics of the Czech Academy of Sciences, Prosecká 76, 190 00 Prague 9, tel. +420 225 443 310, e-mail {fischerc,naprstek}@itam.cas.cz

ISSN: 1805-8256, doi: 10.21495/em2026-45

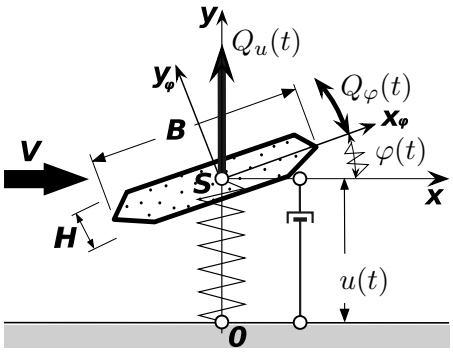

Fig. 1: Schematic representation of TDOF system and its aerodynamic excitation

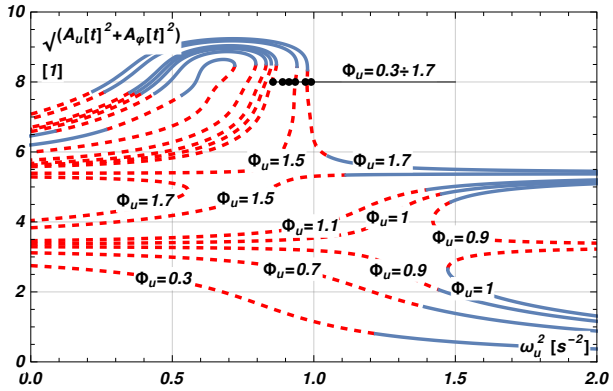

Fig. 2: Stable/unstable stationary generalised response amplitudes versus ω_u^2 for the positive linear damping case

2. Mathematical model

The governing equations of motion of a coupled aeroelastic system with two generalized coordinates corresponding to heave ($\bar{u}$, [m]) and pitch motion ($\bar{\varphi}$, [rad]) of a bluff cross-section are written as

$$m\,\ddot{\bar{u}} + c_u\left(1-\nu_u u^2+\vartheta_u u^4-\zeta_u u^6\right)\dot{\bar{u}} + k_u\bar{u} - \bar{p}\,\bar{\varphi} - \bar{h}\,\bar{q}\,\dot{\bar{\varphi}} = \bar{F}_u(t), \tag{1}$$

$$I\,\ddot{\bar{\varphi}} + c_\varphi\left(1-\nu_\varphi\varphi^2+\vartheta_\varphi\varphi^4-\zeta_\varphi\varphi^6\right)\dot{\bar{\varphi}} + k_\varphi\bar{\varphi} + \bar{g}\,\bar{p}\,\bar{u} + \bar{q}\,\dot{\bar{u}} = \bar{M}_\varphi(t), \tag{2}$$

where m [$\mathrm{kg\,m^{-1}}$] and I [$\mathrm{kg\,m}$] denote the generalized mass and generalized mass moment of inertia per unit span, respectively; c_u [$\mathrm{kg\,(m\,s)^{-1}}$] and c_φ [$\mathrm{kg\,s^{-1}}$] are damping coefficients; k_u [$\mathrm{kg\,s^{-2}}$] and k_φ [$\mathrm{kg\,m\,s^{-2}}$] are stiffness coefficients; $\bar{F}_u(t)$ [$\mathrm{N\,m^{-1}}$] and $\bar{M}_\varphi(t)$ [N] are the generalized external force and moment, respectively. The coefficients $\bar{g}$ and $\bar{h}$ are dimensionless parameters controlling the relative contribution of the coupling terms, while $\bar{p}$ [$\mathrm{kg\,s^{-2}}$] and $\bar{q}$ [$\mathrm{kg\,s^{-1}}$] are stiffness-like and damping-like coupling coefficients, respectively. The nonlinear damping terms are introduced phenomenologically to represent combined structural and aerodynamic effects and depend on the dimensionless generalized coordinates

$$u(t) = \bar{u}(t)/H, \qquad \varphi(t) = \bar{\varphi}(t), \tag{3}$$

where H is the height of the cross-section, see Fig. 1. Since the radian is dimensionless $\varphi(t) = \bar{\varphi}(t)$.

The dimensionless formulation of the model is then obtained by substituting (3) into (1)–(2)

$$\begin{aligned}
&\ddot{u} + b_u\left(1-\nu_u u^2+\vartheta_u u^4-\zeta_u u^6\right)\dot{u} + \omega_u^2 u - p\,\varphi - hq\,\dot{\varphi} = Q_u(t),\\
&\ddot{\varphi} + b_\varphi\left(1-\nu_\varphi\varphi^2+\vartheta_\varphi\varphi^4-\zeta_\varphi\varphi^6\right)\dot{\varphi} + \omega_\varphi^2\varphi + gp\,u + q\,\dot{u} = Q_\varphi(t),
\end{aligned} \tag{4}$$

where the normalized parameters are defined as

$$b_u = \frac{c_u}{m}, \quad \omega_u^2 = \frac{k_u}{m}, \quad b_\varphi = \frac{c_\varphi}{I}, \quad \omega_\varphi^2 = \frac{k_\varphi}{I}, \quad p = \frac{\bar{p}}{mH}, \quad gp = \frac{\bar{g}\,\bar{p}\,H}{I}, \quad q = \frac{\bar{q}\,H}{I}, \quad hq = \frac{\bar{h}\,\bar{q}}{mH},$$

and the excitation terms Q_u and Q_φ represent generalized accelerations:

$$Q_u(t) = \bar{F}_u(t)/(mH), \qquad Q_\varphi(t) = \bar{M}_\varphi(t)/I\,. \tag{5}$$

The external excitation is assumed harmonic

$$Q_u(t) = \Phi_u\cos(\Omega t), \qquad Q_\varphi(t) = \Phi_\varphi\cos(\Omega t)\,, \tag{6}$$

where Φ_u and Φ_φ are amplitudes of generalized acceleration and Ω is the excitation frequency.

The solution is sought in the form

$$u(t) = A_u(t)\cos\left(\Omega t+\psi_u(t)\right), \qquad \varphi(t) = A_\varphi(t)\cos\left(\Omega t+\psi_\varphi(t)\right), \tag{7}$$

where the dimensionless amplitudes A_u, A_φ and phases ψ_u, ψ_φ are assumed to vary on a slow time scale, i.e. their characteristic variation time is much larger than the oscillation period $2\pi/\Omega$.

To eliminate redundancy in the amplitude–phase representation, the orthogonality conditions are imposed:

$$\dot{A}_u \cos(\Omega t + \psi_u) - A_u \dot{\psi}_u \sin(\Omega t + \psi_u) = 0, \tag{8}$$

and analogously for the φ coordinate.

Substituting (7) into (4) and averaging over one excitation period $2\pi/\Omega$ yields a slowly-time system governing the evolution of amplitudes and phase differences ($\Delta = \psi_u - \psi_\varphi$):

$$\dot{\psi}_u = -\frac{(p\cos\Delta + hq\Omega\sin\Delta)}{2\Omega}\frac{A_\varphi}{A_u} - \frac{\left(\Omega^2 - \omega_u^2\right)}{2\Omega} - \frac{\Phi_u \cos\psi_u}{2\Omega A_u}\,, \tag{9a}$$

$$\dot{A}_u = \frac{(hq\Omega\cos\Delta - p\sin\Delta)\,A_\varphi}{2\Omega} - \frac{b_u A_u}{128}\left(64 - 16\nu_u A_u^2 + 8\vartheta_u A_u^4 - 5\zeta_u A_u^6\right) - \frac{\Phi_u \sin\psi_u}{2\Omega}\,, \tag{9b}$$

$$\dot{\psi}_\varphi = \frac{(gp\cos\Delta - q\Omega\sin\Delta)}{2\Omega}\frac{A_u}{A_\varphi} - \frac{15}{128 A_\varphi} b_\varphi \zeta_\varphi A_u^6 A_\varphi \sin 2\Delta - \frac{\left(\Omega^2 - \omega_\varphi^2\right)}{2\Omega} - \frac{\Phi_\varphi \cos\psi_\varphi}{2\Omega A_\varphi}\,, \tag{9c}$$

$$\begin{aligned}\dot{A}_\varphi = &-\frac{(q\Omega\cos\Delta + gp\sin\Delta)\,A_u}{2\Omega} \\ &- \frac{15}{128} b_\varphi \zeta_\varphi A_u^6 A_\varphi \cos 2\Delta - \frac{b_\varphi A_\varphi}{32}\left(16 - 4\nu_\varphi A_\varphi^2 + 2\vartheta_\varphi A_\varphi^4 - 5\zeta_\varphi A_u^6\right) - \frac{\Phi_\varphi \sin\psi_\varphi}{2\Omega}\,.\end{aligned} \tag{9d}$$

For the purpose of stationary solution detection, the averaged slow-flow system is transformed into an autonomous algebraic form by introducing the substitutions $C_u = \cos\psi_u$, $S_u = \sin\psi_u$, $C_\varphi = \cos\psi_\varphi$, $S_\varphi = \sin\psi_\varphi$, together with the identities $C_u^2 + S_u^2 = 1, C_\varphi^2 + S_\varphi^2 = 1$. Setting the slow-flow derivatives equal to zero, $\dot{A}_u = 0, \dot{A}_\varphi = 0, \dot{\psi}_u = 0, \dot{\psi}_\varphi = 0$, leads to a closed algebraic system in the variables $A_u,\ A_\varphi,\ C_u,\ S_u,\ C_\varphi,\ S_\varphi$ and yields the stationary (periodic) solutions of the original nonlinear problem.

Local stability of a stationary solution is assessed using the original four-dimensional slow-flow system Eq. (9), namely the characteristic polynomial $\chi(\lambda)$ of the corresponding Jacobian has the form:

$$\chi(\lambda) = \lambda^4 + a_1\lambda^3 + a_2\lambda^2 + a_3\lambda + a_4. \tag{10}$$

According to the Routh–Hurwitz criterion, the stationary solution is asymptotically stable if and only if

$$a_1 > 0, \qquad a_2 > 0, \qquad a_3 > 0, \qquad a_4 > 0, \qquad a_1 a_2 a_3 > a_3^2 + a_1^2 a_4\,. \tag{11}$$

3. Example analysis

The stationary generalized amplitudes $(A_u^2 + A_\varphi^2)^{1/2}$ of the dimensionless response of the coupled 2DOF system obtained from Eq. (9) are illustrated in Figs. 2 and 3. The amplitudes are plotted as functions of the squared linear natural frequency ω_u^2, while the excitation frequency is kept fixed at $\Omega = 1$. The two cases differ in the character of linear damping.

Figure 2 corresponds to the case of positive linear damping $b_s = 0.2$, with parameter set $g = 1$, $h = 1$, $\nu_s = 0.5$, $\vartheta_s = 0.025$, $\Phi_\varphi = 0$, $p = 0.2$, $q = 0.2$ and biquadratic damping assumed ($\zeta_s = 0$); $s \in \{u, \varphi\}$ The remaining parameters are $\omega_\varphi^2 = 1$ and $\Omega = 1$.

Individual curves correspond to different excitation amplitudes Φ_u, indicated directly in the figure. For each value of Φ_u, the stationary amplitude varies nonlinearly with ω_u^2. Fold (turning) points appear on several branches, separating stable and unstable solution segments. Stable portions are plotted as solid blue curves, whereas unstable portions are shown as dashed red curves. In parameter intervals where folds occur, multiple stationary solutions coexist, indicating bistability and the possibility of jump phenomena under quasistatic parameter variation.

Increasing Φ_u raises the overall amplitude level and modifies the extent of stable and unstable regions. In this configuration, physically realizable stationary responses correspond to those branches satisfying the Routh–Hurwitz stability conditions.

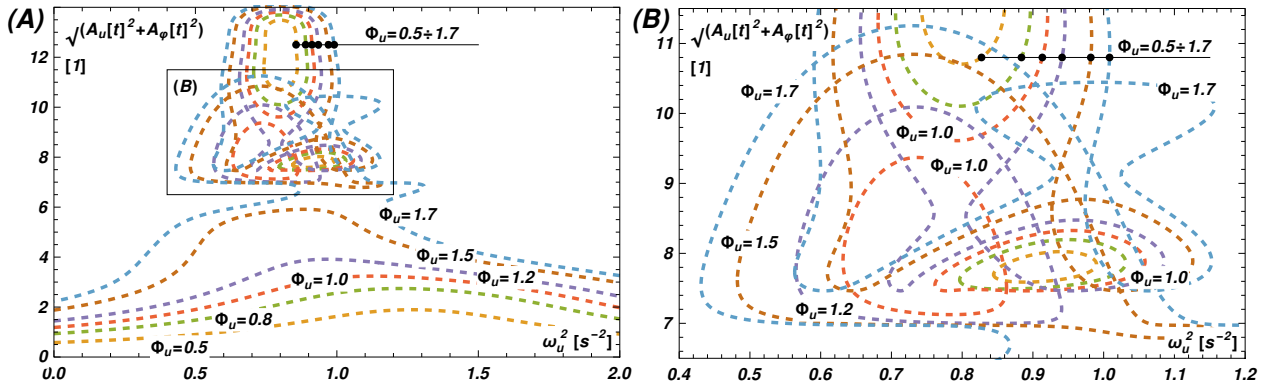

Fig. 3: (A) Stationary response amplitudes versus ω_u^2 for $\omega_\varphi^2 = 1$ and $\Omega = 1$ for negative linear damping $b_u, b_\varphi < 0$, shown for several excitation amplitudes Φ_u. (B) Detail indicated by a rectangle in plot (A).

Figure 3 shows the case of negative linear damping $b_u, b_\varphi = -0.2$. In contrast to the preceding case, the linear damping term supplies energy to the system and the trivial solution becomes unstable. To ensure bounded stationary amplitudes, a sixth–order nonlinear damping polynomial is introduced, $\vartheta_s = 0.00025$.

The figure presents potentially stationary amplitudes for $\omega_\varphi^2 = 0.85$, $\Omega = 1$, excitation amplitudes $\Phi_0 = 0.5,\ 0.8,\ 1.0,\ 1.2,\ 1.5,\ 1.7$ and $\omega_u^2 \in (0, 2)$. Plot (A) shows the global dependence of the stationary amplitudes, whereas plot (B) provides an enlarged detail of the region marked in plot (A), revealing the fine structure of closely spaced curves.

Although the sixth–order nonlinear damping term limits amplitude growth and produces finite solutions of the harmonic balance equations, all computed stationary branches in this parameter range are unstable according to the Routh–Hurwitz criteria. The plotted curves therefore represent mathematical stationary solutions of the algebraic system rather than physically stable steady states.

4. Conclusions

The nonlinear two-degree-of-freedom aeroelastic system was analyzed under harmonic external excitation for positive and negative values of linear damping. The model, formulated in a generalized van der Pol framework, was examined using harmonic balance and stability analysis.

When the excitation frequency is sufficiently far from the system eigenfrequencies, the response is predominantly forced and stationary, with self-excited effects remaining negligible. In contrast, when the excitation frequency approaches one or both eigenfrequencies, synchronization occurs. The system then exhibits large-amplitude stationary oscillations governed by frequency locking. In this regime, the synchronized response may become the only stable solution, representing a potentially dangerous operating condition.

The combined analytical and numerical approach proved effective in identifying synchronization domains and characterizing post-critical forced behavior. Future work will extend the analysis to coupled configurations and stochastic excitation.

Acknowledgments

The kind support of Czech Science Foundation project No. 24-13061S is gratefully acknowledged.

References

Dowell, E. H., edt. (2022) *A modern course in aeroelasticity*. Springer International Publishing.

Náprstek, J. and Fischer, C. (2020) Post-critical behavior of an auto-parametric aero-elastic system with two degrees of freedom. *International Journal of Non-Linear Mechanics*, 121, pp. 103441.

Náprstek, J. and Pospíšil, S. (2012) Response types and general stability conditions of linear aero-elastic system with two degrees-of-freedom. *Journal of Wind Engineering and Industrial Aerodynamics*, 111, pp. 1–13.

Strømmen, E. (2006) *Theory of bridge aerodynamics*. Springer, Berlin.

Vio, G. A., Dimitriadis, G., and Cooper, J. E. (2007) Bifurcation analysis and limit cycle oscillation amplitude prediction methods applied to the aeroelastic galloping problem. *Journal of Fluids and Structures*, 23, 7, pp. 983–1011.

32nd International Conference
ENGINEERING MECHANICS 2026
Medlov, Czech Republic, May 11 – 13, 2026

A NEW SIMPLE BELT FRICTION MODEL

Frydýšek K.[1], Hrabovský L.[2], Čepica D.[3]

Abstract: *Article focuses on the belt friction which obeys Coulomb's Law. It presents a new model, which is compared to the traditional simple Euler-Eytelwein (Capstan) model. Derivations are based on the differential equilibrium of forces in a cylindrical coordinate system on an elementary segment of a rope. Compared to the Euler-Eytelwein model, our new model additionally respects the weight of the rope, the radius of the cylindrical surface, the rope's geometry, and the rope's position relative to gravitational force in space. Experiment using a pulley with a semicircular groove wrapped with a loaded rope and the measuring of the forces in the rope was used to evaluate it. Our new model is slightly more complicated and precise than the Euler-Eytelwein model. Finite Element Method is applied too.*

Keywords: Belt friction, Analytical solutions, Numerical solutions, Experiments

1. Introduction

Belt friction is a classic engineering concept that explains the resistance to motion between a flexible belt (or rope) and a cylindrical surface of radius R /m/. When a belt is wrapped around a surface (wrap angle $\varphi \in (\varphi_1; \varphi_2)$ /rad/), the tension on one side F_2 /N/ is greater than the tension on the other F_1 /N/, see Fig. 1(a,b). This difference exists because the friction (described by coefficient of friction f /1/) between the belt and the surface "absorbs" or "resists" some of the pull.

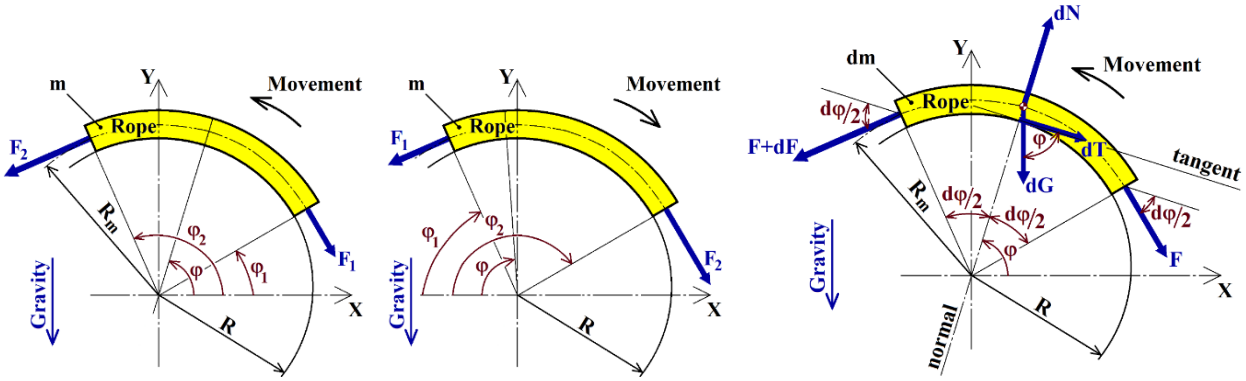

Fig. 1: Basic description of belt friction and force equilibrium on an elementary segment.

Reviewing belt friction involves developments from the classical "capstan" logic to modern dynamic models that account for material deformation and high-speed effects in connections with theories and experiments etc. The transition from simple static equilibrium to complex viscoelastic interactions defines the current state of the field. For example, see references (Bulín, 2019; Euler, 1762; Hrabovský, 2022;

[1] Prof. M.Sc. Karel Frydýšek, Ph.D., ING-PAED IGIP, FEng.: Department of Applied Mechanics, Faculty of Mechanical Engineering, VSB – Technical University of Ostrava, 17. listopadu 2172/15, 708 00 Ostrava, CZ, karel.frydrysek@vsb.cz.

[2] Assoc. Prof. M.Sc. Leopold Hrabovský, Ph.D.: Department of Machine and Industrial Design, Faculty of Mechanical Engineering, VSB – Technical University of Ostrava, 17. listopadu 2172/15, 708 00 Ostrava, CZ, leopold.hrabovsky@vsb.cz.

[3] M.Sc. Daniel Čepica, Ph.D.: Department of Applied Mechanics, Faculty of Mechanical Engineering, VSB – Technical University of Ostrava, 17. listopadu 2172/15, 708 00 Ostrava, CZ, daniel.cepica@vsb.cz.

ISSN: 1805-8256, doi: 10.21495/em2026-49

Imado, 2008; Kong, 2005; Konyukhov, 2021; Kušnerová, 2020; Wasfy, 2016 etc.). However, the Euler-Eytelwein formula is insufficient in some cases and should be modified.

2. New "Simple" Belt Friction Model that Respects a Rope's Weight and its Position Relative to Gravitational Force

The derivation is based on the equilibrium in a cylindrical coordinate system (i.e., equilibrium in the direction of the normal and tangential forces) on an elementary segment of an ideal rope with mass m /kg/, see Fig. 1(c) and Tab. 1. The centroid of the wrapped rope's cross-sectional area is at the distance R_m /m/ and the rope is subjected to the tensile forces F and F + dF /N/. The elementary gravitational force of the rope $dG = g\,dm = a_m R_m\, d\varphi$ /N/ acts in the direction opposite to the Y-axis, where $g = 9.807\ m\,s^{-2}$ is the gravitational acceleration and a_m /kg m^{-1}/ is the specific weight of the rope. Coulomb's law applies $dT = f\,dN$, where dT /N/ is friction force and dN /N/ is normal Force.

Tab. 1: New belt friction model that respects a rope's weight and its position relative to gravity.

New solution considering the rope's weight and wrapping geometry (mass $m \neq 0$, more complex and precise):	
Inhomogeneous differential equation $\frac{dF}{d\varphi} - fF = b_m(cos\varphi + f sin\varphi)$	General solution of the differential equation $F_{(\varphi)} = Be^{f\varphi} + c_m\left[(1-f^2)sin\varphi - 2f\,cos\varphi\right]$, where B /N/ is an integration constant, and constant $c_m = \frac{g\,a_m R_m}{f^2+1}$
The particular solution according to Fig. 1 $F_{(\varphi)} = F_1 e^{f(\varphi-\varphi_1)} + +c_m\left(e^{f(\varphi-\varphi_1)}[2f\,cos\varphi_1 + (f^2-1)sin\varphi_1] + (1-f^2)sin\varphi - 2f\,cos\varphi\right)$ or more precisely for determining the force $F_2 = F_1 e^{f(\varphi_2-\varphi_1)} + +c_m\left(e^{f(\varphi_2-\varphi_1)}[2f\,cos\varphi_1 + (f^2-1)sin\varphi_1] + (1-f^2)sin\varphi_2 - 2f\,cos\varphi_2\right)$	
Nonlinear formula for calculating the coefficient of friction f using a homogeneous equation according to Fig. 1(a,b) $F_1 e^{f\pi} + 2c_m f\left(e^{f\pi}+1\right) - F_2 = 0$	

If the weight of the rope itself is neglected during the derivation of the rope element's equilibrium (i.e., $a_m = 0$), equations in Tab. 1 reduce to the well-known simple form of the Euler-Eytelwein (Capstan) formula, see Tab. 2.

Tab. 2: Classical belt friction model that do not respects a rope's weight and its position relative to gravity.

The classical solution, neglecting the weight of the rope itself (mass $m = 0$, simpler model)	
Homogeneous differential equation $\frac{dF}{d\varphi} - fF = 0$	General solution of the differential equation $F_{(\varphi)} = Ae^{f\varphi}$, where A /N/ is an integration constant.
The particular solution according to Fig. 1, the Euler-Eytelwein (Capstan) formula $F_{(\varphi)} = F_1 e^{f(\varphi-\varphi_1)}$, or more precisely for determining the force $F_2 = F_1 e^{f(\varphi_2-\varphi_1)}$	
Simple formula for calculating the coefficient of friction $f = \frac{\ln\left(\frac{F_2}{F_1}\right)}{\pi}$	

From the initial comparison of the approaches mentioned in Tab. 1 and 2, it is evident that the forces F_1 or F_2 can be characterized as functions of these parameters:

- The classical solution (the Euler-Eytelwein formula, see Tab. 2) without consideration for the weight of the rope itself $\frac{F_1}{F_2} = function(f, \varphi_2 - \varphi_1) = e^{f(\varphi_2-\varphi_1)}$.
- New solution taking the weight of the rope itself into consideration, see Tab. 1, $\frac{F_1}{F_2} = function(f, \varphi_1, \varphi_2, c_m)$.

The formulas in Tab. 1 and 2 are used for comparison with the experiments in the following text.

3. Experiments

The experiment and rope are explained by Hrabovský (2022), in ČSN (2004) and shown in Fig. 2. Hence, $F_1 = F_M + a_m L_1 g$, $F_2 = F_G + a_m L_2 g$, $a_m = 0.246\ \mathrm{kg\,m^{-1}}$, $R_m = R + \frac{h}{2} = 0.164$ m and F_M.and F_G /N/ are forces measured via strain gauges and gravity.

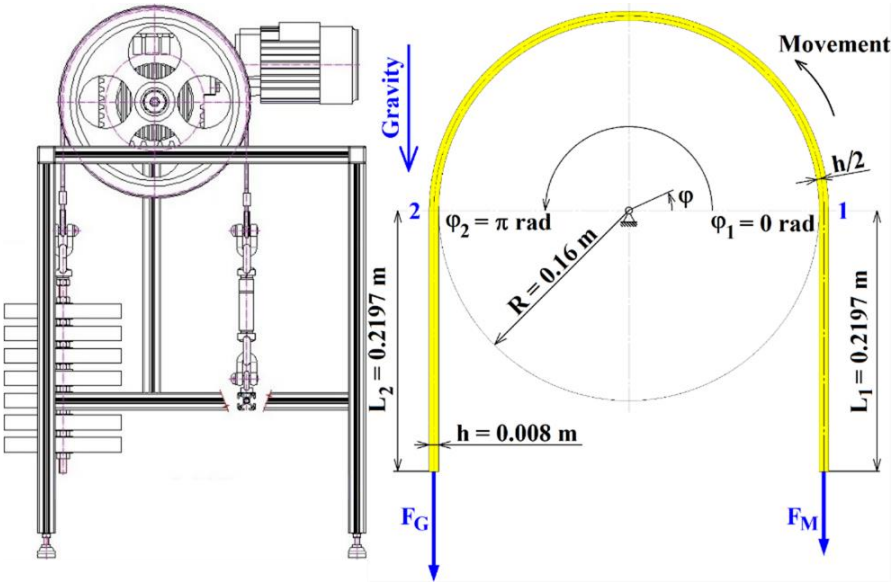

Fig. 2: Experiment set up for rope 6x7+WSC 1960 B sZ.

4. Results of Experiments

Five experiments and calculations were performed for models presented in Tab. 1 and 2. One set of measurements is presented in Tab. 3 together with relative errors.

Tab. 3: Classical belt friction model that do not respects a rope's weight and its position relative to gravity.

Experiment		**Calculation without consideration of the rope weight and geometry (Euler-Eytelwein, see Tab. 2)**			**A new calculation with consideration of the rope weight and geometry (see Tab. 1)**			**Error of calculation without consideration of rope weight, i.e., error of the Euler-Eytelwein formula**		
Given and measured forces		**Forces taken from the experiment**		**Calculated coefficient of friction**	**Given and measured forces**		**Calculated coefficient of friction**	**Error *f* /%/**	**Error F_1 /%/**	**Error F_2/%/**
F_G /N/	**F_M /N/**	**F_1 /N/**	**F_2 /N/**	***f* /1/**	**F_1 /N/**	**F_2 /N/**	***f* /1/**			
49.0	484.6	49.0	484.6	0.7294	49.5	485.1	0.7237	-0.792	1.070	0.109
	564.7		564.7	0.7781		565.2	0.7723	-0.750		0.094
	503.7		503.7	0.7417		504.2	0.7360	-0.781		0.105
	496.5		496.5	0.7371		497.0	0.7314	-0.785		0.107
	523.3		523.3	0.7539		523.8	0.7481	-0.770		0.101

From the results in Tab. 3, it is clear that when solving the belt friction problem in the experiment shown in Fig. 2 (i.e. when ignoring the rope weight), the maximal errors 1.070% occur for small tensile forces. Additionally, the error increases along with an increase in the rope weight or in gravitational acceleration too (e.g., on other planets). Our new model gives lower coefficient of friction.

5. Comparing with the Finite Element Method

An initial solution of the rope friction problem using the Finite Element Method (FEM), for Ansys Workbench 2022 R2 sw, is presented by Hrabovský (2022), see Fig. 3 and Tab. 4.

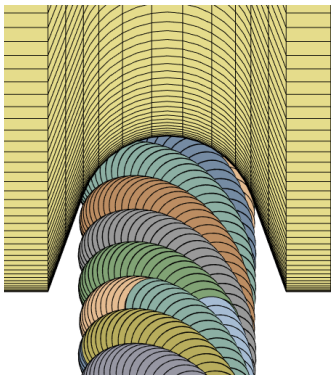

Fig. 3: FEM application.

	Force		Calculated coefficient of friction
	F_1 /N/	F_2 /N/	f /1/
Solution without gravity	49	484.66	0.6327
Solution with gravity	49.5	486.3	0.6238

Tab. 4: Results of FEM.

FEM solution with gravity application gives lower coefficient of friction, similarly to our new friction model. However, differences exist between FEM and the two presented analytical solutions, see Tab.3 and 4.

6. Conclusions

In our article, a new model for Coulomb belt friction that better accounts for belt weight and rope position was introduced. New model was then compared with the classical simple Euler-Eytelwein model. New model, which is more accurate and complex and demonstrated and supported by an experiments, better represents reality and opens up various new possibilities. The results were also compared with FEM solutions. Further possibilities for extending the model primarily lie in dynamics, other friction models, contact geometry description, wear and the probabilistic approach, see Čepica (2023), Lesňák (2020) etc.

Acknowledgement

This work was supported by Specific Research "Computational and Experimental Modeling in Applied Mechanics and Biomechanics" (SP2025/048).

References

Bulín, R., Hajžman, M. (2019) Comparison of Detailed Belt–Cylinder Interaction Model with Classical Belt Friction Formula, *Journal of Mechanical Engineering*, vol. 69, no. 3, 9-16, https://doi.org/10.2478/scjme-2019-0024.

Čepica, D., Frydrýšek, K., Hrabovský, L.; Nikodým, M. (2023) Experimental and Stochastic Application of an Elastic Foundation in Loose Material Transport via a Sandwich Belt Conveyor—Part 2. *Machines*, 11, 715. https://doi.org/10.3390/machines11070715.

ČSN EN12385-4 (2004) Steel Wire Ropes - Safety - Part 4: Stranded Ropes for General Lifting Applications, https://www.technicke-normy-csn.cz/csn-en-12385-4-024302-162156.html.

Euler, M. L. (1762) Remarques sur l'effect du frottement dans l'equilibre, *Mem. Acad. Sci.*, pp. 265–278.

Hrabovský, L., Učeň, O., Kudrna, L., Čepica, D., Frydrýšek, K. (2022) Laboratory Device Detecting Tensile Forces in the Rope and Coefficient of Friction in the Rope Sheave Groove. *Machines* 2022, 10, 590. https://doi.org/10.3390/machines10070590.

Imado, K. (2008) Study of Belt Friction in Over-Wrapped Condition, *Tribology Online*, 3(2), 76-79. https://doi.org/10.2474/trol.3.76.

Kong, L., Parker, R.G. (2005) Microslip friction in flat belt drives, *Proc. IMechE, Vol. 219 Part C: J. Mechanical Engineering Science*, https://doi.org/10.1243/095440605X31959.

Konyukhov, A., Shala, S. (2021) New Benchmark Problems for Verification of the Curve- to- Surface Contact Algorithm Based on the Generalized Euler–Eytelwein Problem, *International Journal for Numerical Methods in Engineering*, vol. 123 (2), https://doi.org/10.1002/nme.6861.

Kušnerová, M., Řepka, M., Harničárová, M., Valíček, J., Danel, R., Kmec, J., Palková, Z. (2020) A New Way of Measuring the Belt Friction Coefficient Using a Digital Servomotor. *Measurement*, 150, 107100. https://doi.org/10.1016/j.measurement.2019.107100.

Lesňák, M., Maršálek, P., Horyl, P., Pištora, J. (2020) Load-Bearing Capacity Modelling and Testing of Single-Stranded Wire Rope, *Acta Montanistica Slovaca*, 25 (2), https://doi.org/10.46544/AMS.v25i2.6.

Wasfy, T. M., Yildiz, C., Wasfy, H. M., and Peters, J. M. (2016) Effect of Flat Belt Thickness on Steady-State Belt Stresses and Slip." *ASME. J. Comput. Nonlinear Dynam.* September 2016; 11(5): 051005. https://doi.org/10.1115/1.4032383.

32nd International Conference
ENGINEERING MECHANICS 2026
Medlov, Czech Republic, May 11 – 13, 2026

VIBRATIONS OF FACIAL TISSUES DURING PHONATION IN "RESONANT" AND "NON-RESONANT" VOICE QUALITY

Horáček J.[1], Radolf V.[2], Švec J.G.[3], Laukkanen AM.[4]

Abstract: *This preliminary study measures the facial vibrations using accelerometric and vibrometric sensors placed on the positions where the vibrations were observed. From acceleration and velocity, the RMS values of displacement were obtained and their spectra were studied. One female with singing background was studied when phonating syllable strings on [pa:], [pi:] and [pu:] in speaking voice using resonant and non-resonant voice qualities. Acoustic signal, oral air pressure and electroglottogram (EGG) were also registered. The results suggested that the facial vibrations are dominantly excited at the fundamental frequency f_0 by the acoustic signal, which is for the resonant voice rather associated with lowering the first formant frequency by prolongation of the vocal tract.*

Keywords: Resonant voice, Accelerometry, Laservibrometry, Oral pressure, EGG and acoustic signals

1. Introduction

The so-called "resonant voice" is an important goal in voice training and therapy. It is well-projecting, feels easy to produce and causes sensations of vibrations on the facial area (Verdolini et al., 1998; Smith et al., 2005). Acoustically, it has been found to imply tuning of the first vocal tract resonance to the lowest voice source harmonics (Barrichelo-Lindström & Behlau, 2009). Physiologically, resonant voice is produced with barely adducted vocal folds (Verdolini et al., 1998). This is, according to modelling, efficient and vocally economic as it reduces impact stress posed on the vocal fold tissue (Zhang, 2020). Phonation with barely adducted vocal folds results in voice with larger glottal flow amplitude and stronger first partial (Sundberg, 2022).

Earlier studies have observed that phonation related facial vibrations are vowel dependent. Forehead, cheek and lower mandible were found to resonate most for closed vowels /i, u/, and least for open vowel /a/ (Kirikae et al., 1964). Since the strongest acoustic component in voice is typically the partial nearest the first formant (F1), facial vibrations have been explained as co-vibrations of F1.

Skull resonates at high frequencies, the lowest resonance frequencies being around 972 Hz and 1230 Hz according to Håkansson et al. (1993). More insights were obtained by the study of Horáček et al. (2004), which was focused on frequency modal analysis of human skull *in vitro*. The influence of the soft brain tissue on dynamics of the skull was simulated by especially prepared gelatin. The lowest resonance frequency was found around 1100 Hz. The most sensitive place to the vibration excitation of the skull was found at the edge of hard palate, behind the front teeth.

[1] Ing. Jaromír Horáček, DSc.: Institute of Thermomechanics of the Czech Academy of Sciences, Dolejškova 1402/5, 182 00 Prague, CZ, jaromirh@it.cas.cz

[2] Ing. Vojtěch Radolf, PhD.: Institute of Thermomechanics of the Czech Academy of Sciences, Dolejškova 1402/5, 182 00 Prague, CZ, radolf@it.cas.cz

[3] Prof. RNDr. Jan G. Švec Ph.D., Palacký University Olomouc, Faculty of Science, Department of Experimental Physics, jan.svec@upol.cz

[4] Prof. Anne-Maria Laukkanen, Tampere University, Virta, Åkerlundinkatu 5, 33014 Tampere, Finland.
Anne-Maria.Laukkanen@tuni.fi

ISSN: 1805-8256, doi: 10.21495/em2026-53

2. Methods

Facial and laryngeal vibrations were registered by two accelerometers (ACC1 and ACC2) and two laser vibrometers (LV1 and LV2) placed on the facial area and on the larynx, to obtain skin acceleration level (SAL) and skin velocity level (SVL). Accelerometer ACC1 and vibrometer LV1 measured the voice source signal on larynx, and ACC2 and LV2 measured the skin acceleration and velocity signals on ear and on nose, respectively, see Fig.1.

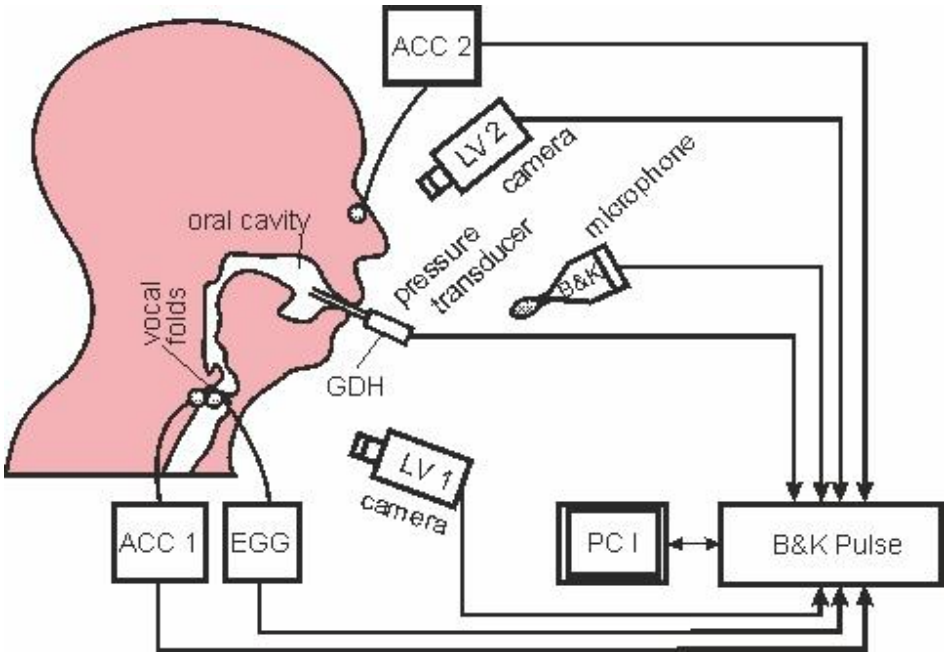

Fig. 1: Scheme of the measurement set-up.

The vibratory displacements in time domain were obtained by numeric integration. For this pilot investigation, we focus on one female subject only. Examples of evaluated vibratory displacements of the facial tissues in time domain are shown in Fig. 2.

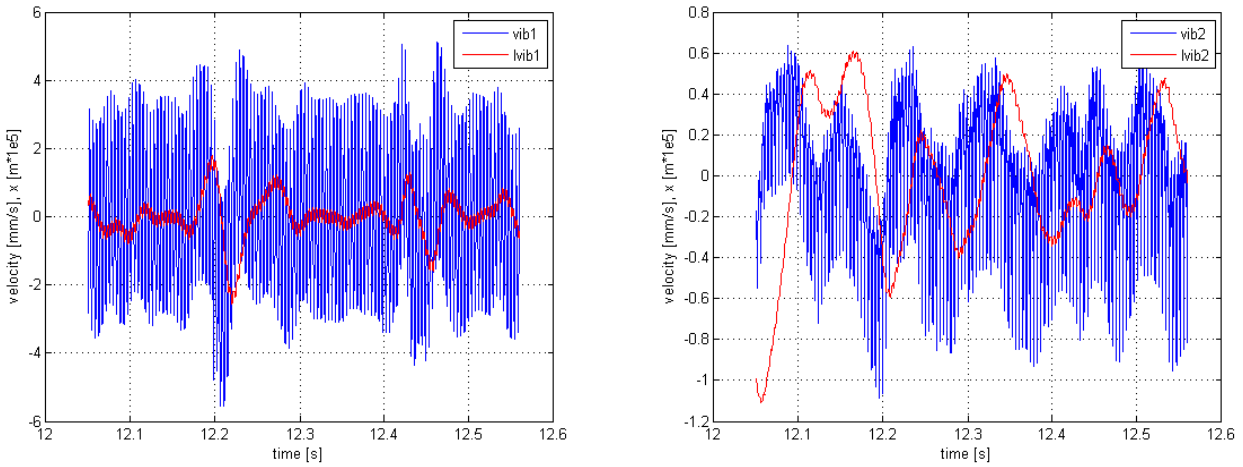

Fig. 2: Estimation of structural displacements (marked by red lines) in time domain obtained from velocities of the skin measured by laser vibrometers LV1 on larynx (marked in subpicture by Ivib1) and by LV2 on nose (marked by Ivib2). Measurement for resonant phonation [pa:] by female 2 within the time interval 12.05-12.55 s with the fundamental frequency f_0=233 Hz.

3. Results

Figure 3 shows examples of spectra obtained from the sounds measured by microphone in front of the lips and by pressure transducer in the mouth. Clearly visible are formants F1=ca 730 Hz, F2=ca 1200 Hz and F3=ca 2800 Hz measured by microphone. The strongest SPL=ca 140 dB is measured at F1 in mouth cavity at the third harmonic.

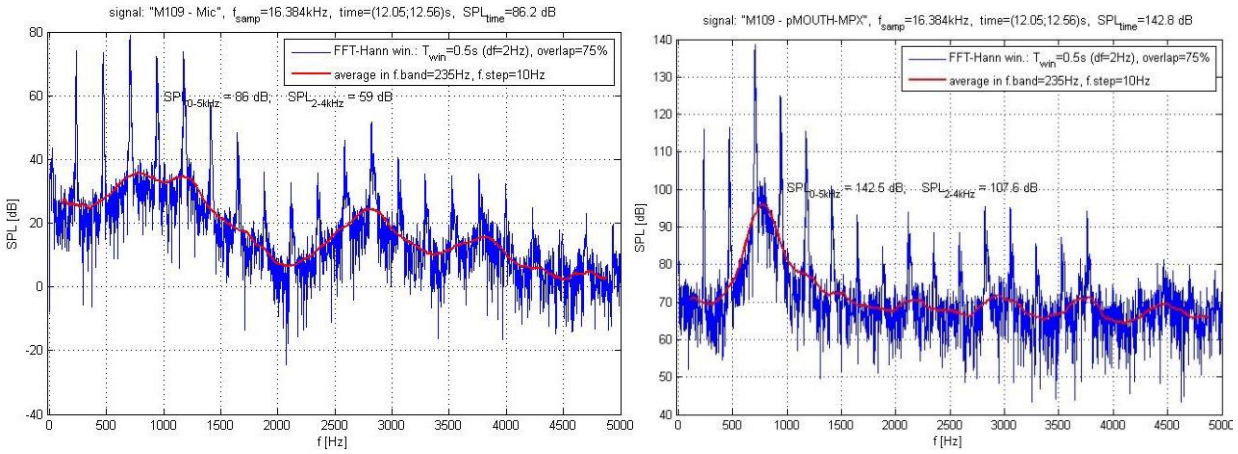

Fig. 3: SPL (sound pressure levels) measured by external microphone 13 cm from the mouth and in oral cavity. Measurement for resonant phonation [pa:] by female 2 within the time interval 12.05-12.55 s with the fundamental frequency f_0 =233 Hz.

Figure 4 presents spectra of the displacement signals obtained by integration of time signals measured by vibrometers VIB1 and VIB2, and by accelerometers ACC1 and ACC2. Maxima of skin displacements levels (SDL) are in all four cases dominant at the first harmonics. Formants F1 and F2 are slightly detectable in the displacement's spectra.

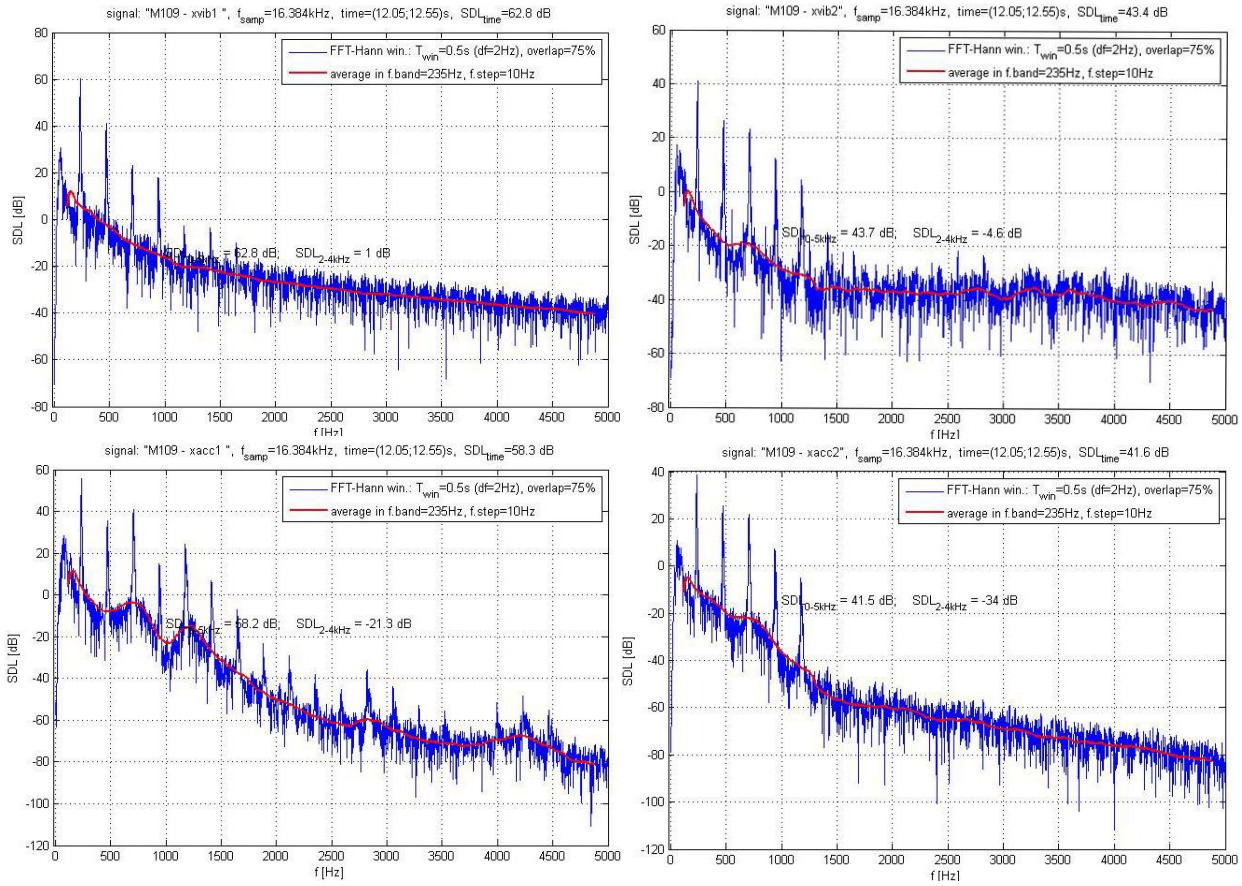

Fig. 4: Spectra of structural skin displacements levels (SDL) measured by laser vibrometers LV1 near larynx (marked by vib1 in first row left) and LV2 on nose (marked by vib2 in first row right) and by accelerometers ACC1 placed on larynx (marked by acc1 in lower row left) and by ACC2 placed near the ear (marked by acc2 in lower row right). Measurement is presented for resonant phonation [pa:] by female 2.

Table 1 compares the measured data for resonant voice, that correspond to Figs. 2-4, with the data for non-resonant voice. The RMS displacement values measured on ear for non-resonant voice are lower than

for resonant voice. In opposite, the RMS and the level of the first harmonic L_1 on nose are higher for non-resonant voice. Formants F1-F4 are visible in the spectrum of the microphone signal.

Tab. 1: Comparison of resonant and non-resonant phonation data for vowel [a:] (from [pa:]).

Displacements computed from time signals:	VIB1 larynx	VIB2 nose	ACC1 larynx	ACC2 ear
RMS displacement [μm] average for resonant voice	5.18	2.68	5.93	2.72
RMS displacements [μm] average for non- resonant voice	3.67	2.93	4.53	1.90
Data resulted from spectra SDL [dB] of displacements				
L_1 [dB] resonant	60.0	41.9	55.8	39.1
L_1 /dB/ non- resonant	58.9	45.0	52.7	40
F1 [Hz] resonant	not detected	640	688	620
F1 [Hz] non-resonant	535	675	725	not detected
F2 [Hz] resonant	1285	1140	1209	1225
F2 [Hz] non-resonant	1450	1400	1250	1400

4. Conclusions

Rather than corresponding to the previously measured mechanical (vibrational) resonances of the human head, the facial vibrations appear to correlate with the acoustic pressure oscillations in the mouth, corresponding to L1 level at the first harmonic frequency f_0 of the voice. The resonant voice shows lowering the first two formant frequencies F1, F2 closer to the frequency f_0. This effect can be attributed to prolongation of the vocal tract. The RMS displacements and the level of the first harmonic show contradicting results at the larynx, nose and ear for the resonant versus non-resonant phonations in these pilot data. We plan these to be readdressed in future investigations.

Acknowledgement

This work was supported by project No. GA 24-11121S of the Czech Science Foundation and by a grant nr 356528 from the Research Council of Finland.

References

Barrichelo-Lindström,V. and Behlau, M. (2009) Resonant voice in acting students: perceptual and acoustic correlates of the trained y-buzz by Lessac. *Journal of Voice*, 23, 5, pp. 603-609.

Håkansson, B., Brandt, A., Carlsson, P. and Tjellström, A. (1994) Resonance frequencies of the human skull in vivo. *The Journal of the Acoustical Society of America*, 95, 3, pp. 1474-1481.

Horáček, J., Veselý, J., Pešek, L. and Vohradník, M. (2004) Fundamental dynamic characteristics of human skull. *Engineering Mechanics*, 11, 2, pp. 139 –158.

Kirikae, J., Sato, T., Oshima, H. and Nomoto, K. (1964) Vibration of the body during phonation of vowels. *Rev. de Laryngologie, Otologie, Rhinologie* 85, pp. 317-345.

Smith, CG., Finnegan, EM. and Karnell, MP. (2005) Resonant voice: spectral and nasoendoscopic analysis. *Journal of Voice*, 19, 4, pp. 607–622.

Sundberg, J. (2022) Objective characterization of phonation type using amplitude of flow glottogram pulse and of voice source fundamental. *Journal of V*oice 36, 1, pp. 4-14.

Verdolini, K., Druker, DG., Palmer, PM. and Samawi, H. (1998) Laryngeal adduction in resonant voice. *Journal of Voice* 12, 3, pp. 315-327.

Zhang, Z. (2020) Laryngeal strategies to minimize vocal fold contact pressure and their effect on voice production. *J Acoust Soc Am*, 148, 2, pp. 1039–1050.

32nd International Conference
ENGINEERING MECHANICS 2026
Medlov, Czech Republic, May 11 – 13, 2026

FLUCTUATION ANIZOTROPY OF ISOTHERMAL FLOW TROUGH NUCLEAR FUEL ROD BUNDLE MODEL WITH SWIRLER-MIXING GRIDS

Janský V.[1] **Duda D.**[2], **Uruba V.**[3] **Yanovych V.**[4],

Abstract: *This document describes the exploration of isothermal flow in nuclear fuel assembly performed at the University of West Bohemia in Pilsen. The spacer and mixing grids of the model fuel assembly are similar to the basic grids used at the VVER (vodo-vodjanoj energetičeskij reaktor), i.e. there are alternating nodes of circle shape and of tri-star shape. The tri-star is modified to create a swirling element, which produce longitudinal vortices in each even inter-rod channel. The fluctuation anisotropy coefficient F displays anisotropic turbulence almost everywhere. This analysis shows a significant contribution of the boundary layers formed at the fuel rods, because the turbulence in the vortex envelopes cannot evolve into full homogeneous and isotropic turbulence.*

Keywords: Particle Image Velocimetry, Nuclear Fuel Assembly, Fluctuation Anisotropy, Vortex

1. Introduction

The bundles of nuclear fuel rods in power reactors are tightly packed and supported by swirling mixing grids to maintain the required design geometry and enhance the mixing of the coolant. These grids are made from thin-walled structures with complex shapes. The geometry of the mixing vanes is important for coolant mixing, in order to normalize the flow velocity of the coolant while improve flow turbulence to break the boundary layer and enhance the heat removal produced in the fuel. In this study, we present an experimental investigation of isothermal air flow through a model rod bundle equipped with swirler-mixing grid of hexagonal symmetry that correspond with the VVER NPPs fuel. Using stereoscopic PIV (Tropea et al., 2007), we observed fluctuation anizotropy of the isothermal flow characterized through the downstream velocity fields.

2. Experimental setup

The measurement is performed inside the larger wind tunnel at the University of West Bohemia; the tunnel is not *large* in world-wide sense, but with test section of size $3.0 \times 0.3 \times 0.2\,\mathrm{m}^3$ is the largest one at the University of West Bohemia, see Yanovych et al. (2019). The velocity within the test section is $U = 20\,\mathrm{m/s}$. The mesh parameter, i.e. the distance between neighboring fuel rods, is $M = 59.1\,\mathrm{mm}$, thus the Reynolds number based on M is $\mathrm{Re}_M = 7.34 \cdot 10^4$. However, in many studies focusing to nuclear fuel assembly experiments such as Nguyen et al. (2019); Turankok et al. (2024); Nazififard (2018), the Reynolds number is defined by using *hydraulic diameter*, which is for hexagonal symmetry equal to

$$D_h = 4 \cdot \frac{\text{Area of free cross-section}}{\text{Length of boundary of free cross-section}} = D \cdot \left(\frac{2\sqrt{3}}{\pi} \left(\frac{M}{D} \right)^2 - 1 \right) = 49.1\,\mathrm{mm} \qquad (1)$$

[1] Ing. Vojtěch Janský: Elektrárna Dukovany II, a. s.; Duhová 2; 140 00, Prague; CZ, vjansky@fst.zcu.cz
[2] Ass. Prof. RNDr. Daniel Duda, Ph.D.: Faculty of Mechanical Engineering, University of West Bohemia in Pilsen, Univerzitní 22; 306 14, Pilsen; CZ, dudad@fst.zcu.cz
[3] Prof. Ing. Václav Uruba, CSc.: Faculty of Mechanical Engineering, University of West Bohemia in Pilsen, Univerzitní 22; 306 14, Pilsen; CZ, uruba@fst.zcu.cz
[4] Ass. Prof. Ing. Vitalii Yanovych, DrSc.: Faculty of Mechanical Engineering, University of West Bohemia in Pilsen; Univerzitní 22; 306 14, Pilsen; CZ, yanovych@fst.zcu.cz

ISSN: 1805-8256, doi: 10.21495/em2026-57

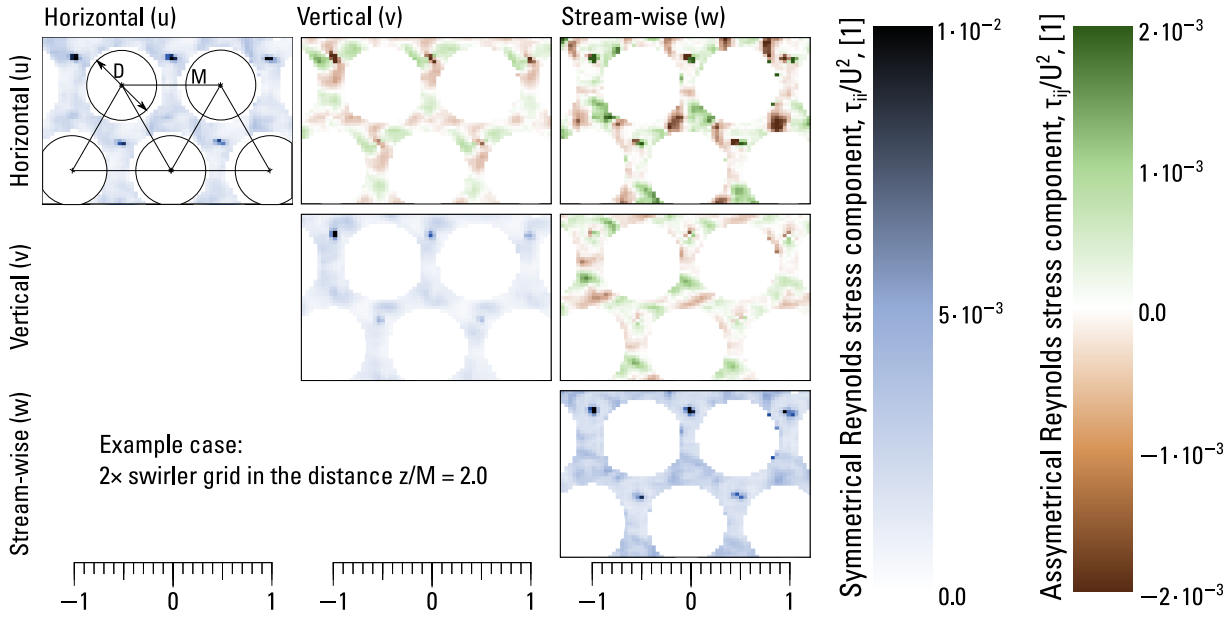

Fig. 1: Example of the spatial distribution of the individual components of the Reynolds stress tensor τ_{ij}, this tensor has 6 independent components.

, where $D = 42.2\,\mathrm{mm}$ is the diameter of fuel rods. Hence, D_h-based Reynolds number is $\mathrm{Re}_{Dh} = 6.11{\cdot}10^4$, this value can be compared with the results of Orosz et al. (2022) or Qu and Xiong (2024). Note that the wind tunnel model is up-scaled, although in many other engineering applications the model is used to be down-scaled. Anyway, we did not reach the Reynolds number of nuclear reactor, which is in order from $2.5 \cdot 10^5$ (VVER440) to $4.5 \cdot 10^5$ (VVER1000) due to the very low viscosity of water ($1.3 \cdot 10^{-7}\,\mathrm{m^2/s}$) under working conditions (pressure $12.3\,\mathrm{MPa}$ or $15.7\,\mathrm{MPa}$ respectively and temperature $268\,^\circ\mathrm{C}$ or $290\,^\circ\mathrm{C}$ respectively). Details about the swirler grid are described by Dolejš et al. (2026).

3. Anizotropy of fluctuations

The *anizotropy* (or sometimes *anisotropy*) can be calculated according to Choi and Lumley (2001), if all three components of the fluctuating velocity field are measured. The velocity signal in each direction can be decomposed to its mean and fluctuating part, $u_i = \langle u_i \rangle_t + u_i'$. The Reynolds stress tensor is

$$\tau_{ij} = \left\langle u_i' \cdot u_j' \right\rangle \tag{2}$$

The structure of this tensor is illustrated in Fig. 1, where the diagonal components are always positive and their sum (trace of the tensor) is known as turbulent kinetic energy (times one half), while the non-diagonal terms are antisymmetric, hence only 6 independent components exist in the tensor. Still, it is quite a large amount of information, see Fig. 1. This figure displays only single measuring plane in a single case. This figure is organized as components of the matrix: top left panel is τ_{xx}, top central panel displays τ_{xy} etc. Note, that we have measured at 5 downstream planes and compared 4 configurations – the base spacer grid with no swirling elements; the case where only the last grid contains swirling elements; the case where two last grids contain swirling elements; and finally the case without fuel rods to compare the behavior of free vortex with a vortex constrained between the fuel rods. To extract the most interesting information – the level of anisotropy independently of the actual orientations of the coordinate system, Lumley and Newman (1977) suggested the invariants of the tensor τ_{ij} to define the *anizotropy coefficient* F:

$$F = 1 + 9I_2 + 27I_3 \tag{3}$$

where

$$I_2 = -b_{ij} \cdot b_{ji} \quad \text{and} \quad I_3 = \frac{1}{3} b_{ij} \cdot b_{jk} \cdot b_{ki} \tag{4}$$

where b is the non-dimensional anizotropic part of Reynolds stress tensor τ

$$b_{ij} = \frac{\tau_{ij}}{\tau_{kk}} - \frac{1}{3}\delta_{ij} \tag{5}$$

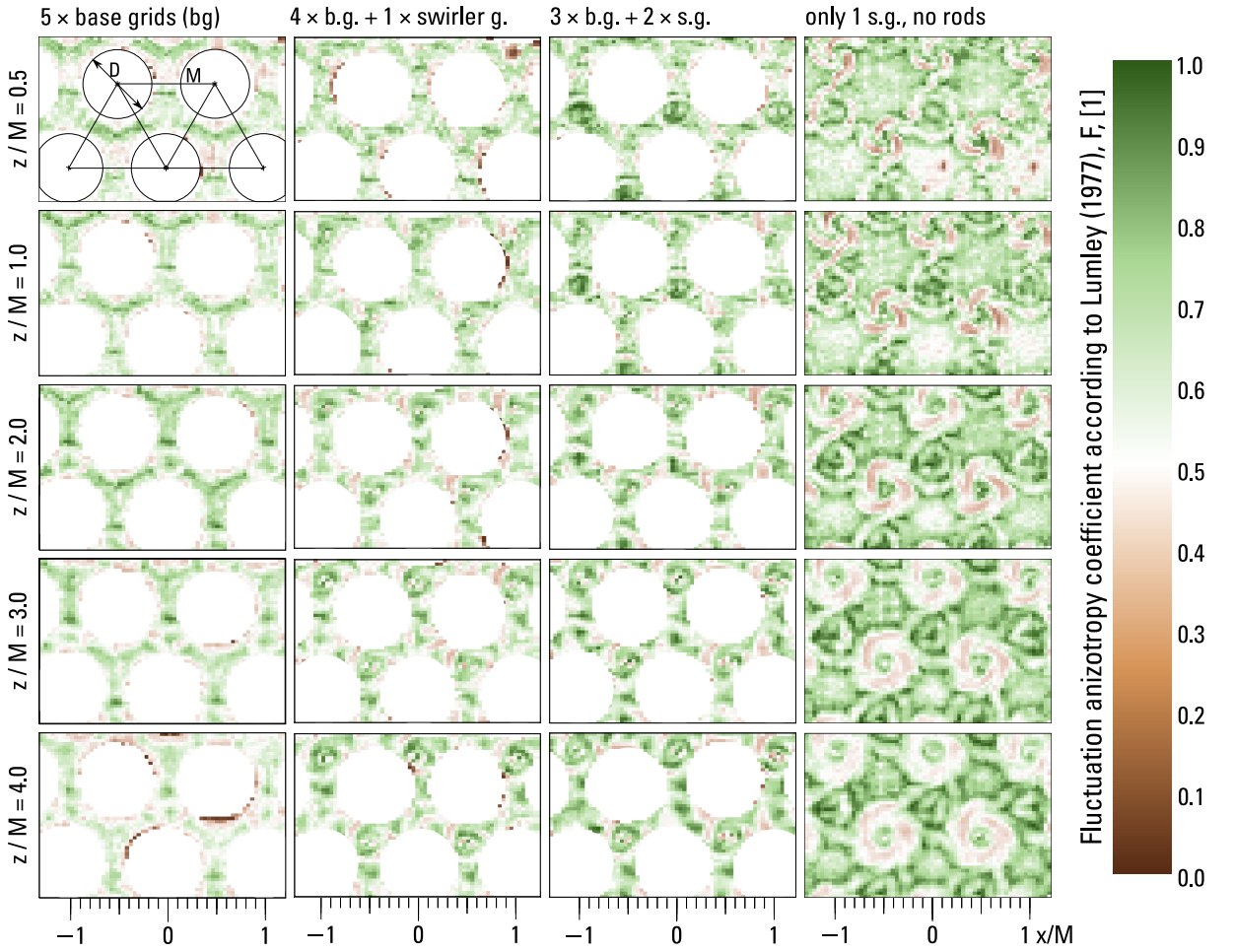

Fig. 2: Spatial map of fluctuation anisotropy coefficient as defined by Lumley and Newman (1977).

4. Results

Figure 2 displays the spatial distribution of F for the four explored cases (columns) and at five distances downstream of the grid (rows). The case past just swirler grids (the right column of Fig. 2) shows large F (green colors) almost everywhere including the areas in the for the fuel rods, where there is low turbulence level. Similarly, the area behind the circle node displays $F \in (0.6; 0.9)$ with downstream developed structure of concentric circles. The only low-anisotropy areas (brown colors in Fig. 2) lie in the envelope of vortices produced by the swirler nodes of the grid. This can be explained by the increased low-scale turbulence in the vortex envelope, which makes the fluctuations more isotropic.

In the cases with fuel rods (middle columns in Fig. 2), we see a different trend: the general level of anisotropy varies less, it is closer to 0.5 everywhere. In the areas pat swirlr nodes is the anizotropy larger; note the residuals of shear layers at the vortex envelopes also depicted by brown colors (i.e. low F).

It is clear that the presence of boundary layers at the fuel rods significantly reduces the peaks in the turbulence anisotropy. This may coincide with the fact that the large-scale coherent structures are blocked by the rods, and the smaller-scale structures, which fit into the interrod channels, display naturally lower anizotropy.

Figure 3 shows the anizotropy of two different length-scales (top row: small scales, bottom row: large scales) at single position $z = 2M$. In the case without fuel rods (right column), we see that the isotropic behavior inside the vortex envelopes is associated with large scales. With fuel rods present (first three columns), the situation is opposite: the isotropic signal of shear layers between neighboring channels comes from the small-scale fluctuations, while the large-scale ones are responsible for strongly anisotropic behavior of the shear layers and vortex centers.

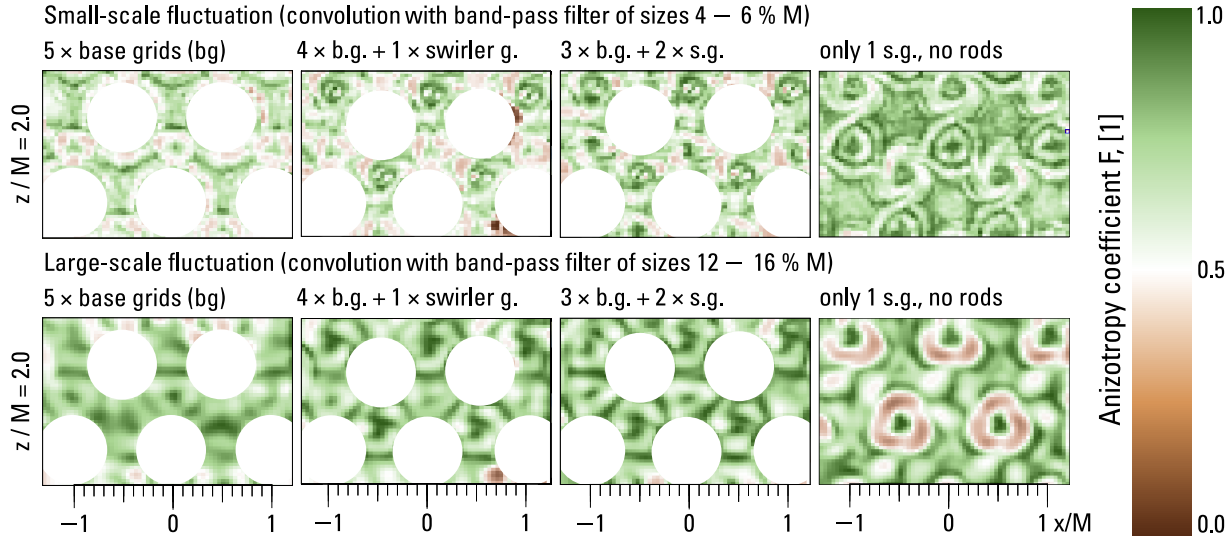

Fig. 3: Anizotropy of length-scale decomposed fields according to Duda and Uruba (2019).

5. Conclusions

The flow through a nuclear fuel assembly model is explored by using a standard method of PIV. The spacer grid contains swirling elements creating longitudinal vortices in every even inter-rod channel. We focus on the anisotropy coefficient defined by Lumley and Newman (1977). This analysis shows a significant contribution of the boundary layers formed at the fuel rods, because the turbulence in the vortex envelopes cannot evolve into full homogeneous and isotropic turbulence. The applied air-tunnel PIV methodology proves to be efficient for assessing the impact of modifications that enable rapid evaluation of geometrical changes and the optimisation of spacer-grid designs for nuclear fuel assemblies.

Acknowledgments

We would like to especially thank Elektrárna Dukovany II, a. s. for the support to present the results of our research.

References

Choi, K. and Lumley, J. (2001) The return to isotropy of homogeneous turbulence. *J. Fluid Meach.*, 436, pp. 59–84.

Dolejš, M., Duda, D., Janský, V., Mrázová, A., Uruba, V., Yanovych, V. P., Vasconcelos da Silva, I. K., and Kovalova, K. V. (2026) Vortices produced by swirl-mixing grids in nuclear fuel assembly: a wind-tunnel experiment. *Flow*, 6, pp. E8.

Duda, D. and Uruba, V. (2019) Spatial spectrum from particle image velocimetry data. *ASME J of Nuclear Rad Sci.*, 5, 030912.

Lumley, J. and Newman, G. (1977) The return to isotropy of homogeneous turbulence. *J. Fluid Meach.*, 82, pp. 161–178.

Nazififard, M. (2018) Cfd simulation of swirl flow in hexagonal rod bundle geometry by split mixing vane grid spacers. *Thermal Science*, 2018, pp. 76–76.

Nguyen, T., White, L., Vaghetto, R., and Hassan, Y. (2019) Turbulent flow and vortex characteristics in a blocked subchannel of a helically wrapped rod bundle. *Experiments in Fluids*, 60, 8.

Orosz, G. I., Magyar, B., Szerbák, D., Kacz, D., and Aszódi, A. (2022) Allegro gas cooled fast reactor rod bundle investigations with cfd and piv method. *Nuclear Engineering and Design*, 400, pp. 112062.

Qu, W. and Xiong, J. (2024) High-fidelity piv measurements of turbulent flow in reactor pressure vessel assisted by high-precision matched index of refraction technique. *Nuclear Engineering and Design*, 420, pp. 112997.

Tropea, C., Yarin, A., and Foss, J. F. (2007) *Springer Handbook of Experimental Fluid Mechanics*. Springer, Heidelberg, DE.

Turankok, N., Lohez, T., Biscay, V., and Rossi, L. (2024) Velocity and pressure fluctuations downstream analytical spacer grids: Structure and transport. *Nuclear Engineering and Design*, 430, pp. 113682.

Yanovych, V., Duda, D., Horáček, V., and Uruba, V. (2019) Research of a wind tunnel parameters by means of cross-section analysis of air flow profiles. *AIP Conference Proceedings*, 2189, 020024.

32st International Conference
ENGINEERING MECHANICS 2026
Medlov, Czech Republic, May 11 – 13, 2026

MODAL TESTS OF TECHNICAL OBJECTS

Kałaczyński T.[1], Liss M.[2], Łukasiewicz M.[3]

Abstract: *The paper presents the process of identifying the technical condition of objects with large spatial dimensions and large masses using the properties of the exploitation modal analysis method, based on measurements of the response to exploitation excitations. The paper presents the possibility of implementing modal analysis in assessing the selected technical objects technical state. The presented procedure demonstrates the possibilities of classifying objects based on their state of wear.*

Keywords: Modal analysis, Technical object, Vibration diagnostics, Technical state, Exploitation

1. Introduction

Contemporary technical facilities are complex, dynamic systems, both structurally and functionally, often occupying large production spaces. The production and exploitation of such facilities requires significant financial, raw material, and energy expenditures on businesses. The increase in technical requirements for the parameters of machines and devices, while reducing the costs of production and operation, has led to fundamental changes in the methods of designing, controlling production and operating technical facilities. The occurrence of unexpected damage or failure generates economic losses resulting from the cessation of production and results in additional expenditure on repair processes, justifying the need to conduct diagnostic tests, which are the basic source of information about the changing state of technical objects exploitation.

Modal analysis is a method for examining the dynamic properties of structures and can be used to conduct diagnostic tests on complex technical objects. Modal analysis produces a modal model consisting of an ordered set of natural frequencies, corresponding damping coefficients, and natural vibration modes. The idea behind this method is to track changes in modal model parameters resulting from misalignment, wear, damage, or failure, based on current observations of the object. Based on knowledge of the modal model, it is possible to predict the object's response to any disturbance, both in the time and frequency domains (Łukasiewicz M.. et al., 2010). It is implemented as theoretical, experimental, or exploitation modal analysis (often referred to interchangeably as exploitation modal analysis) (Furgal, Sz. et al., 2023).

Exploitation modal analysis is a technique based on measuring the system's response to unknown operational forces resulting from the action of technological process forces or kinematic forces and the destruction process of machine components (Żółtowski B. et al., 2012). During testing, measurement points and reference points—constant throughout the measurements—must be determined. The advantage of this method for identifying the dynamic characteristics of objects is the preservation of boundary conditions and excitations typical of their operation (Crocker, M. J. et al., 2007). The properties and research conducted in the implementation of operational modal analysis in assessing the technical condition of technical objects enable the classification of the condition and the quality of repair procedures (Kałaczyński T. et al., 2025). This allows for the identification of wear and tear of technical object components.

[1] Tomasz Kałaczyński, PhD.: Faculty of Mechanical Engineering, Bydgoszcz University of Science and Technology, Al. prof. S. Kaliskiego 7, Bydgoszcz; PL, kalaczynskit@pbs.edu.pl

[2] Michał Liss, PhD.: Faculty of Mechanical Engineering, Bydgoszcz University of Science and Technology, Al. prof. S. Kaliskiego 7, Bydgoszcz; PL, michal.liss@pbs.edu.pl

[3] Marcin Łukasiewicz, PhD.: Faculty of Mechanical Engineering, Bydgoszcz University of Science and Technology, Al. prof. S. Kaliskiego 7, Bydgoszcz; PL, mlukas@pbs.edu.pl

ISSN: 1805-8256, doi: 10.21495/em2026-61

2. Object and research methodology

In this method, modal parameters are estimated based on measured signals at the object's output, as well as signals obtained during measurements at selected reference and measurement points for unknown system excitations. As a result, the system's poles and natural frequencies are identified, and then the mode shapes are estimated based on these values (Żółtowski B. et al., 2012). In exploitation modal analysis, no additional vibration exciters (modal hammers) are used, and measurements are taken for the object during its operation. This approach allows us to obtain measurement data for normal operational excitations (actual object operation) at selected measurement points relative to a reference point. The selection of the number and location of reference points is crucial in this method. The obtained data is further estimated using various computational methods (Łukasiewicz M.. et al., 2019).

The research methodology included the use of the LMS SCADAS Recorder System, which is one of the most modern measurement systems used in diagnostic testing. LMS Test.Lab software was used for data acquisition and analysis of test results. To demonstrate the practical capabilities of the LMS SCADAS measurement system with LMS Test.Lab software for determining the natural frequencies of technical objects, Figure 1 illustrates two impeller blades. One blade was in good working order, while the other was worn after long periods of operation. These blades are shown in Figure 2.

This article presents selected and useful research results and their analysis. The full text of the research is available from the authors. The presented results are part of an ongoing research process focused on the development and exploitation verification of the proprietary MTM Solution repair quality assessment method.

a 

Fig. 1: Blade wheels of a projecting rotor (from left): new wheel, worn wheel.

The measurement results were obtained from a total of 16 measurement points, eight on each side of the paddle wheel. The measurements were taken on two paddle wheels in different technical state. The measurement method was based on exploitation modal analysis, The response signal generated was recorded using standard piezoelectric sensors from 16 measurement points on a single wheel in the form of spectral transfer functions (FRFs). Individual spectral transfer functions (FRFs) were then transferred to other software for analysis.

3. Results and conclusions

The results of the modal analysis are individual modal parameters, such as natural frequencies, damping coefficients, and mode shapes. These parameters are estimated based on the generated stabilization diagram, which is presented for a functioning wheel in Figure 3.

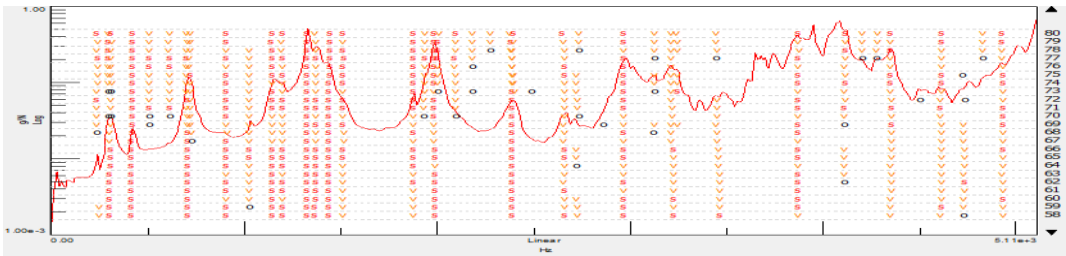

Fig. 2: Stabilization diagram created using the SUM indicator from 16 individual measurements for a new wheel.

Based on the results presented in Table 1, it can be seen that the worn wheel exhibits a second mode of natural vibration around 400 [Hz]. Another characteristic feature clearly illustrating the differences between the two test objects is the damping coefficient, which is generally significantly higher for the worn wheel than for the unworn wheel. Other features include shifts in individual vibration modes on the frequency axis. For a worn paddle wheel, all estimated natural frequencies are lower than for a new paddle wheel.

Tab. 1: Summary of natural frequencies and damping coefficients for both considered paddle wheel cases.

	New wheel		Worn wheel	
Own vibration mode	Frequency	Damping	Frequency	Damping
	[Hz]	[%]	[Hz]	[%]
Mode 1	302,78	3,65	300,73	0,16
Mode 2	415,79	2,36		
Mode 3	709,73	1,46	683,03	0,94
Mode 4	1147,43	1,09	1066,05	0,64
Mode 5	1328,14	0,69	1156,12	0,40
Mode 6	1987,53	0,40	1440,83	0,31
Mode 7	2968,40	0,41	2343,09	0,23

The next step is to estimate the individual vibration modes and visualize their form using a geometric representation. The mode estimation window is shown in Figure 3, along with a geometric representation of the analyzed paddle wheel.

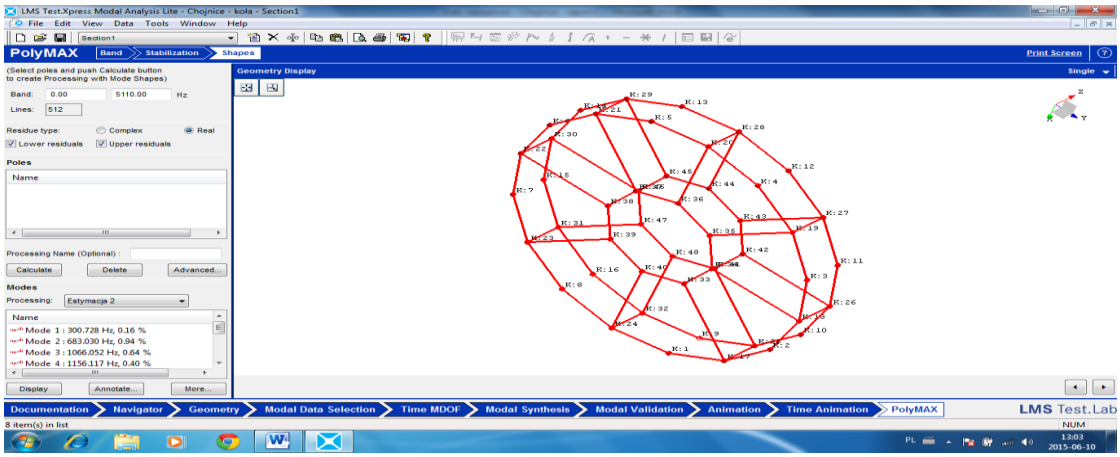

Fig. 3: Mode shape estimation window

The estimated individual own vibration modes can be visualized on the prepared geometric model. A comparison of the individual own vibration modes and their graphical representations is presented in the figures below. Analyzing the individual vibration modes of a worn wheel, numerous similarities can be observed with those of a new wheel. In all cases, these modes are flexural in nature.

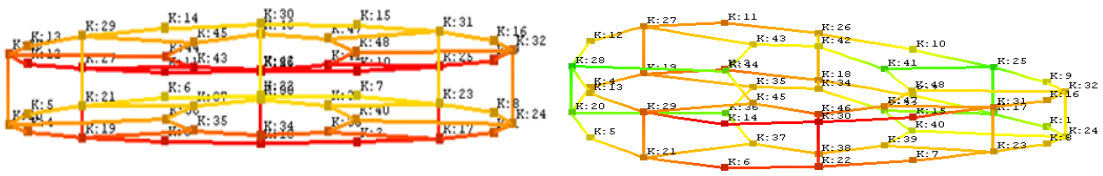

Fig. 4: Comparison of the mode I of the new wheel on the left side (302.775 Hz, 3.65%) with the mode I of the worn wheel on the right side (300.728 Hz, 0.16%)

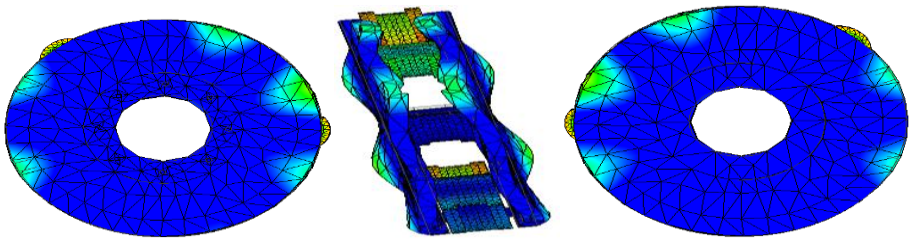

Fig. 5: Mode of Action

The estimated and selected own vibration modes were validated using the AutoMAC method. Validation results are presented in Figure 6.

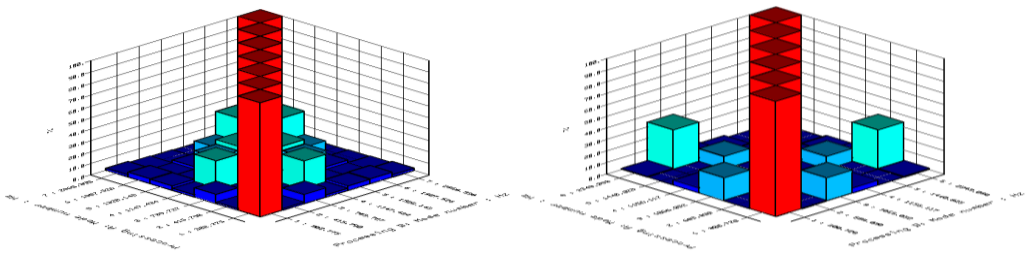

Fig. 6: Summary of AutoMAC validation results: a) (from left) for a new wheel, b) (from right) for a worn wheel

The estimated and selected vibration modes were validated using the AutoMAC method. Validation allowed for verification confirming the feasibility of implementing exploitation modal analysis.

Conclusions:

1) Modal tests of the impeller blade wheel clearly illustrate differences in the results between the individual test object states. This is indicated primarily by shifts in the individual vibration modes on the frequency axis, and even by the complete disappearance of one mode in the case of a worn wheel. In the case of a worn wheel, it can also be observed that the damping coefficient has significantly decreased in some own vibration modes.
2) The advantage of this method is that the tested object can be tested without excluding it from the operational process. Therefore, such tests do not generate additional costs, and the obtained results are based on actual signals generated by the tested object.
3) Modal analysis parameters form the basis for building a model that classifies the degree of wear and tear of technical object components. They are also used in assessing the quality of repair procedures.

References

Crocker, M. J. (2007) *Handbook of Noise and Vibration Control*. Wiley-Interscience. New Jersey.

Furgal, Sz., Kałaczyński, T., Łukasiewicz, M., Martinod, R. (2023) Analysis of the changes impact in the construction of the vehicle exhaust silencer on the noise emission level, *Proc. 21st International Conference Diagnostics of Machines and Vehicles "Hybrid Multimedia Mobile Stage"*, Matec Web of Conferences, Bydgoszcz – Dresden, pp. 1-12.

Kałaczyński T., Łukasiewicz M., Liss M., Mazurkiewicz A. (2025) Vibration diagnostics in the assessment of the vehicles bodywork technical state procedure, ENGINEERING MECHANICS 2024, ISSN 1805-8256 , 30th INTERNATIONAL CONFERENCE May 14 – 16, 2024, Milovy, Czech Republic,pp 109 – 112.

Łukasiewicz M., (2010) Vibration measure as information on machine technical condition, Studies & Procedings of Polish Association for Knowledge Management 35, ISSN 1732-324X, Bydgoszcz.

Łukasiewicz, M., Liss, M., Dluhunovych, N. (2019) Analysis of vibrodiagnostics methods in the technical state study of designed multimedia mobile scenes, *Proc. 18th International Conference Diagnostics of Machines and Vehicles*, Matec Web of Conferences, Bydgoszcz, pp. 1-9.

Żółtowski B., Łukasiewicz M. (2012) *Diagnostyka drganiowa maszyn, Biblioteka Problemów Eksploatacji ITE Radom*, Wydawnictwo Naukowe Instytutu Technologii Eksploatacji - Państwowego Instytutu Badawczego w Radomiu, ISBN 978-83-7789-138-4.

Żółtowski B., Łukasiewicz M., Kałaczyński T. (2012) *Techniki informatyczne w badaniach stanu maszyn*, Wydawnictwa Uczelniane UTP w Bydgoszczy, Bydgoszcz.

32nd International Conference
ENGINEERING MECHANICS 2026
Medlov, Czech Republic, May 11 – 13, 2026

MODELING CONCRETE FLOW IN FORMWORK USING TWO-WAY FLUID-STRUCTURE INTERACTION

Kout K.[1], **Němeček J.**[2], **Němeček J.**[3]

Abstract: *This article investigates the lateral pressure exerted by fresh self-compacting concrete on vertical formwork using an implicit coupled two-way fluid-structure interaction (FSI) approach. Fresh concrete is modeled by the Herschel-Bulkley rheological model, while the formwork is represented as a deformable elastic structure. A three-dimensional numerical model implemented in ANSYS software enabled continuous simulation of the fluid domain due to formwork deformation during casting. The results indicated that the two-way coupling approach provides a more realistic description of concrete-formwork interaction and serves as a reference for assessing the applicability of simplified pressure prediction models. The obtained results confirm that the predicted lateral pressure remained within typical design limits of standard formwork systems, while the corresponding deformation levels were consistent with the assumed support conditions.*

Keywords: **Self-compacting Concrete, Volume of Fluid, Computational Fluid Dynamics, Two-way Fluid-structure Interaction, Formwork**

1. Introduction

Self-compacting concrete (SCC) has become a standard material in contemporary construction practice, primarily due to its high flowability and ability to completely fill formwork without the need for mechanical compaction Geiker and Jacobsen (2019). Despite these advantages, the lateral pressure acting on vertical formwork during casting represents a major design concern. Because fresh SCC exhibits pronounced fluid-like behavior, the resulting pressures may approach hydrostatic conditions, which can significantly increase the structural demands on formwork systems Gowripalan et al. (2021). Reliable prediction of this pressure is therefore a key requirement for ensuring both structural safety and cost-effective formwork design.

The common practice of formwork designs typically assumes hydrostatic pressure, neglecting the time-dependent rheological behavior of fresh concrete. Experimental studies have shown that thixotropy and structural buildup can significantly reduce the exerted pressure compared to the hydrostatic assumption Roussel (2006). Several approaches have been proposed to improve pressure prediction, including experimental measurements Trávníček et al. (2023); Gamil et al. (2023), analytical models Ovarlez and Roussel (2006), and numerical simulations Tichko et al. (2015). While analytical methods provide fast estimates, they rely on simplifying assumptions, and most numerical studies apply one-way coupling in which the concrete flow is solved independently and the resulting pressure is applied to prescribed formwork boundary, neglecting the influence of formwork deformation on the flow field.

Unlike one-way coupled numerical models, the two-way FSI formulation allows the deformation of the formwork to influence the flow field and pressure distribution, while simultaneously capturing the effect of the evolving concrete pressure on the structural response. The limitation of this approach can be addressed by a two-way fluid-structure interaction (FSI) model, in which the mutual interaction between fresh concrete flow and deformable formwork is explicitly taken into account. This article aims to develop a two-way FSI

[1] Bc. Kryštof Kout: Department of Mechanics, Faculty of Civil Engineering, Czech Technical University, Thákurova 2077/7; 166 29, Prague 6; CZ, koutkrys@cvut.cz
[2] Ing. Jiří Němeček, Ph.D., Orcid 0000-0002-5635-695X: Department of Mechanics, Faculty of Civil Engineering, Czech Technical University, Thákurova 2077/7; 166 29, Prague 6; CZ, jiri.nemecek.1@fsv.cvut.cz
[3] Prof. Ing. Jiří Němeček, Ph.D., DSc., Orcid 0000-0002-3565-8182: Department of Mechanics, Faculty of Civil Engineering, Czech Technical University, Thákurova 2077/7; 166 29, Prague 6; CZ, jiri.nemecek@fsv.cvut.cz

ISSN: 1805-8256, doi: 10.21495/em2026-65

model for filling fresh concrete into the formwork while simultaneously capturing the real deformation of the formwork, which is essential for a consistent description of the casting process, particularly in cases where formwork deformability may alter pressure development.

2. Solution Strategy

The numerical analysis presented in this article is based on a coupled solution of fluid flow and structural deformation. Computational fluid dynamics is employed to model the flow of fresh concrete, while structural mechanics is used to describe the response of deformable formwork.

Fresh concrete casting into formwork represents a flow problem involving concrete and air. The evolution of the concrete during casting is described using a multiphase approach using the Volume of Fluid (VOF) method. In this formulation, each computational cell is characterized by a phase volume fraction, which implicitly defines the position of the interface. The fluid motion is governed by the incompressible continuity equation and the momentum balance, solved using mixture properties weighted by the local phase fractions. The momentum and continuity equations are defined as follows, respectively:

$$\frac{\partial}{\partial t}\left(\rho\vec{v}\right) + \nabla\cdot\left(\rho\vec{v}\vec{v}\right) = -\nabla p + \nabla\cdot\left[\eta\left(\nabla\vec{v} + \nabla\vec{v}^{T}\right)\right] + \rho\vec{g} + \vec{F}, \tag{1}$$

$$\nabla\cdot\vec{v} = 0. \tag{2}$$

where $\vec{v}$ is the velocity, t is the time filed, p is the static pressure, ρ is the fluid density, η is the apparent viscosity, g is the gravitational acceleration, and $\vec{F}$ is the force resulting from a sharp tension interface.

FSI describes problems in which fluid flow and structural deformation are mutually coupled. The fluid exerts forces on the structure, causing deformation, while the structural response modifies the fluid domain and influences the flow field. The linear momentum equation (equilibrium equation) in a structure is defined as

$$\int_S \sigma\cdot\vec{n}\,dS + \int_V \vec{f}\,dV = 0, \tag{3}$$

where σ is the stress tensor, $\vec{n}$ is the outward normal, S is the boundary surface and $\vec{f}$ is the body force vector acting over volume V. Accurate representation of such problems requires simultaneous consideration of both physical domains Richter (2017). The two-way FSI is solved using a partitioned implicit coupling approach where fluid flow and structure are solved separately and coupled iteratively through interface force and displacement exchange with the coupling procedure being schematically shown in Fig. 1.

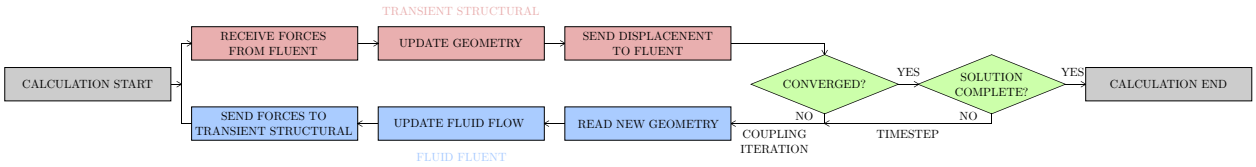

Fig. 1: ANSYS two-way coupling fluid-structure interaction flowchart.

3. Numerical two-way FSI Model

3.1. Geometry and mesh

A three-dimensional numerical model was prepared in Ansys Workbench 2023 R2. The model consists of two interacting domains: (i) a structural domain representing the formwork with dimensions of 100 $\times$ 400 $\times$ 2800 mm, and (ii) a fluid domain surrounding the formwork on both sides with a thickness of 100 mm. This configuration enables concrete flow on one side, where the inlet is located, while simultaneously allowing deformation of the formwork in the opposite direction. The geometry of the model is shown in Fig. 2a.

The fluid (Fig. 2b) and structural (Fig. 2c) domains are discretized independently, both using a quadrilateral mesh with a uniform element size of 50 mm. Additionally, the fluid domain is configured to allow dynamic mesh motion, enabling it to capture the formwork deformation obtained from the structural analysis.

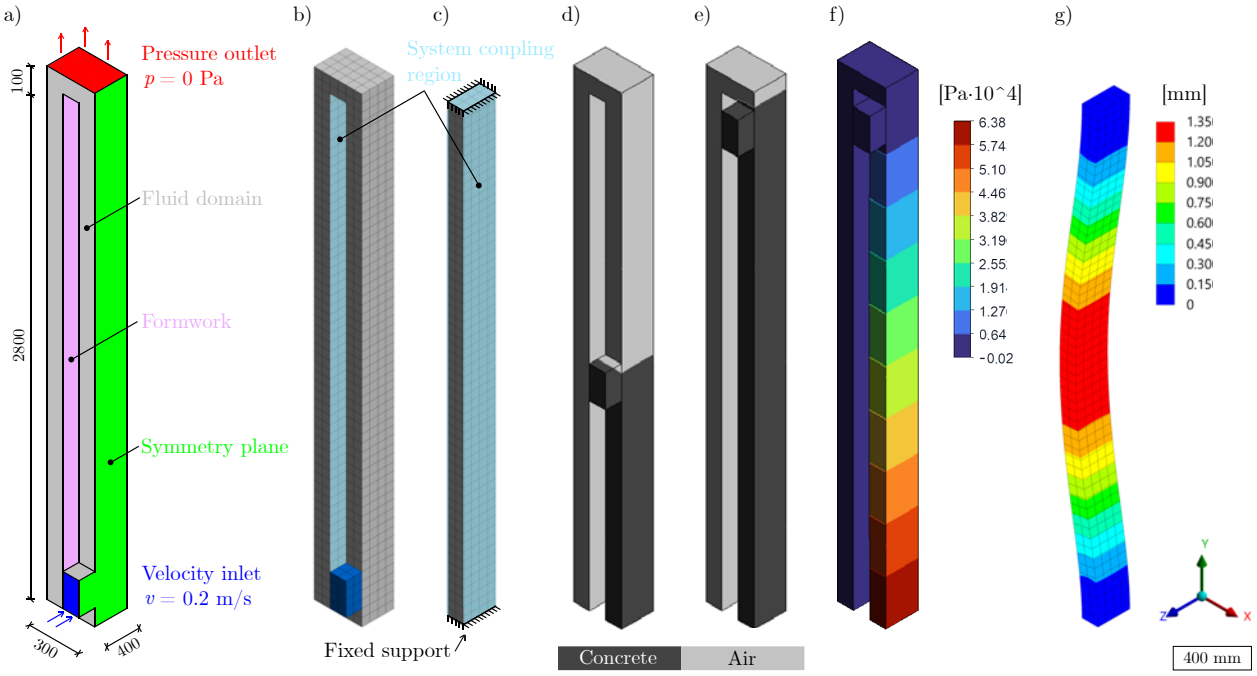

Fig. 2: Ansys model overview of a) boundary conditions, b) Fluent mesh, c) Transient Structural mesh, d) half-filled wall, e) fully filled wall, f) pressure results, g) deformation results.

3.2. Boundary Conditions and Materials

The formwork is modeled as an isotropic, elastic, deformable solid. The formwork material is characterized by a Young's modulus of $E = 43$ GPa, a density of $\rho = 425$ kg·m^{-3}, and a Poisson's ratio of $\nu = 0.3$, representing homogenized properties of wooden plates and steel rods chosen to match the global bending stiffness of a real formwork panel. A fixed support condition (zero displacements in all directions, SOLID186 elements) is prescribed at both the base and the top of the formwork. This boundary condition represents a stiffer support arrangement associated with additional reinforcement, such as formwork tie rods. The formwork surfaces in contact with the fluid domain are defined as system coupling regions (Fig. 2c), allowing bidirectional exchange of forces and displacements between the fluid and structural domains.

At the start of the calculation, the entire domain is filled with air. Fresh concrete is introduced through a user-defined function (UDF) coded moving velocity inlet at the base of the formwork at a constant velocity of 0.2 m·s^{-1}, corresponding to a typical casting rate in practice. To reduce computational cost, geometric symmetry is assumed and only half of the wall-fluid system is modeled. The top boundary is defined as a pressure outlet with zero gauge pressure to allow air evacuation during casting, while no-slip conditions are applied on all remaining solid walls. Gravitational acceleration ($g = 9.81$ m·s^{-2}) is included in fluid domain.

Fresh concrete is modeled as an incompressible non-Newtonian fluid using the Herschel-Bulkley model. The concrete density is set to $\rho = 2400$ kg·m^{-3}. The Herschel-Bulkley model parameters are defined by the yield stress $\tau_0 = 40.71$ Pa, consistency index $k = 0.93$ Pa·s^n, power-law coefficient $n = 1.45$ and critical shear rate $\dot{\gamma}_c = 0.5$ s^{-1}, corresponding to a real SCC mixture used in practice.

The transient simulation is carried out with a fixed time step of 0.1 s and a total simulation time of 150 s. Within each time step, 5 coupling iterations are performed until convergence of the exchanged interface quantities is achieved.

4. Results and discussion

The coupled two-way FSI simulation successfully captures the progressive filling of the formwork by fresh concrete during casting. The evolution of the concrete filling at selected time steps are shown in Fig. 2d and 2e.

The pressure distribution along the height of the formwork is dominated by the hydrostatic component $p = \rho g h$, which for the considered height corresponds to a maximum value of 65.92 kPa. The numerical results follow the hydrostatic trend closely, with small local deviations due to FSI interaction, and a maximum lateral pressure at the bottom of the concrete column of $p_{max} = 63.81$ kPa of the fully filled domain. For comparison, the maximum allowable pressure for standard formwork panels (e.g. PERI systems) is specified as 80 kPa. The obtained value therefore remains below this limit, indicating that the considered formwork configuration satisfies the strength requirement under the given loading conditions. The spatial distribution of lateral pressure obtained from the coupled two-way FSI analysis is shown in Fig. 2f.

The structural response of the formwork under lateral pressure is quantified by the displacement field, as shown in Fig. 2g. The maximum displacement occurs at mid-height of the wall and reaches a value of $u_{\max} = 1.35$ mm. Additionally, the model can be used to represent the effects of formwork tie rods, steel reinforcement during filling, formwork design variations, and interrupted concrete casting.

5. Conclusions

This article demonstrates the applicability of a coupled two-way fluid-structure interaction approach for the analysis of concrete casting into vertical formwork, forming a basis for further model development.

The results show that, although the maximum lateral pressure is largely governed by the concrete height, the coupled model enables simultaneous prediction of both pressure distribution and formwork deformation within a continuously deforming fluid domain. In contrast to simplified or one-way approaches, the presented formulation accounts for the influence of formwork deformation on the concrete flow itself, which allows a consistent description of pressure redistribution under different support conditions. Further improvement in prediction accuracy may be achieved by explicitly modeling individual formwork auxiliary components and by employing material models that capture the thixotropic behavior of SCC.

Acknowledgments

Financial support from the Grant Agency of the Czech Technical University in Prague (project number: SGS25/083/OHK1/2T/11) and from the project of the Technology Agency of the Czech Republic (Trend No. FW01010521) is acknowledged with gratitude.

References

Gamil, Y., Cwirzen, A., Nilimaa, J., and Emborg, M. (2023) The impact of different parameters on the formwork pressure exerted by self-compacting concrete. *Materials*, 16, 2.

Geiker, M. and Jacobsen, S. (2019) 10 - Self-compacting concrete (SCC). In Mindess, S., edt., *Developments in the Formulation and Reinforcement of Concrete (Second Edition)*. Woodhead Publishing, Woodhead Publishing Series in Civil and Structural Engineering, pp. 229–256.

Gowripalan, N., Shakor, P., and Rocker, P. (2021) Pressure exerted on formwork by self-compacting concrete at early ages: A review. *Case Studies in Construction Materials*, 15, pp. e00642.

Ovarlez, G. and Roussel, N. (2006) A physical model for the prediction of lateral stress exerted by self-compacting concrete on formwork. In *2nd International RILEM Symposium on Advances in Concrete through Science and Engineering*. RILEM Publications SARL, 39, pp. 269–279.

Richter, T. (2017) *Fluid-structure Interactions: Models, Analysis and Finite Elements*. Lecture Notes in Computational Science and Engineering. Springer International Publishing.

Roussel, N. (2006) A thixotropy model for fresh fluid concretes: Theory, validation and applications. *Cement and Concrete Research*, 36, 10, pp. 1797–1806.

Tichko, S., De Schutter, G., Troch, P., Vierendeels, J., Verhoeven, R., Lesage, K., and Cauberg, N. (2015) Influence of the viscosity of self-compacting concrete and the presence of rebars on the formwork pressure while filling bottom-up. *Engineering Structures*, 101, pp. 698–714.

Trávníček, P., Němeček, J., Zacharda, V., and Němeček, J. (2023) Monitoring of fresh concrete formwork pressures. *AIP Conference Proceedings*, 2780, 1, pp. 020002.

32nd International Conference
ENGINEERING MECHANICS 2026
Medlov, Czech Republic, May 11 – 13, 2026

SOFTWARE SIMULATION OPTIONS FOR EVTOL TILTWING CONFIGURATIONS

Kukla O.[1]

Abstract: *Tilt-wing electric vertical takeoff and landing (eVTOL) aircraft exhibit strongly nonlinear and configuration-dependent dynamics, with the transition between hover and forward flight representing the most challenging regime to model. While rigid-body dynamics follow conventional aircraft formulations, continuously varying aerodynamic and propulsive characteristics associated with wing tilt significantly increase modeling complexity.*
This paper discusses software-based simulation approaches for tilt-wing eVTOL aircraft with a focus on continuous transition modeling. The wing tilt angle is treated as a continuous state, and aerodynamic and propulsive forces are parameterized as functions of airspeed, angle of attack, and wing tilt. Special attention is given to propulsion–airframe interaction effects and to the representation of path-dependent (hysteresis) behavior through propulsion-dependent aerodynamic parameterization. The proposed approach enables continuous simulation of transition dynamics without introducing discrete mode switching.

Keywords: eVTOL, Tiltwing Aircraft, Flight Dynamics Simulation, Project MiYa

1. Introduction

Tilt-wing electric vertical takeoff and landing (eVTOL) aircraft operate across three distinct flight regimes. In forward flight, the wing is aligned with the freestream and the vehicle behaves similarly to a conventional fixed-wing aircraft. In hover, the wing is rotated to a near-vertical orientation and lift is generated primarily by the propulsive system, resulting in helicopter- or multicopter-like behavior. The transition regime spans the continuous range of intermediate wing tilt angles and occurs during both acceleration from hover to forward flight and deceleration during approach and landing.
The transition phase represents the most challenging regime from a modeling and simulation perspective. Strongly nonlinear aerodynamics, rapidly changing propulsion effects, and pronounced coupling between wing orientation, vehicle attitude, and control effectiveness limit the applicability of classical steady-flight assumptions. Accurate representation of this regime is therefore essential for simulation-based analysis, control design, and evaluation of abnormal or degraded flight conditions.

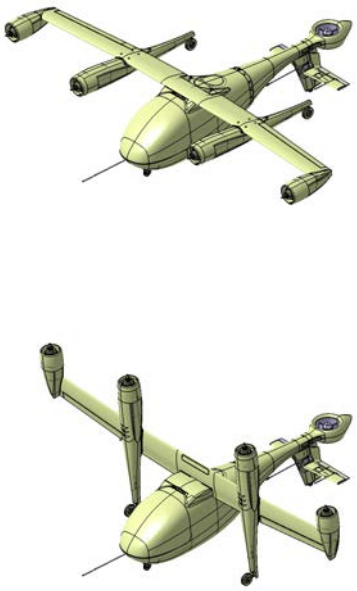

Fig. 1–2: MiYa eVTOL configuration.

[1] Bc. Ondrej Kukla: Czech Aerospace Research Centre (VZLU Aerospace), Beranových 130; 199 00, Prague; CZ, kukla@vzlu.cz

ISSN: 1805-8256, doi: 10.21495/em2026-69

This paper focuses on software-based simulation modeling of tilt-wing eVTOL aircraft, with emphasis on continuous representations of transition dynamics. The wing tilt angle is introduced as an explicit state variable, and aerodynamic and propulsive effects are parameterized as functions of flight condition and propulsion state. Particular attention is given to propulsion–airframe interaction and to the representation of path-dependent behavior through continuous, propulsion-dependent aerodynamic modeling. The approach is demonstrated on a tilt-wing configuration developed within the MiYa project (VZLU Aerospace, 2025).

2. Continuous Tilt-Wing Transition Modeling

Unlike steady forward or hover flight, the transition regime exhibits strongly nonlinear and configuration-dependent dynamics. Experimental and numerical studies show that aerodynamic forces and moments during transition are not solely functions of the instantaneous configuration. In particular, unsteady simulations indicate that the aerodynamic response differs depending on whether the wing is tilting toward forward flight or toward hover, revealing direction- and path-dependent behavior in the transition dynamics (Huang, 2024).

To capture this behavior within a continuous framework, the wing tilt angle must be treated as an explicit modeling variable rather than a discrete mode identifier. Aerodynamic and propulsive forces are parameterized as functions of airspeed, angle of attack, and wing tilt angle based on wind-tunnel measurements or CFD data, enabling smooth variation of forces and moments while preserving the strong coupling between vehicle attitude, wing orientation, and propulsion.

The hysteresis effect between hover and forward flight does not originate in the static aerodynamic characteristics. Instead, the aerodynamic coefficients are additionally parameterized by the thrust coefficient T_{Cs}, which depends on the propulsion system state. As the wing is influenced by both the freestream and the propeller slipstream, an effective dynamic pressure q_s is introduced as

$$q_s = q + \frac{\overline{T}}{A_p}, \tag{1}$$

from which the thrust coefficient is defined as

$$T_{Cs} = \frac{\overline{T}}{q_s A_p}. \tag{2}$$

In both expressions, the total thrust $\overline{T}$ and propeller area A_p play a central role. The hysteresis arises from differences in propeller operating conditions during acceleration and deceleration. During transition from hover to forward flight, higher RPM (and thus thrust) is required to accelerate the aircraft, whereas during deceleration lower thrust is sufficient to maintain trimmed flight. This asymmetry directly affects the thrust coefficient T_{Cs} and introduces path-dependent aerodynamic behavior.

To illustrate this effect, three wing transition trajectories with constant translational accelerations were defined, bringing the aircraft from hover (horizontal speed 0.1 m/s) to forward flight (wing tilt 30° and speed 25.5 m/s), and back.

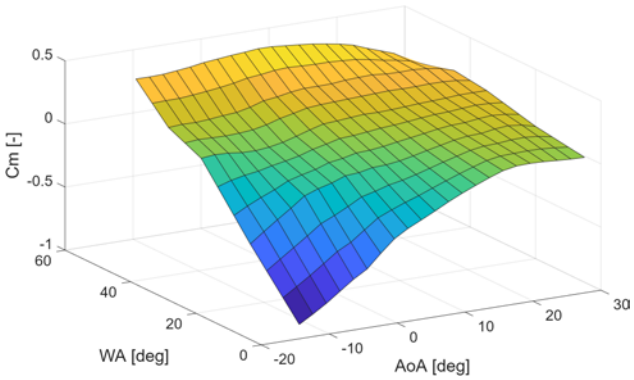

Fig. 3: Static pitch moment coefficient of the MiYa tilt-wing eVTOL aircraft obtained from wind tunnel measurements, shown for zero sideslip and a thrust coefficient of $T_{Cs} = 0.25$.

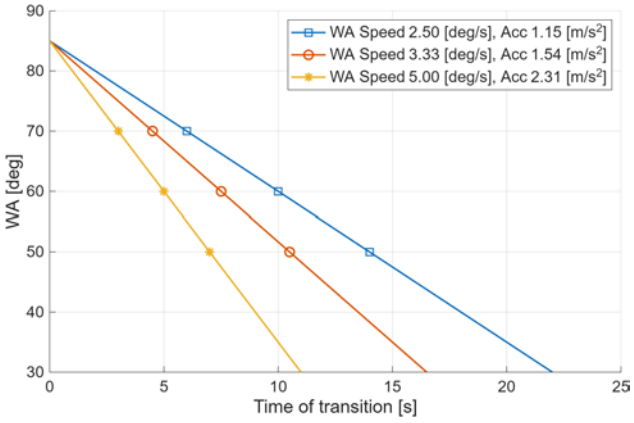

Fig. 4: Wing tilt transition trajectories for the three acceleration profiles considered.

Trimmed states of the aircraft were computed at the initial and final conditions (zero acceleration), as well as at wing tilt angles of 70°, 60°, and 50° for each acceleration level. The resulting differences in required propeller RPM between acceleration and deceleration are shown in Fig. 5. This demonstrates that hysteresis can be represented within a continuous model through propulsion-dependent aerodynamic parameterization, without introducing discrete mode switching.

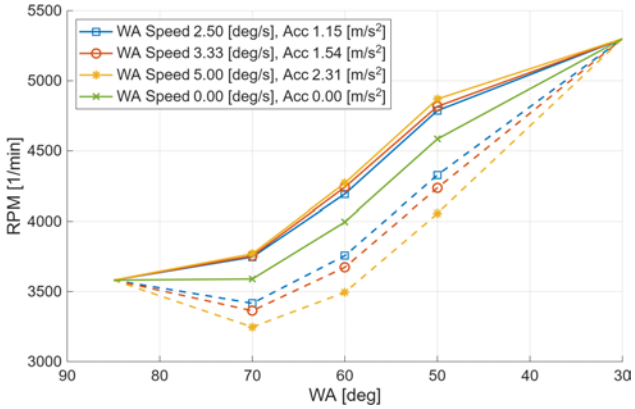

Fig. 5: Propeller RPM during acceleration (solid line) and deceleration (dashed line), illustrating hysteresis. The steady-flight (trimmed, no transition) RPM values are shown in green for comparison.

2.1. Propeller Force and Moment Contributions

The force and moment contributions of wing-mounted propellers must be carefully considered within the overall aircraft dynamics, particularly when differential thrust is included for control design or failure-case and degraded flight condition simulations. The total moment acting on the aircraft in the body coordinate system can be expressed as

$$[m]^B = [m_a]^B + [S_{CLB}]^B [F_a]^B + [m_{prop}]^B + [m_{ctrl}]^B, \tag{3}$$

where $[m_a]^B$ and $[F_a]^B$ denote aerodynamic moments and forces, $[S_{CLB}]^B$ represents the skew-matrix form of the moment arm from the center of lift to the center of gravity, $[m_{prop}]^B$ captures propulsion-induced moments, and $[m_{ctrl}]^B$ accounts for control effects from the aircraft's stabilizer and tail mounted ventilator.

During transition flight, the propulsion term becomes particularly significant. At higher levels of deployment, wing-mounted propellers contribute significantly to the pitching moment, first through their direct thrust force and second through their normal thrust component, which becomes non-zero at higher incidence angles. The propeller force coefficients c_T, c_N, and c_P are modeled as functions of the effective incidence angle,

$$AOI = AoA + WA + \delta Na. \tag{4}$$

The effective propeller incidence angle captures the combined influence of vehicle angle of attack, wing tilt, and nacelle orientation with respect to the wing on propeller force generation.

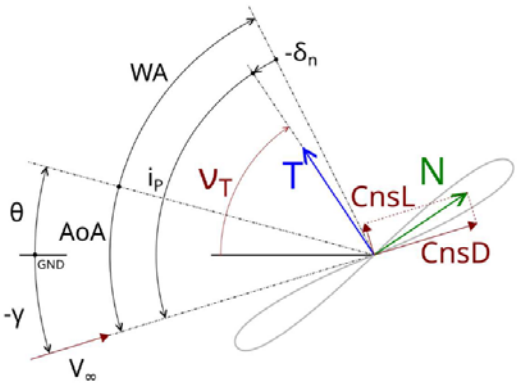

Fig. 6: Direct and Normal thrust components generated by the propeller under incidence angle.

The resulting propulsion forces $[F_T]^{Na}$ and $[F_N]^{Na}$ representing the direct and normal thrust components are transformed into the body coordinate system and contribute to both translational forces and rotational moments acting on the aircraft.

$$\begin{aligned} [m_{T_i}]^B &= [S_{Na_iB}]^B [T]^{BNa} [F_{T_i}] \\ [m_{N_i}]^B &= [S_{Na_iB}]^B [T]^{BNa} [F_{N_i}] \end{aligned} \tag{5}$$

where the matrices $[S_{Na_iB}]^B$ are the skew-matrix form of displacement vectors $[s_{Na_iB}]^B$ pointing from aircraft's center of gravity to the tip of the i-th nacelle (root of the propeller). The transformation matrix

$[T]^{BNa}$ is itself a function of the wing tilt angle WA modified for the nacelle orientation angle δNa. The displacement vector is constructed with the knowledge of the position of the wing tilt joint with respect to center of gravity and position of the i-th nacelle in respect to the joint as:

$$[s_{Na_iB}]^B = [T]^{BNa} \begin{bmatrix} r_i \\ 0 \\ 0 \end{bmatrix} + \begin{bmatrix} 0 \\ l_i \\ 0 \end{bmatrix} \tag{6}$$

where r_i is the distance of the point Na_i from point J along the $[x]^{Na}$ axis and l_i is the distance of the same point with respect to J along the $[y]^{Na}$ axis. The nacelle coordinate system $]^{Na}$ is in unity with the aircraft's body system $]^B$ for $WA + \delta Na = 0$. (Zipfel, 2014).

2.2. Propeller-Induced Flow Effects on Control Surfaces

Another significant effect of propeller–wing coupling is the change in aileron functionality across flight regimes. In forward flight, the ailerons are influenced by both the freestream and the propeller slipstream, and therefore behave similarly to those of a conventional fixed-wing aircraft, producing roll about the $[x]^B$ axis. However, their effectiveness is modified by the increased local flow velocity and disturbances induced by the propellers.

In hover, where the freestream velocity is negligible, the airflow over the ailerons is dominated by the propeller slipstream. Due to the near-vertical orientation of the wing, the control action no longer produces a conventional rolling moment, but instead induces rotation primarily about the $[z]^B$ axis.

These propeller-induced flow effects introduce strong state- and configuration-dependent variations in control effectiveness. In particular, the aerodynamic response of the control surfaces becomes a function of wing tilt angle, propulsion state, and local flow conditions. Within a continuous modeling framework, this behavior can be represented by parameterizing control surface effectiveness with respect to these variables, allowing smooth variation of control authority across the transition regime.

3. Conclusions

This paper has presented a continuous modeling approach for tilt-wing eVTOL flight dynamics, emphasizing wing tilt as an explicit state variable and the role of propulsion–airframe coupling. A key result is that path-dependent (hysteresis) behavior can be represented without introducing discrete mode switching or jump functions. Instead, hysteresis emerges naturally through propulsion-dependent aerodynamic parameterization, where thrust level and effective dynamic pressure govern the aerodynamic coefficients. This enables continuous representation of transition dynamics across both acceleration and deceleration phases within a unified formulation. The presented framework provides a consistent basis for simulation of tilt-wing eVTOL aircraft across the entire transition envelope.

Acknowledgments

The author would like to express his sincere gratitude to VZLU Aerospace and to his colleagues from the MiYa project for the opportunity to work alongside them and to further develop his modeling and simulation skill set. The author also acknowledges the use of the ChatGPT and DeepL language models for assistance with language editing; all suggestions were carefully reviewed and revised by the author.

References

Huang, Q. (2024) Numerical simulation on aerodynamic characteristics of transition section of tilt-wing aircraft. *Aerospace*, 11, 4, pp. 12–13.

VZLU Aerospace (2025) Miya – evtol uas platform. https://miya.cz/.

Zipfel, P. H. (2014) *Modeling and Simulation of Aerospace Vehicle Dynamics*. American Institute of Aeronautics and Astronautics, Reston, VA, 3 edition.

32nd International Conference
ENGINEERING MECHANICS 2026
Medlov, Czech Republic, May 11 – 13, 2026

MODAL ANALYSES OF THE BOVINE FEMUR USING CT, EXPERIMENTS AND FEM

Kulštejn D.[1], Frydrýšek K.[2], Čepica D.[3], Cienciala J.[4], Mizera O.[5], Šotola M.[6]

Abstract: *Modal analysis is very important in study of vibrations in biomechanics or mechanics. This article focuses on the creation of an anatomical model of a bovine cadaveric femur (i.e. CT scanning and image processing). The study itself focuses on experimental and numerical (FEM) approaches to modal analysis and a subsequent comparison of the results.*

Keywords: Modal analysis, Bovine femur, Anatomical model, Experiments, Finite Element Method

1. Introduction

Modal analysis is the popular fundamental technique in mechanics/biomechanics used to determine mainly the natural frequencies, mode (modal) shapes and damping ratios of structures and tissues. In biomechanics, it plays a critical role in understanding the vibrational behaviour of biological tissues. The bovine femur, as the typical strongest mammals' bone, is frequently studied due to its load-bearing function and susceptibility to fractures. However, in some cases, the bovine femur is widely adopted as a surrogate biomechanical model for human bone because of its comparable size, geometry, and mechanical characteristics. Understanding the modal behaviour of the bovine femur has important applications for human too. For example, in fracture prediction and prevention, implant and prosthesis design, impact biomechanics (e.g., automotive safety), bone health assessment etc. Modal analysis of such biological structures can be performed using experimental techniques, numerical simulations, or a combination of both. Each approach usually offers distinct advantages and limitations. For example, references Eiba et al. (2024), Frame et al. (2018), Gautam et al. (2021), Henyš et al. (2017), Nobakhti et al. (2017), Patel et al. (2021), Presas et al. (2021), Tarzjani et al. (2023), Yassine et al. (2018), Zanetti et al. (2009) and Zanganeh et al. (2025), Zhou et al. (2020) etc., present the state of the art.

2. Anatomical Model of a Bovine Femur

The femur was taken from an adult bull (approx. 400 kg, crossbreed of Dexter and Aberdeen Angus) with a height at the withers of 1.35 m. CT scan was performed (i.e. acquired DICOM files). Using the own

[1] Dan Kulštejn: Department of Applied Mechanics, Faculty of Mechanical Engineering, VSB – Technical University of Ostrava, 17. listopadu 2172/15, 708 00 Ostrava, CZ, dan.kulstejn@vsb.cz.

[2] Prof. M.Sc. Karel Frydrýšek, Ph.D., ING-PAED IGIP, FEng.: Department of Applied Mechanics, Faculty of Mechanical Engineering, VSB – Technical University of Ostrava, 17. listopadu 2172/15, 708 00 Ostrava, CZ, karel.frydrysek@vsb.cz.

[3] M.Sc. Daniel Čepica: Department of Applied Mechanics, Faculty of Mechanical Engineering, VSB – Technical University of Ostrava, 17. listopadu 2172/15, 708 00 Ostrava, CZ, daniel.cepica@vsb.cz.

[4] M.Sc. Jakub Cienciala: Department of Applied Mechanics, Faculty of Mechanical Engineering, VSB – Technical University of Ostrava, 17. listopadu 2172/15, 708 00 Ostrava, CZ, jakub.cienciala@vsb.cz.

[5] M.Sc. Ondřej Mizera, Ph.D.: Department of Machining, Assembly and Engineering Metrology, Faculty of Mechanical Engineering, VSB – Technical University of Ostrava, 17. listopadu 2172/15, 708 00 Ostrava, CZ, ondrej.mizera@vsb.cz.

[6] M.Sc. Martin Šotola, Ph.D.: Department of Applied Mechanics, Faculty of Mechanical Engineering, VSB – Technical University of Ostrava, 17. listopadu 2172/15, 708 00 Ostrava, CZ, martin.sotola@vsb.cz.

ISSN: 1805-8256, doi: 10.21495/em2026-73

software MADIFEM, see Čepica et al. (2025), the distribution of density /kg×m^{-3}/ and Young's modulus (modulus of elasticity) /MPa/ was determined in individual finite elements based on Hounsfield units, see Valášek et al. (2011). Hence, CAD/FEM models were created, see Fig. 1. The obtained CAD/FEM model accurately describes the inhomogeneity in the distribution of density and Young's modulus in each region of the bone, see Fig. 1(d, c).

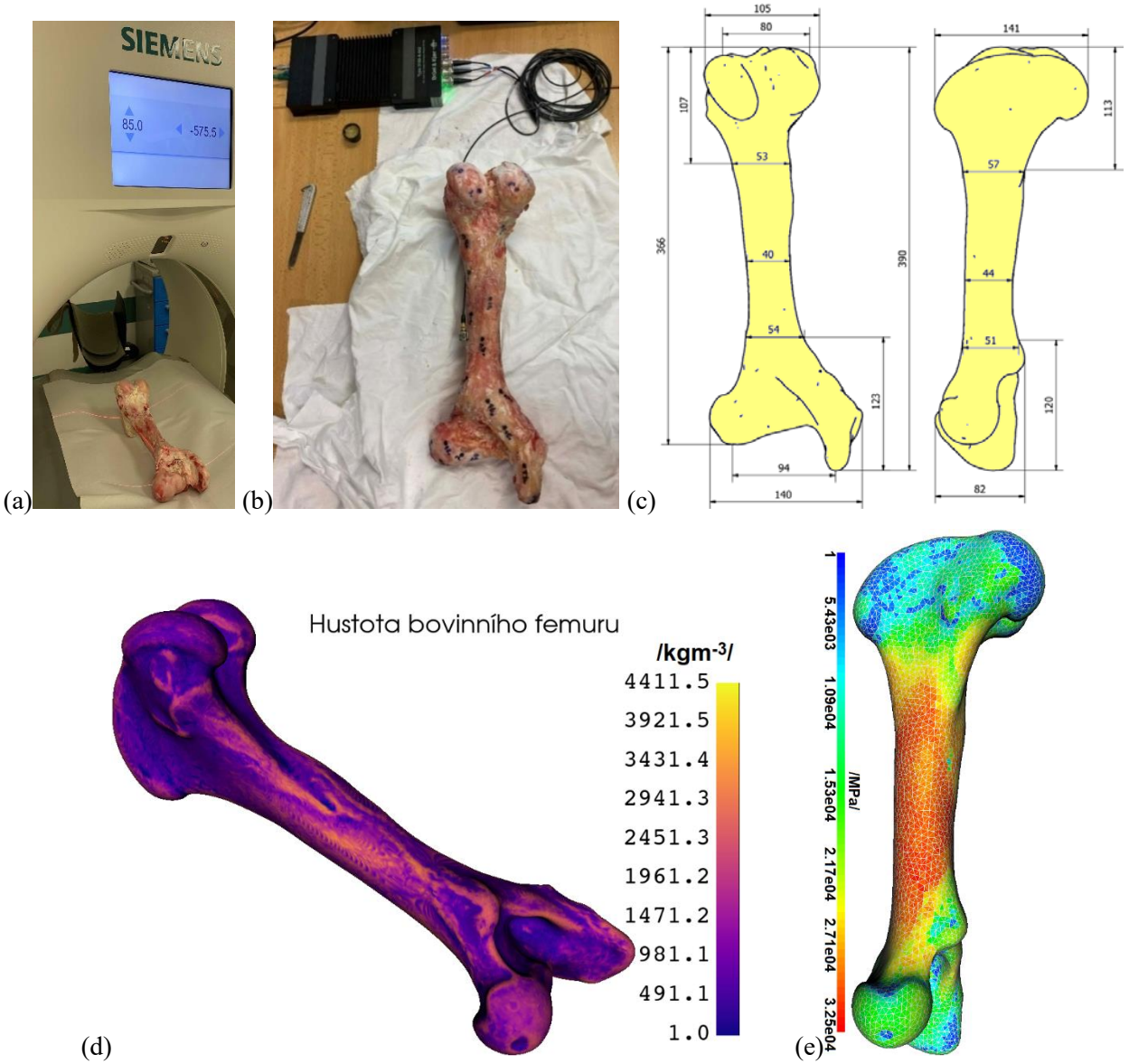

Fig. 1: Bovine femur – (a) CT - cadaver, (b) Measurement - cadaver, (c) CAD/FEM - dimensions, (d) FEM – material density distribution, (e) FEM – modulus of elasticity distribution.

3. Modal Analysis via Experiment

The bovine femur was placed on a soft foam pad. Thirty-five reference points were marked on a bovine femur to adequately cover the diaphysis, metaphyses, and epiphyses. The impact (percussive) hammer was used to hit these points and accelerometer was applied. Both the response and the excitation were recorded and evaluated by Brüel & Kjær tools, see Fig. 1(b), Tab. 1 and Fig. 2.

Tab. 1: Bovine femur – Results of experiment.

Mode	Damped frequency /Hz/	Damping /%/
1	582.57	2.00
2	641.58	5.54
3	662.75	2.03
4	731.30	2.21

5	1464.81	1.03

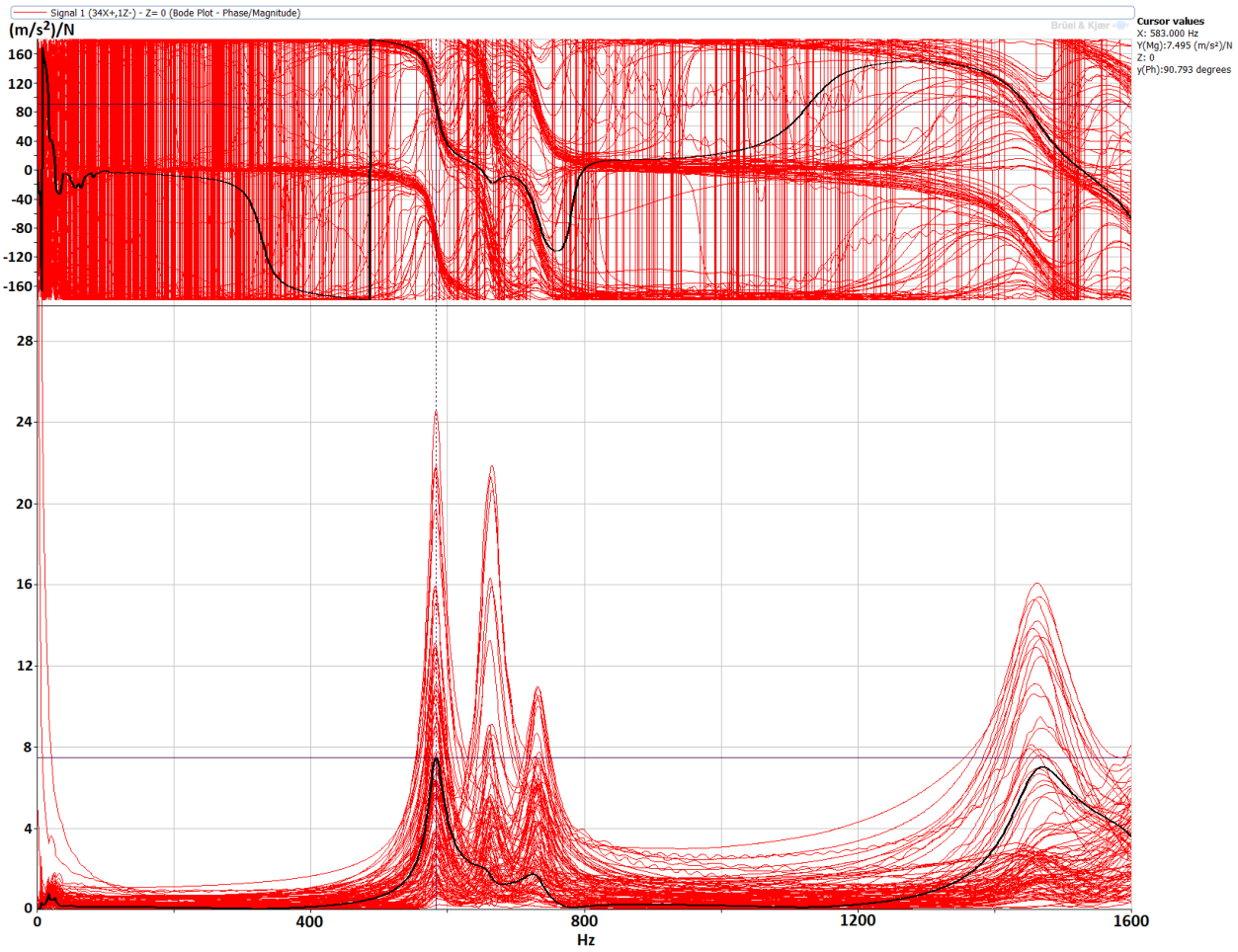

Fig. 2: Bovine femur - Bode diagram (amplitude and phase) of all measured transfer functions.

4. Modal Analysis via FEM

Modal analysis via FEM was performed by Simcenter 3D 2512 sw. The same boundary conditions were used in the FEM calculation and experiment. Some results, i.e. modal shapes and frequencies, are presented Fig. 3 and Tab. 2.

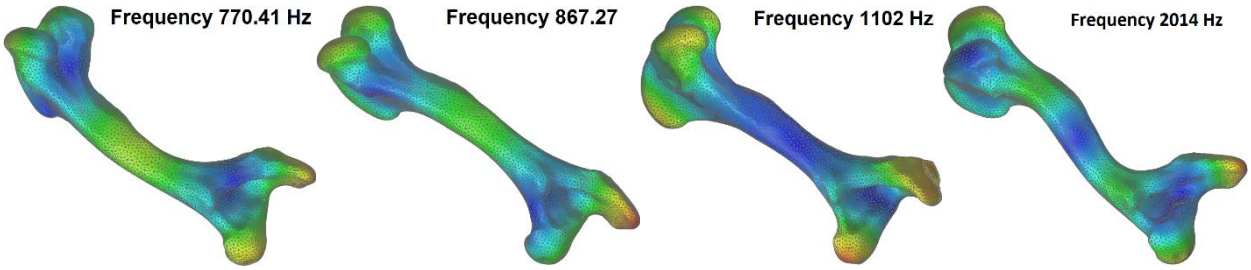

Fig. 3: Bovine femur (deformed structure) – Modal shapes for mode 1, 2, 3 and 4.

Tab. 2: Bovine femur – Results of FEM.

Mode	Frequency /Hz/
1	770.41
2	867.27
3	1102
4	2014
5	2179

5. Conclusions

A bovine femur from a cadaver was used to create the anatomical CAF/FEM model that relatively well respects the inhomogeneity in the distribution of density and elastic modulus. The modal analysis was performed using experiments and FEM. At first sight, the natural frequencies obtained by these two approaches do not match very well, see Tab. 1 and 2, which is also important information. The differences are primarily due to the complicated anisotropy and inhomogeneities of real bone, as well as the limitations of experiments and FEM. For these reasons, it is advisable to continue investigating this issue.

Acknowledgement

This work was supported by Specific Research "Computational and Experimental Modeling in Applied Mechanics and Biomechanics" (SP2025/048).

References

Čepica, D., Frydrýšek, K. (2025) *MADIFEM - A Software for Working with DICOM Images and Finite Element Meshes to Assign Realistic Mechanical Properties to Each Finite Element (Software pro práci s DICOM snímky a sítí konečných prvků pro přiřazení reálných mechanických vlastností jednotlivým konečným prvkům)*, software 019/22-09-2025_SW, Faculty of Mechanical Engineering, VSB – Technical University of Ostrava, Czech Republic

Eiba, P.; Frydrýšek, K.; Zanganeh, B.; Čepica, D.; Maršálek, P.; Handlos, P.; Timkovič, J., Štembírek, J., Cienciala, J., Onderka, A. et al. (2024) Simulation of Orbital Fractures Using Experimental and Mathematical Approaches: A Pilot Study. *J. Funct. Biomater.*, 15, 143. https://doi.org/10.3390/jfb15060143.

Frame, J. C., Wheel, M. A., Riches, P. E. (2018) A numerical investigation and experimental verification of size effects in loaded bovine cortical bone. *International Journal for Numerical Methods in Biomedical Engineering*, 34(1), e2903, https://doi.org/10.1002/cnm.2903.

Gautam, D., & Rao, V. K. (2021). Nondestructive evaluation of mechanical properties of femur bone. *Journal of Nondestructive Evaluation*, 40(1), 22, https://doi.org/10.1007/s10921-021-00754-0.

Henyš, P., Čapek, L. (2017) Material model of pelvic bone based on modal analysis: a study on the composite bone. *Biomechanics and modeling in mechanobiology*, 16(1), 363-373, https://doi.org/10.1007/s10237-016-0822-1.

Nobakhti, S., Katsamenis, O. L., Zaarour, N., Limbert, G., Thurner, P. J. (2017) Elastic modulus varies along the bovine femur. *Journal of the mechanical behavior of biomedical materials*, 71, 279-285, https://doi.org/10.1016/j.jmbbm.2017.03.021.

Patel, S., Jain, R. K., & Patil, M. (2021) Analyse the Elastic Properties of Bovine Femur Bone Using ANSYS. Trends in Biomaterials & Artificial Organs, 35(4).

Presas, A., Valentin, D., Deering, J., et al. (2021) Resonance vibration interventions in the femur: Experimental-numerical modelling approaches. *Journal of the mechanical behavior of biomedical materials*, 124, 104850, https://doi.org/10.1016/j.jmbbm.2021.104850.

Tarzjani, H. D., Nazari, M. A., Mahjoob, M. (2023) The effect of soft tissues on dynamical behavior of bovine tibia using modal analysis, https://doi.org/10.21203/rs.3.rs-3349678/v1.

Valášek, J., Krpalek, D., Florian, Z (2011) *Vztahy pro převod HU jednotek na Youngův modul* [online]. Brno: Vysoké učení technické v Brně, Fakulta strojního inženýrství, http://biomechanika.fme.vutbr.cz/index.php?option=com_phocadownload&view=category&download=106%3Avztahy-pro-prevod-hu-jednotek-na-younguv-modul.pdf&id=6%3Afrvs-valasek-krpalek&Itemid=96&lang=en.

Yassine, R., Fakhreddine, A., Sayegh, M., Mustapha, S., Hamade, R. F. (2018) Dynamic assessment and modeling of the modal frequencies and shapes of bovine tibia. *Journal of Nondestructive Evaluation, Diagnostics and Prognostics of Engineering Systems*, 1(4), 041006-041006, https://doi.org/10.1115/1.4040797.

Zanetti, E. M., Bignardi, C. (2009) Structural analysis of skeletal body elements: numerical and experimental methods. In *Biomechanical Systems Technology*: Volume 3: Muscular Skeletal Systems, pp. 185-225, https://doi.org/10.1142/6506-vol3.

Zanganeh, B., Maršálek, P., Handlos P., Timkovič J., Štembírek J., Cienciala J. (2025) Modal Analysis of Cranium via Experimental and Numerical Approaches, *31st International Conference ENGINEERING MECHANICS 2025*, Medlov, Czech Republic, May 12–14, pp. 217-220 https://doi.org/10.21495/em2025-217.

Zhou, Y., Kastner, M., J., Tigheet, T., B., Du, J. (2020) Elastic modulus mapping for bovine cortical bone from submillimeter- to submicron-scales using PeakForce Tapping atomic force microscopy. *Extreme Mechanics Letters*, vol. 41, art. no. 101031, https://doi.org/10.1016/j.eml.2020.101031 .

32nd International Conference
ENGINEERING MECHANICS 2026
Medlov, Czech Republic, May 11 – 13, 2026

CFD ANALYSIS OF BLOCKAGE EFFECT FOR RECTANGULAR CYLINDERS IN WIND TUNNEL FLOW

Ledvinková B.[*], Hračov S. [*], Macháček M. [*]

Abstract: *The blockage effect, arising from the confinement of flow by solid walls in wind tunnel testing, can significantly influence the aerodynamics of bluff bodies. In this study, its impact is numerically investigated using 2D RANS simulations of flow around rectangular cylinders with a side ratio of 2:1 at various angles of attack. The simulations were performed in computational domains with different distances between the upper and lower boundaries to represent varying levels of blockage. Key aerodynamic quantities, including mean drag, lift, and moment coefficients, were evaluated. Results obtained in domains with significant blockage were corrected using the Maskell method and compared with reference simulations in domains where blockage effects are negligible.*

Keywords: U-profile, Blockage effect, RANS simulation, Aerodynamic characteristics, Maskell correction

1. Introduction

Experimental data obtained in wind tunnels can be affected by the blockage effect, which occurs when the presence of a bluff body reduces cross-sectional area of the tunnel. This phenomenon often leads to the increase of the local airflow velocity resulting in discrepancies in aerodynamic quantities and to the distortion of the flow characteristics. When the blockage ratio - defined as the ratio of the body's frontal area to the tunnel cross-section- exceeds a threshold (typically 5 %) the application of appropriate correction is recommended (cf. Koloušek et. al 1983). A widely adopted approach is the Maskell correction (Maskell, 1965)

$$\frac{C_{Ff}}{C_F} = \frac{1}{1+\varepsilon C_D S/A} \tag{1}$$

where C_{Ff} represents the corrected force (drag C_D, lift C_L or moment C_M) coefficient, C_F is uncorrected force coefficient, C_D is uncorrected drag coefficient, S is frontal area of the body, A is the tunnel cross section area and ε is the blockage correction parameter related to a shape of the body. In this study, the correction parameter $\varepsilon = 0.83$ valid for rectangular cross section with side ratio equal to 2 was adopted.

To systematically investigate the blockage effect, RANS k–ω SST simulations were carried out for two rectangles ($B \times D = 300 \times 150$ mm and 150×75 mm, where B denotes the width and D the height of the body). The simulations were performed in a computational domain replicating the dimensions of the Vincenc Strouhal climatic wind tunnel at the Institute of Theoretical and Applied Mechanics of the Czech

[*] Ing. Blanka Ledvinková, PhD.: Institute of Theoretical and Applied Mechanics of the Czech Academy of Sciences, Prosecká 809/76; 190 00, Prague; CZ, ledvinkova@itam.cas.cz

[*] Ing. Stanislav Hračov, PhD.: Institute of Theoretical and Applied Mechanics of the Czech Academy of Sciences, Prosecká 809/76; 190 00, Prague; CZ, hracov@itam.cas.cz

[*] Ing. Michael Macháček, PhD.: Institute of Theoretical and Applied Mechanics of the Czech Academy of Sciences, Prosecká 809/76; 190 00, Prague; CZ, machacek@itam.cas.cz

ISSN: 1805-8256, doi: 10.21495/em2026-77

Academy of Sciences (cf. Hračov and Macháček, 2023), as well as in an enlarged domain representing conditions with a negligible blockage ratio.

2. Computational settings

The simulations involved a 2:1 rectangles positioned at various angles of inclination (0°–12°) within the computational domain (cf. Figure 1a). The wall spacing of the domain, *w*, was varied: for the larger rectangle, *w* was set to 1.9 m (corresponding to the actual tunnel width) and 7.5 m (unconfined reference case); for the smaller rectangle, *w* was 1.9 m and 3.75 m. The blockage ratios, *S/A*, related to each analyzed case are summarized in Table 1.

Tab. 1: Blockage ratio for rectangular cylinders at different inclination in computational domains. (Values exceeding recommended value 5% are marked in bold.)

Width of domain w	**Angle of attack [°]**					
	0	2.5	5	7.5	10	12
1.9 m large rectangle	**7.9%**	**8.6%**	**9.2%**	**9.9%**	**10.5%**	**11.0%**
7.5 m large rectangle	2.0%	2.2%	2.3%	2.5%	2.7%	2.8%
1.9 m small rectangle	3.9%	4.3%	4.6%	4.9%	**5.3%**	**5.5%**
3.75 m small rectangle	2.0%	2.2%	2.3%	2.5%	2.7%	2.8%

A hybrid mesh was employed to ensure high near-wall resolution while maintaining a reasonable computational cost. Two computational meshes with different structures were used to verify mesh independence. The resulting aerodynamic coefficients showed only slight differences. The mesh structure used for all subsequent computations is described below. The boundary layer around the rectangular cylinder consists of 16 layers of quadrilateral elements with an expansion ratio of 1.23 and a first-layer thickness of 1×10^{-5} m and 5×10^{-6} m for the larger and smaller rectangles, respectively, ensuring that the dimensionless wall resolution remains below one over most of the perimeter. This boundary layer is followed by 13 layers of a structured quadrilateral mesh extending to a distance of 10 mm and 5 mm from the walls of the larger and smaller rectangles, respectively. Within this quadrilateral region, the ratio of the thickness of the first to the last element is 6, while the longer and shorter sides of the rectangle are discretized using 100 and 50 elements, respectively. The arrangement of the boundary layer and the quadrilateral mesh is illustrated in Figure 1d.

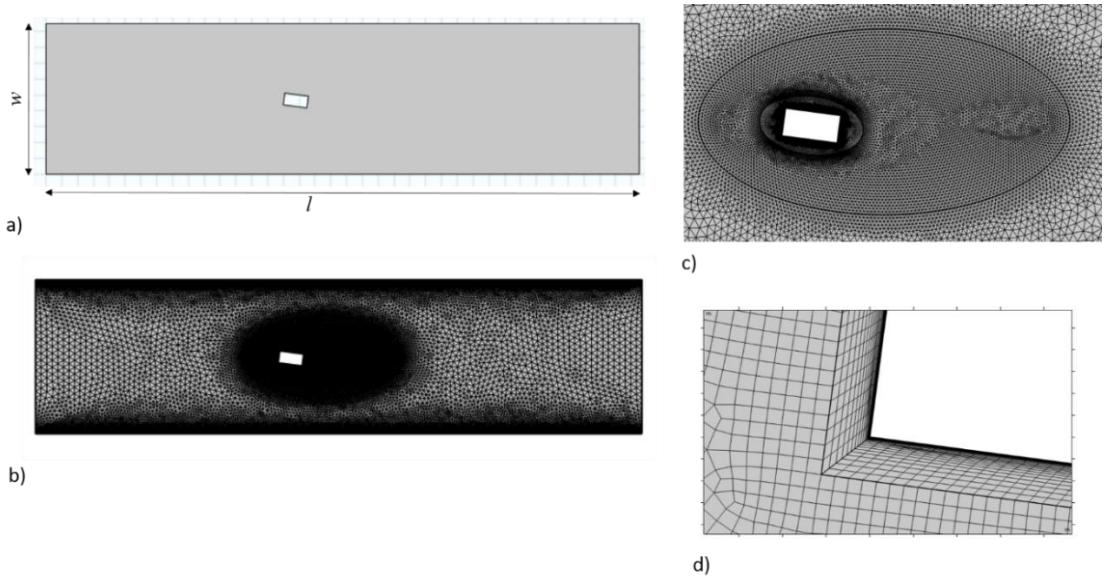

Fig. 1: a) Rectangle 2:1 in the computational domain, b) computational mesh, c) detail of the meshed wake, d) boundary layer on the walls of rectangle.

Two auxiliary ellipses were employed in the mesh generation process, with semi-axis lengths of 0.28 m and 0.205 m for the smaller ellipse, and 1 m and 0.5 m for the larger ellipse. Within the smaller ellipse, an unstructured quadrilateral mesh with a maximum element size of 0.01 m was used, transitioning into a triangular mesh with a maximum element size of 0.02 m in the larger ellipse, thereby ensuring adequate resolution of the wake behind the rectangle (cf. Figure 1c). The length of the finely resolved wake corresponds to four times the characteristic length of the rectangle, B. A boundary layer consisting of six layers with an expansion ratio of 1.23 and a total thickness of 0.02 m was applied near the top and bottom walls of the computational domain, while the remaining regions were discretized using a coarser triangular mesh, as shown in Figure 1b. Regarding the boundary conditions, a no-slip condition was applied to all solid surfaces, including both the model and the confining wind tunnel walls. A zero-pressure condition was prescribed at the outlet, while a uniform inlet velocity of $v = 14$ m/s (corresponding to Re=1.4x10^5) and a turbulence intensity of 1% were imposed, corresponding to the parameters used in the reference experiments (Hračov and Macháček, 2023).

3. Results

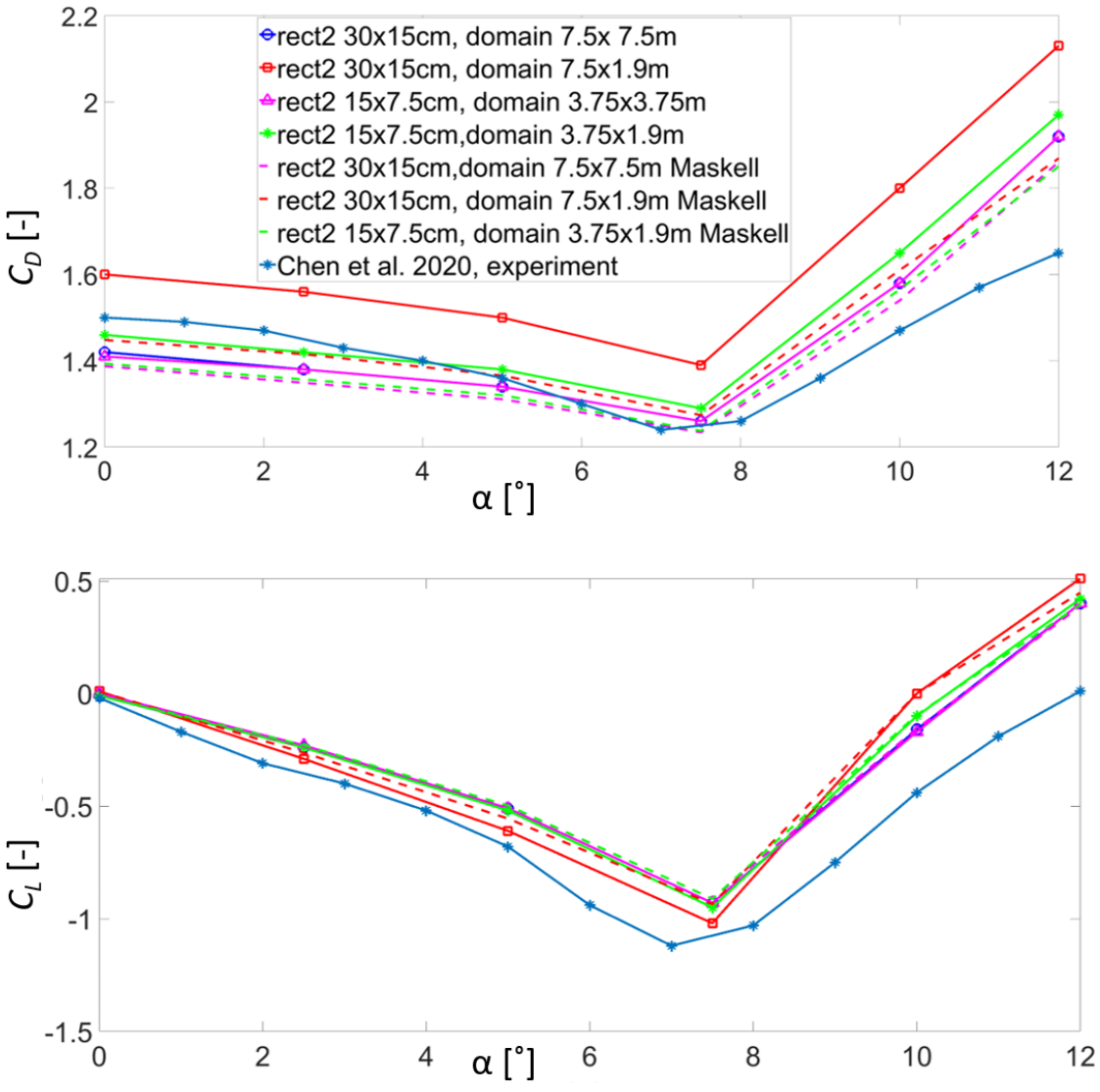

Fig 2: Drag and lift coefficients vs. angle of wind attack under different blockage conditions, before and after Maskell correction.

The aerodynamic characteristics, including the mean drag, lift, and moment coefficients (C_D, C_L and C_M) were evaluated for both rectangle scales and various computational domain widths. As illustrated in Figure 2, the mean aerodynamic coefficients for the larger and smaller rectangles show no significant

deviation in domains where the blockage effect is below 3%. This consistency confirms the scalability of the numerical approach under unconfined flow conditions. To compare calculated values with experiment, experimental drag and lift coefficient data, obtained by Chen et al. (2020) for a rectangle 12x6 cm within a 1.2 m wide tunnel at Re=$6x10^4$, are also plotted in Figure 2.

The application of the Maskell correction method (dashed curves in Figure 2) to cases with non-negligible blockage ratios resulted in values approaching those obtained for domains with negligible blockage, cf. Table 2.

Tab. 2: Relative error of the drag coefficient for selected angles of attack. Reference values consist of aerodynamic coefficients for small rectangle in unconfined domain (uncorrected for columns 1–2; adjusted by Maskell's correction for columns 3–4).

	Large rect. non corrected	Small rect. non corrected	Large rect. Maskell	Small rect. Maskell
0˚	13.4%	9.6%	5.1%	1.1%
5˚	11.9%	8.9%	4.1%	0.7%
10˚	13.9%	8.8%%	3.2%	1.6%

4. Conclusions

This study presents a numerical investigation of the wind tunnel blockage effect on the aerodynamic characteristics of sharp-edged rectangular cylinders with a 2:1 aspect ratio. By comparing results across different domain widths, it was demonstrated that inaccuracies due to blockage effects become significant when the blockage ratio exceeds approximately 5%, in accordance with established aerodynamic theories.

Following the application of the Maskell correction, the corrected drag and lift coefficients showed improved agreement with results obtained from unconfined domains, confirming the method's reliability for adjusting global aerodynamic forces.

Acknowledgements

The kind support of Czech Scientific Foundation project No. 24-13061S is gratefully acknowledged.

Computational resources were provided by the e-INFRA CZ project (ID:90254), supported by the Ministry of Education, Youth and Sports of the Czech Republic.

References

Chen, C., Mannini, C., Bartoli, G., Thiele, K. (2020) Experimental study and mathematical modeling on the unsteady galloping of a bridge deck with open cross section. J. Wind Eng. Ind. Aer. 203, article 104170.

Hračov, S., Macháček, M. (2023). Experimental investigation of galloping susceptibility of u-beams with different flange porosity. In: Wu, Z., Nagayama, T., Dang, J., Astroza, R. (eds) Experimental Vibration Analysis for Civil Engineering Structures. Lecture Notes in Civil Engineering, vol 224, pp.183-193.

Koloušek, V., Pirner, M., Fischer, O. and Náprstek, J. (1983) Wind Effects on Civil Engineering Structures. *Academia,* Prague.

Ledvinková, B., Hračov, S., Macháček, M. (2024) The influence of the blockage effect on the aerodynamic characteristics of the bluff body in the air flow. In: Adámek, V., Jonášová, A., Plánička, S., eds. *Computational mechanics 2024. Proceedings of computational mechanics 2024*. Plzeň: University of West Bohemia, 2024, pp. 68-71. ISBN 978-80-261-1249-5

Maskell, E.C., 1965. A theory of the blockage effect on bluff bodies and stalled wings in a closed wind tunnel. ARC R&M 3400, Aeronautical Research Council, UK, Nov. 1965

32nd International Conference
ENGINEERING MECHANICS 2026
Medlov, Czech Republic, May 11 – 13, 2026

POST-CRITICAL FLUTTER MODE AT THE ONSET OF INSTABILITY IN A FOOTBRIDGE DECK SECTION MODEL WITH AERODYNAMIC MODIFICATIONS

Macháček M.[1], Hračov S.[2], Dejmal K.[3]

Abstract: *This study investigates the post-critical flutter mode of a footbridge deck section model at the onset of instability. Wind tunnel tests were performed on a two-degree-of-freedom model, and the response was evaluated from limit cycle oscillations immediately following flutter onset. The analysis focused on the amplitude ratio and phase relationship between heave and pitch, as well as the flutter frequency and critical wind speed. The results show that aerodynamic modifications significantly affect not only the critical flutter velocity, but also the character of the flutter mode. The modified leading edge promotes torsion-dominated oscillations, while longitudinal ribbons result in a predominantly heave-dominated response.*

Keywords: Flutter, Post-critical response, Aeroelastic instability, Footbridge deck, Wind tunnel testing

1. Introduction

The aeroelastic stability of slender pedestrian bridges is an important issue in modern bridge engineering. Due to their low mass and limited structural damping, such structures are highly susceptible to wind-induced instabilities, particularly flutter, which may lead to rapidly growing oscillations and potential structural failure. The aerodynamic behavior of bridge decks is strongly influenced by their cross-sectional geometry. Previous studies have shown that relatively small geometric modifications, such as deck edge shaping or the addition of aerodynamic devices, can significantly affect flow separation and improve aeroelastic stability, as demonstrated by Macháček et al. (2025). The self-excited aerodynamic forces are commonly described using the flutter derivative formulation introduced by Scanlan and Tomko (1971). These derivatives are typically identified from wind tunnel experiments using free-decay or forced vibration methods, as shown, for example, by Bartoli et al. (2009), Buljac et al. (2017), and Král et al. (2016). In previous work by the authors, the aeroelastic stability of a footbridge deck was investigated experimentally, focusing on the identification of flutter derivatives and the determination of critical wind velocities for several modified configurations. The results demonstrated that aerodynamic modifications can significantly delay the onset of flutter. However, less attention is usually devoted to the structural response at and immediately beyond the onset of instability. In this regime, the character of the oscillatory motion, including the relative contribution of vertical and torsional components and their phase relationship, may vary depending on the aerodynamic configuration of the deck. The present study therefore focuses on the post-critical flutter behavior at the onset of instability. Using experimental data obtained from a sectional model with two degrees of freedom, the modal characteristics of the response are evaluated in terms of amplitude ratio and phase shift between heave and pitch motion, with particular emphasis on the effect of aerodynamic modifications.

[1] Ing. Michael Macháček, Ph.D.: Department of dynamics and aerodynamics, Institute of theoretical and applied mechanics of the Czech Academy of Sciences, Prosecká 76; 190 00, Prague; CZ, machacek@itam.cas.cz

[2] Ing. Stanislav Hračov, Ph.D.: Department of dynamics and aerodynamics, Institute of theoretical and applied mechanics of the Czech Academy of Sciences, Prosecká 76; 190 00, Prague; CZ, hracov@itam.cas.cz

[3] RNDr. Karel Dejmal, Ph.D.: Department of dynamics and aerodynamics, Institute of theoretical and applied mechanics of the Czech Academy of Sciences, Prosecká 76; 190 00, Prague; CZ, dejmal@itam.cas.cz

ISSN: 1805-8256, doi: 10.21495/em2026-81

2. Experimental setup

The investigated configurations of the footbridge deck are illustrated in Fig. 1. Three cross-section variants were considered, including the original deck geometry and two modified configurations incorporating aerodynamic measures. These modifications were designed to alter flow separation and improve the aeroelastic performance of the structure. The right part of the figure shows the sectional aeroelastic model installed in the aerodynamic wind tunnel in Telč. The model was mounted to allow coupled vertical and torsional motion, enabling the investigation of flutter behavior under controlled aerodynamic conditions. The experimental setup corresponds to that used in the authors' previous study, ensuring consistency in the comparison of aerodynamic characteristics across the investigated configurations. The sectional model was characterized by a heave natural frequency of 2.26 Hz with a damping ratio of 1.18%, and a pitch natural frequency of 3.49 Hz with a damping ratio of 0.94%. The mass per unit length was 4.933 kg/m, the mass moment of inertia was 0.0376 kg·m²/m, and the deck width and model length were 0.30 m and 1.00 m, respectively. The aeroelastic response of the sectional model was investigated using the free-decay method. The model was initially displaced and released, and the resulting oscillations were recorded over a range of wind velocities. Based on these measurements, the flutter derivatives were identified following the same procedure as in the authors' previous study. As the wind velocity approached the critical condition, the onset of flutter was observed. Immediately beyond this point, the model exhibited sustained oscillations in the form of limit cycle motion. These post-critical responses were subsequently recorded and evaluated.

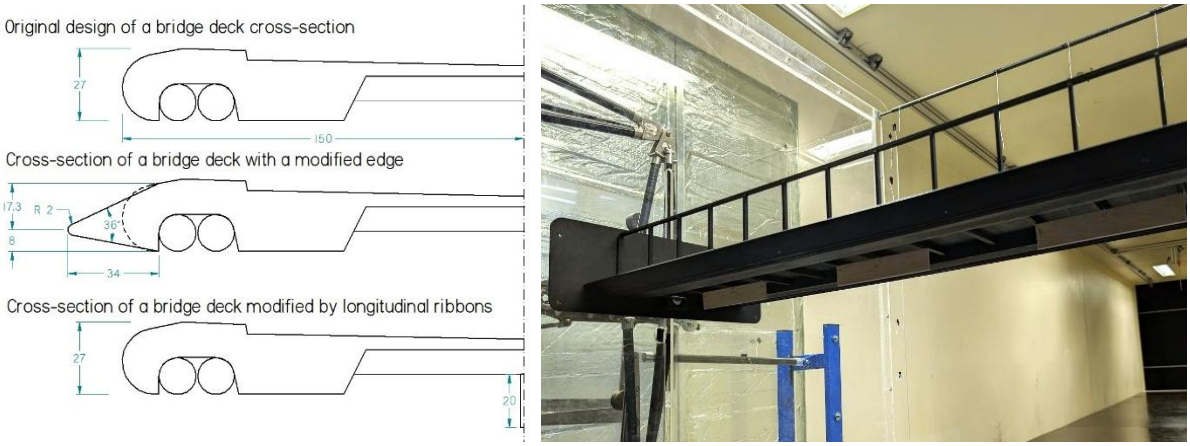

Fig. 1: Three cross-section variants of the footbridge (left); view of the experimental section model of the footbridge with longitudinal ribbons (right).

3. Results

The analysis focused on the modal characteristics of the motion, including the phase shift between vertical displacement and torsional rotation, the amplitude ratio, and the oscillation frequency at the onset of flutter. In addition, the critical wind velocity was determined in model scale. The post-critical aeroelastic response of the sectional model was evaluated at the onset of instability for all three investigated configurations. The results are summarized in Table 1. The ratio P/H denotes the ratio of torsional (pitch) to vertical (heave) oscillation amplitudes at flutter onset, while the phase shift P vs H represents the phase difference between torsional and vertical motion. The flutter wind speed corresponds to the critical wind velocity in model scale, and the flutter frequency is defined as the coupled frequency of the heave and pitch modes at flutter onset. The pitch and heave frequency changes represent the relative changes in torsional and vertical natural frequencies with respect to the zero-wind condition. A significant influence of aerodynamic modifications on the modal character of the flutter response was observed. For the original deck configuration, the amplitude ratio was 0.629, indicating a response dominated by vertical motion with a moderate torsional contribution. The modified leading edge resulted in a substantial increase in the amplitude ratio to 1.299, indicating a clear shift towards torsion-dominated oscillations. In contrast, the configuration with longitudinal ribbons exhibited a reduced amplitude ratio of 0.326, corresponding to a predominantly heave-dominated mode with a significantly diminished torsional contribution. These results demonstrate that aerodynamic modifications affect not only the critical flutter velocity, but also fundamentally alter the character of the post-critical flutter mode. In particular, the leading edge modification promotes torsional dominance, while the application of aerodynamic ribbons shifts the response towards a heave-dominated regime. The phase shift between vertical and torsional motion remains close to 180° for all configurations,

with values of 167°, 171°, and 165° for the original, modified edge, and ribbon configurations, respectively. This confirms that the observed instability corresponds to a classical coupled flutter mode with nearly anti-phase motion between heave and pitch. The critical wind velocity increases significantly with aerodynamic modifications, from 6.3 m/s for the original configuration to 7.17 m/s and 9.13 m/s for the modified edge and ribbon configurations, respectively, confirming the stabilizing effect of the applied measures.

Tab. 1: Post-critical limit cycle oscillation characteristics

	Original design	Modified edge	Longitudinal ribbons
P/H (°/mm)	0.629	1.299	0.326
Phase shift P vs H (°)	167	171	165
Flutter wind speed (m/s)	6.3	7.17	9.13
Flutter frequency (Hz)	2.95	3.11	2.71
Pitch frequency change (%)	-15.5	-10.9	-22.3
Heave frequency change (%)	30.5	37.6	19.9

The flutter frequency, defined as the common frequency at which the heave and pitch modes coalesce, varies between the investigated configurations. The highest value of 3.11 Hz is observed for the modified edge, while the ribbon configuration exhibits the lowest value of 2.71 Hz. The changes in modal frequencies further support the observed differences in flutter behavior. The torsional frequency decreases in all cases, with reductions of −15.5%, −10.9%, and −22.3% for the original, modified edge, and ribbon configurations, respectively. At the same time, the heave frequency increases by 30.5%, 37.6%, and 19.9%, indicating a convergence of the two modes at the onset of flutter. The most pronounced torsional softening occurs for the ribbon configuration, which is consistent with its reduced torsional contribution to the resulting oscillation mode.

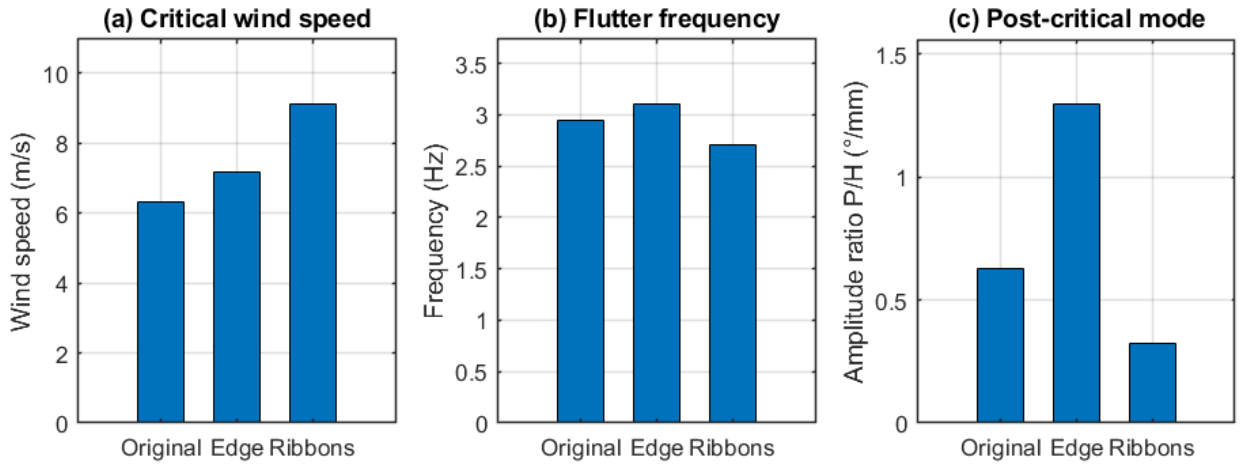

Fig. 2: (a) Critical wind speed, (b) flutter frequency, and (c) post-critical flutter mode characterized by the amplitude ratio of torsional to vertical motion.

The results are further illustrated in Fig. 2. Fig. 2(a) shows the critical wind speed, highlighting the increase in flutter onset velocity for the modified configurations. Fig. 2(b) presents the corresponding flutter frequency, while Fig. 2(c) illustrates the post-critical flutter mode expressed by the amplitude ratio between torsional and vertical motion. A clear shift in modal character is observed, with the modified leading edge promoting torsion-dominated behavior, whereas the ribbon configuration leads to a predominantly heave-dominated response.

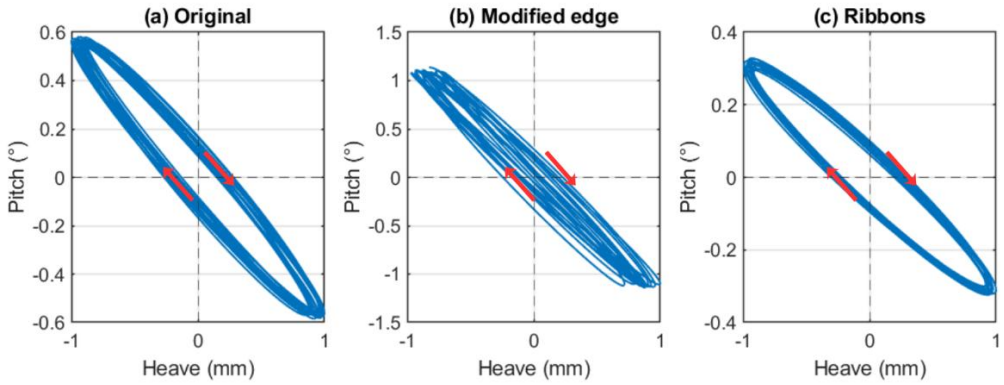

Fig. 3: Normalized phase-plane plots of post-critical oscillations at flutter onset

The post-critical response is further illustrated in Fig. 3 using phase-plane plots of heave and pitch motion. The trajectories form closed curves corresponding to limit cycle oscillations established immediately after flutter onset. The plots are normalized with respect to the heave amplitude, allowing direct comparison of the modal character between the investigated configurations while preserving the relative contribution of torsional motion. A clear change in the shape of the trajectories is observed. The modified leading edge exhibits an elongated trajectory in the pitch direction, indicating a torsion-dominated response. In contrast, the configuration with longitudinal ribbons shows a flatter trajectory, corresponding to a predominantly heave-dominated mode, while the original configuration exhibits an intermediate behavior with a mixed contribution of both components. The direction of motion, indicated by arrows, confirms a nearly anti-phase relationship between heave and pitch, consistent with the classical coupled flutter mechanism.

4. Conclusions

The presented study investigated the post-critical flutter behavior of a footbridge deck section model at the onset of instability, with particular emphasis on the influence of aerodynamic modifications. The results confirm that such modifications significantly increase the critical wind velocity, with the highest improvement observed for the configuration equipped with aerodynamic ribbons. In addition to this stabilizing effect, substantial changes in the character of the flutter mode were identified. The amplitude ratio analysis revealed a shift from a mixed or heave-dominated response in the original configuration to a torsion-dominated mode for the modified leading edge, while the ribbon configuration promoted a predominantly heave-dominated response. The phase relationship between heave and pitch remained close to anti-phase for all cases, confirming a classical coupled flutter mechanism. The findings demonstrate that aerodynamic modifications affect not only the stability limit, but also the modal structure of the flutter response. This highlights the importance of considering the character of oscillations at the onset of instability, in addition to the critical wind velocity, when evaluating the aeroelastic performance of footbridge decks.

Acknowledgement

The kind support of Czech Scientific Foundation project No. 24-13061S is gratefully acknowledged.

References

Bartoli, G., Mannini, C., Ricciardelli, F. and Tubino, F. (2009) Flutter and limit-cycle oscillations of a bridge deck section model: Experimental and numerical investigation. Journal of Bridge Engineering, 14(6), pp. 401–412.

Buljac, A., Kozmar, H. and Procino, L. (2017) Experimental investigation of flutter derivatives of bridge decks. Journal of Wind Engineering and Industrial Aerodynamics, 164, pp. 89–102.

Král, R., Pospíšil, S. and Kuznetsov, S. (2016) Identification of flutter derivatives using free vibration technique. Journal of Wind Engineering and Industrial Aerodynamics, 153, pp. 32–44.

Macháček, M., Hračov, S. and Dejmal, K. (2025) Analysis of aeroelastic stability improvement in pedestrian suspension bridges through deck edge variation and longitudinal ribbon implementation. Proc. 40th conf. Computational Mechanics 2025, Srni, Czech Republic, pp. 104–107.

Scanlan, R. H. and Tomko, J. J. (1971) Airfoil and bridge deck flutter derivatives. Journal of Engineering Mechanics Division, 97(6), pp. 1717–1737.

32nd International Conference
ENGINEERING MECHANICS 2026
Medlov, Czech Republic, May 11 – 13, 2026

MICROMECHANICAL PROPERTIES OF STEEL CORROSION PRODUCTS

Němeček J.[1], **Prošek Z.**[2], **Lukeš J.**[3], **Němeček J.**[4]

Abstract:
The micromechanical properties of the steel corrosion layer formed in cement paste under accelerated conditions were investigated using micro-pillar compression. Micro-pillars were fabricated by Xe plasma focused ion beam and tested in situ using a picoindenter. The results show clear mechanical degradation of the corrosion products compared to the original steel rod, manifested by reduced yield strength, peak stress, elastic modulus, and strain at peak stress. Additionally, the corrosion products exhibit less ductility and sudden failure during compression after reaching the maximum load.

Keywords: Steel corrosion, Micro-pillar, Focused ion beam, Accelerated test

1. Introduction

Corrosion of steel reinforcement is a problem in many building structures exposed to environmental influences such as moisture and ion transport. In a freshly cast concrete structure, the steel is protected from corrosion by a thin oxide layer, which causes the steel to be in a passive state and corrosion occurs at a significantly lower rate. The passive layer is maintained by the high pH of the concrete (pH>12). If the pH is reduced, for example by carbonation of the concrete (pH<10) or by the presence of chlorides from de-icing agents, then the passive layer is disrupted and corrosion occurs, often in localized places, later even over the entire surface of the reinforcement. Active corrosion, in the presence of moisture and oxygen, causes the formation of a series of hydroxides and oxides around the reinforcement, resulting in cracks in the concrete and ultimately the covering layer falling off. The main corrosion products found with X-ray diffraction (XRD) measurements were iron oxides (FeO, $\alpha - Fe_2O_3$, Fe_3O_4) and iron hydroxy-oxides ($\alpha, \beta, \gamma, \delta - FeOOH$). The rust layer exhibits also increased porosity compared to original metal (Zhao et al., 2011).

Due to a number of influencing factors, the mechanical properties of corrosion products show a significant dispersion of values in the literature (Zhao and Jin, 2016). In addition, their measurement requires special procedures in layers of only a few micrometers, which leads to the use of microscopic methods (Němeček et al., 2016; Shahrin and Bobko, 2019). These data provide essential inputs for numerical models that simulate the corrosion process (Korec et al., 2023, 2024). For examination of corrosion products, accelerated tests can be used, where the formation of corrosion products is controlled by an impressed corrosion current (Zhang et al., 2019; Andrade, 2023). This work, therefore, focuses on the characterization of corrosion products in a thin corrosion layer prepared in an accelerated test under galvanostatic conditions using scanning electron microscopy (SEM) and nanoindentation.

[1] Ing. Jiří Němeček, Ph.D., Orcid 0000-0002-5635-695X: Department of Mechanics, Faculty of Civil Engineering, Czech Technical University, Thákurova 2077/7; 166 29, Prague 6; CZ, jiri.nemecek.1@fsv.cvut.cz
[2] Doc. Ing. Zdeněk Prošek, Ph.D.: Department of Mechanics, Faculty of Civil Engineering, Czech Technical University, Thákurova 2077/7; 166 29, Prague 6; CZ, zdenek.prosek@fsv.cvut.cz
[3] Ing. Jaroslav Lukeš, Ph.D.: Division of biomechanics, Faculty of Mechanical Engineering, Czech Technical University, Technická 1902/4; 166 29, Prague 6; CZ, jaroslav.lukes@fs.cvut.cz
[4] Prof. Ing. Jiří Němeček, Ph.D., DSc., Orcid 0000-0002-3565-8182: Department of Mechanics, Faculty of Civil Engineering, Czech Technical University, Thákurova 2077/7; 166 29, Prague 6; CZ, jiri.nemecek@fsv.cvut.cz

ISSN: 1805-8256, doi: 10.21495/em2026-85

2. Experiments and methods

To conduct accelerated steel corrosion tests, cylindrical samples with a diameter of 27 mm and a height of 70 mm were fabricated and filled with cement paste.The mixture was prepared from Portland cement CEM I 42.5R with a water/cement ratio of 0.4 and the addition of 1% NaCl relative to the weight of cement. A 3 mm structural steel rod (cold-formed low carbon steel H9 S235JRC+C) was placed in the middle of the cylinder, 10 mm from the bottom, while the upper part of the rod was protected with an electrical insulation. After the fabrication the samples were stored in lime-saturated water for 14 days.

After curing, the samples were placed in an electrolytic cell with DC power source, where the positive pole of the source was connected to the reinforcement and the negative pole was connected to a stainless steel mesh electrode placed around the circumference of the sample at a distance of approximately 5 mm. The cell space was filled with electrolyte in the form of 0.3 M NaOH. The source maintained a constant current flowing through the reinforcement with a prescribed nominal current density of $500\,\mu A/cm^2$ for a duration of 3 days. This procedure led to a massive increase in corrosion products on the surface of the reinforcement and the formation of cracks in the direction from the reinforcement to the surface.

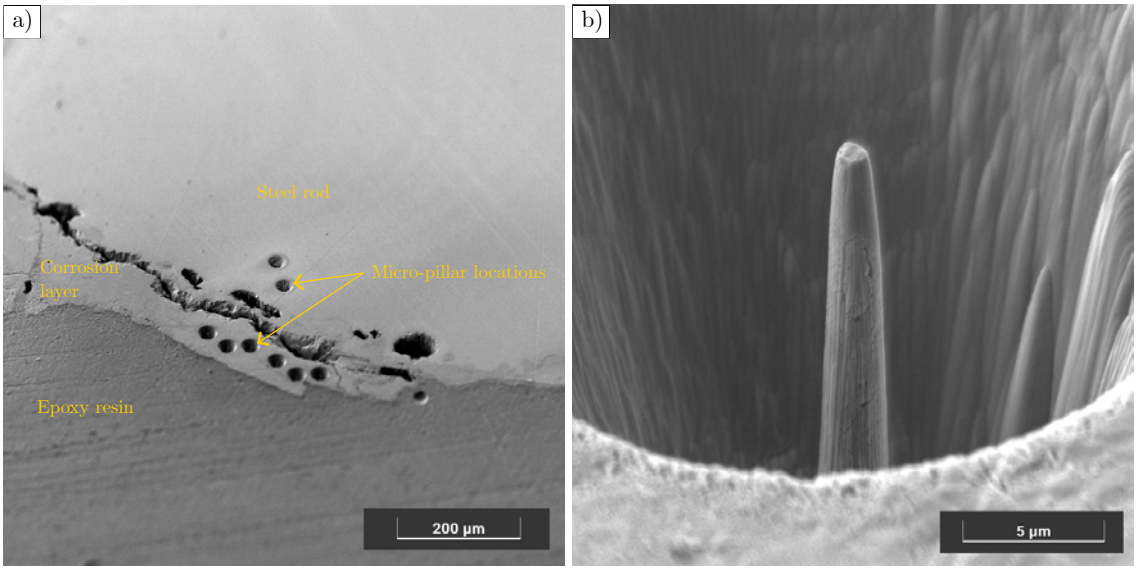

Fig. 1: SEM-SE images of (a) sample overview showing locations of the corrosion layer and fabricated micro-beams, (b) example of a fabricated micro-beam in the corrosion layer.

After the accelerated test, the samples were cut into thinner slices, dried at $50\,^{\circ}C$ for 1 day, and then embedded in epoxy resin to stabilize the corrosion layer formed around the steel rod during the polishing. The samples were subsequently polished using silicon carbide papers following the procedure described in Němeček et al. (2020). An example of a polished surface at the steel rod with the corrosion layer is shown in Fig. 1a. A Phenom XL desktop SEM was used to characterize the corrosion layer by EDS mapping over an area of $163\,\mu m^2$. The measurements were performed at an accelerating voltage of 15 kV.

A Tescan Amber X microscope was used to fabricate micro-pillars with Xe plasma focused ion beam (FIB) positioned primarily in the corrosion layer, as shown in Fig. 1a. FIB milling was performed with an accelerating voltage of 30 kV and decreasing current values from 10 nA to 250 pA when approaching the micro-pillar. An example of a fabricated pillar in the corrosion layer is shown in Fig. 1b. The dimensions of the micro-pillar are $\sim 12\,\mu m$ in height, $\sim 1.1\,\mu m$ at the top diameter, and $\sim 2.5\,\mu m$ at the bottom diameter. Then, a Hysitron PI-89 SEM PicoIndenter was used to compress the micro-pillars with diamond conical tip with a flat end with a radius of $5\,\mu m$. The loading was performed under displacement control up to a maximum displacement of 2000 nm, with a constant loading rate of 100 nm/s.

2.1. Results and discussion

The SEM characterization is shown in Fig. 2, which also shows the elemental composition (EDS maps) of the steel-corrosion layer transition region. The corrosion layer is clearly distinguishable in the BSE image (Fig. 2a), forming an irregular shape compared with the original steel rod. EDS mapping shows a

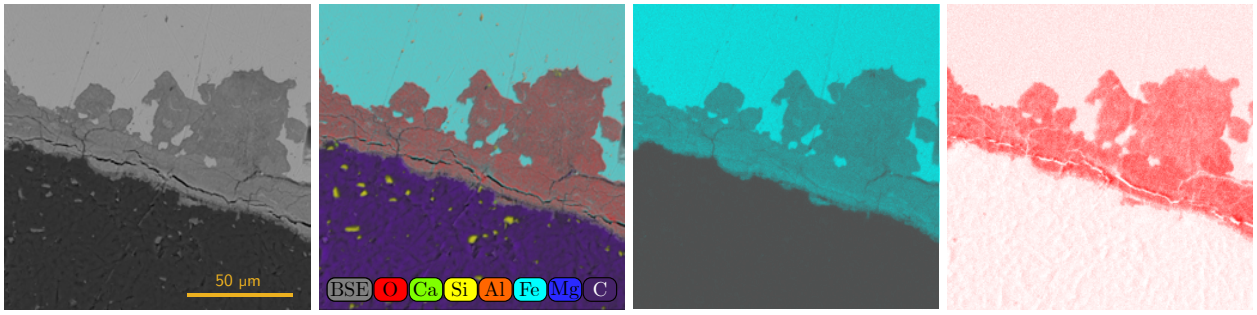

(a) Original BSE image. (b) EDS combined map. (c) Iron map. (d) Oxygen map.

Fig. 2: Characterization of steel-corrosion layer-epoxy resin by EDS mapping. a) Original BSE image, b) EDS combined map, c) Iron map, d) Oxygen map.

reduced iron content and a simultaneous increase in oxygen, confirming the formation of new corrosion products. However, precise phase identification requires complementary methods, such as XRD or Raman spectroscopy (Mi et al., 2023). Additionally, no Ca or Si was detected in the corrosion layer, indicating no intermixing with the surrounding cement paste.

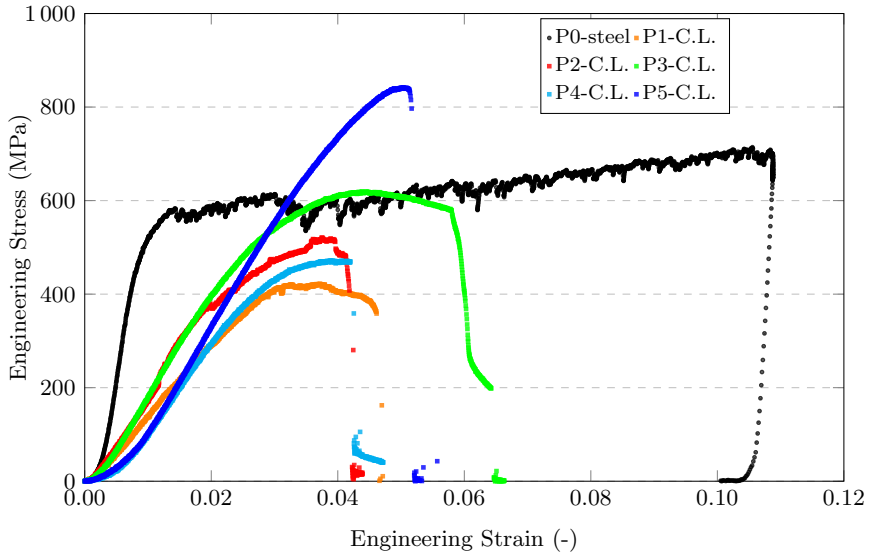

Fig. 3: Measured stress–strain curves from micro-pillar compression in the corrosion layer (C.L.) and in the steel rod.

The engineering stress-strain response from micro-pillar compression is presented in Fig. 3. The reference pillar fabricated in the steel rod exhibits behavior characterized by an initial linear elastic regime, followed by yielding and stable plastic flow with noticeable strain hardening, reaching a peak stress of 714 MPa. Since the pillar did not undergo a complete fracture during compression, the unloading segment follows an approximately linear elastic path. In contrast, micro-pillars prepared in the corrosion layer show an initial elastic response, followed by limited plastic deformation, followed by a rupture or instability. After reaching the peak stress, all corrosion-layer pillars undergo abrupt stress drops associated with sudden failure. The peak strength and failure strain vary among pillars, indicating pronounced microstructural heterogeneity. The evaluated mechanical properties are summarized in Table 1. The mechanical parameters generally reveal a decrease in the values for the corrosion products compared to the original steel. The corrosion layer exhibits a lower average yield strength (478 ± 126 MPa) and peak stress (575 ± 148 MPa) than the steel pillar (535 MPa and 714 MPa, respectively). The strain at peak stress is significantly smaller for corrosion products (0.041 ± 0.005) compared to the steel pillar (0.105) which is a consequence of the greater brittleness of corrosion products compared to the ductile steel. It is worth noting that the size of the reference steel pillar is probably smaller than the size of the ferrite grain (α-Fe). Ferrite in S235JRC+C steels occupies approximately 90% of the volume, is anisotropic with a grain size of around 20 μm. The reference value is therefore not a unique value for differently oriented grains and in further studies it would

be appropriate to perform measurements for more orientations, or possibly for a larger size, which would lead to the determination of the average properties of the steel for a larger volume.

The most significant reduction is observed in the elastic modulus. It should be noted that these values are most likely underestimated due to imperfect contact between the tip and the end of the pillar or other geometric inaccuracies. For a more accurate evaluation, further optimization of the micro-pillar geometry along with the application of a cyclic loading protocol would be necessary (Shahrin and Bobko, 2019).

Tab. 1: Parameters measured during micro-pillar compression.

Parameter	Steel (1 test)	Corrosion products (5 tests)	Change (%)
Yield Strength (MPa)	535	478 ± 126	-10.6
Peak Stress (MPa)	714	575 ± 148	-19.5
Elastic Modulus (GPa)	84.8	20.3 ± 2.5	-76.0
Strain at Peak Stress (-)	0.105	0.041 ± 0.005	-61.0

3. Conclusions

The micro-pillar compression results performed in this study demonstrate a clear mechanical degradation of the corrosion products compared to the steel substrate. While the pillar in steel exhibits significant ductility and high load-bearing capacity, the pillars in corrosion-layer show reduced strength, significantly lower stiffness, and limited deformability, followed by premature, unstable failure. The large scatter in the corrosion-layer response reflects pronounced microstructural heterogeneity.

Acknowledgments

This work was financially supported by the Czech Science Foundation under grant number 26-22195S and the Grant Agency of the Czech Technical University in Prague (SGS25/083/OHK1/2T/11). The authors also acknowledge the support of the Laboratory of Special Microscopy, Faculty of Civil Engineering, CTU in Prague.

References

Andrade, C. (2023) Steel corrosion rates in concrete in contact to sea water. *Cement and Concrete Research*, 165, pp. 107085.

Korec, E., Jirásek, M., Wong, H., and Martínez-Pañeda, E. (2023) A phase-field chemo-mechanical model for corrosion-induced cracking in reinforced concrete. *Construction and Building Materials*, 393, pp. 131964.

Korec, E., Jirásek, M., Wong, H., and Martínez-Pañeda, E. (2024) Unravelling the interplay between steel rebar corrosion rate and corrosion-induced cracking of reinforced concrete. *Cement and Concrete Research*, 186, pp. 107647.

Mi, T., Wang, J., McCague, C., and Bai, Y. (2023) Application of raman spectroscopy in the study of the corrosion of steel reinforcement in concrete: A critical review. *Cement and Concrete Composites*, 143, pp. 105231.

Němeček, J., Lukeš, J., and Němeček, J. (2020) High-speed mechanical mapping of blended cement pastes and its comparison with standard modes of nanoindentation. *Materials Today Communications*, 23, pp. 100806.

Němeček, J., Králík, V., Šmilauer, V., Polívka, L., and Jäger, A. (2016) Tensile strength of hydrated cement paste phases assessed by micro-bending tests and nanoindentation. *Cement and Concrete Composites*, 73, pp. 164–173.

Shahrin, R. and Bobko, C. (2019) Micropillar compression investigation of size effect on microscale strength and failure mechanism of calcium-silicate-hydrates (C-S-H) in cement paste. *Cement and Concrete Research*, 125, pp. 105863.

Zhang, W., Chen, J., and Luo, X. (2019) Effects of impressed current density on corrosion induced cracking of concrete cover. *Construction and Building Materials*, 204, pp. 213–223.

Zhao, Y. and Jin, W. (2016) Chapter 2 - steel corrosion in concrete. In Zhao, Y. and Jin, W., eds, *Steel Corrosion-Induced Concrete Cracking*, Butterworth-Heinemann, pp. 19–29.

Zhao, Y., Ren, H., Dai, H., and Jin, W. (2011) Composition and expansion coefficient of rust based on x-ray diffraction and thermal analysis. *Corrosion Science*, 53, 5, pp. 1646–1658.

32nd International Conference
ENGINEERING MECHANICS 2026
Medlov, Czech Republic, May 11 – 13, 2026

WAVE-BASED CONTROL FOR MECHANICAL SYSTEMS WITH FORCE FEEDBACK

Neusser Z.[1]

Abstract: *This paper presents wave-based control with force feedback and its incorporation into wave model and subsequently into the wave-based control. The force feedback allows the suppression of the influence of external forces acting on the system, which is a problem in wave-based control with position feedback only.*

Keywords: Wave-Based Control, Force Feedback, Vibration Suppression

1. Introduction

The concept of wave-based control (WBC) was presented in O'Connor and Lang (1998). The idea is based on longitudinal waves propagating in a compliant structure. In a flexible system, due to an imposed force (actuator, disturbance), the effect of a so-called launched wave is induced, which is at the same time accompanied by a returned (reflected) wave in the system, schematically shown in Figure 1a.

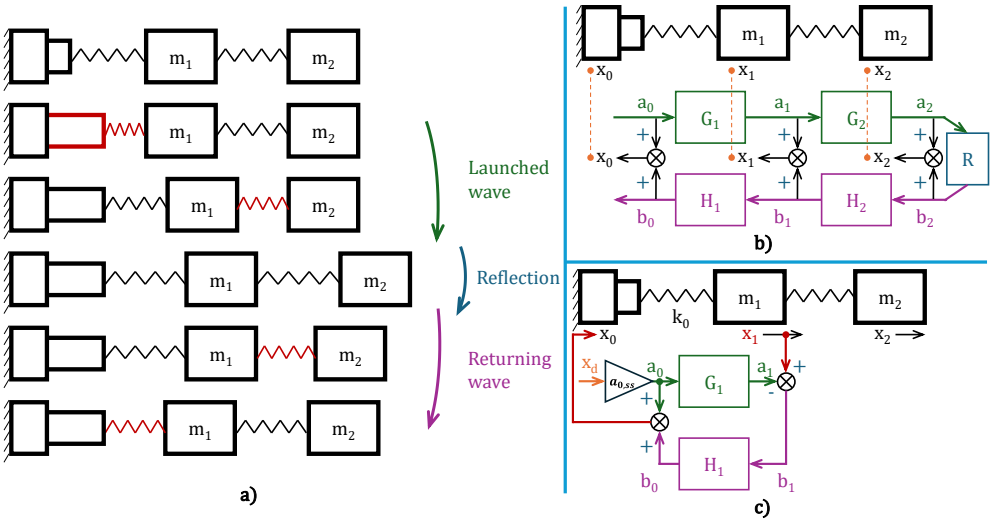

Fig. 1: The idea of a launched and returned wave in a mechanical system.

Based on this inspiration, the so-called wave model is developed, which describes the above wave behavior using transfer functions.

Wave-based control is typically used for flexible, multibody systems. The WBC is used for one-dimensional position control of mechanical systems O'Connor (2004); O'Connor (2006); O'Connor (2007b) as well as for angular position control (O'Connor, 2005; Marek and Valasek, 2009). Flexible systems are treated by WBC in O'Connor et al. (2009); Beneš et al. (2018). Modal properties are investigated in O'Connor and McKeown (2008); O'Connor (2011). There are some other applications suitable for WBC or control inspired by wave-based technique. Control of synchronous machine Valášek et al. (2016), mass-rope system O'Connor (2002); O'Connor (2004), adaptive cruise control for vehicles Martinec et al. (2014); Valasek et al. (2016) are some examples of WBC usage.

[1] Ing. Zdeněk Neusser, Ph.D.: Faculty of Mechanical Engineering, Czech Technical University in Prague, Technická 4; 166 00, Prague; CZ, zdenek.neusser@fs.cvut..cz

ISSN: 1805-8256, doi: 10.21495/em2026-89

2. Wave model and wave-based control

An alternative model to the mechanical model is developed; Figure 1b shows schematically the wave and mechanical models. The wave model is composed of transfer functions describing the launched (G_i) and reflected wave (H_i). The mechanical model is connected to the wave model through the coordinates of the individual bodies, as shown in Figure 1b. The interconnection is written in the equation (1).

$$x_i = a_i + b_i \tag{1}$$

Wave-based control is based on feedback, in this case measuring the position of the first mass. We cut out everything behind the measured mass from the wave model, see Figure 1c. The reflected wave can be determined based on the knowledge of the reflected wave and the aforementioned feedback. The control law can be constructed based on the first mass measurement and wave model.

$$x_0 = a_0 + b_0 \tag{2}$$

where

$$a_0 = a_{0,ss} x_d \tag{3}$$

$$a_1 = G_1 a_0 \qquad b_0 = H_1 b_1 \tag{4}$$

$$b_1 = x_1 - a_1 \tag{5}$$

with k_0 representing the spring between actuator x_0 and first mass x_1 and m_1 is first mass weight. The launched wave a_0 in equation (3) is composed of the desired position of the first mass x_d and the coefficient $a_{0,ss}$, whose value is derived in Marek (2013); Valasek et al. (2019). The launched wave, reflected wave and the relationships between their quantities are in (4); these are the relationships of the wave model. The b_1 magnitude in (5), used for determination of b_0, is obtained from the launched wave a_1 and from the measured value of the first mass position x_1. After substituting and adjusting, the control law is obtained

$$x_0 = H_1 x_1 + (1 - H_1 G_1)\, a_{0,ss} x_z \tag{6}$$

$$G_1 = \frac{\omega^2}{s^2 + \omega s + \omega^2} \qquad H_1 = G_1 \qquad \omega = \sqrt{\frac{k_0}{m_1}}$$

where $H_1 x_1$ represents output feedback and $(1 - H_1 G_1)\, a_{0,ss} x_z$ forward control with input x_z as the desired position of the system. Such control is called absolute wave-based control (WBC-A). The transfer functions G_1 and H_1 in (6) are determined as second order transfer functions according to O'Connor (2007a).

3. Wave-based control with force feedback

Force and position feedback control, first used in the article O'Connor and Fumagalli (2009), is placed in the context of the philosophy of the wave approach using force interaction, nested in the wave model. The feedback in the control can also be implemented by force measurement (Fig. 2), which complements the position measurement.

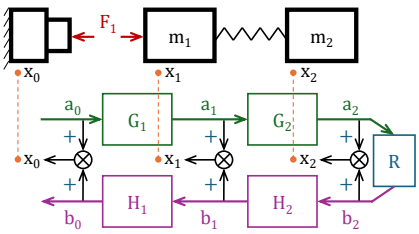

Fig. 2: The wave model and the force between bodies.

From the expression of the relative force acting between the bodies of the mass chain in Figure 2, the relation for the reflected wave (quantity b_0), can be obtained. The force acting on mass 1 is determined as:

$$F_1 = k_0 \left(x_0 - x_1\right) \tag{7}$$

By introducing substitutions according to (1) we obtain the force expressed in the coordinates of the wave model:

$$F_1 = k_0 \left(a_0 + b_0 - a_1 - b_1\right) \tag{8}$$

From the equations of the launched wave (4), a_0 is eliminated, then, thanks to the x_1 position measurement (5), the equation is converted to the coordinates of the reflected wave. Using the equations of the reflected part of the wave model (4), the expressions are converted to a function of the variable b_0.

$$\begin{aligned} F_1 &= k_0 \left(\left(\frac{1}{G_1} - 1 \right) \left(x_1 - b_1\right) + b_0 - b_1 \right) \\ F_1 &= k_0 \left(\frac{1 - G_1}{G_1} x_1 + \frac{G_1 H_1 - 1}{G_1 H_1} b_0 \right) \end{aligned} \tag{9}$$

Express the reflected wave on the actuator (b_0):

$$b_0 = H_1 \left(\frac{G_1}{\left(G_1 H_1 - 1\right) k_0} F_1 - \frac{1 - G_1}{G_1 H_1 - 1} x_1 \right) \tag{10}$$

The control law of WBC with position and force feedback is following:

$$x_0 = a_{0,ss} x_d + H_1 \left(\frac{G_1}{\left(G_1 H_1 - 1\right) k_0} F_1 - \frac{1 - G_1}{G_1 H_1 - 1} x_1 \right) \tag{11}$$

with the measured force F_1 and the position x_1 on the mass m_1. This control is called absolute, force wave-based control (F-WBC-A).

4. Simulation experiment

The system of three masses with springs and dampers is subjected to a step demand on position, force pulses on the individual masses (in ascending order) and a constant force on the first mass.

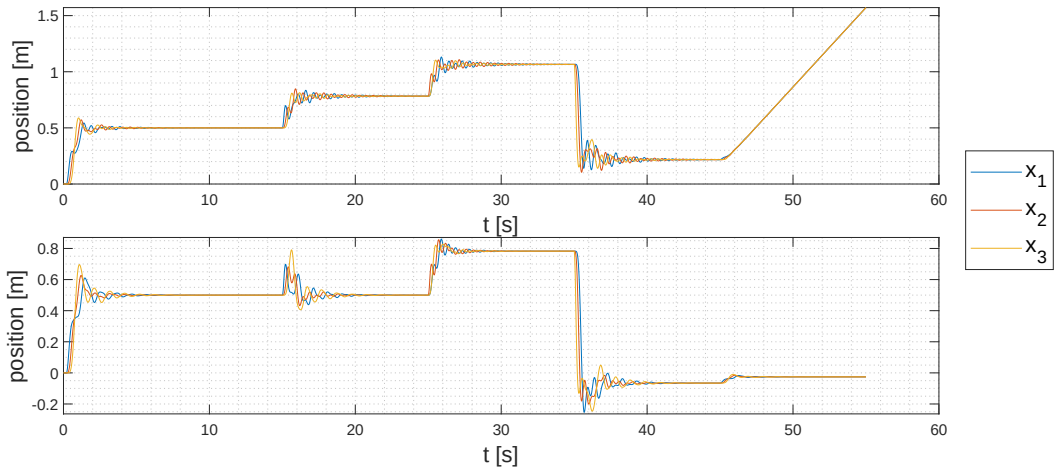

Fig. 3: Three mass system position behavior, WBC-A on the top, F-WBC-A (with force feedback) on the bottom.

Figure 3 shows the response of the system with wave-based control (WBC-A on top) and wave-based control with force feedback (F-WBC-A on bottom).

5. Conclusions

The extension of wave-based control with force feedback is presented in this paper. In contrast to existing work, the implementation of force in control is derived. A simulation comparison of WBC-A and F-WBC-A (with force feedback) is performed. Both approaches suppress vibrations, and force feedback also eliminates the influence of external forces acting on the body where the force is measured. Further research will focus on removing the influence of forces on all bodies.

Acknowledgments

This work was possible thanks to the grant released within the Framework Programme for Research and Innovation (2021–2027), grant n∘ 101159722, with project name "Twinning for Excellence in Morphing and Aeromechatronic Wing Control: A Leap Towards Eco-Smart Aviation" acronym (MechaTwing). I would like to thank professor Michael Valášek for his guidance and valuable advice in wave-based control research.

References

Beneš, P., Neusser, Z., Sika, Z., Valášek, M., and Zavrel, J. (2018) Wave-based control of a planar mechanical structure by piezoelectric actuators. In *Proceedings of ISMA 2018 - International Conference on Noise and Vibration Engineering and USD 2018 - International Conference on Uncertainty in Structural Dynamics*. p. 303 – 307.

Marek, O. (2013) *Řízení polohy poddajných struktur vlnovou metodou*. dizertační práce, České Vysoké Učení Technické v Praze, Praha, Česká republika.

Marek, O. and Valasek, M. (2009) Wave-based control of motion of flexible bodies. In *Multibody Dynamics 2009*. p. 1 – 6.

Martinec, D., Herman, I., Hurák, Z., and Šebek, M. (2014) Refinement of a bidirectional platooning controller by wave absorption at the leader. In *2014 European Control Conference (ECC)*. pp. 2845–2850.

O'Connor, W. (2002) Gantry crane control: a novel solution explored and extended. In *Proceedings of the 2002 American Control Conference (IEEE Cat. No.CH37301)*. 1, pp. 250–255.

O'Connor, W. (2004) Wave-echo position control of flexible systems: towards an explanation and theory. In *Proceedings of the 2004 American Control Conference*. 5, pp. 4837–4842.

O'Connor, W. (2005) Excellent control of flexible systems via control of the actuator-system interface. In *Proceedings of the 44th IEEE Conference on Decision and Control*. pp. 6181–6186.

O'Connor, W. J. (2007a) Control of flexible mechanical systems: wave-based techniques. In *2007 American Control Conference*. pp. 4192–4202.

O'Connor, W. J. (2007b) Wave-based analysis and control of lump-modeled flexible robots. *IEEE Transactions on Robotics*, 23, 2, pp. 342–352.

O'Connor, W. J., Ramos de la Flor, F., McKeown, D. J., and Feliu, V. (2009) Wave-based control of non-linear flexible mechanical systems. *Nonlinear Dynamics*, 57, 1-2, pp. 113–123.

O'Connor, W. and Lang, D. (1998) Position control of flexible robot arms using mechanical waves. *Journal of Dynamic Systems, Measurement, and Control*, 120, 3, pp. 334–339.

O'Connor, W. J. (2004) A gantry crane problem solved. *Journal of Dynamic Systems, Measurement, and Control*, 125, 4, pp. 569–576.

O'Connor, W. J. (2006) Wave-echo control of lumped flexible systems. *Journal of Sound and Vibration*, 298, 4, pp. 1001–1018.

O'Connor, W. J. (2011) Wave-like modelling of cascaded, lumped, flexible systems with an arbitrarily moving boundary. *Journal of Sound and Vibration*, 330, 13, pp. 3070–3083.

O'Connor, W. J. and Fumagalli, A. (2009) Refined wave-based control applied to nonlinear, bending, and slewing flexible systems. *Journal of Applied Mechanics*, 76, 4, pp. 041005.

O'Connor, W. J. and McKeown, D. J. (2008) A new approach to modal analysis of uniform chain systems. *Journal of Sound and Vibration*, 311, 3, pp. 623–632.

Valasek, M., Marek, O., Olgac, N., and Neusser, Z. (2019) Rigorous treatment of wave-based control concept, structured procedures and critical observations. *IET Control Theory & Applications*, 13, pp. 2620–2629.

Valasek, M., Neusser, Z., and Gordon, T. (2016) Wave-based control for intelligent longitudinal traffic column. In *Dynamics of Vehicles on Roads and Tracks*. pp. 181–188.

Valášek, M., Neusser, Z., Neuman, P., and Nečas, M. (2016) Wave-based modeling and control of interconnected synchronous machines-application on mechanical model. In *IFAC Workshop on Control of Transmission and Distribution Smart Grids CTDSG 2016*. 49, pp. 352–357.

32nd International Conference
ENGINEERING MECHANICS 2026
Medlov, Czech Republic, May 11 – 13, 2026

EFFECT OF TEMPERATURE AND STRAIN RATE ON HARDENING OF METALLIC MATERIALS

Novotný R.[1], **Šebek F.**[2]

Abstract: *The influence of temperature and strain rate on the hardening behaviour of three metallic materials is studied. Standard tensile tests were carried out under quasi-static, dynamic, and elevated temperature conditions, including static tensile tests with loading pauses to determine the static stress–strain response of AISI 316L steel, Inconel 718 and EN AW 2024-T351. Then the constitutive model was calibrated using a particle swarm optimization and subsequently validated through finite element simulations performed in LS-DYNA. The calibrated models showed good agreement with the experimental data up to the ultimate tensile strength. Larger errors occurred beyond the ultimate tensile strength due to a slight overestimation of the strain hardening exponent. The thermal softening parameter was not identified for Inconel 718 because elevated-temperature tests were not performed for this nickel-based alloy. Despite this limitation, calibrated material models provide sufficient accuracy for engineering simulations and structural design applications under moderate strain rates and elevated temperatures.*

Keywords: Aluminium alloy, Equivalent plastic strain, Evolutionary algorithm, Flow stress, Uniaxial stress state

1. Introduction

Structural materials generally exhibit different mechanical behaviour depending on the type and conditions of loading. Understanding this behaviour is essential for accurate material modelling and reliable numerical simulations of structures.

Three materials were selected for the current study. The first material is the corrosion resistant stainless steel AISI 316L, which is commonly applied in the energy and chemical industries due to its high corrosion resistance and good mechanical performance. The second investigated material is the nickel-based superalloy Inconel 718. This alloy retains its mechanical properties at elevated temperatures, making it suitable for demanding applications, particularly in the aerospace sector, where it is used for jet engine components, turbine blades and fastening elements. The third material is the aluminium alloy EN AW 2024-T351, which is characterized by high strength and excellent fatigue resistance. Owing to its favourable strength-to-weight ratio, it is widely used in the automotive and aerospace industries.

The main objective of constitutive modelling of these materials is to cover a wide range of temperatures and strain rates. The results will enable numerical simulations that incorporate a wide spectrum of loading rates and thermal conditions, including the material response under static loading that was achieved by interrupting the tests according to Huang and Young (2014).

2. Material and methods

2.1. Quasi-static, dynamic and high-temperature tensile testing

Experimental data were obtained using a uniaxial tensile test. Test was performed using standardized tensile specimens with circular cross-sections of 6 and 8 mm in diameter having gauge lengths of 30 and 40 mm.

[1] Ing. Radek Novotný: Brno University of Technology, Faculty of Mechanical Engineering, Institute of Solid Mechanics, Mechatronics and Biomechanics; Technická 2896/2; 616 69, Brno; CZ, Radek.Novotny3@vutbr.cz

[2] doc. Ing. František Šebek, Ph.D.: Brno University of Technology, Faculty of Mechanical Engineering, Institute of Solid Mechanics, Mechatronics and Biomechanics; Technická 2896/2; 616 69, Brno; CZ, sebek@fme.vutbr.cz

ISSN: 1805-8256, doi: 10.21495/em2026-93

Dynamic tensile tests were performed to capture the effect of loading speed, while elevated temperature tests were performed to capture the temperature dependence, all summarized in the Tab. 1 including quasi-static tests (Novotný, 2025).

Tab. 1: Parameters of the uniaxial tensile tests (Novotný, 2025).

Tensile test	Material	Temperature [°C]	Loading rate [mm/min]
Quasi-static	AISI 316L	22	1
	Inconel 718		
	EN AW 2024-T351		
Dynamic	AISI 316L	22	100
	Inconel 718		100
	EN AW 2024-T351		100
	EN AW 2024-T351		200
High-temperature	AISI 316L	400	1
	EN AW 2024-T351	150	
	EN AW 2024-T351	200	

2.2. Static tensile testing

Furthermore, static tensile tests were carried out after Huang and Young (2014). These experiments followed a similar protocol to quasi-static tests, however, included the pauses during loading. Three pauses of 100 seconds each were chosen. These pauses resulted in a decrease in the measured force. A static curve can then be determined from these static drops. It should represent the static behaviour of the material without the influence of quasi-static loading (Novotný, 2025).

3. Constitutive modelling

The Johnson–Cook model was considered as (Johnson and Cook, 1983)

$$\bar{\sigma} = \left(A + B\bar{\varepsilon}_p^n\right)\left(1 + C\ln\frac{\dot{\bar{\varepsilon}}_p}{\dot{\bar{\varepsilon}}_0}\right)\left(1 - \left(\frac{T - T_r}{T_m - T_r}\right)^m\right), \tag{1}$$

where $\bar{\sigma}$ is the equivalent stress, A, B and C are the material parameters, $\bar{\varepsilon}_p$ is the equivalent plastic strain, n is the strain hardening exponent, $\dot{\bar{\varepsilon}}_p$ is the equivalent plastic strain rate, $\dot{\bar{\varepsilon}}_0$ is the reference plastic strain rate, T is the temperature, T_r is the reference temperature, T_m is the melting temperature and m is the thermal softening exponent.

All of the material parameters mentioned above were calibrated in MATLAB 2024b using particle swarm optimization (PSO). PSO is a computational method based on the movement of organisms such as a flock of birds or fish schools that are used to find local extremes. The main parameter for PSO is the number of particle swarms. A total of 10^4 particles were used, each particle representing a potential solution to the optimization problem under investigation. The maximum number of iterations was limited to 10^2 and the optimization ends if the change in the objective function value between iterations falls below 10^{-6}. The final set of material parameters is given in the Tab. 2 (Novotný, 2025).

Tab. 2: Material parameters of the Johnson–Cook model (Novotný, 2025).

Material	A [MPa]	B [MPa]	n [–]	C [–]	$\dot{\bar{\varepsilon}}_0$ [s^{-}1]	T_r [°C]	T_m [°C]	m [–]
AISI 316L	270.0	1130	0.688	0.014			1400	1.244
Inconel 718	380.0	1821	0.718	0.009	$6 \cdot 10^{-6}$	22	1300	–
EN AW 2024-T351	270.0	747.0	0.607	0.009			500	2.250

ANSYS Workbench 2024 R2 and the implicit solver in LS-DYNA were used for numerical simulations. All analyses were calculated as axisymmetric. The specimen geometry was modelled without clamping parts with only half of the gauge length, making the geometry a rectangle with radious and gauge length of the specimens. Shell elements were used to create a structured mesh. The global size of the finite element was 0.1 mm (Novotný, 2025).

A complete Johnson–Cook material model marked *MAT_015 was chosen as the only model defined for the implicit solver in LS-DYNA, which can be used in thermal analysis. This material model has to be supplemented with an equation of state (EOS). The EOS is responsible for calculating the pressure based on changes in volume, density and possibly energy or temperature (Novotný, 2025).

4. Results and discussion

The stress–strain curves obtained from the numerical simulations were compared with the experiments in Figs. 1–3, where the dashed and solid lines refer to the numerical simulations and experiments, respectively. The results indicate that the material model captures the dependence on strain rate and temperature (Novotný, 2025).

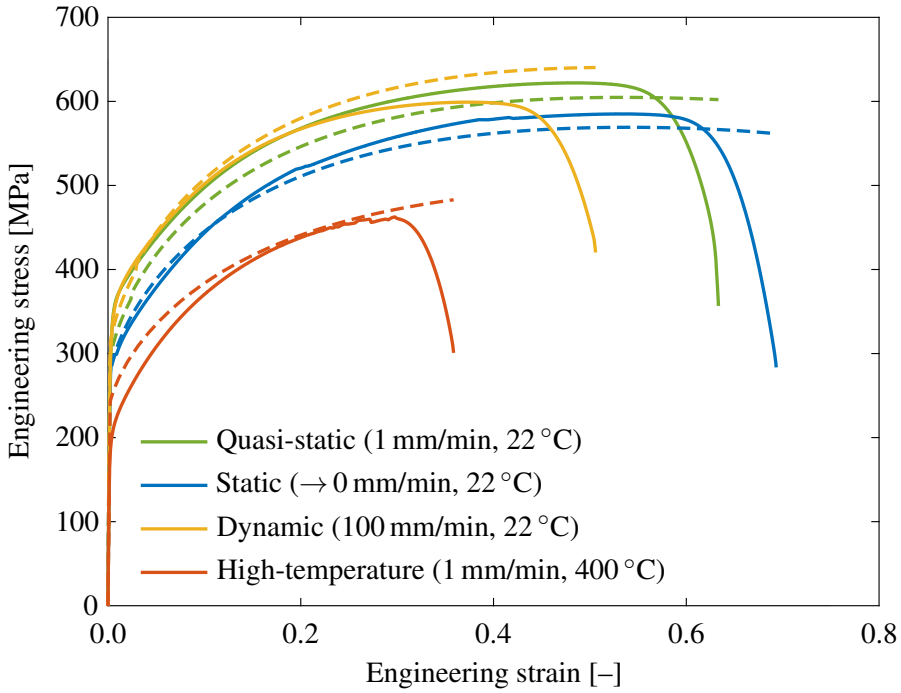

Fig. 1: Stress–stress curves compared from numerical simulations and experiments of AISI 316L.

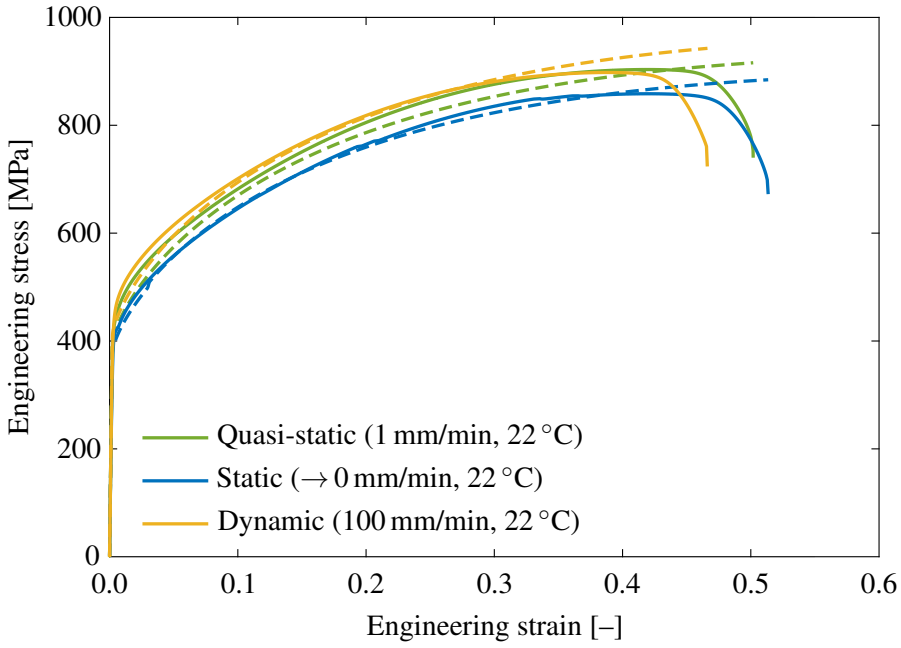

Fig. 2: Stress–stress curves compared from numerical simulations and experiments of Inconel 718.

The largest differences were observed beyond the ultimate tensile strength during necking. This inaccuracy is caused by a slight overestimation of the strain hardening exponent, which, on the other hand, well described the region prior to plastic instability (Novotný, 2025).

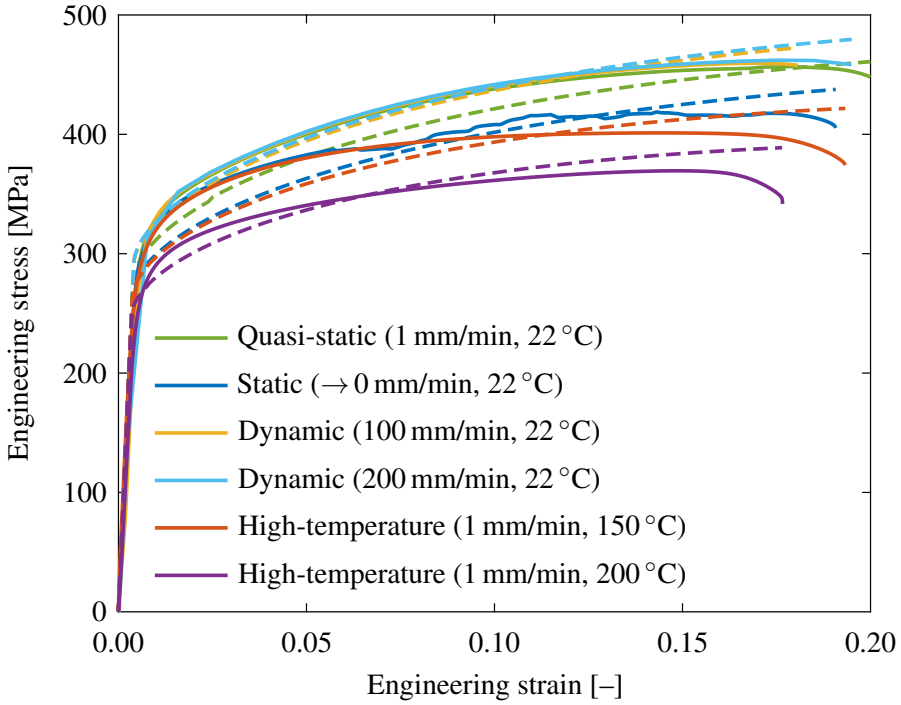

Fig. 3: Stress–stress curves compared from numerical simulations and experiments of EN AW 2024-T351.

5. Conclusions

The present work deals with constitutive modelling, which includes the effects of strain rate and temperature for three metals, AISI 316L, Inconel 718 and EN AW 2024-T351. The percent error was up to 10 % for nine of the numerical simulations, while the remaining two were up to 20 %. It should be noted that the temperature effect was not considered for Inconel 718 due to the absence of thermal testing. The material models presented provide a basis for engineering applications and structural designs, particularly for strain rates up to approximately $0.0\bar{5}$ and $0.\bar{1}\,\mathrm{s}^{-1}$ and temperatures up to 400 °C for AISI 316L and 200 °C for EN AW 2024-T351. Future work could focus on extending the proposed methodology to additional material classes. Furthermore, performing a larger number of tests at higher strain rates would enable improved modelling of dynamic events such as impacts and crashes. Additional high-temperature experiments would refine the description of thermal effects and allow identification of the thermal softening exponent for Inconel 718.

Acknowledgments

This work is an output of the project Computational modelling of ductile fracture of identical wrought and printed metallic materials under ultra-low-cycle fatigue created with financial support from the Czech Science Foundation under the registration no. 23-04724S.

References

Huang, Y. and Young, B. (2014) The art of coupon tests. *Journal of Constructional Steel Research*, 96, pp. 159–175.

Johnson, G. R. and Cook, W. H. (1983) A constitutive model and data for metals subjected to large strains, high strain rates and high temperatures. In *Proceedings of the 7th International Symposium on Ballistics*, The Hague. International Ballistics Committee, pp. 541–547.

Novotný, R. (2025) *Analysis of the effect of size, temperature and strain rate on the hardening of metallic materials*. Master's Thesis, Brno University of Technology.

32nd International Conference
ENGINEERING MECHANICS 2026
Medlov, Czech Republic, May 11 – 13, 2026

FINITE ELEMENT MODELING OF PATIENT-SPECIFIC MANDIBULAR PLATES FOR CONDYLAR FRACTURE

Ouldyerou A.[1], Mehboob H.[2]

Abstract: *Condyle fractures are the most common type of mandibular fracture. This study aims to evaluate the biomechanical performance of four proposed designs and ensure the optimum plate design. Four models were constructed using CAD software (Plates A, B, C, and D). A normal chewing force (100 N) was applied to the first molar location of the non-fractured site. Stresses in plates and reaction forces at the left and right mandibular necks were evaluated using finite element method. Results showed that the lowest peak von Mises stress was in plate D (217 MPa), while the highest stress was with plate A (351 MPa), followed by plate C (250 MPa), then plate B (287 MPa). Higher reaction forces were on the left side non-fracture side. Plate B showed the highest reaction force in the fracture side (33 N), while the lowest value was with plate A, followed by plate C and D (20 N). For the mandibular movement, plate B showed less displacement. It was concluded that among the four designs, plate D demonstrated lower stress distribution and lowest micromotion at the fracture gap compared to the other plates.*

Keywords: Condyle fracture, Plate, Finite element, Stress, Biomechanics

1. Introduction

The mandible forms the lower portion of the face and is essential not only for facial aesthetics but also for key functions such as chewing, speaking, and keeping the airway open. As a result, damage to the mandible can severely impact both appearance and overall quality of life (Conforte et al., 2016). Mandibular fractures are grouped based on location into symphysis, parasymphysis, body, angle or ramus, and condylar process fractures. Fractures at the top of the condyle are called intracapsular or diacapitular, and those at the bottom are called subcondylar fractures. About 20 to 40% of all mandible fractures happen in the condyle. Various techniques for osteosynthesis have been proposed for the surgical treatment of condylar fractures, ranging from miniplates (Brito et al., 2025)(Leonhardt et al., 2025) to various types of screw and resorbable polylactide pins (McLeod & Saeed, 2016), as well as titanium-based cannulated headless bone screws (Franke et al., 2025). This can be considered as an open reduction and internal fixation technique for mandibular condyle fracture, which is beneficial for restoring the jaw functions, and it is the standard treatment approach so far (Alyahya et al., 2020). However, the management of fractures involving the mandibular condyle is a subject of significant debate within the field of maxillofacial trauma (Bhatti et al., 2025).

In the present study, our primary aim was to compare various bone plate designs that can be planned preoperatively using patient-specific CAD/CAM technology for the osteosynthesis of subcondylar fractures. By using finite element analysis, we aimed to evaluate the biomechanical performance of the four plate designs and ensure the optimum one.

[1] Abdelhak Ouldyerou, PhD.: Department of Engineering Management, College of Engineering, Prince Sultan University, Riyadh, Saudi Arabia, aouldyerou@psu.edu.sa

[2] Hassan Mehboob, PhD.: Department of Engineering Management, College of Engineering, Prince Sultan University, Riyadh, Saudi Arabia, hmehboob@psu.edu.sa

ISSN: 1805-8256, doi: 10.21495/em2026-97

2. Materials and methods

2.1. Construction of 3D models

Cone beam computed tomography (CBCT) scan model of the mandible was obtained from 3D Slicer 5.8.0 software (CBCT-MR library). The datasets were donated to 3D Slicer by medical institutions for public access and are available without restrictions, ensuring compliance with ethical standards (Fedorov et al., 2012). As these datasets do not contain private or identifiable patient information, the study adheres to ethical guidelines for using open-access medical data. Semi-automatic segmentation was performed to reconstruct the STL file of the mandible. The 3D geometry was offset by 1.5 mm to create the internal architecture of the cancellous bone, while the external layer was considered as cortical bone. The bone was split with a 0.5 mm gap (Mehboob et al., 2025) to create a condyle fracture. The plate thickness was modeled as 1 mm with a length of 20 mm (Jung et al., 2020), as shown in Fig. 1(a). The length and diameter of the screw were 6.0 mm and 2.0 mm, respectively. Four plate models were constructed with the same thickness but different shapes, as shown in Fig. 1(b). Mechanical properties of bones, screws, and plate was taken from a previous study conducted by Jung et al. (Jung et al., 2020).

2.2. Computational modelling

Chewing and biting forces can vary significantly with age, with younger individuals typically exerting lower forces compared to adults. In this study, a normal chewing force of 100 N (Orassi et al., 2022) was applied at the first molar location, as shown in Fig. 1(c). Muscle forces were not considered in this work. The tie contact was applied between the screws and the plate, as well as between the screws and the bone, assuming full osseointegration. The proximal ends of the left and right mandibular necks were fully constrained in all directions to simulate fixation and eliminate rigid body motion. All components in the model were meshed with tetrahedral elements using ABAQUS 2017 (Dassault Systemes, France, Abaqus), except for the plates, which were meshed with hexahedral elements.

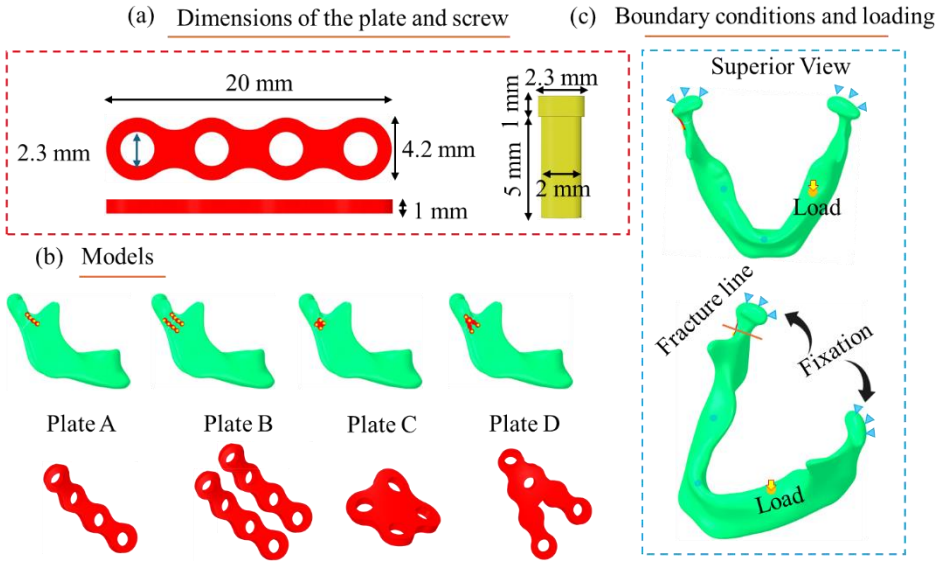

Fig. 1: Finite element models. (a) Dimensions of the plate; (b) Various plate models and (c) loading and boundary conditions.

3. Results and discussion

von Mises stress distribution in the plates is shown in Fig. 2(a). The highest von Mises stress of 351 MPa was observed in plate A, the straight single plate, with stress concentrated at the center of the plate, where it maintains the gap between the bones at the gap location. In contrast, plate D exhibited the lowest von Mises stress of 217 MPa. This plate features a lambda-shaped structure, which helps to distribute the load more effectively. Plate B, consisting of two straight plates, had a maximum stress of 287 MPa, while plate C, with a square structure, showed a maximum stress of 250 MPa.

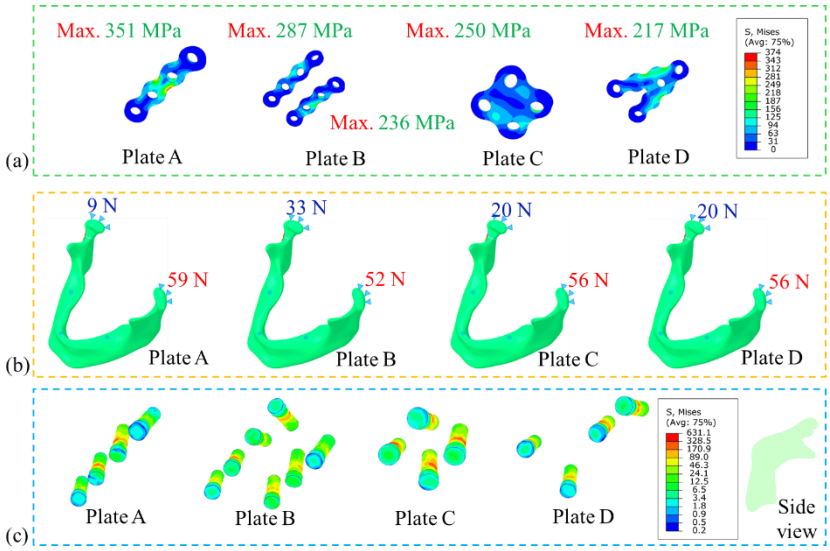

Fig. 2: (a) von Mises stress distribution in all plates; (b) reaction forces at mandibular neck and (c) von Mises stress in screws.

Figure 2(b) shows the reaction forces at the left (non-fractured) and right (fractured) sides of the mandibular neck. It can be observed that the non-fractured side, where the load was applied, generally exhibited higher reaction forces. In some cases, patients may be unable to bite or chew on the fractured side, which can affect the movement of the mandible and stress transfer to the plate. Notably, plate B demonstrated a higher reaction force on the fractured side compared to the other designs, likely due to its double straight-plate configuration. Additionally, the patient's mandibular geometry, which is not perfectly symmetrical between the left and right sides, may also influence the biomechanical performance of the plates.

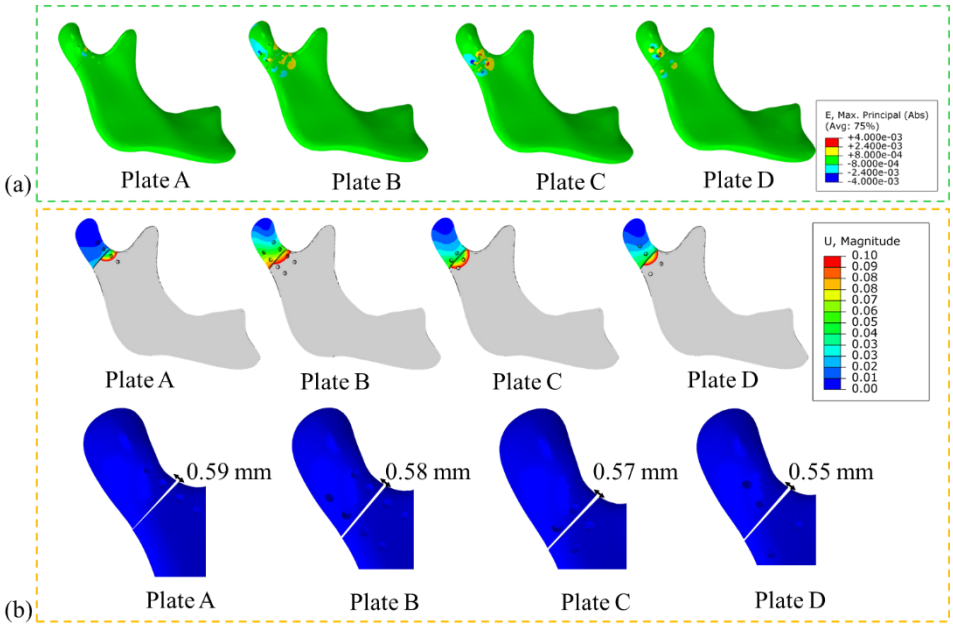

Fig. 3: (a) Maximum principal strain in mandible and (b) displacement within the mandibular condyle.

Figure 2(c) showed von Mises stress in screws. The stress values in all screws remain below the yield strength of titanium, indicating that the screws are safe under the applied loading conditions. Figure 3(a) shows the maximum principal strain in mandible. Plate A showed lower strain at the bone–screw interface, indicating reduced fixation stability. In plate B, the strain exceeded 0.4%, the typical strain limit of human cortical bone (Liokatis et al., 2021), in only one screw region. Plate C exhibited higher strain at all bone–screw interfaces, whereas plate D showed increased strain in only one screw region. Figure 3(b) shows the displacement within the mandibular condyle. Plate A showed a larger gap between the two bone segments at the fracture site, while plate D showed less compared to other plates, this suggests better

approximation of the bone segments and potentially improved load sharing between the bone and the fixation plate and screws.

This study compared four different plate designs for condylar fractures. The analysis has certain limitations, including the exclusion of muscle forces and the assumption of linear elastic properties for the bone tissue. Moreover, the cortical bone of the mandible does not have uniform thickness across its anatomical regions, which may influence the stress distribution in the screws and plates. Future studies should focus on callus gap healing, topology optimization of bone plate designs, and validation through in-vitro experiments.

4. Conclusion

Among the four plate designs evaluated for condylar fractures, plate D (lambda-shaped) demonstrated lower stress distribution and lowest micromotion at the fracture gap compared to the other plates.

Acknowledgement

The authors would like to acknowledge the support of Prince Sultan University.

References

Alyahya, A., Bin Ahmed, A., Nusair, Y., Ababtain, R., Alhussain, A., & Alshafei, A. (2020). Mandibular condylar fracture: a systematic review of systematic reviews and a proposed algorithm for management. *British Journal of Oral and Maxillofacial Surgery*, *58*(6), 625–631. https://doi.org/10.1016/j.bjoms.2020.03.014

Bhatti, N., Mohamedbhai, H., Poon, X., Khan, P., der Cruyssen, F. Van, & Holmes, S. (2025). Open management of condylar head fractures. The first 50 cases: What have we learnt and where are we going? *British Journal of Oral and Maxillofacial Surgery*, *63*(1), 19–24. https://doi.org/10.1016/j.bjoms.2024.08.005

Brito, G. C., de Assis, A. F., & de Moraes, M. (2025). Assessment of the trapezoidal miniplate with posterior extension for open management of condylar fractures: Can it be used instead of straight miniplates? *Oral Surgery*, *18*(2), 159–168. https://doi.org/10.1111/ors.12934

Conforte, J. J., Alves, C. P., Sánchez, M. delP. R., & Ponzoni, D. (2016). Impact of trauma and surgical treatment on the quality of life of patients with facial fractures. *International Journal of Oral and Maxillofacial Surgery*, *45*(5), 575–581. https://doi.org/10.1016/j.ijom.2015.11.022

Franke, A., Matschke, J. B., Sembdner, P., Seidler, A., McLeod, N. M. H., & Leonhardt, H. (2025). Long-term outcomes of open treatment of condylar head fractures using cannulated headless bone screws—a retrospective analysis. *International Journal of Oral and Maxillofacial Surgery*. https://doi.org/10.1016/j.ijom.2025.01.018

Jung, B. T., Kim, W. H., Park, B., Lee, J.-H., Kim, B., & Lee, J.-H. (2020). Biomechanical evaluation of unilateral subcondylar fracture of the mandible on the varying materials: A finite element analysis. *PLOS ONE*, *15*(10), e0240352. https://doi.org/10.1371/journal.pone.0240352

Leonhardt, H., Matschke, J. B., Bräuer, C., Remschmidt, B., McLeod, N. M. H., Lauer, G., & Franke, A. (2025). Treatment of mandibular condyle fractures with a rhombic 3D condylar fracture plate – Does the surgical approach matter? *Journal of Cranio-Maxillofacial Surgery*, *53*(5), 533–542. https://doi.org/10.1016/j.jcms.2025.01.029

Liokatis, P., Tzortzinis, G., Gerasimidis, S., & Smolka, W. (2021). Finite Element Analysis of Different Titanium Plates for Internal Fixation of Fractures of the Mandibular Condylar Neck. *Journal of Oral and Maxillofacial Surgery*, *79*(3), 665.e1-665.e10. https://doi.org/10.1016/j.joms.2020.09.038

McLeod, N. M. H., & Saeed, N. R. (2016). Treatment of fractures of the mandibular condylar head with ultrasound-activated resorbable pins: early clinical experience. *British Journal of Oral and Maxillofacial Surgery*, *54*(8), 872–877. https://doi.org/10.1016/j.bjoms.2016.05.027

Mehboob, A., Barsoum, I., Mehboob, H., Ouldyerou, A., & Abu Al-Rub, R. K. (2025). Computational modelling and optimization of porous plates for mandibular fracture fixation accounting for bone healing. *Materials & Design*, *254*, 114060. https://doi.org/10.1016/j.matdes.2025.114060

Orassi, V., Fischer, H., Duda, G. N., Heiland, M., Checa, S., & Rendenbach, C. (2022). In Silico Biomechanical Evaluation of WE43 Magnesium Plates for Mandibular Fracture Fixation. *Frontiers in Bioengineering and Biotechnology*, *9*. https://doi.org/10.3389/fbioe.2021.803103

32nd International Conference
ENGINEERING MECHANICS 2026
Medlov, Czech Republic, May 11 – 13, 2026

FATIGUE ASSESMENT OF TURBINE BLADE BASED ON SURFACE COATING DEGRADATION AFTER EXTREME LOADING

Pavlas J. [1], **Slavík S.** [2], **Růžička M.** [3], **Mára V.** [4], **Krčil J.** [5]

Abstract: *This study investigates fatigue damage in protective coatings and fatigue crack initiation in the substrate of the nickel-based superalloy ZhS6K, widely used in helicopter turboshaft engine turbine blades, within the framework of the damage tolerance principle. Despite its widespread use in service, the relationship between surface damage and subsurface fatigue crack development in ZhS6K has not been thoroughly investigated. The effect of coating degradation on the initiation and propagation of fatigue microcracks in the substrate material is analyzed and the damage tolerance methodology is implemented. A key contribution of this work is the identification of specific operational manoeuvres that produce high mechanical loads, leading to minor surface damage while causing major fatigue damage in the substrate. The proposed approach allows for an evaluation of blade damage that does not rely on complete load history data. This new approach can be generalized to other turbine blade materials and operating conditions.*

Keywords: Fatigue assessment, Turboshaft engines, Turbine blade, Surface coating

1. Introduction

Helicopters with a turboshaft power unit are sometimes exposed to extreme operating conditions, such as military training or rescue missions, which generate higher mechanical loads than originally designed and tested. These conditions may result in visually minor coating damage while causing major fatigue cracks within the substrate material. Such loading, coupled with barely visible degradation, can lead to non-standard defects with specific failure mechanisms. Failure of a turbocompressor rotor blade during flight can cause a power unit malfunction, leading to a highly probable catastrophic scenario.

Nickel-based superalloys are widely used in turbine blades of helicopter turboshaft power units due to their exceptional high temperature strength, creep resistance, and fatigue properties. Among these materials, the cast superalloy ZhS6K has been extensively applied in critical rotor blade components. Previous studies on nickel-based superalloys have primarily focused on creep–fatigue interaction or coating oxidation resistance (Swadźba et al., 1992; Chmiela et al., 2012), with limited attention given to the role of coating fatigue damage in the initiation of fatigue cracks within the substrate. For the ZhS6K material, the relationship between localized coating degradation and the formation of subsurface fatigue microcracks has

[1] Ing. Jiří Pavlas: Faculty of Mechanical Engineering, Czech Technical University in Prague, Technická 4; 160 00, Prague; CZ, jiri.pavlas@fs.cvut.cz

[2] doc. Ing. Svatomír Slavík, CSc.: Faculty of Mechanical Engineering, Czech Technical University in Prague, Technická 4; 160 00, Prague; CZ, svatomir.slavik@cvut.cz

[3] prof. Ing. Milan Růžička, CSc.: Faculty of Mechanical Engineering, Czech Technical University in Prague, Technická 4; 160 00, Prague; CZ, milan.ruzicka@fs.cvut.cz

[4] Ing. Vladimír Mára, PhD.: Faculty of Mechanical Engineering, Czech Technical University in Prague, Technická 4; 160 00, Prague; CZ, vladimir.mara@fs.cvut.cz

[5] Ing. Jan Krčil, PhD.: Faculty of Mechanical Engineering, Czech Technical University in Prague, Technická 4; 160 00, Prague; CZ, jan.krcil@fs.cvut.cz

ISSN: 1805-8256, doi: 10.21495/em2026-101

not yet been comprehensively investigated. This knowledge gap limits the accuracy of current damage tolerance (DT) models for estimating the remaining service life of turbine blades in service. By establishing a link between surface coating condition and subsurface fatigue damage, this work proposes an additional DT procedure that enables blade operability assessment without requiring complete load history data.

Protective coatings are applied to mitigate oxidation, corrosion, and thermal degradation; however, these coatings degrade over time due to thermal, mechanical and chemical load. Coating degradation can initiate fatigue microcracks that may propagate into the substrate, potentially leading to blade failure if undetected. While fatigue microcracks may already be present in blades after general overhaul (GO), the protective coating is required to be free of integrity defects (Fig. 1). Technical documentation specifies an allowable coating thickness range. If the coating is thicker than the upper limit, it may peel off during operation. If it is thinner than the minimum allowable limit, it may burn through. As the quality of the protective coating degrades during service, extensive coating loss can leave the substrate unprotected, leading to rapid damage and potential destruction of the blade material.

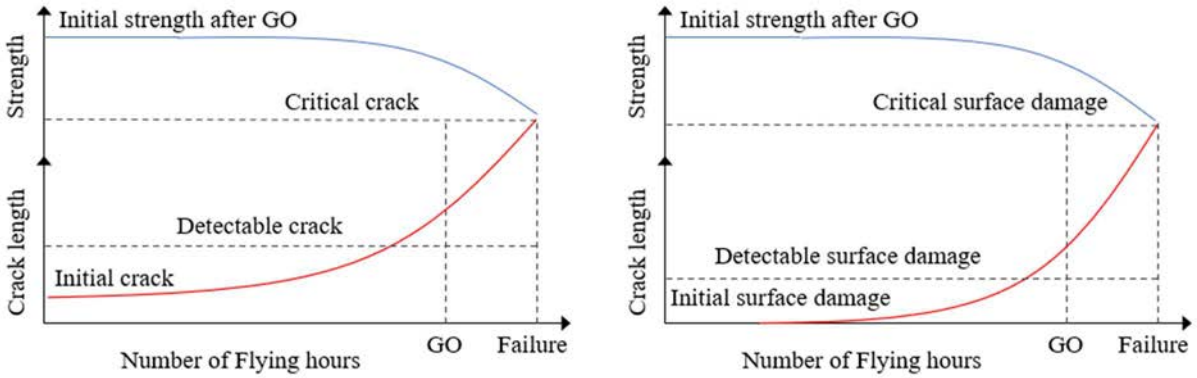

Fig. 1: Fatigue crack growth (left) and protective coating damage (right) during the service life

Several accidents have demonstrated the difficulty of identifying turbine blade damage mechanisms, highlighting the need for improved safety procedures. This article therefore proposes a DT oriented process based on image processing techniques to assess coating degradation, enabling earlier detection of critical damage and improved life management of helicopter engines.

2. Damage tolerance methodology

Damage tolerance is a key design and certification philosophy in structural engineering, ensuring that components can safely sustain a defined level of damage until inspection or repair (Howard, 1979; AFGROW). Unlike safe-life approaches, which assume defect-free structures, damage-tolerant design explicitly considers pre-existing defects such as microcracks, material inhomogeneities, or coating defects.

There are three basic types of rotor turbine blade damage during the service life. The first one is a fatigue crack. It is expected that this degradation can grow from the maximum allowable initial length a_{IN} to a length shorter than the critical crack length a_{CR} which would otherwise cause structural failure of the blade. The Time Between Overhaul (TBO) and GO procedures including visual inspection, Non-Destructive Testing (NDT) and a minimal safety limit defined by airworthiness standards (e.g. FAR or STANAG) ensure that no fatigue crack longer than a_{CR} can be operated after GO. An example of failure analysis of a turbine blade is described by Mishra (2017).

The second typical damage is high temperature corrosion. This type of damage grows from the surface to the substrate material and creates notch and material absence. From such an area a new fatigue crack can be initiated. During the GO the blades are cleaned from the old residual protective coating, then the blade is subjected to the visual check. No blade with this type of damage can be operated after GO but, in some cases, the damaged micro areas can be false negative defined. This type of degradation effect initiates the first fatigue microcracks in the substrate material leading to failure.

The third type of damage is the absence of protective coating. As in the previous type of damage, during GO the blades are cleaned from the old residual protective coating, then the blade is subjected to the visual and NDT check and then the new protective coating is applied. The proposed method suggests using a standard borescope procedure between the flights combined with automated microscopic image analysis to

define the real state of surface damage. Such service data can be obtained, and the damage assessment can be defined.

3. Experiment

This chapter describes an experimental program focused on the turbocompressor second stage rotor blade of the helicopter turboshaft engine TV3-117 (Fig. 2). The blade structure consists of two different materials. Nickel alloy ZhS6K is the substrate material of the blade covered by a protective aluminium layer. Such designed blades should withstand aerodynamic pressure, centrifugal force, high temperature and exhaust gases. The chemical composition is defined by Swadźba (1992). The operational regimes, revolution and temperatures before the turbocompressor is defined by Furda (2016). Thirteen TV3-117 turboshaft engines and their turbine blades were subjected to visual and microscopic analysis. Digital microscopy analyses were performed using an Olympus DSX1000 optical microscope. Subsequently, the surface quality of the images was analyzed using image processing techniques in MATLAB to determine the surface integrity, defined as the percentage of residual protective coating.

Fig. 2: The turbine blade after the service life

Some helicopters are used for special missions, such as rescue or training. Even when the engine is operated within its operational limits, the blades may be subjected to higher than normal loads. One example is an immediate engine shutdown after first ground contact. In this case, outside air enters the hot engine, causing the blades to cool very rapidly. Such rapid cooling generates uneven and non-standard thermal loads, leading to increased stress and deformation, especially in the trailing edge region where the material thickness is minimal. Another example of extreme loading is an autorotation manoeuvre, which can cause abnormal heat distribution, especially when transitioning from hover mode, even if the helicopter is otherwise operating within its nominal limits.

4. Observation and results

Protective coating damage is classified into three basic categories. After GO, the blade surface is smooth and free of damage. During service, the first visually detectable material loss may occur. Major damage, characterized by large areas of missing protective coating, can rapidly lead to burn-out of the substrate material (Fig. 3).

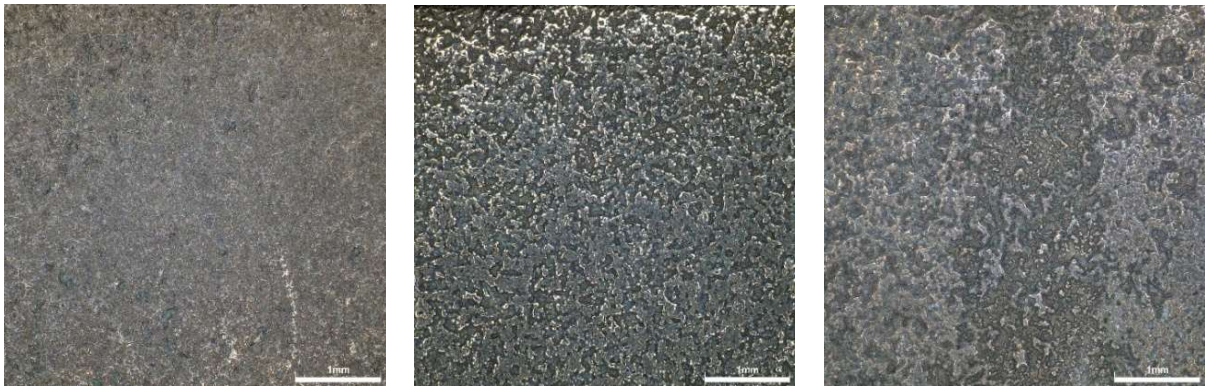

Fig. 3: The turbine blade coating damage during the service life: initial (after GO procedure including ground test: less than 1% coating damage - left), first visual detectable damage (after 520 Flight hours: 13% coating damage - middle), major damage (after 819 Flight hours: 32% coating damage - right)

The fatigue cracks initiated from protective coating damage are shown in Fig. 4. Several fatigue cracks are across the protective coating. In some areas the protective coating is damaged. Initial fatigue microcracks are also present in the substrate material.

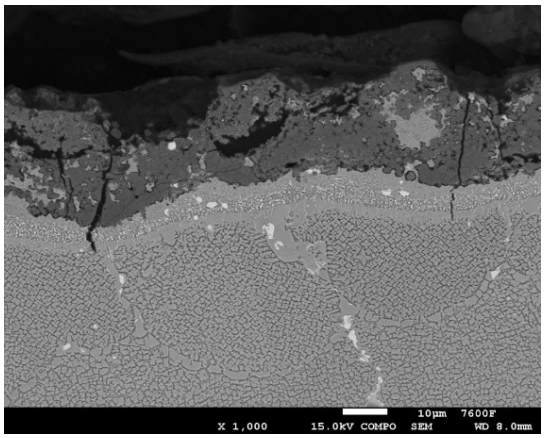

Fig. 4: The cross section of the turbine blade with first microcracks in the coating layer and substrate material (after 1132 Flight hours)

5. Discussion

Degradation of the protective coating leads to the initiation of fatigue microcracks in the substrate material of turbine blades, even when the visible surface damage appears limited. Critical regions include thin-walled areas such as the trailing edge, where non-standard operational events, including rapid engine shutdowns and autorotation manoeuvres, induce non-uniform thermal fields and elevated local stress concentrations. These conditions may result in significant subsurface fatigue degradation that remains difficult to detect using conventional inspection techniques. The proposed surface integrity–based evaluation captures the cumulative effect of such complex operational loading and enables its interpretation within a damage tolerance framework. The surface integrity parameter may thus be regarded as a surrogate damage metric linking observable surface condition with hidden fatigue risk, providing an additional decision criterion for blade operability in cases where complete operational load history is unavailable. This approach extends existing maintenance procedures by introducing a physically interpretable indicator of early fatigue damage initiation. The industrial aspects of this research will help predict potential hidden major damage and reduce the number of future helicopter accidents. The methodology is not limited to ZhS6K and may be extended to other turbine blade materials and operating regimes, contributing to improved reliability and safety of gas turbine engine components. Future steps will be focused on the numerical simulation and probabilistic approach of protective coating damage.

Acknowledgement

This publication was supported by the Czech Technical University in Prague, Faculty of Mechanical Engineering.

References

Swadźba, L., Maciejny, A. and Formanek, B. (1992) Microstructure and resistance to cracking of modified Al-Si and Al-Cr diffusion coatings on ŻS6K nickel-based superalloys, *Surface and Coatings Technology*, 54–55, Part 1, Pages 84-90

Chmiela, B., Kianicová, M., Sozańska, M., Swadźba, L. (2012) Degradation of Si-Al aluminide coating after service of turbine blades made of ZhS6K superalloy, *IOP Conference Series*: Materials Science and Engineering, 35.

Howard, A. and Engle, R. (1979) USAF Damage tolerant design handbook: Guidelines for the analysis and design of damage tolerant, Report ADA078216, *Defence Tactical Information Center, U.S. Air Force*

AFGROW: Handbook for Damage Tolerant Design: https://www.afgrow.net/applications/dtdhandbook/, *Air Force Research Laboratory*

Mishra, K., E., et al. (2017) Failure analysis of an un-cooled turbine blade in an aero gas turbine engine, *Engineering Failure Analysis*, 79, pp. 836–844.

32nd International Conference
ENGINEERING MECHANICS 2026
Medlov, Czech Republic, May 11 – 13, 2026

DESIGN OF A SENSOR-INTEGRATED ROBOTIC HEAD FOR AUTONOMOUS INDOOR NAVIGATION OF A BIPEDAL ROBOT

Pohludka J.[1], **Vechet S.**[2], **Krejsa J.**[2], **Chen K. S.**[3]

Abstract: *This article describes the design of a robotic head desingned for the autonomous indoor navigation of a bipedal walker. The head features modular mechanical interface allowing the use of various panels equipped with different sensors, displays and other devices, depending on the use-case. The system is powered by a Raspberry Pi 5 running a Python script handling the operation of the LiDAR sensor, cameras and other modules. System also runs a lightweight local YOLO model for object detection. A TCP communication is implemented to send raw sensor data, camera frames and optionally YOLO results to an external device for processing or monitoring. System provides data necessary for localization using a Particle Filter. The fusion of these sensors creates a foundation for robust SLAM algorithms.*

Keywords: Particle Filter, Walking Robot, Biped Robot

1. Introduction

Autonomous and humanoid bipedal robots operating indoors require stable and adaptive motion, but another very important factor is the reliable perception of their surroundings. Although significant progress has been made in the field of controlling bipedal walking using model-based and reinforcement methods (Grandia et al., 2024; Schulman et al., 2017), effective autonomous navigation highly depends on the robot's perception abilities for reliable obstacle recognition, localization, and planning safe trajectories.

The primary focus of previous research was to design robust locomotion and gait optimization to compensate for the inherent instability of bipedal systems (Krejsa and Vechet, 2018). However, even well-optimized locomotion controllers are insufficient for fully autonomous operation without reliable sensory feedback and environmental awareness (Vechet et al., 2020). Additionally, for humanoid robots designed to interact with humans and operate in shared spaces safely, perception and visual object recognition must be integrated with the motion control itself.

Vision sensors play a key role in perception capabilities. Cameras provide rich visual information about the environment, while LiDAR sensors offer more accurate geometric measurements and are much less dependent on ambient lighting conditions. Their combination provides a suitable solution for autonomous indoor navigation, where both factors are required. Therefore, integrating these sensors into a compact, mechanically stable, and customizable form factor is crucial for such systems.

In this paper, the design and implementation of a robotic head equipped with a LiDAR sensor, cameras, and other devices specifically developed to support the autonomous indoor movement of a bipedal humanoid robot is presented. The proposed head architecture serves as a unified sensory platform, providing the necessary data for the tasks mentioned above. The design emphasizes modularity, mechanical robustness and focuses on ease of use, implementation, and production.

This contribution builds on previous work in learning-based locomotion control Vechet et al. (2024), forming another step toward a fully autonomous bipedal walker.

[1] Ing. Jan Pohludka: Brno University of Technology, v.v.i., Technicka 2, 616 69, Brno; CZ, 216846@vutbr.cz
[2] Assoc. Prof. Stanislav Vechet, Ph.D., Assoc. Prof. Jiri Krejsa, Ph.D.: Institute of Thermomechanics AS CR, v.v.i., Technicka 2, 616 69, Brno; CZ, vechet@it.cas.cz, krejsa@it.cas.cz
[3] Prof. Kuo-Shen Chen, PhD.: National Cheng Kung University, Department of Mechanical Engineering, No.1, Ta-Hsueh Road, Tainan 701; Taiwan, kschen@ncku.edu.tw

ISSN: 1805-8256, doi: 10.21495/em2026-105

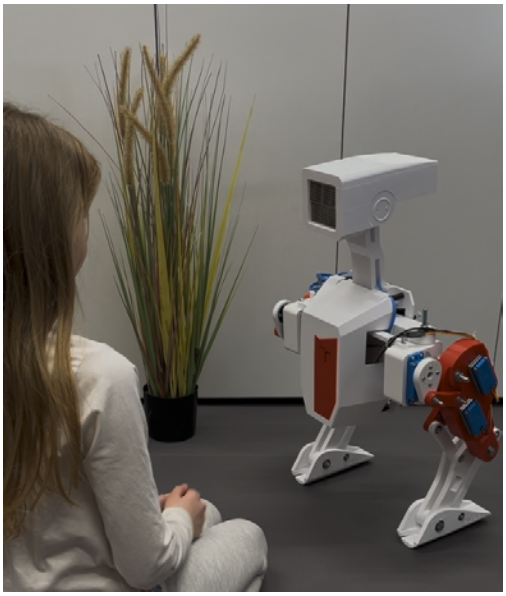

Fig. 1: Personal Autonomous Walking Optimizer (PAWO) robot in it's latest design configuration during social interaction with human operator.

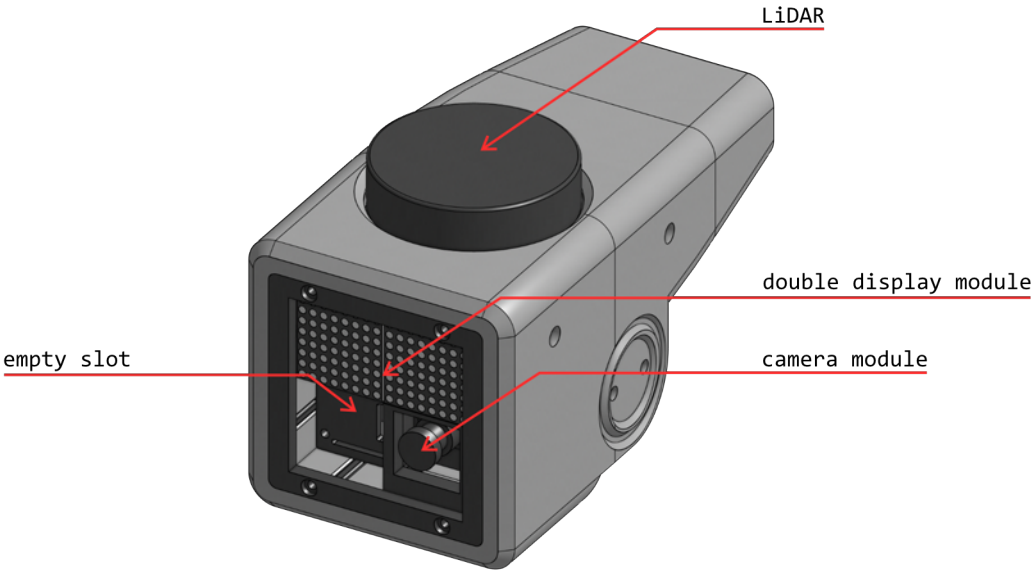

Fig. 2: CAD model of the modular robotic sensor head assembly, showing the 2x2 reconfigurable panel (currently featuring dot-matrix displays, camera and empty slot) and the top-mounted 360° LiDAR sensor.

2. Materials and Methods

The robotic head was designed as a universal sensory platform adaptable for image processing, human-robot interaction, and navigation. Serving as an extension of the original PAWO bipedal walker's head, this article describes its mechanical design, electronic/software architecture, and future localization methods.

2.1. Modular Mechanical Design

The mechanical architecture features a front modular panel that allows versatility through interchangeable components. The panel consists of four fields arranged in a 2x2 matrix, secured by a locking frame. This layout accommodates larger components or single-field modules, such as a PiCamera or matrix display (Fig. 2). By swapping panels, the head is easily reconfigured from the human-interaction mode (Fig. 1) to a spatial navigation mode.

Prioritizing accessibility, all structural parts are designed for Fused Deposition Modeling (FDM) 3D printing, ensuring easy reproduction in typical lab settings. A dedicated top mount provides the Light Detection and Ranging (LiDAR) sensor with an unobstructed 360-degree field of view. The LiDAR holder is structurally separate, allowing simple integration of different models.

2.2. Electronics and Software Architecture

The Raspberry Pi 5 was selected as the central computing unit due to its balance of computing power, low weight, cost-effectiveness, and extensive Python/OpenCV community support. This ensures compatibility with standard libraries while maintaining the low power consumption essential for independent bipedal operation.

The main Python script manages the sensor operations, storing measured data temporarily. The system supports local object detection using a lightweight You Only Look Once (YOLO) model (Redmon et al., 2016), enabling the robot to recognize humans or obstacles.

For advanced data analysis, the program can send data to external devices using the TCP protocol. The transmitted data includes full image matrices for complex vision models as well as 2D point clouds from the LiDAR sensor. The communication is bidirectional; based on the received data, an external device can send instructions back to control components, such as LED modules. This data transfer can also be used for monitoring purposes, as illustrated in Figure 3, which displays the camera output with YOLO object detection alongside the LiDAR data visualization.

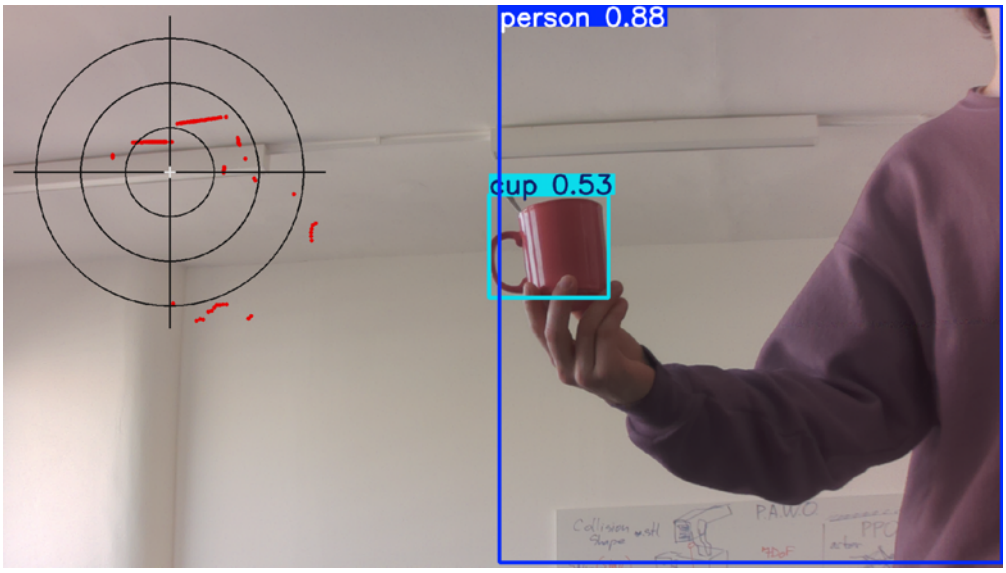

Fig. 3: Visualization of the data available for remote monitoring: 2D LiDAR point cloud (top-left) and the camera's RGB stream with object detection (YOLO) performed locally on Raspberry Pi 5.

2.3. Mathematical Framework for Localization

Spatial localization relies on LiDAR data to implement the Particle Filter algorithm. Frequently used for walking robots, it is significantly more reliable than simple odometry by reducing cumulative error. It can be extended to full mapping using Fast Simultaneous Localization and Mapping (FastSLAM) (Thrun et al., 2004).

The Particle Filter represents the position of the robot using particles defined by a state vector $x_t = [x, y, \theta]^T$. Their probability distribution is calculated iteratively:

$$p(x_t|z_{1:t}, u_{1:t}) \propto p(z_t|x_t) \int p(x_t|u_t, x_{t-1}) p(x_{t-1}|z_{1:t-1}, u_{1:t-1}) dx_{t-1} \tag{1}$$

Here, u_t describes the movement command (represented as step lengths and velocity vectors for the biped), and z_t represents the LiDAR data (formatted as a 2D array of angles and distances). By comparing real-time scans with a virtual map (Thrun et al., 2005), the particles converge on the most probable location. The autonomous control system then uses the estimated state vector x_t to plan safe trajectories and avoid obstacles in real time. SLAM allows mapping (Krejsa and Vechet, 2018) in unmapped environments.

3. Conclusions

This integrated robotic head marks a significant step toward fully autonomous operation for the PAWO bipedal walker. Its modular design supports diverse tasks, from complex human-robot interaction to obstacle avoidance.

The Raspberry Pi 5 provides sufficient performance for local YOLO object detection, sensor management, and wireless data transmission. Future work will deploy Particle Filter localization in known environments, utilizing real-time state vectors for trajectory planning, followed by SLAM for unknown areas. Fusing LiDAR geometry with camera-based recognition will yield a robust autonomous navigation system.

Acknowledgments

This study was realized with the institutional support RVO: 61388998.

References

Grandia, R., Knoop, E., Hopkins, M., Wiedebach, G., Bishop, J., Pickles, S., Müller, D., and Bächer, M. (2024) Design and control of a bipedal robotic character. In *Robotics: Science and Systems XX*.

Krejsa, J. and Vechet, S. (2018) Fusion of local and global sensory information in mobile robot outdoor localization task. In *Proceedings of the 2018 18th International Conference on Mechatronics - Mechatronika (ME)*.

Redmon, J., Divvala, S., Girshick, R., and Farhadi, A. (2016) You only look once: Unified, real-time object detection. In *Proceedings of the IEEE Conference on Computer Vision and Pattern Recognition (CVPR)*.

Schulman, J., Wolski, F., Dhariwal, P., Radford, A., and Klimov, O. (2017) Proximal policy optimization algorithms. *arXiv preprint arXiv:1707.06347*.

Thrun, S., Burgard, W., and Fox, D. (2005) *Probabilistic robotics*. MIT Press.

Thrun, S., Montemerlo, M., Koller, D., Wegbreit, B., Nieto, J., and Nebot, E. (2004) FastSLAM: An efficient solution to the simultaneous localization and mapping problem with unknown data association. *Journal of Machine Learning Research*, 4, 3.

Vechet, S., J., K., and Chen, K. (2024) Vertical stabilization of bipedal walking drone PAVO with proximal policy optimization. In *2024 21st International Conference on Mechatronics - Mechatronika (ME)*.

Vechet, S., Krejsa, J., and Chen, K.-S. (2020) Agvs mission control support in smart factories by decision networks. In *2020 19th International Conference on Mechatronics - Mechatronika (ME)*.

32nd International Conference
ENGINEERING MECHANICS 2026
Medlov, Czech Republic, May 11 – 13, 2026

COMPUTATIONAL AND EXPERIMENTAL SUPPORT FOR THE DEVELOPMENT OF MOBILE HYDROGEN REFUELING STATION

Polach P.[1], Bělohoubek M.[2], Václavík J.[3]

Abstract: *This paper falls within the field of applied research and focuses on emerging hydrogen technologies, particularly the use of hydrogen as a vehicle fuel in the transportation sector. The deployment of hydrogen-powered vehicles requires a network of refueling infrastructure; however, stationary hydrogen refueling stations are currently economically feasible only at selected locations. To complement this limitation, a mobile hydrogen refueling station was developed, offering relatively low initial investment costs together with flexible hydrogen delivery and dispensing capabilities. The paper outlines the main parameters of the mobile station prototype and presents the computational tools developed to determine optimal filling parameters. The final part of the paper deals with the experimental verification of the structural loading of the trailer carrying the station and with the evaluation of the driving performance of the complete vehicle–trailer combination.*

Keywords: Hydrogen, Mobile refueling station, Prototype design, CFD, Stress measurement

1. Introduction

In line with the strategy for decarbonizing the transport sector, which includes the use of hydrogen as a fuel, it is essential to ensure a sufficient number of refueling locations for vehicles using hydrogen technologies. For this reason, a prototype mobile hydrogen refueling station (see Fig. 1) was developed (Polach et al., 2025), intended to complement stationary refueling stations by providing the same service in locations that are not currently, or will not soon be, covered by the stationary network.

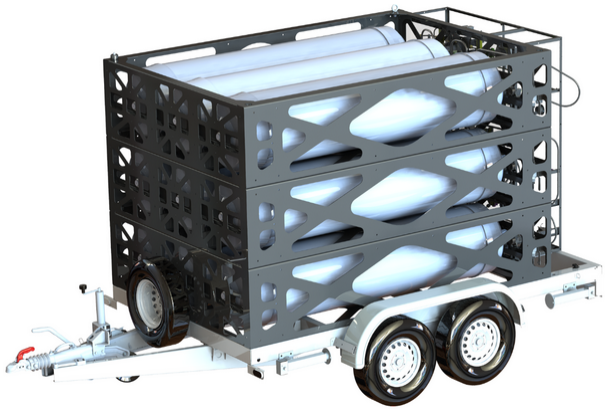

Fig. 1: Trailer with the mobile refueling station (reproduced from DEVINN, 2026).

[1] Assoc. Prof. Dr. Ing. Pavel Polach: Research and Testing Institute Plzen, Research Centre Řež, Tylova 1581/46; 301 00, Plzeň; CZ, pavel.polach@vzuplzen.cz

[2] Ing. Marek Bělohoubek: Research and Testing Institute Plzen, Research Centre Řež, Tylova 1581/46; 301 00, Plzeň; CZ, marek.belohoubek@vzuplzen.cz

[3] Ing. Jaroslav Václavík: Research and Testing Institute Plzen, Research Centre Řež, Tylova 1581/46; 301 00, Plzeň; CZ, jaroslav.vaclavik@vzuplzen.cz

ISSN: 1805-8256, doi: 10.21495/em2026-109

A representative overview of the current state of knowledge regarding hydrogen use in transportation, including hydrogen refueling stations, is presented by Genovese and Fragiacomo (2023), which reviews the latest literature on hydrogen stations, describes the global technological status, and highlights research on key components and processes, and by Genovese et al. (2023), which examines the major phenomena occurring during hydrogen refueling through analysis of relevant theory and existing modeling approaches. Pereira et al. (2024) review hydrogen's application as a fuel, summarizing the main systems involved in hydrogen refueling stations, from production to the final refueling stage. Klymovskyi et al. (2023) report that approximately 78,000 hydrogen-powered vehicles were in operation globally, supported by 1,100 publicly accessible hydrogen refueling stations. In the Czech context, Bošković et al. (2025) address the challenge of locating hydrogen refueling stations from the driver's perspective, focusing on the Pardubice region.

During the development of the mobile hydrogen refueling station presented here, it was necessary, in addition to the design work (DEVINN, 2026), to determine optimal operating parameters for refueling with non-cooled hydrogen at ambient temperatures (Polach et al., 2025), and to assess the stress levels in the load-bearing modules of the hydrogen tanks, the trailer structure carrying the station, and to analyze axle displacements and trailer accelerations (Václavík, 2023).

2. Mobile hydrogen refueling station

The developed mobile hydrogen refueling station is a system designed for the easy transport of compressed hydrogen and subsequent refueling of hydrogen-powered vehicles or other compatible devices. It enables refueling of passenger cars at a hydrogen operating pressure of 700 bar, buses (and trucks) at 350 bar, and material-handling equipment at 350 bar. The system is designed for outdoor operation.

The mobile station (Fig. 1) consists of a compressed hydrogen storage unit made up of three bundles of high-pressure cylinders with a cascaded distribution system and a unique control system for maximizing hydrogen utilization, a trailer, and a dispensing unit. The high-pressure mobile storage comprises a bundle of nine cylinders rated up to 500 bar, capable of storing nearly 100 kg of hydrogen. The bundle is mounted in a frame that ensures both the safety and proper function of the cylinders. The entire system is installed on an AGADOS cargo trailer and is designed to meet the requirements for towing behind a passenger vehicle in the up-to-3.5 t category. The station does not include a hydrogen compressor; hydrogen transfer relies solely on pressure differences between the station and the receiving device. The system can also operate at locations without connection to the electrical grid.

3. Computational support for determining optimal refueling parameters

The hydrogen refueling process, particularly for automotive storage tanks, has several specific features. Because of its very low molecular mass, hydrogen is an extremely light gas, and transferring a significant mass into a storage vessel requires very high pressures, typically on the order of tens of MPa. Both the storage tanks and the refueling infrastructure consist of one or more thick-walled pressure vessels, between which the gas is transferred either actively (e.g., by means of a compressor) or passively through pressure equalization. During refueling, rapid variations in pressure and temperature occur both within the refueling system and inside the receiving tank. These transient thermodynamic effects may result in excessive heating of the hydrogen within the tank, which can compromise the prescribed limits for safe operation of the filled system.

Existing standards could not be used for the design of the filling control system, in terms of setting the control elements of the filling cascade—such as filling rates and the timing of individual cylinders. The current version of SAE J2601 (SAE, 2020) covers only cases of filling with pre-cooled hydrogen at temperatures between –10 °C and –40 °C. For this reason, a mathematical-computational model was developed and implemented in custom software within the MATLAB environment. This model allows simulation of vehicle tank filling while considering a wide range of input parameter variations, including different tank volumes and types, ambient and tank temperatures, and varying initial pressures in the tank or the filling station cascade (Polach et al., 2025). The model is based on the conservation of mass and energy and evaluates the balance of physical quantities across four primary subsystems: the refueling station, the station supply line, the vehicle supply line, and the vehicle storage tank. The refueling station is represented as a set of independent pressure-vessel banks that can be selectively connected or switched

during the refueling process. Depending on the vehicle configuration, the storage system is modelled either as a single pressure vessel or as multiple vessels being filled simultaneously. The developed software enables the evaluation of heat exchange with the surroundings across all considered subsystems. The basic scheme of the modelled thermal balance of the hydrogen refueling process is shown in Fig. 2.

Using the simulation results, control algorithms were designed to ensure the safe filling of all tanks for which the mobile filling station is intended.

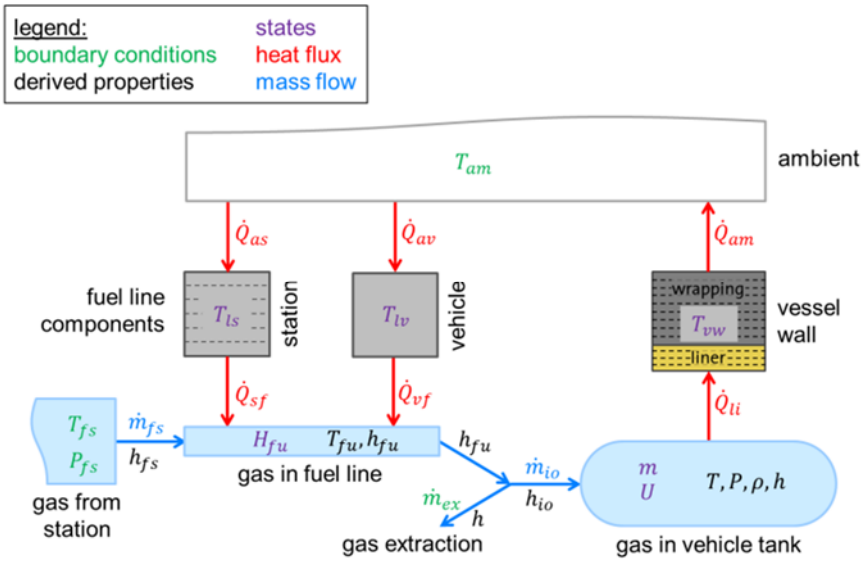

Fig. 2: Basic diagram of the modeled thermal balance of the hydrogen refueling process (T = temperature, P = pressure, H = enthalpy, h = specific enthalpy, ρ = density, $\dot{Q}$ = heat flux, m = mass, $\dot{m}$ = mass flow, U = internal energy; and subscripts according to the SAE J2601 standard: am = ambient, as = ambient-station, av = ambient-vehicle, ex = extraction, fs = fuel station, fu = fuel unit, li = liner, ls = line station, lv = line vehicle, io = inlet-outlet, sf = station-fuel unit, vf = vehicle-fuel unit, vw = vessel wall) (reproduced from Polach et al., 2025)

4. Experimental measurement of driving performance and structural loading of a trailer

The experimental measurements primarily focused on evaluating stress levels in the load-bearing modules of the hydrogen tanks and in the trailer frame, as well as on analyzing axle displacements and trailer accelerations (Václavík, 2023). Test runs were conducted with the trailer coupled to a passenger van, an Opel Combo (Fig. 3). As noted above, the objective of these tests was to verify both the structural integrity of the trailer and the driving behavior of the complete vehicle–trailer combination. For structural integrity assessment, the trailer repeatedly passed over an artificial vertical bump with a height of 58 mm during three separate test runs at speeds of 28 km·h^{-1}, 33 km·h^{-1}, and 38 km·h^{-1}. To evaluate driving behavior, a test drive was carried out on roads in the village of Spojil, including sections with pronounced road irregularities, curves, turning maneuvers, and reversing maneuvers.

Structural loading of the trailer was evaluated by measuring strain in one direction using resistive strain gauges (with a grid length of 6 mm). The strain gauges were installed primarily on the lower load-bearing module, where the highest stress levels were expected. Stress in the trailer frame was also monitored at the most critical welded joints, and their permanent strength relative to the material yield strength was evaluated based on repeated passes over the artificial vertical bump. The behavior of the entire vehicle–trailer combination was assessed by measuring axle displacements using two Panasonic laser triangulation sensors with a measurement range of ±80 mm, together with trailer accelerations in three axes and vertical acceleration at the trailer drawbar measured by four ICP accelerometers with a sensitivity of 100 mV/g.

For evaluation of the trailer frame with respect to permanent strength, a limit corresponding to 0.7 % of the material yield strength was applied, representing approximately 200 MPa. Test data were obtained from runs over the artificial vertical bump, and this limit was not exceeded at any strain gauge location. For the assessment of high-cycle fatigue strength, a stress amplitude of 60 MPa corresponding to the fatigue limit was used. This evaluation was performed using data obtained from the sample route through the village.

On the main load-bearing frame, stress amplitudes reached approximately one half of this value, whereas on the trailer subframe the amplitudes were comparable to the fatigue limit.

Based on the evaluation of all measured quantities, it was concluded that the trailer satisfies the requirements for safe operation with respect to both structural loading and the driving behavior of the vehicle–trailer combination.

Fig. 3: Trailer attached to an Opel Combo and passing over an artificial vertical bump.

5. Conclusions

The paper reports the prototype specifications, presents the computational tools for optimizing filling parameters, and describes the experimental evaluation of the trailer's structural performance and the overall driving behavior of the combination. The development of computational support for filling is currently ongoing for other design variants of hydrogen refueling stations.

Acknowledgement

This work was supported by institutional funding for the long-term conceptual development of the research organization provided by the Ministry of Industry and Trade of the Czech Republic and by the project CZ.01.01.01/08/25_079/0008531 "Mobile Hydrogen Refueling Station and Its Market Introduction" funded under the Operational Programme Technologies and Applications for Competitiveness (OP TAC).

References

Bošković, S., Švadlenka, L., Dobrodolac, M., Jovčić, S., Chatterjee, P. and Bauer, L. (2025) Hydrogen Refueling Station Selection Using the AROMAN Method: A Case Study in the Pardubice Region. *Transport Research Procedia*, 91, pp. 99-106.

DEVINN (2026) *H2PORT: mobile hydrogen filling station*. DEVINN s.r.o. [online]. [cit. 2026-02-06]. Available on: https://en.devinn.cz/products/h2port.

Genovese, M., Cigolotti, V., Jannelli, E. and Fragiacomo, P. (2023) Hydrogen Refueling Process: Theory, Modeling, and In-Force Applications. *Energies 2023*, 16, 6, paper 2890.

Genovese, M. and Fragiacomo, P. (2023) Hydrogen refueling station: Overview of the technological status and research enhancement. *Journal of Energy Storage*, 61, paper 106758.

Klymovskyi, A., Kabza, A., Schlumberger, G., Jörissen, L. and Jenne, M. (2025) Applications – Transportation Applications | Hydrogen Refueling Stations. *Encyclopedia of Electrochemical Power Sources (Second Edition)*, 7, pp. 391-400.

Pereira, R., Monteiro, V., Alfonso, J. L. and Teixeira, J. (2024) Hydrogen Refueling Stations: A Review of Technology Involved from Key Energy Consumptions Process to Related Energy Management Strategies. *Energies 2024*, 17, 19, paper 4906.

Polach, P., Bělohoubek, M. and Lazar, J. (2025) Mobile Hydrogen Refueling Station and Calculation Support for Determining Optimal Refueling Parameters, in Fischer, C. and Náprstek, J., eds., *Proc. 31st International Conference Engineering Mechanics 2025*, Institute of Theoretical and Applied Mechanics of the Czech Academy of Sciences, Medlov, pp. 161-164.

SAE (2020) *SAE J2601, Fueling Protocols for Light Duty Gaseous Hydrogen Surface Vehicles*. SAE International, Standard.

Václavík, J. (2023) *Stress Analysis and Driving Performance Evaluation of a Mobile Hydrogen Refueling Station*. Research report VZU-VZ-54/23/010, Research and Testing Institute Plzen, Plzen (in Czech).

32nd International Conference
ENGINEERING MECHANICS 2026
Medlov, Czech Republic, May 11 – 13, 2026

MODELLING MASS TRANSFER DURING CRYOPRESERVATION IN A BIOLOGICAL SAMPLE TREATED AS A HOMOGENEOUS AND POROUS MATERIAL WITH UNCERTAIN PARAMETERS

Skorupa A.[1], Piasecka-Belkhayat A.[2]

Abstract: *Biological tissues are often modelled as homogeneous materials, but their structure can also be treated as a porous medium. In addition, models of biological processes contain uncertain quantities that are introduced as deterministic numbers. The article presents a numerical simulation of the cryopreservation process of articular cartilage, using homogeneous and porous material models (Analyses 1 and 2). Analysis 1 considers the uncertainty of thermophysical parameters by introducing interval set theory. The mathematical model includes a description of coupled heat and mass transfer phenomena, and the diffusion coefficient is estimated using the Einstein-Stokes equation in Analysis 1 and using a relationship that accounts for the porous structure of the sample in Analysis 2. Finally, the simulation results are compared with the experimental data for validation. The maximum relative error equals 15.82% for Analysis 1 and 24.96% for Analysis 2.*

Keywords: Diffusion coefficient, Porous material, Interval numbers, Mass transfer, Heat transfer

1. Introduction

Porous media are materials in which the matrix contains fluid-filled pores. Biological tissues can also be considered porous materials because they consist of dispersed cells between which nutrients are transported, for example (Khaled & Vafai, 2003).

Several transport phenomena occur in biological materials. Heat transfer is induced by heat conduction as well as blood perfusion (blood convection). Thermal phenomena can be described, for example, using Fourier's equation. On the other hand, mass transfer is driven by diffusion and is associated with the transport of nutrients, drugs, and cryoprotectants (CPAs) during cryopreservation (Khaled & Vafai, 2003).

Additionally, modelling biological processes involves an inherent degree of uncertainty. This is because the parameters of biological materials are determined experimentally and depend on their individual characteristics. Uncertain variables in the model can be analysed using probabilistic or non-probabilistic approaches. The latter approach uses the fuzzy numbers and interval numbers. In fuzzy set theory, each element of the set is described by a membership function. Meanwhile, interval numbers are defined by lower and upper bounds, which determine the membership of a given element in the set (Wang & Matthies, 2021).

The article presents a mathematical and numerical model of a cylindrical sample of cryopreserved articular cartilage. As experimental studies indicate, this biological tissue contains pores with sizes ranging from 2 nm to 6 nm or from 11 nm to 14 nm, depending on the testing method (Skorupa & Piasecka-Belkhayat, 2025). Therefore, the study compares the temperature and CPA concentration

[1] Anna Skorupa, PhD.: Department of Computational Mechanics and Engineering, Silesian University of Technology, Konarskiego 18A, 44-100 Gliwice, PL, anna.skorupa@polsl.pl

[2] SUT Prof. Alicja Piasecka-Belkhayat, DSc.: Department of Computational Mechanics and Engineering, Silesian University of Technology, Konarskiego 18A, 44-100 Gliwice, PL, alicja.piasecka-belkhayat@polsl.pl

ISSN: 1805-8256, doi: 10.21495/em2026-113

distributions in a two-dimensional computational domain by modelling the tissue as a homogeneous material (Analysis 1) and as a porous medium (Analysis 2). Additionally, in the homogeneous material model, thermophysical parameters are introduced as interval numbers.

2. Methodology

The cryopreservation process can be performed using conventional methods such as slow freezing and vitrification. The article presents an alternative method named the liquidus-tracking (LT) protocol, in which the temperature of the bath solution and the concentration of the cryoprotectant are appropriately regulated. In this study, the CPA is assumed to be a solution of dimethyl sulfoxide (DMSO) and water (Pegg et al., 2006; Yu et al., 2019). Cryoprotectants such as DMSO differ from standard diffusing species due to their temperature-dependent viscosity, which affects the transport process. In the present model, this effect is partially taken into account through the temperature-dependent diffusion coefficient.

2.1. Mathematical model

To determine the distribution of the CPA in the computational domain as interval numbers, the following relation is used (Skorupa & Piasecka-Belkhayat, 2025; Yu et al., 2019):

$$\frac{\partial \bar{c}_d(r,z,t)}{\partial t} = \nabla\left(\overline{D}_{eff}\nabla\bar{c}_d(r,z,t)\right), \tag{1}$$

where $\bar{c}_d$ [%(w/w) or mol m^{-3}] is the interval DMSO concentration in the sample, $\overline{D}_{eff}$ [m^2 s^{-1}] is the interval effective diffusion coefficient, and t, r, and z are the time and the spatial coordinates, respectively. The value of the interval effective diffusion coefficient is estimated using three relationships depending on whether the sample is treated as a homogeneous or porous material.

In Analysis 1, where the articular cartilage is homogeneous material, the Einstein-Stokes equation is applied (Skorupa & Piasecka-Belkhayat, 2025):

$$\overline{D}_{eff} = \frac{k_B\overline{T}(r,z,t)}{6\pi r_s\mu_d}, \tag{2}$$

where k_B [J K^{-1}] is the Boltzmann constant ($k_B = 1.38\times10^{-23}$ J K^{-1}), $\overline{T}$ [K] is the temperature, r_s [m] is the radius of the spherical particle, and μ_d [Pa s] is the dynamic viscosity of DMSO.

Considering the sample as a porous medium (Analysis 2), the effective diffusion coefficient is calculated as a deterministic value using the following relationship (Skorupa & Piasecka-Belkhayat, 2025; Yu et al., 2019):

$$\overline{D}_{eff} = D_{dw}\frac{\varepsilon}{\tau^2}, \tag{3}$$

where D_{dw} [m^2 s^{-1}] is the diffusion coefficient of DMSO in water, ε is the water content in the sample, and τ is the tortuosity factor. A detailed description of the diffusion coefficient calculation in water and other required variables is provided in the literature (Skorupa & Piasecka-Belkhayat, 2025; Yu et al., 2019).

The interval temperature distribution is defined by the Fourier equation (Skorupa & Piasecka-Belkhayat, 2025; Yu et al., 2019):

$$\bar{c}_p\bar{\rho}\frac{\partial\overline{T}(r,z,t)}{\partial t} = \nabla\left(\bar{k}\nabla\overline{T}\right), \tag{4}$$

where $\bar{c}_p$ [J kg^{-1} K^{-1}] is the interval specific heat capacity, $\bar{\rho}$ [kg m^{-3}] is the interval density, and $\bar{k}$ [W m^{-1} K^{-1}] is the interval thermal conductivity.

The mathematical model includes the following initial condition:

$$t = 0:\ \ \overline{T}(r,z,t) = T_{init}\ \ and\ \ \bar{c}_d(r,z,t) = c_{init}, \tag{5}$$

and boundary conditions:

$$\begin{cases} r = R \text{ and } z = 0: & -\mathbf{n}\bar{k}\cdot\nabla\overline{T} = \alpha[\overline{T}(r,z,t) - T_{bath}] \text{ and } -\mathbf{n}\overline{D}_{eff}\cdot\nabla\bar{c}_d = 0.9c_{bath}, \\ r = 0 \text{ and } z = \dfrac{H}{2}: & -\mathbf{n}\bar{k}\cdot\nabla\overline{T} = 0 \text{ and } -\mathbf{n}\overline{D}_{eff}\cdot\nabla\bar{c}_d = 0, \end{cases} \tag{6}$$

where α is the natural convection heat transfer coefficient, and **n** is the normal vector, T_{bath} and c_{bath} are the temperature and the DMSO concentration of the bath solution, respectively, R and H are the sample dimensions. The axisymmetric cylindrical geometry was selected to simplify the problem and to enable comparison with available experimental data.

2.2. Numerical model

The finite difference method (FDM) is used to perform numerical simulations. A fixed time grid is assumed ($t^0 < t^1 < \cdots < t^{f-1} < t^f < t^{f+1} < \cdots < t^\infty$, where $\Delta t = t^f - t^{f-1}$ is the constant time step) and the geometric mesh is prepared applying the five-point stencil (Skorupa, 2023).

The interval distribution of CPA in the sample for central nodes is estimated using FDM by:

$$(\bar{c}_d)_{i,j}^f = (\bar{c}_d)_{i,j}^{f-1} - \Delta t \sum_{a=1}^4 \frac{\Phi_e}{\bar{W}_e}\left((\bar{c}_d)_e^{f-1} - (\bar{c}_d)_{i,j}^{f-1}\right), \tag{7}$$

where $i = 2, 3, \ldots, n-1$, $j = 2, 3, \ldots, m-1$, with n and m denoting the number of nodes in the z- and r-directions, respectively. The index a corresponds to the set of neighbouring nodes $e = \{(i, j+1); (i, j-1); (i+1, j); (i-1, j)\}$, Φ_e [m^{-1}] is the shape function, and $\bar{W}_e$ [s m^{-1}] is the interval mass resistance. The shape function and the interval mass resistance can be expressed as:

$$\Phi_{i,j-1} = \frac{r_{i,j}-0.5h_1}{r_{i,j}h_1}, \quad \Phi_{i,j+1} = \frac{r_{i,j}+0.5h_1}{r_{i,j}h_1}, \quad \Phi_{i-1,j} = \Phi_{i+1,j} = \frac{1}{h_2}, \tag{8}$$

$$\bar{W}_{i,j-1} = \bar{W}_{i,j+1} = \frac{h_1}{\bar{D}_{eff}}, \quad \bar{W}_{i-1,j} = \bar{W}_{i+1,j} = \frac{h_2}{\bar{D}_{eff}} \tag{9}$$

where $r_{i,j}$ [m] is the radial coordinate of the node (i, j), h_1 [m] and h_2 [m] denote the mesh steps in the r- and z-directions, respectively.

The interval temperature distribution in the computational domain for central nodes is given by:

$$\bar{T}_{i,j}^f = \bar{T}_{i,j}^{f-1} - \frac{\Delta t}{\bar{c}_p\bar{\rho}} \sum_{a=1}^4 \frac{\Phi_e}{\bar{R}_e}\left(\bar{T}_e^{f-1} - \bar{T}_{i,j}^{f-1}\right), \tag{10}$$

where $\bar{R}_e$ [m^4 K W^{-1}] represents the thermal resistance given by:

$$\bar{R}_{i,j-1} = \bar{R}_{i,j+1} = \frac{h_1}{\bar{k}}, \quad \bar{R}_{i-1,j} = \bar{R}_{i+1,j} = \frac{h_2}{\bar{k}}. \tag{11}$$

Details about the derivation for boundary nodes and the rules for mathematical operations on interval numbers can be found in the literature (Skorupa, 2023). The adopted time step and mesh resolution were selected based on preliminary numerical tests, ensuring stable and consistent results.

3. Results of computation

The study modelled the cryopreservation process based on the LT protocol proposed by Pegg et al., which consisted of eight steps in the cooling phase, during which the following values were adopted: $T_{bath} \in \{22; 22; -5; -8.5; -16; -23; -35; -48.5\}$ ºC, $c_{bath} \in \{10; 20; 29; 38; 47; 56; 63; 72\}$ %(w/w) and each step lasts: $t_{bath} \in \{10; 10; 30; 30; 30; 30; 30; 30\}$ s (Pegg et al., 2006). The simulation assumed the initial condition T_{init} = 22 °C, c_{init} = 0%(w/w), the natural convection heat transfer coefficient α = 525 W·m^{-2}·K^{-1} and the dimensions of the computational domain are R = 3 mm and H = 1 mm. The following parameter values are applied: the specific heat capacity c_p = 3567.5 J kg^{-1} K^{-1}, the density ρ = 1100 kg m^{-3}, the thermal conductivity k = 0.518 W m^{-1} K^{-1}, the dynamic viscosity of DMSO $\mu_d = 1.996\times10^{-3}$ Pa s, the radius of the spherical particle $r_s = 2.541\times10^{-10}$ m, the water content in the sample ε = 0.78, the tortuosity τ = 1.4. The step of the time grid equals Δt = 0.005 s, the mesh steps are h_1 = 0.1 mm and h_2 = 0.05 mm. In Analysis 1, thermophysical parameters were introduced as interval numbers, where $\bar{c}_p = [c_p - 0.05c_p, c_p + 0.05c_p]$, $\bar{\rho} = [\rho - 0.05\rho, \rho + 0.05\rho]$, $\bar{k} = [k - 0.05k, k + 0.05k]$.

Fig. 1 shows (a) a graph of the DMSO concentration in the sample as a function of time and (b) a graph of the first 10 seconds of step 2 of the LT protocol, which confirms that the values obtained are in the form of intervals. The diagrams represent the results for the point r = 0.050 mm, z = 0.475 mm. The plot also contains the concentration of the bath solution (black dotted line) and the experimental results (green points). One can see that the simulation results differ from the experimental values, mainly in the last

steps of the protocol. Based on the experimental results (Pegg et al., 2006), the relative error was calculated, which for Analysis 1 varied between 1.38% and 15.82%, while for Analysis 2 it ranged from 10.05% to 24.96%.

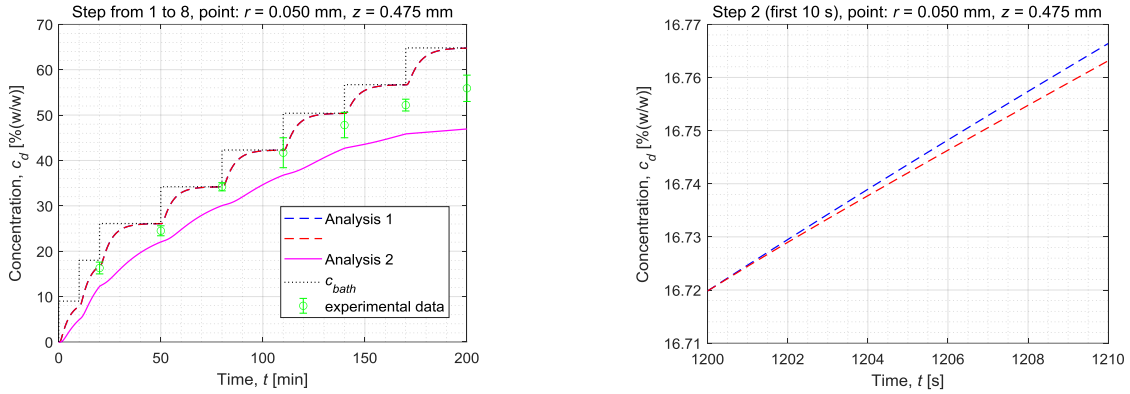

(a) (b)

Fig. 1: Concentration of DMSO as a function of time: (a) the entire simulation time and (b) the first 10 s of the second step of the protocol.

4. Conclusions

The aim of the article was to perform a numerical simulation of cryopreservation in a cylindrical sample of articular cartilage modelled as a homogeneous material (Analysis 1) and a porous material (Analysis 2). The obtained DMSO concentration values were validated with the experimental results. On this basis, the results from Analysis 1 are closer to the experimental data. The higher relative error observed in Analysis 2 may result from several factors, for example, by the sensitivity of the model to tissue parameters, such as porosity, tortuosity, and pore size distribution. These parameters may vary significantly between biological specimens and are difficult to determine accurately. It should also be noted that the thermophysical parameters used in the numerical simulations were not measured directly on the experimentally tested sample. In summary, interval set theory works well for describing uncertain parameters occurring in the model. The novelty of the study lies in the application of interval arithmetic to the modelling of coupled heat and mass transfer and in the comparison between homogeneous and porous material models.

Acknowledgement

Publication is funded by the Excellence Initiative – Research University programme realized at the Silesian University of Technology, in 2024-2026 (grant no. 10/040/SDU/10-22-03). The research is also partially funded from financial resources from the statutory subsidy of the Faculty of Mechanical Engineering, Silesian University of Technology.

References

Khaled, A.-R. A., & Vafai, K. (2003). The role of porous media in modeling flow and heat transfer in biological tissues. *International Journal of Heat and Mass Transfer*, *46*(26), 4989-5003. https://doi.org/10.1016/S0017-9310(03)00301-6

Pegg, D. E., Wang, L., & Vaughan, D. (2006). Cryopreservation of articular cartilage. Part 3: The liquidus-tracking method. *Cryobiology*, *52*(3), 360-368. https://doi.org/10.1016/j.cryobiol.2006.01.004

Skorupa, A. (2023). *Multi-scale modelling of heat and mass transfer in tissues and cells during cryopreservation including interval methods* [Doctoral thesis, Politechnika Śląska].

Skorupa, A., & Piasecka-Belkhayat, A. (2025). Analysis of Cryoprotectant Concentration During Cryopreservation in Articular Cartilage Sample Using Homogeneous and Porous Material Models. *Annals of Biomedical Engineering*. https://doi.org/10.1007/s10439-025-03925-6

Wang, C., & Matthies, H. G. (2021). Coupled fuzzy-interval model and method for structural response analysis with non-probabilistic hybrid uncertainties. *Fuzzy Sets and Systems, Fuzzy Intervals and Their Applications*, *417*, 171–189. https://doi.org/10.1016/j.fss.2020.06.002

Yu, X., Zhang, S., & Chen, G. (2019). Modeling the addition/removal of dimethyl sulfoxide into/from articular cartilage treated with the liquidus-tracking method. *International Journal of Heat and Mass Transfer*, *141*, 719–730. https://doi.org/10.1016/j.ijheatmasstransfer.2019.07.032

32nd International Conference
ENGINEERING MECHANICS 2026
Medlov, Czech Republic, May 11 – 13, 2026

ENTROPY GENERATION ANALYSIS FOR PRANDTL POWER LAW VELOCITY PROFILES IN CIRCULAR PIPES

Smyk E.[1]

Abstract: *The purpose of this study is to verify whether calculating total entropy generation can serve as a method for evaluating flow quality when the velocity profile is determined using theoretical formulas, such as Prandtl's power law. Current methods for assessing flow straighteners rely mainly on qualitative analysis of the velocity profile shape, which impedes objective comparisons. The investigation involved calculations for a pipe with a diameter of 100 mm at a Reynolds number of 10,000, analysing power-law exponents n ranging from 5 to 12 as well as laminar flow. The results indicate that specific generated entropy increases with the exponent n, implying that a more turbulent profile generates higher entropy. Although the total entropy for n=5 was found to be lower than for laminar flow, literature suggests such low exponents are practically impossible in real-world scenarios. This confirms that the assumption of using generated entropy to evaluate flow conditioning is valid for practical applications.*

Keywords: Velocity profile, Inner flow, Channels, Flow conditioning

1. Introduction

Stream straighteners are used for flow conditioning in many applications, such as wind tunnels, biomedical engineering, and flow rate measurements. While the use of these devices is widespread, there are still no good methods for comparing their performance.

Jurga et al. (2024) investigated the impact of flow straighteners on the flow behind 90° pipe bend. Evaluation of the impact of the straightener was based mainly on the velocity profile analysis. However, the swirl intensity and nondimensional pressure coefficient were also taken into account. Smyk et al. (2025) analyzed velocity and turbulence intensity profile, kinetic energy correction factor, and pressure drop on the straightener. The investigation was conducted for a straight duct with a fan as a disturbance generator. Analysis of other articles shows that researchers often rely on analysis of the shape of the speed profile (Spearman et al., 1996, Kühnen et al., 2018, 2019), which does not allow for clear comparisons of the performance of straighteners. This data is often more qualitative than quantitative and relates to a specific case.

It seems that a good way to evaluate the flow objectively and therefore the operation of the straightener is to measure the generated entropy (related to the dissipation of energy through viscous friction), which can be defined by the formula (Kock and Herwig, 2004):

$$\begin{aligned}\dot{S}_{gen} = \frac{\Phi}{T} = \frac{\mu}{T}\left[2\left\{\left(\frac{\partial \bar{u}}{\partial x}\right)^2 + \left(\frac{\partial \bar{v}}{\partial y}\right)^2 + \left(\frac{\partial \bar{w}}{\partial z}\right)^2\right\}\right. \\ \left. + \left(\frac{\partial \bar{u}}{\partial y} + \frac{\partial \bar{v}}{\partial x}\right)^2 + \left(\frac{\partial \bar{u}}{\partial y} + \frac{\partial \bar{w}}{\partial x}\right)^2 + \left(\frac{\partial \bar{v}}{\partial y} + \frac{\partial \bar{w}}{\partial x}\right)^2\right] \\ + \frac{\mu}{T}\left[2\left\{\overline{\left(\frac{\partial u`}{\partial x}\right)^2} + \overline{\left(\frac{\partial v`}{\partial y}\right)^2} + \overline{\left(\frac{\partial w`}{\partial z}\right)^2}\right\}\right.\end{aligned} \tag{1}$$

[1] Emil Smyk, PhD.: Department of Mechanics and Computer Methods, Bydgoszcz University of Science and Technology, Al. Prof. S. Kaliskiego 7, 85-796 Bydgoszcz, Poland, PL, emil.smyk@pbs.edu.pl

ISSN: 1805-8256, doi: 10.21495/em2026-117

$$+\left(\frac{\partial u`}{\partial y}+\frac{\partial v`}{\partial x}\right)^2}+\overline{\left(\frac{\partial u`}{\partial z}+\frac{\partial w`}{\partial x}\right)^2}+\overline{\left(\frac{\partial v`}{\partial z}+\frac{\partial w`}{\partial y}\right)^2}\Bigg]$$

where Φ is the viscous dissipation function dependent on the strain tensor [Pa/s], T is the absolute temperature of the flowing fluid [K], μ is the dynamic viscosity [Pa·s], u, v and w are the velocity components in x, y, z directions [m/s], respectively. The symbol $\bar{}$ denotes the time-averaged value, while ` represents the fluctuating component.

If we assume that the flow is axisymmetric and the velocity depends only on the radius, then Eq. (1) can be significantly simplified and written as:

$$\dot{s}_{gen}=\frac{\Phi}{T}=\frac{\mu}{T}\left[\left(\frac{\partial \bar{u}}{\partial r}\right)^2+\overline{\left(\frac{\partial u`}{\partial r}\right)^2}\right] \tag{2}$$

where r is a radial coordinate [m]. If we omit the part concerning flow fluctuations, Eq. (2) takes the form:

$$\dot{s}_{gen}=\frac{\mu}{T}\left[\left(\frac{\partial \bar{u}}{\partial r}\right)^2\right] \tag{3}$$

The Eq. (3) is the entropy distribution in the pipe, which, although important, is difficult to interpret case by case. In the case of stream analysis, it seems better to measure the total entropy, which can be understood as the amount of entropy generated per meter of length. This value can be expressed by the formula:

$$\dot{s}_{total,gen}=2\pi\int_0^R \dot{s}_{gen} r dr \tag{4}$$

Where R is the radius of pipe [m].

The purpose of this study is to verify whether Eq. (4) can be used to evaluate flow if the velocity profile is calculated using theoretical formulas (Prandtl's power law). Since the calculations will be theoretical, entropy generated by fluctuations will be ignored. The calculations will be performed for an assumed flow rate and various velocity profiles, which reflect the state that occurs after flow conditioning or relaminarization.

2. Methods

The velocity profile in a round pipe can be calculated with the Prandtl power law for laminar flow or with a modified Prandtl law for turbulent flow (Salama, 2021):

$$\frac{\bar{u}}{u_{max}}=1-\left(\frac{r}{R}\right)^2 \tag{5}$$

$$\frac{\bar{u}}{u_{max}}=\left(1-\left(\frac{r}{R}\right)^2\right)^{\frac{1}{n}} \tag{6}$$

where u_{max} is the maximal velocity [m/s], and n is an exponent that depends on the Reynolds number.

The calculations were performed for the pipe with a diameter 100 mm (with step 1 mm), and for Reynolds number 10 000. Air flow for a temperature of 21°C (294.15 K), atmospheric pressure of 1025hPa, and air humidity of 37 %. For such conditions, the air and flow parameters are: density $\rho = 1.21$ kg/m^3, dynamic viscosity $\mu = 1.818 \cdot 10^{-5}$ Pa·s, mean velocity $\bar{u} = 1.5$ m/s, and volume flow rate $Q = 42.5$ m^3/h.

Salama (2021) indicates that the n coefficient is most often equal to 7, while experimental data presented by Smyk et al. (2025) show that it can be much larger. Therefore, it was decided to analyze flows for n coefficients from 5 to 12 with a step size of 1.

3. Results and discussion

To better illustrate the relationship between the velocity profile exponent n and entropy generation, the analytical formulas can be explicitly derived. By substituting Eq. (6) into Eq. (3) and introducing the dimensionless radial coordinate $\rho = r/R$, the specific generated entropy is proportional to:

$$\dot{s}_{gen}(\rho, n) \sim \frac{4\rho^2}{n^2}(1-\rho^2)^{2\frac{1-n}{n}} \tag{7}$$

Consequently, integrating this local generation over the pipe cross-section (Eq. 4) yields an analytical expression for the total entropy generation:

$$\dot{s}_{total,gen} \sim \frac{2\pi}{n(n-2)} \left[(1-\rho^2)^{\frac{2}{n}-1} \cdot (n(\rho^2-1) - 2\rho^2) \right]_0^1 \quad (8)$$

This analytical formulation reveals the continuous nature of the dependence on n. However, it should be noted that for exponents $n > 2$, the gradient of the pure Prandtl power-law profile approaches infinity at the wall ($\rho \to 1$), which mathematically leads to a divergence of the total entropy integral. For this reason, in the practical engineering approach adopted in this study, the total generated entropy was evaluated using numerical integration with a discrete step size of 1 mm (as mentioned in methods section). This allows for a robust, objective comparison of the bulk flow properties without the unbounded wall singularity artificially dominating the results.

Figure 1a presents a maximum velocity as a function of the exponent *n*. The exponent *n* equal to 1 means the laminar flow. The calculations were based on theoretical profiles calculated from Eqs. (5) and (6), and the maximum velocity value for the laminar profile was equal to the two average velocities (in accordance with theory, see Salama 2021). The maximum velocity for the remaining *n* exponent values was found through optimization to achieve the assumed flow rate for a given profile. The higher the *n* exponent value, the smaller the maximum velocity. In the turbulent flow range, this relationship is linear ($R^2 = 0.938$). However, it should be noted that the dependence presented in Fig. 1a is a continuous function in the entire interval and therefore the approximation function is only informative.

Figure 1b shows the specific generated entropy as a function of the exponent n. As expected, the generated entropy increases with increasing exponent n. This means that the more turbulent the velocity profile, the greater the generated entropy. It should be noted that since the calculations were based on theoretical data, the calculations were performed based on Eq. (4), and therefore, the energy of velocity fluctuations was not taken into account. The generated entropy is positively corelated with the *n* exponent and the dependence between this two value can be approximated by a quadratic function with a very good approximation ($R^2 = 0.99$). It can therefore be expected that the entropy values generated for $n < 5$ also slope along the line shown in Fig.1b. However, such a low exponent value as $n = 5$ is rarely encountered in practical engineering applications. A literature review did not reveal any studies reporting an exponent as low as 5. For instance, Smyk et al. (2025) reported a minimum value of $n = 5.28$, corresponding to $\dot{s}_{total,gen} = 1.01 \cdot 10^{-5}$ J/(K·m·s) for analyzed theoretical model.

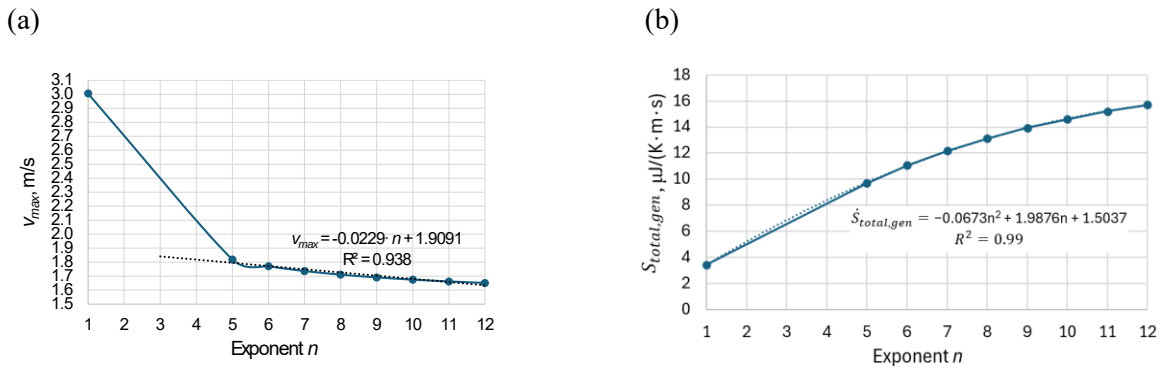

Fig. 1: The maximum velocity (a) and the specific generated entropy (b) in function of exponent n, where n=1 means the laminar flow.

Figure 2b presents the distribution of generated entropy as a function of distance from the axis. To unify the scales, the ratio of generated entropy to the maximum value of generated entropy is presented as the y-axis. It should be noted that the distribution of entropy generated in the duct cross-section is logarithmic for laminar flow, reflecting the logarithmic nature of the velocity profile. In the case of turbulent flow, entropy is generated primarily at the wall. It should be noted that a 1 mm step was used during the calculations, which corresponds to $r/R = 0.02$ for the assumed parameters. Note that increasing the exponent *n* does not cause a noticeable shape change in the generated entropy distribution. Even with a significant fine step size near the wall, the largest jump in entropy generation is observed at

the wall itself. This is related to the shape of the velocity profile (see Smyk et al. 2025, Salama 2021). The velocity profiles are illustrated in Figure 2b.

(a) (b)

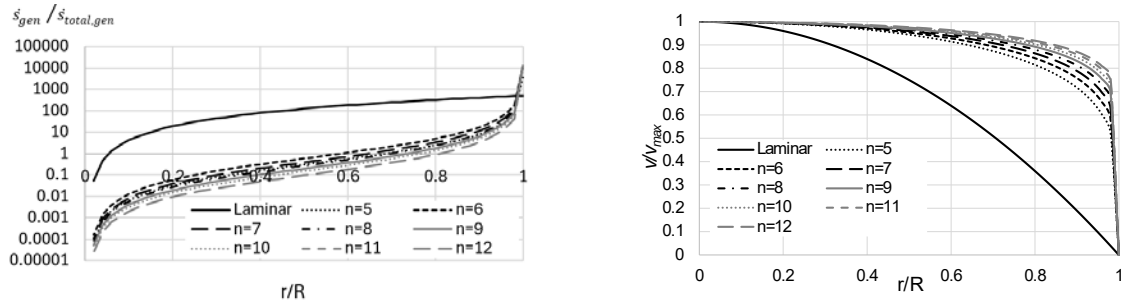

Fig. 2: The generated entropy profile (a) and the velocity profile calculated from Eq. (5) for laminar flow and from Eq. (6) for turbulent flow(b).

As can be seen, for turbulent profiles, the greatest velocity increase occurs between the wall and the first measurement point. Therefore, this will also correspond to the highest value of entropy generated, see Eq. (3).

4. Conclusions

The paper analysed the utility of measuring total entropy generation to evaluate flow after conditioning, based on theoretical velocity profiles. A linear relationship was demonstrated between the maximum velocity and the exponent n within the turbulent flow range. A key finding is that generated entropy rises as the exponent n increases, with the most significant generation occurring at the pipe wall due to the shape of the velocity profile. It was determined that the theoretical drop in entropy below the laminar value for $n = 5$ is an anomaly not encountered in practice, where the lowest observed exponents are higher. It is also crucial to emphasize that the presented analysis focused solely on the entropy generated by the mean velocity gradients (viscous dissipation), omitting the turbulent dissipation component caused by velocity fluctuations. Therefore, the calculated values should be interpreted as a lower bound estimate of the total entropy generation. In real flows, the contribution of turbulent fluctuations would further increase the total entropy production, thereby reinforcing the observed trend that profiles with higher Reynolds numbers (and higher exponents) result in greater energy losses. Ultimately, the study confirms that the method based on integrating entropy generation over the pipe radius allows for a correct and quantitative assessment of flow characteristics.

Acknowledgement

This research was fully funded by the National Science Centre under project number 2023/49/N/ST8/03737.

References

Jurga, A., Janocha, M., Ong, M., Yin, G. (2024) Numerical Investigations of Turbulent Flow Through a 90-Degree Pipe Bend and Honeycomb Straightener. *Journal of Fluids Engineering*, 146, 021307.

Kock, F.; Herwig, H. (2004) Local Entropy Production in Turbulent Shear Flows: A High-Reynolds Number Model with Wall Functions. *International Journal of Heat and Mass Transfer*, 47, 2205–2215.

Kühnen, J.; Scarselli, D.; Schaner, M.; Hof, B. (2018) Relaminarization by Steady Modification of the Streamwise Velocity Profile in a Pipe. *Flow, Turbulence and Combustion*, 100, 919–943.

Kühnen, J.; Scarselli, D.; Hof, B. (2019) Relaminarization of Pipe Flow by Means of 3D-Printed Shaped Honeycombs. *Journal of Fluids Engineering*, 141, 111105.

Salama, A. (2021) Velocity Profile Representation for Fully Developed Turbulent Flows in Pipes : A Modified Power Law. *Fluids*, 6, 369

Smyk, E., Stopel, M., Rachwalski, A. (2025) Impact of honeycomb straightener parameters on operation in a straight duct. *Journal of Theoretical and Applied Mechanics*, 63(4), 781-794.

Spearman, E.P.; Sattary, J.A.; Reader-Harris, M.J. (1996) Comparison of Velocity and Turbulence Profiles Downstream of Perforated Plate Flow Conditioners. *Flow Measurement and Instrumentation*, 7, 181–199

32nd International Conference
ENGINEERING MECHANICS 2026
Medlov, Czech Republic, May 11 – 13, 2026

A FRAMEWORK FOR WIND TURBINE STRUCTURAL DAMAGE DETECTION VIA UAV IMAGING AND ARTIFICIAL INTELLIGENCE

Stopel M.[1], Szyca M. [2], Seńko J. [3], Radtke K. [4]

Abstract: *The purpose of this study is to present a methodological framework for wind turbine damage detection using unmanned aerial vehicles supported by artificial intelligence techniques. Traditional inspection procedures are often costly, time-consuming, and contribute significantly to the operational and maintenance share of the Levelized Cost of Energy. The investigation includes an overview of the most common wind turbine structural designs, typical damage mechanisms, and power control strategies required to maintain voltage and frequency stability. Particular attention is given to the role of cyclic condition monitoring as a key factor in ensuring high efficiency and reliability of wind power systems. The proposed approach combines UAV-based visual inspection with AI-assisted damage identification, enabling safer and more effective assessment of turbine technical condition. Safety principles for conducting UAV operations in close proximity to wind turbine infrastructure are also discussed. The results confirm that integrating autonomous aerial inspection with intelligent detection methods may significantly improve maintenance strategies and support the development of more sustainable energy systems.*

Keywords: Wind turbine, Damage detection, Unmanned aerial vehicles (UAV), Artificial intelligence

1. Introduction

In recent decades, issues related to environmental protection, sustainable development, and global warming have become central topics in social, political, and scientific debates worldwide. One of the key challenges addressed in these discussions is the global dependence on conventional energy sources, particularly fossil fuels, and the question of how future energy systems should evolve.

Along with industrial growth and technological progress, global electricity consumption has steadily increased (Luty et al., 2023). For many years, the primary response to this growing demand was a significant expansion in the use of non-renewable energy sources (Fouquet, 2009). At the same time, modern societies have become increasingly aware of sustainability concerns and the responsibility to protect the natural environment. As a result, efforts are being made to meet energy needs by improving the efficiency of existing generation technologies and shifting toward renewable energy resources.

Among renewable energy technologies, wind power has emerged as one of the most important and dynamically developing solutions. Wind energy can supply electricity not only for small households but also for large-scale industrial applications (Du et al., 2020). Currently, wind energy represents the second-largest share among renewable sources, accounting for 13.2% of the total contribution. The largest share is provided by solid biofuels (41.4%), while hydropower ranks third with 11.9% (Eurostat, 2023).

[1] Michał Stopel, PhD.: Department of Mechanics and Computer Methods, Bydgoszcz University of Science and Technology, Al. Prof. S. Kaliskiego 7, 85-796 Bydgoszcz, Poland, PL, michal.stopel@pbs.edu.pl

[2] Mikołaj Szyca, MSc.: Faculty of Automotive and Construction Machinery Engineering, Warsaw University of Technology, pl. Politechniki 1, 00-661 Warsaw; PL, mikolaj.szyca.dokt@pw.edu.pl

[3] Jarosław Seńko, PhD.: Faculty of Automotive and Construction Machinery Engineering, Warsaw University of Technology, pl. Politechniki 1, 00-661 Warsaw; PL, Jaroslaw.Senko@pw.edu.pl

[4] Krzysztof Radtke , Engr.: Intel Technology Poland Sp. z o.o., Juliusza Słowackiego 173, 80-298 Gdańsk, Poland, PL, krzysztof.radtke@gmail.com

ISSN: 1805-8256, doi: 10.21495/em2026-121

A major factor determining the competitiveness of any electricity generation technology is the Levelized Cost of Energy (LCoE). A substantial portion of LCoE is associated with Operation and Maintenance (O&M). In the case of wind turbines, O&M costs may account for up to 25% of the total energy cost (Shafiee et al., 2021; Shihavuddin et al., 2019). Regular technical inspections play a crucial role in preventing failures and maintaining turbine performance (Liu & Ishihara, 2015; Kulsinskas et al., 2021). Additionally, reducing turbine downtime is directly linked to economic efficiency, as each day out of service may generate losses ranging from 800 to 1600 US dollars (Katsaprakakis et al., 2021).

In recent years, increasing attention has been given to modern inspection approaches aimed at improving the efficiency of wind turbine condition assessment while reducing operational costs and risks to maintenance personnel. One of the most promising directions involves the application of unmanned aerial vehicles (UAVs), which enable rapid acquisition of high-resolution visual data from difficult-to-access turbine components. Furthermore, artificial intelligence and machine learning techniques provide tools for supporting the automated identification and classification of typical defects such as cracks, erosion, or delamination.

Therefore, the integration of UAV-based inspection with AI-assisted damage detection constitutes a relevant methodological pathway for wind turbine maintenance practices. This paper focuses on outlining such an inspection framework and discussing key operational and safety aspects of implementing UAV and AI technologies in wind energy systems. The main contribution of this work is the proposed inspection procedure and workflow, rather than a performance evaluation or final damage detection results.

2. Methodology

Inspection of wind turbines using aerial systems has become a standard practice in the wind energy maintenance market, driven by the demand for safer, faster and more cost-efficient condition monitoring (CM) solutions. The proposed methodology aligns with current industrial procedures for visual inspection and automated damage analysis, integrating unmanned aerial vehicles (UAVs) with artificial intelligence (AI)-supported identification tools.

Industrial-grade UAV platforms equipped with high-resolution imaging sensors are widely used in commercial inspection services due to their ability to capture detailed visual data in challenging environments. In this framework, a professional multi-rotor system with RGB imaging and optical zoom is treated as a reference configuration. For example, platforms such as DJI Matrice M300, DJI Matrice 350 RTK or DJI Matrice 30T, paired with a high-zoom camera (e.g., Zenmuse-series), represent typical solutions adopted in the market for turbine inspection tasks. These systems offer extended flight endurance, high wind resistance, and long-range operation suitable for wind turbine sites, while optical zoom enables detailed observation of structural elements from a safe distance.

The first step of the methodology involves acquiring photo and video material during an on-site inspection. This is consistent with prevailing practices among professional UAV service providers, who focus on capturing comprehensive visual coverage of critical turbine components. The inspection scope in this methodology emphasizes wind turbine blades, as blade damage typically accounts for a large proportion of maintenance costs and operational risks. Both aerodynamic sides of the blade—the suction side and the pressure sidem – are included, with particular attention given to the leading edge and trailing edge. When feasible and cost-effective, additional visual assessment of the nacelle and tower may be integrated into the inspection flight plan.

After visual data acquisition, the collected material is transferred to a digital processing environment. In current market practices, data annotation and preprocessing serve as a foundation for developing AI models capable of supporting automated damage detection and classification. Following this trend, the proposed workflow integrates expert-supported annotation with iterative AI model development. Initial interpretation of selected samples may be performed by an engineer experienced in wind turbine operation, and the annotated dataset is subsequently used for training an AI-based model. Iterative refinement of model parameters and evaluation cycles continues until an appropriate level of reliability is achieved for the intended inspection scope, in line with strategies reported in recent literature.

The above methodology schematic representation was presented in Fig. 1.

Fig. 1: Workflow of the proposed UAV-based inspection and YOLOv8-assisted damage detection framework for wind turbine blade condition assessment.

It should be emphasized that the presented research represents an initial stage of ongoing work. At this phase, preliminary analyses were conducted, and a first proof-of-concept implementation of an AI-based detection model was developed using the YOLOv8 architecture. YOLO (You Only Look Once) belongs to the family of one-stage object detection algorithms, where localization and classification are performed simultaneously in a single forward pass. The preliminary detection capability of the model is demonstrated in Fig. 2, which presents example UAV inspection images with bounding boxes highlighting damage candidate regions. These include typical surface defect patterns such as erosion marks, cracks, and discoloration. Although the current results should be treated as exploratory, they confirm the feasibility of integrating UAV inspection workflows with modern deep-learning detection frameworks. Future work will focus on expanding the dataset and performing systematic quantitative validation under operational conditions.

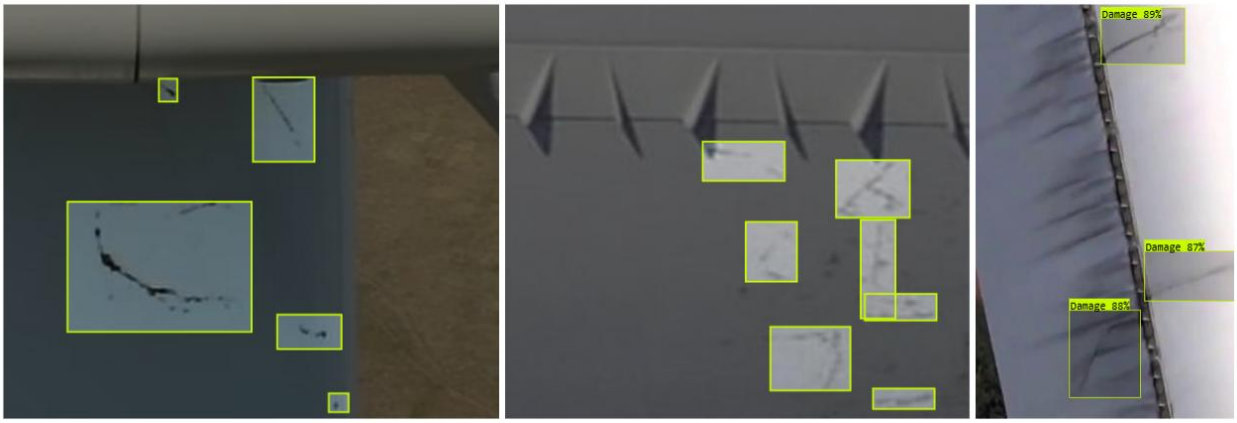

Fig. 2: Preliminary detection results of the YOLOv8 damage model applied to UAV images.

The methodology also highlights the importance of large and diverse datasets, a recognized challenge in both academic research and industrial deployment. Market actors and research initiatives have begun to address this limitation by sharing inspection datasets and benchmarks; such collaborative actions may contribute to accelerating the development of robust AI-assisted inspection tools.

3 Conclusions

The application of unmanned aerial vehicles (UAVs) in wind turbine inspection represents a significant advancement in operation and maintenance strategies. Compared to traditional inspection methods, such as rope-access techniques, UAV-based visual assessment substantially improves safety by reducing the need for personnel to work in hazardous conditions and at great heights. Moreover, this technology is already widely accessible and enables inspections to be performed not only more safely, but also faster and at lower cost.

It has been estimated that UAV inspections can generate savings of up to 40% in comparison with conventional rope-based procedures (Stout & Thompson, 2019). As operation and maintenance costs account for a considerable share of the Levelized Cost of Energy (LCoE), the adoption of aerial inspection methods can contribute directly to improving the economic competitiveness of wind energy systems.

Furthermore, the integration of condition monitoring processes with artificial intelligence algorithms offers additional potential for cost reduction and efficiency improvement. Although the development of AI-supported damage detection models requires substantial initial investment, particularly related to building and annotating large datasets, such tools may significantly enhance the automation and reliability of defect identification. In the long term, this may reduce inspection effort, minimize turbine downtime, and support predictive maintenance approaches.

Overall, the proposed framework combining UAV imaging with AI-assisted damage detection provides a promising pathway toward more sustainable and effective wind turbine maintenance. Continued research and industrial collaboration, especially in the area of shared datasets and model benchmarking, will be essential for the broader deployment of autonomous inspection technologies and for further reductions in LCoE, making wind-generated electricity even more attractive within future energy systems.

Acknowledgement

This research was fully funded by the National Science Centre under project number 2023/49/N/ST8/03737.

References

Du, Y., Zhou, S., Jing, X., Peng, Y., Wu, H., & Kwok, N. (2020). Damage detection techniques for wind turbine blades: A review. *Mech. Syst. Signal Process*., 141, pp. 106445

Eurostat. (2023). Sustainable development in the European Union — Monitoring report on progress towards the SDGs in an EU context. In *Publications Office of the European Union*. Publications Office of the European Union, Luxembourg.

Fouquet, R. (2009). A brief history of energy, in Evans, J., end Hunt, L., C., eds., *International Handbook of the Economics of Energy*, . Edward Elgar Publications, Cheltenham, United Kingdom, pp. 1-20.

Katsaprakakis, D. Al, Papadakis, N., & Ntintakis, I. (2021). A comprehensive analysis of wind turbine blade damage. *Energies,* 14(18), pp. 5974

Kulsinskas, A., Durdevic, P., & Ortiz-Arroyo, D. (2021). Internal wind turbine blade inspections using uavs: Analysis and design issues. *Energies*, 14(2), pp. 0294

Liu, Y., & Ishihara, T. (2015). Fatigue Failure Accident of Wind Turbine Tower in Taikoyama Wind Farm, in Anbrun, J., Mann, J., end, Muskulus, M., eds., *Proc. 2015 EWEA Scientific Proceedings*, European Win Energy Assosiation, pp. 121-125.

Luty, L., Zioło, M., Knapik, W., Bąk, I., & Kukuła, K. (2023). Energy Security in Light of Sustainable Development -Goals. *Energies*, 16(3), pp. 1390.

Shafiee, M., Zhou, Z., Mei, L., Dinmohammadi, F., Karama, J., & Flynn, D. (2021). Unmanned aerial drones for inspection of offshore wind turbines: A mission-critical failure analysis. *Robotics*, 10(1), pp. 0026

Shihavuddin, A., Chen, X., Fedorov, V., Christensen, A. N., Andre, N., Riis, B., Branner, K., Dahl, A. B., & Paulsen, R. R. (2019). Wind Turbine Surface Damage Detection by Deep Learning Aided Drone Inspection Analysis. Energies 12(4), pp. 0676.

Stout, C., & Thompson, D. (2019). UAV Approaches to Wind Turbine Inspection Reducing Reliance on Rope-Access. Offshore Renewable Energy Catapult (OREC), Mar. 2019. Accessed: Feb. 02, 2023. [Online]. Available: https://cms.ore.catapult.org.uk/wp-content/uploads/2019/03/Cyberhawks-Approach-to-UAV-Inspection-Craig-Stout-ORE-Catapult.pdf

32nd International Conference
ENGINEERING MECHANICS 2026
Medlov, Czech Republic, May 11 – 13, 2026

STUDY ON THE IMPACT OF SINGLE-LEAF DOOR DESIGN IN TRAMS ON THE RATE OF PASSENGER EXCHANGE

Szyca M.[1], Smyk E.[2], Bučko M.[3]

Abstract: *This paper addresses the design of side-door systems in tram vehicles with regard to achieving the highest possible passenger throughput. It is a well-known fact that in the rail vehicle design process, the primary criterion determining the number of doors is the expectations of the operator ordering the vehicles. This article analyzes whether the use of single-leaf doors at the rear of a single-ended tram has a positive effect on efficient passenger exchange at stops. The analysis is based on data obtained from recordings of passenger flows captured using a drone and an action camera in Polish cities characterized by medium and high levels of passenger turnover. The analysis is further supported by the use of a YOLOv10s convolutional neural network. The conclusions drawn from this study may contribute to changes in the way tender requirements for new tram vehicles are formulated in cities.*

Keywords: Public transport, Tram design, Passenger flow, Artificial intelligence, YOLO, Data analysis

1. Introduction

Effective planning of public transport operations in cities represents a significant challenge in transport engineering. Example studies (Du et al., 2025; Liu et al., 2025) show that successful planning of pedestrian movement directions requires both detailed analyses and strategic thinking, often supported by object-tracking techniques based on artificial intelligence.

Tram design constitutes a specific subfield—indeed, almost a separate branch—of rail vehicle engineering, as it relies more heavily on adapting the vehicle to local conditions and the client's requirements than is the case for passenger railway vehicles. This results naturally from operation on dedicated networks that differ between cities in terms of track gauge, supply voltage, and other distinguishing factors. In contrast, railway vehicles are subject to a higher level of standardization, for example through Technical Specifications for Interoperability (TSIs) (European Commission, 2014).

For tram vehicles, guidance is provided by Regulation No. 107 (United Nations Economic Commission for Europe, 2015). This regulation specifies only a minimum of two doors and a maximum distance of 7 m to an emergency exit from any passenger-accessible area of the vehicle. In practice, compliance with these requirements typically leads to door spacing of approximately 5–6 m, considering a standard vehicle width of about 2.0–2.5 m. At the tram ends, these guidelines must be adapted to the interior layout. The ends of the vehicle may contain driver's cabs in bidirectional trams or gondola-type end sections in single-unit trams. Consequently, in both multi-unit and single-unit trams, a portion of the space otherwise available to passengers is allocated to staff areas or seating.

This engineering task therefore constitutes a dual-domain challenge. From the perspective of transport engineering on the client's side, it is necessary to assess how many vehicle entrances are realistically

[1] Mikołaj Szyca, MSc.: Faculty of Automotive and Construction Machinery Engineering, Warsaw University of Technology, pl. Politechniki 1, 00-661 Warsaw; PL, mikolaj.szyca.dokt@pw.edu.pl

[2] Emil Smyk, PhD.: Faculty of Mechanical Engineering, Bydgoszcz University of Science and Technology, Al. Prof. S. Kaliskiego 7, 85-796 Bydgoszcz; PL, emil.smyk@pbs.edu.pl

[3] Martin Bučko, MSc.: Faculty of Mechanical Engineering, University of Žilina, Univerzitná 8215/1, 010-26 Žilina, SK, martin.bucko@fstroj.uniza.sk

ISSN: 1805-8256, doi: 10.21495/em2026-125

required. From the mechanical engineering perspective, the vehicle must be designed to meet both safe evacuation requirements and the client's expectations regarding the usable floor area in the passenger compartment. This issue represents the core problem addressed in this article. The study analyzes whether the use of single-leaf doors at the ends of trams is advantageous from a passenger-flow perspective. Preliminary observations from passenger-flow studies indicate the formation of bottlenecks near single-leaf end doors when these are the closest doors to the platform entrance.

2. Materials and Methods

The tram boarding and alighting process was examined based on video footage recorded with a DJI Air 3 Fly More Combo (RC-N2) drone and a GoPro 13 HERO action camera. The drone's positioning and the mounting location of the action camera (using a magnetic mount) were adapted to the specific recording site and tram stop. The equipment was arranged to avoid obstructing the tram doors, to capture as many doors as possible within the field of view, and to maintain a recording angle between 45 and 90 degrees. The research was conducted based on the methodology described in more detail in (Szyca et al., 2025, Szyca et al., 2026).

The recordings were made in 4 cities in Poland, the data on the measurement points is presented in Tab. 1. The total number of analysed recordings was 200. For each city 50 measurements.

Tab. 1: Data on the measurement

City	Number of inhabitants	Name of tram stop	Hours of recordings	Types of operating trams
Bydgoszcz	324.000	Rondo Jagiellonów	1-3 p.m.	122NaB, 121NaB, 122N
Gdańsk	488.000	Galeria Bałtycka 02	8-10 a.m.	122NaG, 128NG, N8C-NF. NGT6
Katowice	278.000 (2.500.000 in Silesian Conurbation)	Katowice Rondo	1-3 p.m.	19T, 105NWr, LF 07AC. MF 17AC, MF 19AC, MF 24AC
Wrocław	670.000	Wrocław Dworzec Główny	7-9 a.m.	105Na, 105N (mod.), 116Nd, 2012N, 2017N, 146N, HF 11AC

Stops in all analyzed locations are situated in the strict city centres and generate some of the highest passenger flows in these cities. The stops in Katowice and Wrocław have an open layout, allowing access from multiple directions. In contrast, the stops in Gdańsk and Bydgoszcz have only a single functional entrance. This situation made it possible to verify the occurrence of passenger accumulation near the last doors of a given tram set through a comparative analysis of stop layouts.

3. Results and discussion

As can be observed in Fig. 1, under specific boundary conditions a phenomenon of passenger accumulation occurs in the area of the vehicle's last door, when this door serves as the last boarding entrance. Fig. 2 illustrates the mechanism by which this phenomenon occurs. Studies have shown that the average passenger exchange time at a stop ranges between 15 and 30 seconds, depending on the level of occupancy of both the tram and the stop. In the case of the stops Gdańsk – Galeria Bałtycka and Bydgoszcz – Rondo Jagiellonów, dwell times approximately 5 seconds longer were recorded under comparable tram and stop occupancy conditions. This is indirectly reflected in the measurement results presented in Tab 2. which presents the analysis results for individual cities. A clear difference can be observed between Gdańsk and Bydgoszcz, where the stops have a single access point, in contrast to Katowice and Wrocław, where there are multiple access points to the stop from different directions.

Fig. 1: Screenshot from a recording made in Gdańsk during measurements conducted in 2024 at the Galeria Bałtycka stop

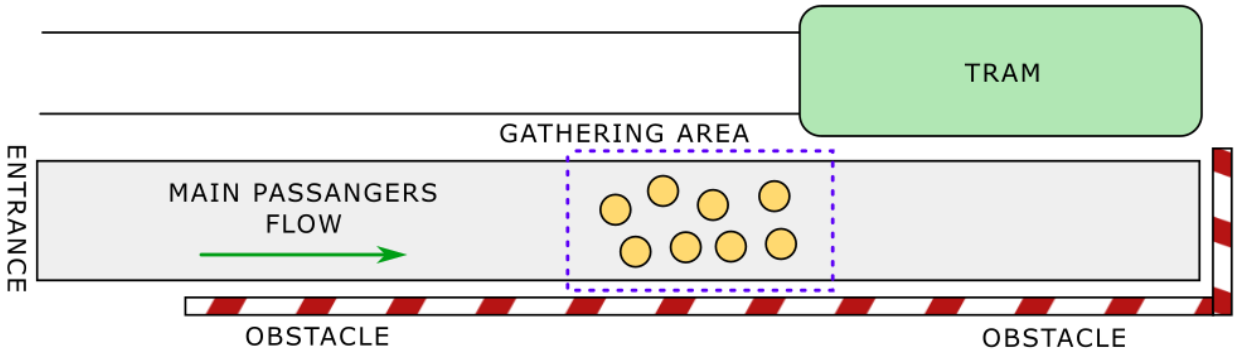

Fig. 2: Visualization of passenger flow conditions at the stop Rondo Jagiellonów (Bydgoszcz) and partially at Galeria Bałtycka (Gdańsk)

Tab. 2: Data on the measurement; Measurement results marked as Type A – cases in which passenger exchange through the last door lasted the longest and could have extended the tram dwell time; Type B – cases in which, due to an insufficient number of passengers waiting at the stop, passenger exchange through the last door did not take place; Type C – cases in which passenger exchange through the last door did not last the longest.

City	Type A	Type B	Type C
Bydgoszcz	88%	0%	12%
Gdańsk	44%	36%	20%
Katowice	4%	20%	76%
Wrocław	2%	12%	86%

4. Conclusions

The conducted observations and measurement data showed that trams equipped with single-leaf doors at the ends of the vehicle exhibited a lower capacity for smooth passenger exchange at stops. This phenomenon is particularly evident when a platform has only one functional access point, or when the stop is located in the vicinity of a company or institution that naturally generates significant passenger flows, forcing boarding to occur at the front or rear of the vehicle. The analyses demonstrated that when the above-mentioned factors accumulate, trams experienced dwell times longer by at least 5 s in more than 50% of cases.

Even very small-time savings achieved at the level of individual stops can, at the scale of the entire public transport system, lead to noticeable operational effects. To illustrate this phenomenon, a hypothetical example of a tram line serving a route consisting of 20 stops can be considered. Assuming that at 50% of them, i.e. at 10 stops, organizational or infrastructural improvements allow the dwell time or running time to be reduced by 5 s, the total time saving per single trip amounts to 50 s.

Although this value may appear negligible at the level of an individual run, its significance increases with the number of services operated. Assuming that one vehicle performs 30 trips per day, which is typical for an intensively operated tram line, the daily time saving per tram equals 1500 s, i.e. 25 min. For a line operated by 10 vehicles, this translates into 250 min, or approximately 4 h 10 min of cumulative time savings per day across the system.

This effect becomes even more pronounced over a longer time horizon. On an annual scale, assuming operation over 365 days, this results in approximately 1520 h of saved operational time. When converted to a standard 8-hour working day, this corresponds to the equivalent of approximately 190 working days, or more than 60 days of continuous vehicle operation. Such a substantial value does not result from a single, capital-intensive investment, but from the systematic elimination of minor time losses recurring multiple times throughout the day.

From the perspective of a public transport authority, such micro-level time savings can be utilized in several ways. They may increase schedule slack, improving punctuality and system resilience to disruptions, enable reductions in travel times perceptible to passengers, or—in the longer term—lead to optimization of the number of vehicles required to operate a given line. This example demonstrates that even improvements measured in individual seconds can generate significant benefits at the scale of an entire transport system.

Acknowledgement

This research was fully funded by the National Science Centre under project number 2023/49/N/ST8/03737.

References

Du, Y., Aoki, T. and Fujiwara, N. (2025) A review of human mobility: Linking data, models, and real-world applications. Journal of Computational Social Science, 8, Article 90, pp. 1–25.

European Commission (2014) Commission Regulation (EU) No 107/2014 on the technical specifications for interoperability relating to the ‘control-command and signalling trackside’ subsystem of the rail system in the European Union. Official Journal of the European Union, L 57, pp. 1–82.

Liu, Y., Liao, X., Ma, H., He, B. Y., Stanford, C. and Ma, J. (2025) Human mobility modeling with limited information via large language models. arXiv preprint arXiv:2409.17495, pp. 1–25.

Szyca, M., Smyk, E. and Dižo, J. (2025) Analysis of the boarding and disembarking process time on the example of the Pesa 122NaB tram operated in the city of Bydgoszcz. Polish Journal of Technology, Issue 1, Article 4, pp. 1.

Szyca, M., Smyk, E., Radtke, K. and Dižo, J. (2026) Measurement of the time of boarding and alighting from trams. Smart Cities, Issue 9, Article 2, pp. 25.

United Nations Economic Commission for Europe (2015) Regulation No. 107: Uniform provisions concerning the approval of category M2 or M3 vehicles with regard to their general construction. UNECE Regulations – Vehicle Construction, Rev. 3, pp. 1–178.

32nd International Conference
ENGINEERING MECHANICS 2026
Medlov, Czech Republic, May 11 – 13, 2026

VELOCITY CALIBRATION OF A WIND TUNNEL WITH BYPASS FLOW FOR BLADE CASCADE AEROELASTIC STUDIES

Šnábl P.[1], **Procházka P.**[2], **Skála V.**[3],

Abstract: *This paper presents a calibration methodology for an Eiffel-type wind tunnel equipped with a bypass flow system designed for aeroelastic investigations of a blade cascade subjected to a radial flow component. Since flutter onset is highly sensitive to incoming flow conditions, precise and repeatable setting of flow velocities in both the main and bypass tunnels is essential. The main tunnel velocity is determined from static pressure differences across the contraction section using Bernoulli's equation. The bypass tunnel velocity, which cannot be measured directly due to spatial and geometric constraints, is evaluated using particle image velocimetry near the blowing orifice. Velocities are measured across 30 combinations of variable-frequency drive settings of both tunnel fans. A third-order polynomial surface is fitted to the measured data using a least-square minimisation with outlier rejection. To avoid the need for numerical inversion of the fitted surfaces, dense lookup tables with linear interpolation are constructed, and iso-velocity contour diagrams are produced. The resulting calibration tool allows straightforward and reliable identification of fan frequency combinations corresponding to any desired pair of main and bypass tunnel velocities.*

Keywords: Wind tunnel calibration, Bypass flow, Particle image velocimetry, Surface fitting

1. Introduction

Modern thermal power plants are increasingly required to operate under off-design conditions due to the growing share of intermittent renewable energy sources in the power grid. Under such conditions, reduced mass flow alters the pressure distribution within the turbine stages, strengthening the radial velocity component and modifying the effective angle of attack of the blades. This promotes flow separation and increases the risk of aeroelastic instabilities, particularly stall flutter, which can lead to severe blade damage. The last stage of the low-pressure turbine is especially susceptible due to its long, slender blades and low-camber profiles Procházka et al. (2026).

To study such phenomena experimentally, an Eiffel-type wind tunnel with a 700 mm × 700 mm square cross-section, driven by a 14 kW axial fan, has been equipped with a bypass flow system. The bypass tunnel introduces a controlled cross-flow jet into the main test section through a blowing orifice located upstream of the blade roots, while a suction orifice downstream of the blade tips closes the bypass loop. The bypass duct, driven by an independent radial fan, has a cross-sectional area approximately eight times smaller than that of the main tunnel, so that comparable jet and main-flow velocities can be achieved at a proportionally lower bypass flow rate. A fine mesh screen at the blowing orifice homogenises flow non-uniformities originating from the elbow wakes in the bypass piping. The initial design idea is described in Šnábl et al. (2024) and the experimental facility CAD model is shown in Fig. 1.

Because flutter onset is highly sensitive to incoming flow conditions, precise and repeatable setting of the operating point is essential for the planned aeroelastic investigations. Unlike the main tunnel, the bypass duct contains neither a contraction nor a sufficiently long straight pipe section to allow reliable direct flow-rate measurement. As demonstrated in Procházka et al. (2026), where the bypass jet topology was characterised using particle image velocimetry (PIV), the interaction between the bypass jet and the main

[1] Ing. Pavel Šnábl: Ústav termomechaniky AV ČR, v. v. i., Dolejškova 1402/5; 182 00, Prague; CZ, snabl@it.cas.cz
[2] Ing. Pavel Procházka, PhD.: Ústav termomechaniky AV ČR, v. v. i., Dolejškova 1402/5; 182 00, Prague; CZ, prochap@it.cas.cz
[3] Ing. Vladislav Skála, PhD.: Ústav termomechaniky AV ČR, v. v. i., Dolejškova 1402/5; 182 00, Prague; CZ, skala@it.cas.cz

ISSN: 1805-8256, doi: 10.21495/em2026-129

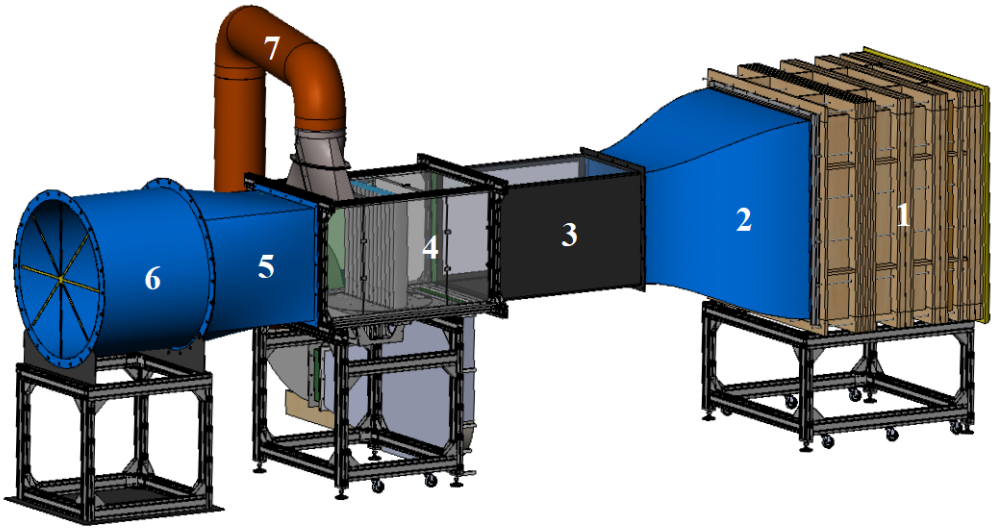

Fig. 1: CAD model of the wind tunnel with bypass flow: 1 – settling chamber, 2 – contraction, 3 – test section extension, 4 – test section, 5 – diffuser, 6 – main tunnel fan, 7 – bypass loop.

tunnel flow is complex: the jet deflects and narrows with increasing main tunnel velocity, and the penetrating jet imposes an additional pressure loss on the main tunnel, requiring simultaneous adjustment of both fan speeds. This coupling motivates the need for a systematic calibration of the two-tunnel system. The present paper therefore focuses on the velocity evaluation methodology, surface fitting of the measured data, and the construction of a practical iso-velocity diagram that allows straightforward identification of the fan frequency settings corresponding to any desired pair of main and bypass tunnel velocities.

2. Evaluation of Velocities

2.1. Main Tunnel

The main tunnel velocity was calculated from measured pressure difference on the contraction (2 in Fig. 1). From the Bernoulli's equation for incompressible flow we have:

$$p_A + \frac{1}{2}\rho v_A^2 = p_B + \frac{1}{2}\rho v_B^2 + p_L, \tag{1}$$

where p_A and p_B are pressures at the contraction inlet and outlet, v_A and v_B are velocities at the contraction inlet and outlet and ρ is the air density. The pressure loss p_L is neglected, as it is expected to be lower than the resolution of our pressure sensor.

From the continuity equation for the incompressible flow we get:

$$A v_A = B v_B, \tag{2}$$

where A and B are the respective inlet and outlet areas of the contraction. By substituting of v_B from (2) into (1) and rearranging, we get an equation to calculate the contraction outlet velocity, i.e. the main tunnel velocity, from pressure difference on the contraction inlet and outlet:

$$v_B = \sqrt{\frac{2(p_A - p_B)}{\rho\left[1 - \left(\frac{B}{A}\right)^2\right]}}. \tag{3}$$

2.2. Bypass Tunnel

The bypass velocity was measured by using particle image velocimetry in a plane located in the middle of the tunnel width above the bypass inlet. The velocities were evaluated at horizontal line 20 mm above the tunnel floor. Further information about the evaluation procedure is described in Procházka et al. (2026).

3. Velocities Surface Fitting

Variable-frequency drives (VFD) of the main and bypass tunnel motors were set in all combinations of the following frequencies: $f_M = (10,\ 20,\ 30,\ 40,\ 50)$ Hz and $f_B = (0,\ 10,\ 20,\ 30,\ 40,\ 50)$ Hz. Measurements were not performed for $f_M = 0$ Hz since the bypass flow is intended only for modification of the main tunnel flow. Turning on the bypass only actually creates a backflow in the main tunnel.

Several other measurements had to be discarded from the measured data sets:

- Main tunnel velocity measurement at $f_M = 10$ Hz and $f_B = (30,\ 40,\ 50)$ Hz — at those VFD frequencies the bypass flow dominates, hits the top wall of the tunnel and creates big recirculation area in the test section extension (3 in Fig. 1) and possibly disturbs the pressure measurement on the contraction.
- Bypass tunnel measurement at $f_M = (30,\ 40,\ 50)$ Hz and $f_B = 10$ Hz — here, the bypass outlet velocity is negligible to the main tunnel velocity and the particle-saturated bypass air is blown away before reaching the evaluation line for the PIV measurement.
- Bypass tunnel measurement at $f_M = (0,\ 10)$ Hz and $f_B = 50$ Hz — not enough particles were fed into the bypass tunnel and the PIV evaluation was unreliable.

All of the kept measured velocities are plotted in Fig. 2 as circles.

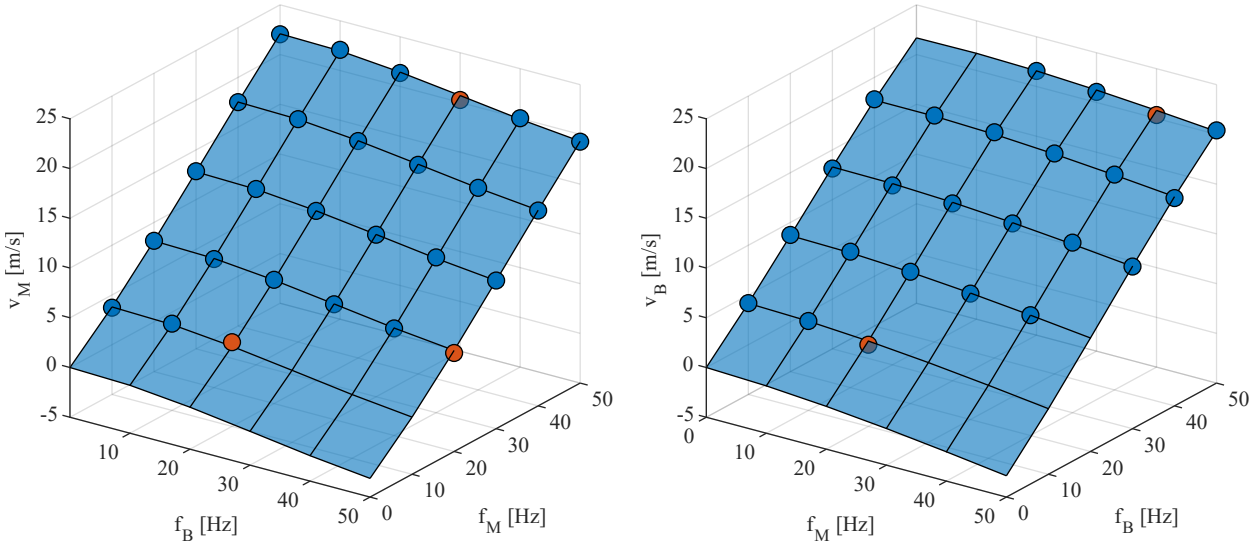

(a) Main tunnel velocity. *(b) Bypass tunnel velocity.*

Fig. 2: Measured main tunnel velocities v_M and bypass tunnel velocities v_B for main and bypass tunnel frequencies f_M and f_B with fitted surfaces.

Next, surface fitting was performed to obtain functions for main and bypass tunnel velocities. As a suitable function, a 7-parameter third order polynomial surface was chosen for both velocities:

$$v = c_1 f_M + c_2 f_M^2 + c_3 f_M^3 + c_4 f_B + c_5 f_B^2 + c_6 f_B^3 + c_7 f_M f_B. \tag{4}$$

To obtain well-fitting function, a 3-step fitting was performed using a least-square error minimisation:

1. The function constants were fitted using all of the measured data points.
2. Points with residuals higher than $1.5\times$ the standard deviation were discarded as outliers (red points in Fig. 2).
3. The function constants were re-fitted after discarding the outliers.

The fitted surface functions for both main tunnel and bypass tunnel velocities are shown in Fig. 2.

At the end, an inverse task had to be solved. For given flow velocities, we need the corresponding VFD frequencies. Since the velocity functions given by (4) are not linear, the inverse functions would need to be solved numerically. To overcome the numerical solution, that could experience numerical instability, find multiple solutions etc., a more practical engineering approach was chosen. Velocities were calculated for frequencies with small increment, creating dense lookup tables. Linear interpolation was then used to find

the frequencies corresponding to the chosen velocity pair. Also, the data from the lookup tables were used to construct the graph in Fig. 3 with velocity isolines over the frequencies grid that allows to find the desired operating point optically.

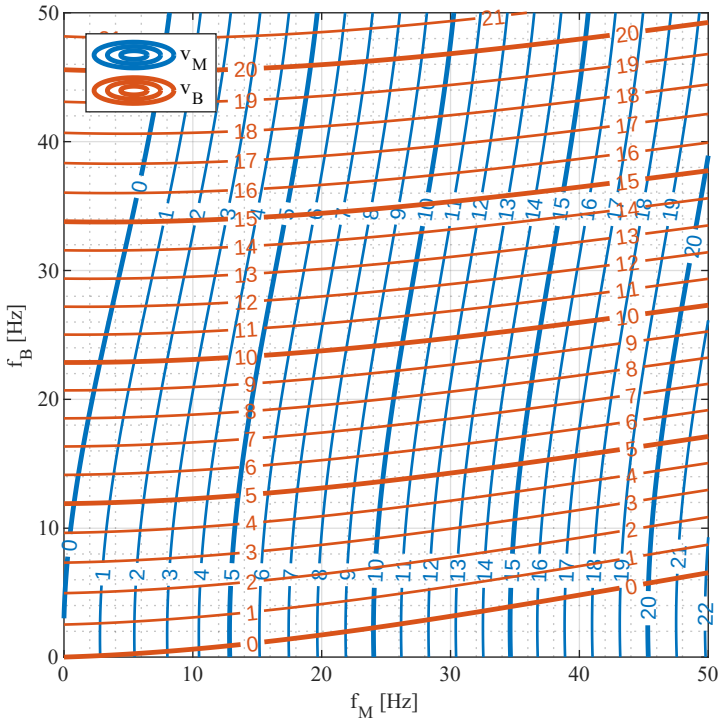

Fig. 3: Isolines of main tunnel velocity v_M and bypass tunnel velocity v_B for main and bypass tunnel frequencies f_M and f_B.

4. Conclusions

A calibration methodology for a coupled main and bypass wind tunnel system has been developed and validated. Main tunnel velocities were determined from contraction pressure differences, while bypass velocities were evaluated using PIV. A third-order polynomial surface fitted to the measured data, combined with outlier rejection, provided accurate velocity predictions across the full operating range. The resulting lookup tables and iso-velocity diagram enable straightforward and repeatable setting of desired flow conditions, providing a reliable basis for future aeroelastic investigations of the blade cascade under controlled radial flow.

Acknowledgments

This work was supported by the project GA26-22907S: “Friction-induced instabilities in dynamic systems with rolling-sliding contact under transient conditions”

References

Procházka, P., Šnábl, P., and Skála, V. (2026) On the calibration of the bypass tunnel used for cascade aeroelastic study. In Zolotarev, I., Pešek, L., and Kozień, M., eds, *DYMAMESI 2026 Proceedings*, Prague. Institute of Thermomechanics of the CAS, Prague, pp. 43–46.

Šnábl, P., Pešek, L., Procházka, P., and Prasad, C. S. (2024) Computer-aided engineering in the design of an experimental blade cascade for fluid-structure interaction studies. In Beran, J., Bílek, M., Václavík, M., and Žabka, P., eds, *Advances in Mechanism Design IV: Proceedings of TMM 2024*, Cham. Springer, pp. 114–122.

32nd International Conference
ENGINEERING MECHANICS 2026
Medlov, Czech Republic, May 11 – 13, 2026

CORRELATION OF LOCAL MICROMECHANICAL PROPERTIES WITH EDS CHEMICAL PROFILES IN BLENDED CEMENT PASTE

Špaková A.[1], **Němeček J.**[2], **Němeček J.**[3]

Abstract: *This study investigates the correlation between micromechanical properties and chemical composition in a blended cement paste containing fly ash and limestone. Micromechanical characterization was performed using grid nanoindentation with a spatial resolution of* $2.5\,\mu\mathrm{m}$ *to acquire the local Young's modulus across the different cement paste phases. Additionally, Energy Dispersive X-ray Spectroscopy (EDS) line scans provided pointwise elemental composition, enabling the calculation of (Ca–S)/Si and Al/Si ratios for each measurement location. By combining the mechanical and chemical datasets, the spatial distribution of element content and corresponding stiffness was visualized, allowing segmentation of the paste into distinct phases such as low- and high-density C–S–H, Portlandite, and fly ash regions.*

Keywords: Nanoindentation, Scanning electron microscopy, Cement Paste, Energy Dispersive X-ray Spectroscopy

1. Introduction

Cementitious materials exhibit a complex and heterogeneous microstructure composed of hydration products such as low-density Calcium Silicate Hydrate (LD C–S–H), high-density Calcium Silicate Hydrate (HD C–S–H), Portlandite (CH), and unhydrated clinker Jennings et al. (2007). When supplementary cementitious materials such as slag, fly ash, or silica fume are added, the microstructure changes significantly, and new hydration products are formed Li et al. (2021).

Nanoindentation is commonly used to characterize the micromechanical behavior of these phases Němeček et al. (2013); Luo et al. (2018); Němeček et al. (2020). In previous studies, separation into individual phases has been achieved either by statistical analysis Němeček et al. (2013) or by correlating nanoindentation data with BSE images Hilloulin et al. (2018). However, purely statistical approaches require large datasets, while BSE-based segmentation may not reliably capture the underlying phase composition, as BSE contrast alone is sometimes insufficient for accurate phase identification.

By combining nanoindentation with SEM–BSE imaging and Energy Dispersive X-ray Spectroscopy (EDS) line scans, it is possible to correlate local mechanical properties with elemental composition, enabling more reliable identification of individual cement paste phases. In particular, (Ca–S)/Si and Al/Si ratios obtained from EDS serve as effective indicators for phase differentiation, linking oxide distribution to variations in local stiffness.

Although such chemical–mechanical correlations have been applied to synthetic C–S–H and some blended pastes Pelisser et al. (2012), systematic studies integrating nanoindentation grids with SEM–EDS line scans in cement pastes containing fly ash and limestone are still limited.

In this study, a blended cement paste with fly ash and limestone is investigated. By mapping local Young's modulus alongside chemical composition, individual phases can be identified, and the influence of oxide distributions on micromechanical behavior is revealed.

[1] Bc. Andrea Špaková, Orcid 0009-0008-2784-3995: Department of Mechanics, Faculty of Civil Engineering, Czech Technical University, Thákurova 2077/7; 166 29, Prague 6; CZ, spakoand@student.cvut.cz
[2] Ing. Jiří Němeček, Ph.D., Orcid 0000-0002-5635-695X: Department of Mechanics, Faculty of Civil Engineering, Czech Technical University, Thákurova 2077/7; 166 29, Prague 6; CZ, jiri.nemecek.1@fsv.cvut.cz
[3] Prof. Ing. Jiří Němeček, Ph.D., DSc., Orcid 0000-0002-3565-8182: Department of Mechanics, Faculty of Civil Engineering, Czech Technical University, Thákurova 2077/7; 166 29, Prague 6; CZ, jiri.nemecek@fsv.cvut.cz

ISSN: 1805-8256, doi: 10.21495/em2026-133

2. Experiments and methods

2.1. Sample preparation

A cement paste with a water–cement ratio of 0.5 was prepared using blended Portland cement CEM II/B-M (V-LL) 32.5 R with an addition of 18 wt.% fly ash. The prepared paste mixture was poured into plastic cylindrical molds of 27 mm diameter and 70 mm height, followed by mechanical vibration. Once hardened, the samples were removed from the molds and cut to a height of approximately 19 mm using a Struers Secotom-50 diamond saw.

The sample surfaces were polished for nanoindentation and SEM analysis using a multi-step polishing procedure with SiC foils of grit sizes from 1200 to 4000 on a Struers Tegramin 20 machine, following the procedure described in Němeček et al. (2020).

2.2. Nanoindentation

Nanoindentation was conducted using a Hysitron TI-980 equipped with a Berkovich diamond tip. Eight grids of 22 × 22 indents, with a spacing of 2.5 µm, were performed on the sample using accelerated property mapping with a trapezoidal loading protocol, each test lasting 0.1 s as described in Němeček et al. (2020). Young's modulus, E, was evaluated from the measured load-displacement curves using the method of Oliver and Pharr (1992). An example of a performed mechanical map is shown in Fig. 1.

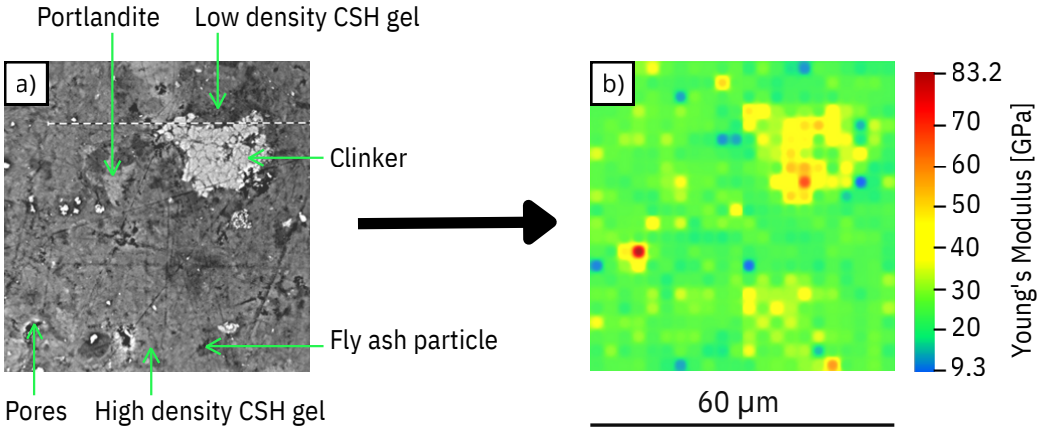

Fig. 1: a) SEM–BSE image of the cement paste area subjected to nanoindentation, with individual cement phases identified; b) Visual Young's modulus map of the same area.

2.3. Energy Dispersive X-ray Spectroscopy

SEM–BSE images at 2000× magnification, with a size of 110×110 µm^2, were taken to perform EDS line scans along the 60 µm lines of mechanical indents location. The scans were acquired with a pixel resolution of 107 nm, using 10 passes at a scanning velocity of 10 ms per pixel, with a BSD full detector and an accelerating voltage of 15 kV. Fig. 2 shows the overlap of the SEM–BSE and mechanical maps.

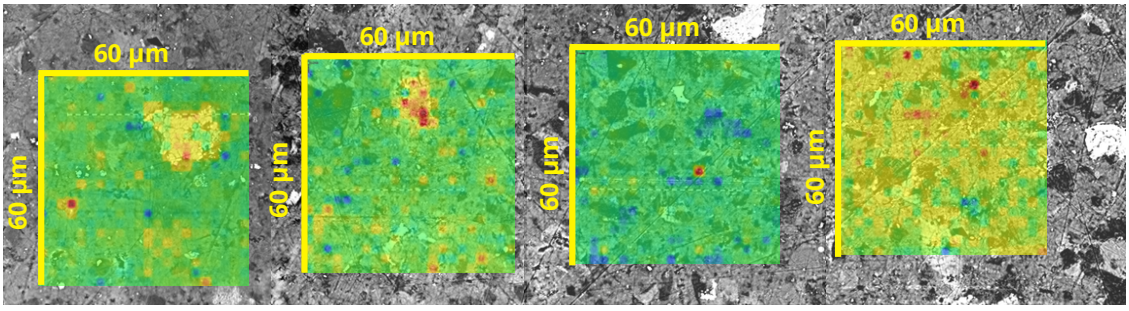

Fig. 2: Overlap of SEM-BSE images and the area of nanoindented grids of the tested sample.

3. Results and discussion

Fig. 3 presents the line profiles results of the elemental composition of Ca, Si, S, and Al obtained from EDS line scans, the calculated (Ca–S)/Si and Al/Si ratios, the BSE image, and the local Young's modulus values from nanoindentation. Based on all these line profiles, the segmentation into individual phases was performed. This procedure enabled the identification of distinct cement paste phases, including HD C-S-H, LD C-S-H gels, CH, and hydrated fly ash with Al content above and below 9%.

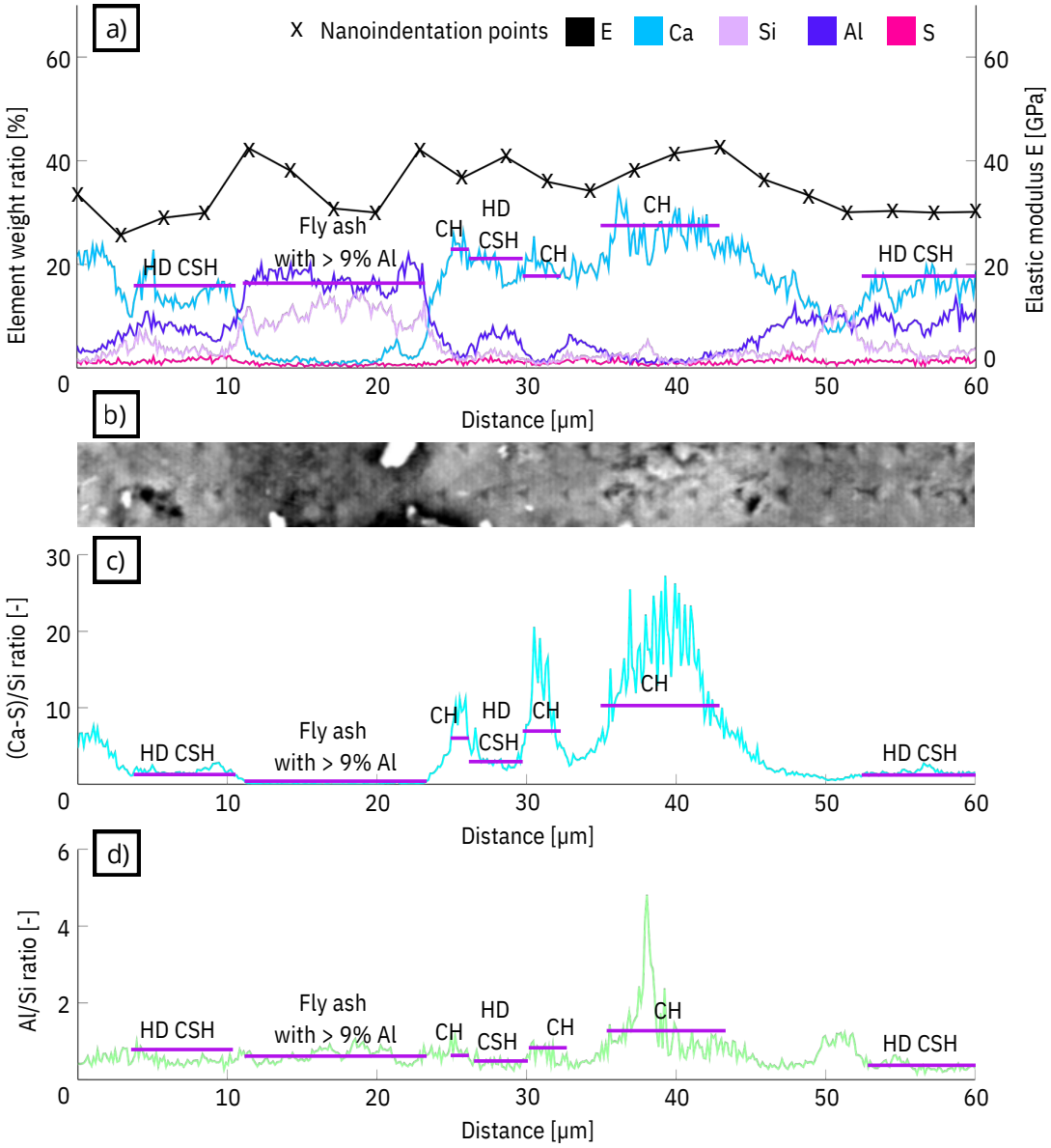

Fig. 3: a) Element profiles from EDS line scans with corresponding Young's modulus values measured at the nanoindentation points along the same profile; b) SEM–BSE image showing the EDS line scan; c) (Ca–S)/Si and d) Al/Si ratios calculated from the EDS data along the nanoindentation profile.

The mean values of the separated phases are summarized in Table 1. The differences in micromechanical behavior of the individual phases correlate well with variations in chemical composition. In particular, fly ash with high Al content (>9%) exhibits a lower Young's modulus (24.4 GPa) compared to fly ash with low Al content (<9%) (32.4 GPa), which is also reflected in the (Ca–S)/Si and Al/Si ratios. The Young's modulus values of the separated phases are consistent with literature reports Hu (2015); Zhu et al. (2007); Mondal et al. (2007); Jennings et al. (2007).

Specifically, the Young's modulus of LD C–S–H gel measured in this study (24.9 $\pm$ 0.3 GPa) closely matches Hu's reported value of 25 GPa for a cement paste with a water-to-cement ratio of 0.4. Similarly,

the HD C–S–H gel exhibits a modulus of 31.2 ± 2.9 GPa, compared to Hu's 30.9 GPa. Furthermore, the stiffness of portlandite in this study (36.4 ± 3.4 GPa) is in close agreement with literature-reported values of 36–43 GPa Hu (2015); Mondal et al. (2007).

Tab. 1: Correlation results of nonoindentation and EDS line scans for various cement phases.

	C-S-H gel		Portlandite	Fly ash content with	
Observed property [%]	low density	high density	-	< 9% Al	> 9% Al
E [GPa]	24.9 ± 0.3	31.2 ± 2.9	36.4 ± 3.4	32.4 ±6.1	24.4± 4.0
(Ca-S)/Si ratio [-]	2.07 ± 0.41	2.82 ± 1.26	14.98 ± 3.16	0.015 ± 0.13	9.48 ± 0.35
Al/Si ratio [-]	0.84 ± 0.35	0.56 ± 0.28	0.58 ± 0.30	0.88 ± 0.38	5.83 ± 0.34

4. Conclusions

This study demonstrates that combining local chemical composition analysis (Ca, Si, S, and Al) from EDS line scans with BSE imaging is highly effective for distinguishing micromechanical properties in blended cement paste. The calculated (Ca–S)/Si and Al/Si ratios served as reliable indicators for phase identification, enabling segmentation into distinct phases such as LD and HD C–S–H gels, Portlandite, and hydrated fly ash. The measured Young's modulus values (LD C–S–H: 24.9 ± 0.3 GPa; HD C–S–H: 31.2 ± 2.9 GPa; Portlandite: 36.4 ± 3.4 GPa) are in close agreement with literature, validating the approach.

Acknowledgments

This work was financially supported by the Czech Science Foundation under grant number 26-22195S and Grant Agency of the Czech Technical University in Prague (SGS25/083/OHK1/2T/11).

References

Hilloulin, B., Robira, M., and Loukili, A. (2018) Coupling statistical indentation and microscopy to evaluate micromechanical properties of materials: Application to viscoelastic behavior of irradiated mortars. *Cement and Concrete Composites*, 94, pp. 153–165.

Hu, C. (2015) Nanoindentation as a tool to measure and map mechanical properties of hardened cement pastes. *MRS Communications*, 5, 1, pp. 83–87.

Jennings, H. M., Thomas, J. J., Gevrenov, J. S., Constantinides, G., and Ulm, F.-J. (2007) A multi-technique investigation of the nanoporosity of cement paste. *Cement and Concrete Research*, 37, 3, pp. 329–336.

Li, L., Yang, J., Li, H., and Du, Y. (2021) Insights into the microstructure evolution of slag, fly ash and condensed silica fume in blended cement paste. *Construction and Building Materials*, 309, pp. 125044.

Luo, Z., Li, W., Wang, K., and Shah, S. P. (2018) Research progress in advanced nanomechanical characterization of cement-based materials. *Cement and Concrete Composites*, 94, pp. 277–295.

Mondal, P., Shah, S. P., and Marks, L. (2007) A reliable technique to determine the local mechanical properties at the nanoscale for cementitious materials. *Cement and Concrete Research*, 37, 10, pp. 1440–1444.

Němeček, J., Králík, V., and Vondřejc, J. (2013) Micromechanical analysis of heterogeneous structural materials. *Cement and Concrete Composites*, 36, pp. 85–92.

Němeček, J., Lukeš, J., and Němeček, J. (2020) High-speed mechanical mapping of blended cement pastes and its comparison with standard modes of nanoindentation. *Materials Today Communications*, 23, pp. 100806.

Oliver, W. and Pharr, G. (1992) An improved technique for determining hardness and elastic modulus using load and displacement sensing indentation experiments. *Journal of materials research*, 7, 6, pp. 1564–1583.

Pelisser, F., Gleize, P. J. P., and Mikowski, A. (2012) Effect of the ca/si molar ratio on the micro/nanomechanical properties of synthetic csh measured by nanoindentation. *The Journal of physical chemistry C*, 116, 32, pp. 17219–17227.

Zhu, W., Hughes, J. J., Bicanic, N., and Pearce, C. J. (2007) Nanoindentation mapping of mechanical properties of cement paste and natural rocks. *Materials characterization*, 58, 11-12, pp. 1189–1198.

32nd International Conference
ENGINEERING MECHANICS 2026
Medlov, Czech Republic, May 11 – 13, 2026

FINITE ELEMENT SIMULATION OF INCOMPRESSIBLE AIRFLOW THROUGH HUMAN VOCAL FOLDS

Vacek K.[1], **Sváček P.**[2],

Abstract: *This study investigates incompressible airflow through the human vocal folds. The fluid motion is formulated within the arbitrary Lagrangian–Eulerian (ALE) framework to account for the moving computational domain. The governing equations are discretized using the finite element method (FEM) with Taylor–Hood elements. To ensure numerical stability in convection-dominated regimes, streamline upwind Petrov–Galerkin (SUPG) and grad–div stabilization techniques are employed. The proposed numerical framework is applied to simulations with prescribed vocal fold motion based on a kinematic model. Numerical results are validated against available experimental data for the static M5 vocal folds geometry, showing good agreement. In addition, a simulation of the soft voice regime is presented.*

Keywords: Finite element method, Taylor-Hood element, Vocal folds, Soft voice

1. Introduction

Fluid–structure interaction (FSI) plays a key role in many scientific and engineering applications, including biomechanics, where it is essential to understand airflow–tissue interaction during human phonation. In this process, incompressible airflow from the lungs induces vibrations of the vocal folds, and accurate numerical modeling is crucial to studying voice production mechanisms and supporting experimental and clinical research, see Kumar and Svec (2019).

This paper focuses on the numerical simulation of incompressible airflow interacting with the vocal folds in the M5 geometry, see Scherer et al. (2001). The flow is governed by the incompressible Navier–Stokes equations, while the motion of the vocal folds is prescribed using a kinematic mucosal wave model, see Kumar and Svec (2019). The interaction with the moving boundaries is treated within the arbitrary Lagrangian–Eulerian (ALE) framework, allowing a consistent description of the time-dependent computational domain, see Vacek and Sváček (2025) and John (2016). Challenges such as convection-dominated flow and strong outflow effects are addressed.

The governing equations are discretized using the finite element method with Taylor–Hood elements. To ensure the numerical stability under phonation conditions, the streamline upwind Petrov–Galerkin (SUPG) and the grad–div stabilization are employed, see e.g. John (2016). The proposed framework is applied to soft-voice phonation simulations and validated against experimental pressure measurements for the M5 geometry, demonstrating its suitability for analyzing airflow-induced loading in vocal folds dynamics.

2. Governing equations

This section presents the mathematical formulation of the fluid-structure interaction problem considered in this study.

Let $\Omega_t \subset \mathbb{R}^2$ denote a bounded, time-dependent computational 2D domain with boundary $\partial\Omega_t = \Gamma_D \cup \Gamma_{D,\text{wall}} \cup \Gamma_O \cup \Gamma_{W_t}$, where Γ_D, $\Gamma_{D,\text{wall}}$, Γ_O, and Γ_{W_t} represent the inlet, walls, outlet, and movement of the vocal fold, respectively, see Fig. 1.

[1] Ing. Karel Vacek.: Czech Technical University Department of Technical Mathematics, Karlovo náměstí 13, 121 35 Praha 2, karel.vacek@fs.cvut.cz
[2] prof. RNDr. Petr Sváček, Ph.D.: Czech Technical University Department of Technical Mathematics, Karlovo náměstí 13, 121 35 Praha 2, petr.svacek@fs.cvut.cz

ISSN: 1805-8256, doi: 10.21495/em2026-137

The fluid motion is described within the arbitrary Lagrangian-Eulerian (ALE) framework, see Vacek and Sváček (2025). The incompressible Navier-Stokes equations in ALE form read: find the velocity $\boldsymbol{u} : \Omega_t \to \mathbb{R}^2$ and pressure $p : \Omega_t \to \mathbb{R}$ such that

$$\frac{D^A}{Dt}\boldsymbol{u} + ((\boldsymbol{u} - \boldsymbol{w}) \cdot \nabla)\boldsymbol{u} - \nu\Delta\boldsymbol{u} + \nabla p = 0, \qquad \nabla \cdot \boldsymbol{u} = 0, \tag{1}$$

where ν is the kinematic viscosity, $\frac{D^A}{Dt}$ denotes the ALE time derivative, and $\boldsymbol{w}$ is the domain velocity.

The system is supplemented with the initial condition $\boldsymbol{u}(x, 0) = \boldsymbol{u}_0$ in Ω_0 and boundary conditions $\boldsymbol{u} = \boldsymbol{g}$ on Γ_D, $\boldsymbol{u} = \boldsymbol{w}$ on Γ_{W_t}, together with a directional "do-nothing" condition at the outlet, $-(p - p_{\text{ref}})\boldsymbol{n} + \nu\frac{\partial \boldsymbol{u}}{\partial \boldsymbol{n}} - \frac{1}{2}(\boldsymbol{u} \cdot \boldsymbol{n})_-\boldsymbol{u} = 0$ on Γ_O, which stabilizes backflow while preserving physically consistent outlet behavior, see John (2016).

The motion of the vocal fold is prescribed using a kinematic mucosal wave model based on the M5 geometry, see Scherer et al. (2001). The model describes phase-delayed oscillatory motion of surface points to represent upward propagation of the mucosal wave and is suitable for soft voice conditions, see Kumar and Svec (2019). The vertical wave velocity is given by $c = \frac{360\, f_0\, T}{\phi}$, where f_0 is the fundamental frequency, T the vertical thickness of the vocal fold, and ϕ the phase delay.

The trajectory of a surface point $P_i = (x_i, y_i)$ is prescribed as

$$x_i(t) = x_i^0 + A_i \sin\left(2\pi f_0 \left(t - \frac{d}{c}i\right)\right), \qquad y_i(t) = y_i^0 + aA_i \cos\left(2\pi f_0 \left(t - \frac{d}{c}i\right)\right), \tag{2}$$

where (x_i^0, y_i^0) are the initial coordinates, A_i the local amplitude, a the amplitude ratio and d the spacing between the surface points, for more details see Kumar and Svec (2019).

3. Discretization method

Problem (1) is semi-discretized in time using a constant step Δt. At times $t_n = n\Delta t$, the velocity, pressure and domain velocity are approximated by $\boldsymbol{u}^n(x) \approx \boldsymbol{u}(x, t_n)$, $p^n(x) \approx p(x, t_n)$, and $\boldsymbol{w}^{n+1}(x) \approx \boldsymbol{w}(x, t_{n+1})$. Using the BDF2 scheme, the ALE formulation yields

$$\begin{aligned} \frac{3\boldsymbol{u}^{n+1} - 4\tilde{\boldsymbol{u}}^n + \tilde{\boldsymbol{u}}^{n-1}}{2\Delta t} + ((\boldsymbol{u}^{n+1} - \boldsymbol{w}^{n+1}) \cdot \nabla)\boldsymbol{u}^{n+1} - \nu\Delta\boldsymbol{u}^{n+1} + \nabla p^{n+1} = 0, \\ \nabla \cdot \boldsymbol{u}^{n+1} = 0, \end{aligned} \tag{3}$$

where $\tilde{\boldsymbol{u}}^i = \boldsymbol{u}^i \circ A_{t_i} \circ A_{t_{n+1}}^{-1}$ denotes the ALE mapping, see Vacek and Sváček (2025).

The weak formulation is considered at t_{n+1} with $\boldsymbol{u} = \boldsymbol{u}^{n+1}$, $\boldsymbol{w} = \boldsymbol{w}^{n+1}$, $p = p^{n+1}$, and $\Omega = \Omega_{t_{n+1}}$. The test spaces are

$$\boldsymbol{\mathcal{V}} = \{\boldsymbol{\varphi} \in \boldsymbol{H}^1(\Omega) : \boldsymbol{\varphi} = 0 \text{ on } \Gamma_D \cup \Gamma_W\}, \qquad \mathcal{Q} = L^2(\Omega).$$

Defining the bilinear and linear forms

$$\begin{aligned} a(U^*, U, V) &= \tfrac{3}{2\Delta t}(\boldsymbol{u}, \boldsymbol{v})_\Omega + \nu(\nabla\boldsymbol{u}, \nabla\boldsymbol{v})_\Omega + c(\boldsymbol{u}^* - \boldsymbol{w}, \boldsymbol{u}, \boldsymbol{v}) \\ &\quad - (p, \nabla \cdot \boldsymbol{v})_\Omega - (\nabla \cdot \boldsymbol{u}, q)_\Omega, \qquad (4) \\ F(V) &= \tfrac{1}{2\Delta t}(4\tilde{\boldsymbol{u}}^n - \tilde{\boldsymbol{u}}^{n-1}, \boldsymbol{v})_\Omega, \qquad (5) \end{aligned}$$

the weak problem reads: find $U = (\boldsymbol{u}, p) \in \boldsymbol{\mathcal{V}} \times \mathcal{Q}$ such that $a(U, U, V) = F(V) \quad \forall V \in \boldsymbol{\mathcal{V}} \times \mathcal{Q}$. The nonlinear convective term is treated by Oseen linearization, see John (2016).

Let τ_h be an admissible triangulation of Ω. The spatial discretization employs the Taylor–Hood element with quadratic (P_2) velocity and linear (P_1) pressure approximations: $\boldsymbol{\mathcal{V}}_h \subset \boldsymbol{\mathcal{V}}$, $\mathcal{Q}_h \subset \mathcal{Q}$. This element pair satisfies the inf-sup condition, though incompressibility is enforced only in a discrete sense, see John (2016) (this issue is treated using the well-known grad–div stabilization). The discrete problem reads: find $U_h \in \boldsymbol{\mathcal{V}}_h \times \mathcal{Q}_h$ such that

$$a(U_h^*, U_h, V_h) = F(V_h), \quad \forall V_h \in \boldsymbol{\mathcal{V}}_h \times \mathcal{Q}_h. \tag{6}$$

For flows dominated by convection, SUPG stabilization is applied to the convective term, see John (2016).

4. Numerical results

This section presents numerical results obtained with the proposed framework. The approach is first validated for airflow at ambient temperature through a static vocal fold configuration by comparing the pressure distribution along the fold surface with experimental data from Scherer et al. (2001) (the symmetric case of M5 geometry with divergent angle 10°). The method is then applied to a soft-voice phonation regime to investigate unsteady flow features. The computational domain and boundary conditions are shown in

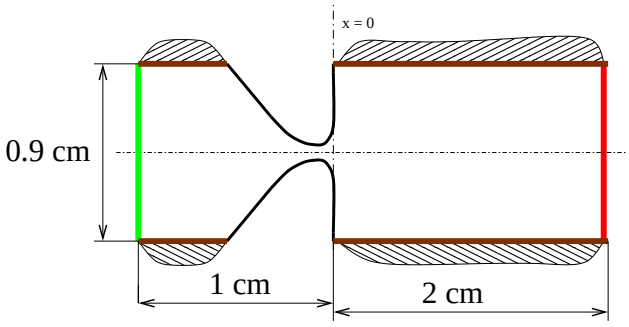

Fig. 1: Computational domain and boundary conditions. Green indicates the inlet Γ_D with prescribed velocity, brown the rigid walls $\Gamma_{D,\text{wall}}$, black the moving vocal folds Γ_{W_t}, and red the outlet Γ_O with a directional do-nothing condition.

Fig. 1, where the channel depth is 1.1 cm. The discretization consists of 40 572 elements and 20 653 vertices, resulting in 184 407 degrees of freedom. Boundary layer refinement is applied near the vocal fold surfaces. The M5 geometry represents an idealized convergent–divergent glottal channel capturing the essential features of human phonation.

For the static configuration, Fig. 2 shows the pressure distribution along the vocal-fold surface for inlet-to-outlet pressure drops of 306 Pa, 510 Pa, and 1020 Pa ($x = 0$ is at the glottal exit). The numerical results reproduce the characteristic pressure drop in the glottal constriction and show good qualitative agreement with the experimental measurements.

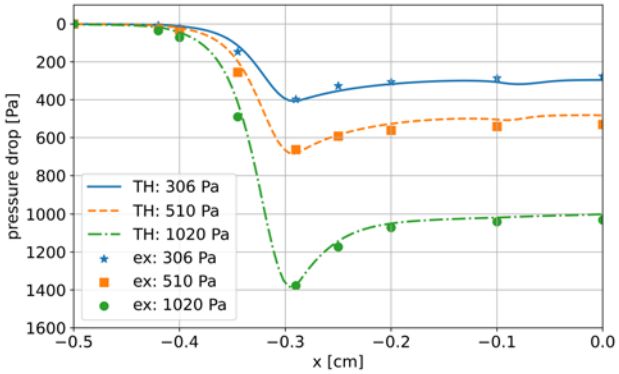

Fig. 2: Local pressure drop along the vocal fold surface in the static M5 geometry, with $\Delta p = 0$ at the inlet. Taylor–Hood (TH) simulations are shown as lines, and experimental data as symbols, for inlet pressures of 306 Pa, 510 Pa, and 1020 Pa.

The validated model is subsequently applied to a soft-voice phonation case with prescribed vocal fold motion based on a kinematic model, see Kumar and Svec (2019). The prescribed inlet velocity leads to the 0.1 l/s flow rate. Fig. 3 shows snapshots of the velocity magnitude in a closed channel and a fully open configuration. In addition, there is the pressure along the centerline over time. The channel is displayed in a vertical orientation to facilitate physical interpretation; gravity effects are neglected and therefore the orientation does not influence the flow dynamics. A high-speed glottal jet downstream of the folds becomes unstable in the supraglottal region, generating large-scale vortical structures. The occurrence of backflow motivates the use of a directional "do-nothing" outlet boundary condition, which improves numerical stability while preserving physically consistent flow behavior.

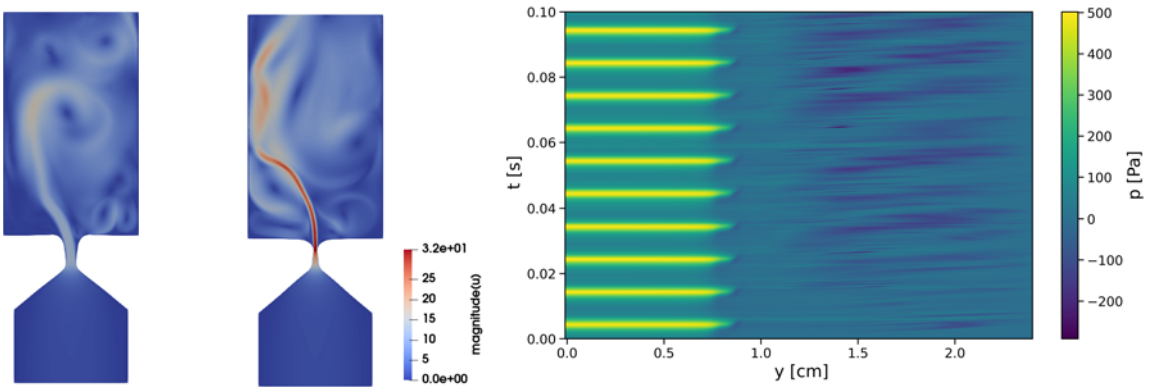

(a) *(b)* *(c)*

Fig. 3: Velocity magnitude $|\boldsymbol{u}|$ at (a) $t = 0.210$ and (b) $t = 0.21135$, and the pressure along the centerline as a function of time (c).

5. Conclusions

A numerical framework for simulating incompressible airflow in human phonation has been presented, focusing on flow through the M5 vocal fold geometry under soft-voice conditions with prescribed vocal fold motion, see Kumar and Svec (2019). The fluid problem is formulated within the arbitrary Lagrangian–Eulerian (ALE) framework and discretized using the finite element method with Taylor–Hood elements, complemented by streamline upwind Petrov–Galerkin (SUPG) and grad–div stabilization to ensure numerical robustness John (2016); Vacek and Sváček (2025).

The approach was validated on a static M5 configuration, where the computed pressure distribution along the vocal fold surface shows good agreement with available experimental measurements Scherer et al. (2001). It was then applied to simulations with prescribed vocal fold motion based on a kinematic mucosal wave model Kumar and Svec (2019). The numerical results capture the formation of a high-speed glottal jet and the development of large-scale vortical structures in the supraglottal region, together with intermittent reverse flow near the outlet.

Acknowledgments

This work was supported by project No. GA 25-15289K of the Czech Science Foundation and by the Czech Technical University in Prague under the grant No. *Grant SGS25/123/OHK2/3T/12* and the grant No. *Grant SGS24/120/OHK2/3T/12*.

References

John, V. (2016) *Finite element methods for incompressible flow problems*, 51 of *Springer Series in Computational Mathematics*. Springer.

Kumar, S. P. and Svec, J. (2019) Kinematic model for simulating mucosal wave phenomena on vocal folds. *Biomedical Signal Processing and Control*, 49, pp. 328–337.

Scherer, R. C., Shinwari, D., De Witt, K. J., Zhang, C., Kucinschi, B. R., and Afjeh, A. A. (2001) Intraglottal pressure profiles for a symmetric and oblique glottis with a divergence angle of 10 degrees. *J. Acoust. Soc. Am.*, 109, 4, pp. 1616–1630.

Vacek, K. and Sváček, P. (2025) Finite element method analysis of flutter: Comparing Scott–Vogelius and Taylor–Hood elements. *Journal of Computational and Applied Mathematics*, 469.

32nd International Conference
ENGINEERING MECHANICS 2026
Medlov, Czech Republic, May 11 – 13, 2026

OPTIMAL STIFFNESS OF MECHATRONIC STIFFNESS

Valášek M.[1], Zavřel J. [2], Nečas M. [3], Vatandas O.E.[4]

Abstract: *The paper deals with the application of the concept of mechatronic stiffness for the design of a mechanism of aircraft wing that is capable to provide both morphing of aircraft wing profile and its aeroelastic control. It requires the wing structure to have both low stiffness for morphing with small forces and high dynamic stiffness with good aeroelastic properties. Such different demands can be satisfied by mechatronic stiffness. The development of mechanism for aircraft wing morphing and its aeroelastic control is briefly described. However, the optimal choice of stiffness of auxiliary construction and its possible deformation is formulated and solved. The optimal stiffness of auxiliary structure of mechatronic stiffness as the key result of the paper is described.*

Keywords: Dynamic stiffness, Mechatronic stiffness, Actuator force authority, Auxiliary structure, Morphing

1. Introduction

The concept of mechatronic stiffness Valasek (2014) has improved the dynamic stiffness of compliant mechanical structures Necas (2007). The advantage of this concept is the efficient use of actuator force when acting on a mechanical structure. The actuator force effect has a transfer ratio of one and higher. Therefore this concept has been extended towards the control of the deformation of the load-bearing structures Valasek (2024). And this extended concept has been applied for design of morphing mechanisms of aircraft wings. The space inside the wing for the construction of the morphing mechanism is limited and this opens the question of the optimal choice of mechatronic stiffnesses, which has not yet been addressed. This paper is devoted to that.

2. Mechatronic stiffness

The concept of mechatronic stiffness originated within a project for suppression of deformation of quill of machine tools. The quill (Fig, 1 left) is a beam with a cutting tool that machines in the cavity of the workpiece. The quill is deformed by gravity and cutting forces, i.e. disturbance forces. Traditionally, this deformation is compensated by a horizontal actuator at the quill root, but then the ratio of disturbance and actuator force is 10 and more. The ideal solution would be a frame support below the disturbance force, but that is not possible because the quill is inside the cavity. This contradiction is resolved by the concept of mechatronic stiffness (Fig. 1 right). The concept is following. Mechanical construction/structure is equipped with concurrent auxiliery structure and both structures are connected in connecting points by

[1] Prof. Ing. Michael Valášek, DrSc.: Czech Technical University in Prague, Faculty of Mechanical Engineering, Center of Aviation and Space Research, Technická 4; 16000 Prague; CZ

[2] Ing. Jan Zavřel, Ph.D.: Czech Technical University in Prague, Faculty of Mechanical Engineering, Department of Mechanics, Biomechanics and Mechatronics, Technická 4; 16000 Prague; CZ

[3] Ing. Martin Nečas, Ph.D. MSc.: Czech Technical University in Prague, Faculty of Mechanical Engineering, Department of Mechanics, Biomechanics and Mechatronics, Technická 4; 16000 Prague; CZ

[4] Prof. Dr. Ing. Osman Ergüven Vatandas: Istanbul Gelisim University, Faculty of Engineering and Architecture, Department of Aeronautical Engineering, Istanbul; Turkey; Czech Technical University in Prague, Faculty of Mechanical Engineering, Center of Aviation and Space Research, Technická 4; 16000 Prague; CZ

ISSN: 1805-8256, doi: 10.21495/em2026-141

one or more actuators that are controlled based on deformation/motion of connecting points The ratio of disturbance and actuator force is 1 and less.

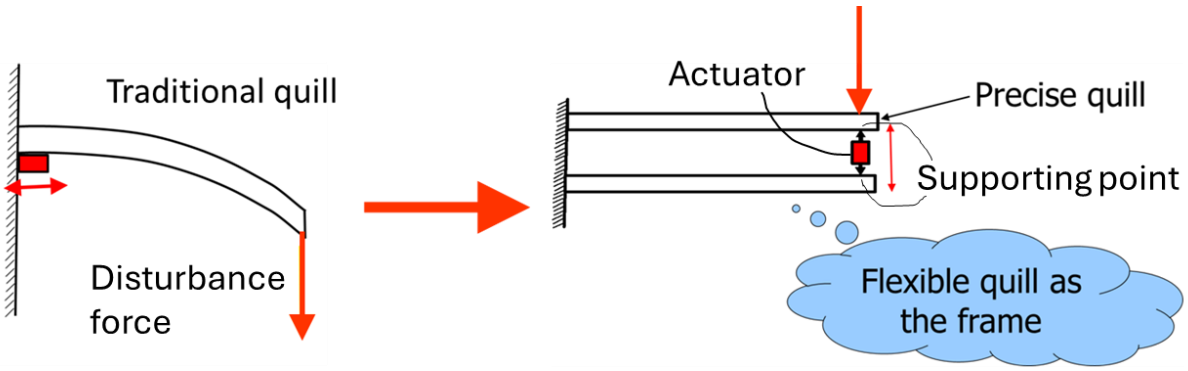

Fig. 1: Concept of mechatronic stiffness.

The comparison of frequency response of both structures from Fig. 1 is in Fig. 2. One actuator removes the influence of one eigenfrequency. Two actuators remove the influence of two eigenfrequencies. The resulting dynamic stiffness is increased by ten times.

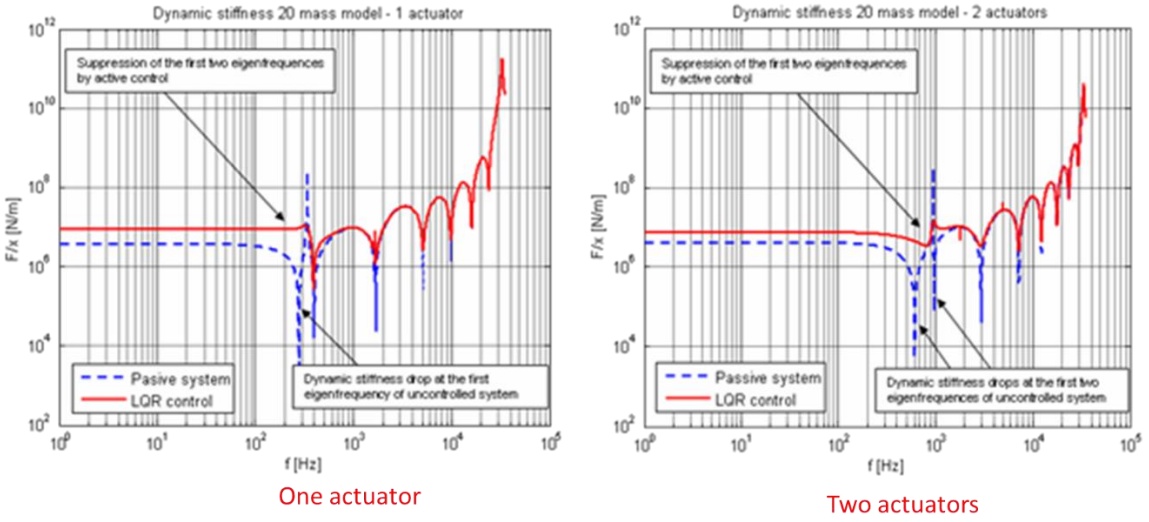

Fig. 2: Frequency response of mechatronic stiffness.

The mechatronic stiffness is advantageously made as a tube in tube (Fig. 3).

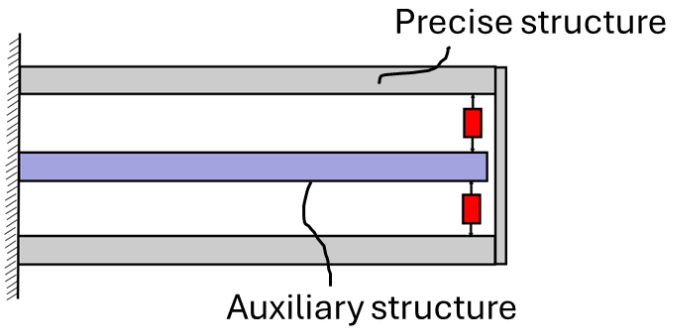

Fig. 3: Mechatronic stiffness as a tube in tube.

3. Mechanisms for control of deformation of structures

The change of shape of structures requires certain deformation force that is equivalent of disturbance force at mechatronic stiffness. The advantage of ratio of disturbance and actuator force being 1 and less is used for concepts of mechanisms for control of deformation of structures. The concept of mechatronic

stiffness as a tube in tube in Fig. 3 can be immediately used for mechanisms for control of deformation of precise structure in Fig. 4. Based on that a morphing mechanism of aircraft wing trailing edge in Fig. 5 was developed. This mechanism provides not only morphing but also aeroelastic control capability.

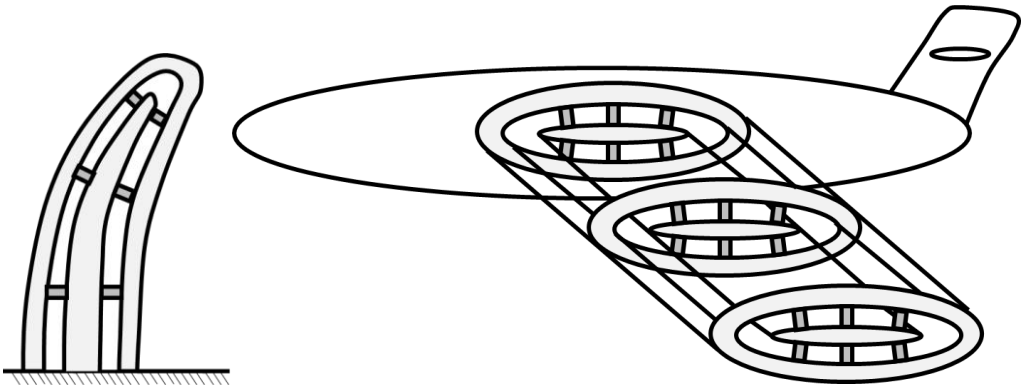

Fig. 4: The concept of mechatronic stiffness used for deformation of blades or wings.

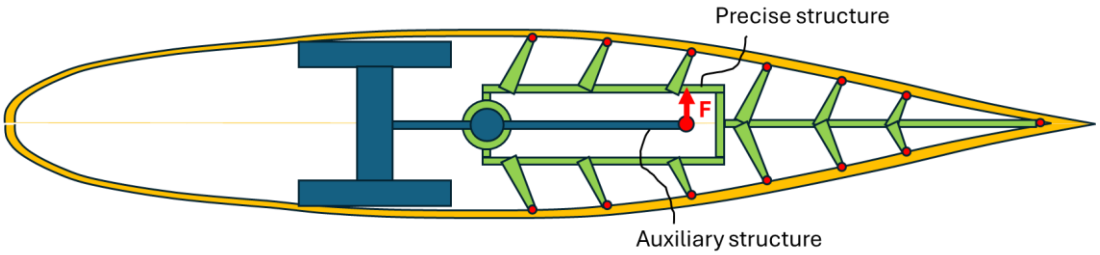

Fig. 5: The morphing mechanism of trailing edge of aircraft wing.

4. Optimal stiffness of auxiliary structure

Thus the mechanism from Fig. 5 has two functions: applying force F and morphing motion. The application of the force F creates the deformation of the auxiliary structure and this deformation is limiting the possible morphing motion (Fig. 6). The deformation of auxiliary structure is given by its thickness and available space for the deformation (Fig. 7).

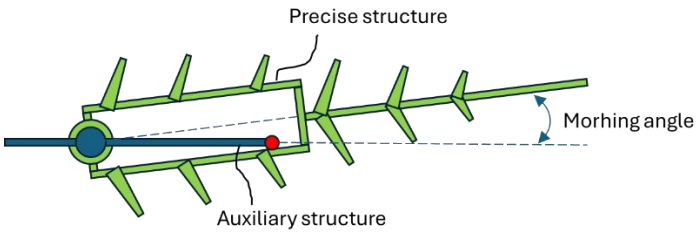

Fig. 6: Limited possible morphing motion.

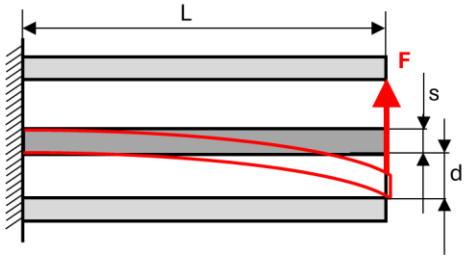

Fig. 7: Deformation of auxiliary structure.

For simplicity let us suppose that both precise and auxiliary structures are beams with rectangular cross sections. The sum of height of auxiliary structure s and the available height for deformation d is limited by the size Lim (Fig. 7)

$$s + d = Lim \tag{1}$$

The maximum possible deformation d of cantilever beam of length L by the force F with width b is

$$d = \frac{FL^3}{3EJ}, \quad J = \frac{1}{12} bs^3 \tag{2}$$

Substituting into (1)

$$s + \frac{4FL^3}{Ebs^3} = Lim \tag{3}$$

Expressing the force F and finding its optimum

$$F = \frac{Eb}{4L^3}(Lim\,s^3 - s^4) \tag{4}$$

$$\frac{dF}{ds} = \frac{Eb}{4L^3}(3Lim\,s^2 - 4s^3) = 0 \tag{5}$$

It gives the optimal size of height s and space d

$$s = \frac{3}{4}Lim, \quad d = \frac{1}{4}Lim \tag{6}$$

The dependence of force F on the thickness s and the extreme is in Fig. 8. It is evident that the optimal choice influences the accessible loading force significantly. The possible ratio <0,27> of optimal/non-optimal forces is quite large.

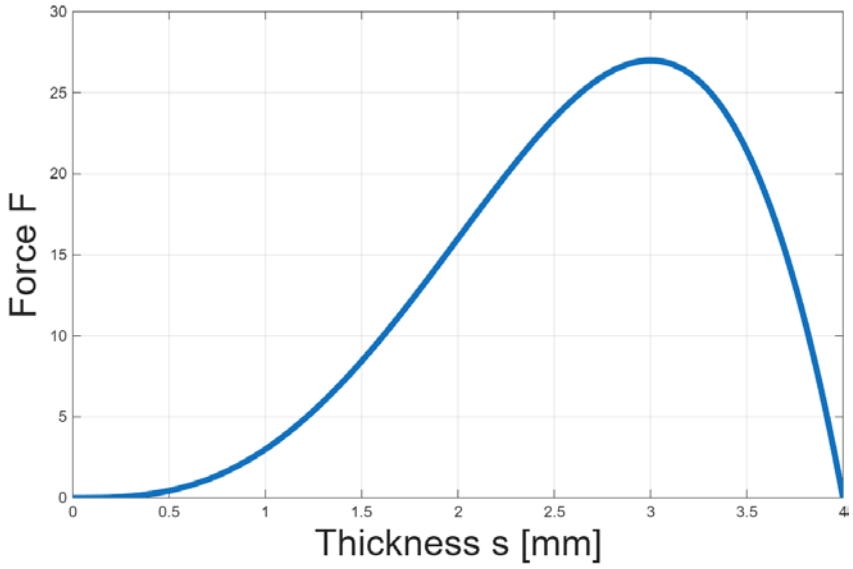

Fig. 8: Dependence of force F on thickness s.

5. Conclusions

The paper describes the optimal dimensions of mechatronic stiffness used for combined mechanism for morphing and aeroelastic control of aircraft wing. The contribution of the optimization is quite large, The development of such mechanism from the concept of mechatronic stiffness is included.

Acknowledgement
This work was possible thanks to the grant released within the Framework Programme for Research and Innovation (2021–2027), grant n◦ 101159722, with project name “Twinning for Excellence in Morphing and Aeromechatronic Wing Control: A Leap Towards Eco-Smart Aviation” acronym (MechaTwing).

References

Necas, M. (2007) Increase of dynamic stiffness of constructions by mechatronic approach, PhD Thesis, CVUT in Prague.

Valasek, M. and Necas, M. (2009) Innovative concept of increasing dynamic stiffness of compliant structures by mechatronic approach. *Bulletin of Applied Mechanics*, *4*(16), pp.129-137.

Nečas, M. and Valášek, M. (2008) Mechatronic stiffness of MIMO compliant branched structures by active control from auxiliary structure. In *Recent Advances in Mechatronics* (pp. 167-172). Berlin, Heidelberg: Springer Berlin Heidelberg.

Valasek, M. (2014) Method of and apparatus for change in rigidity of mechanical structures, Patent CZ304667, UPV

Smrz, M. (2015) Design and properties of mechatronic stiffness, PhD Thesis, CVUT in Prague (in Czech).

Valasek, M. (2024) An equipment to control the deformation of the load-bearing structure, Patent CZ 310279, UPV.

32nd International Conference
ENGINEERING MECHANICS 2026
Medlov, Czech Republic, May 11 – 13, 2026

DESIGN OF AN INFRARED HEATING SYSTEM FOR AUTOMATED FIBER PLACEMENT OF THERMOPLASTIC TAPES

Vomáčko V.[1], **Miller V.**[2]

Abstract: *This paper presents the design and development of an infrared heating system for automated thermoplastic tape winding with in-situ consolidation. The primary objective is to develop a cost-effective alternative to laser-based heating by concentrating infrared radiation from a low-cost source using optical elements. Ray-tracing simulations of several focusing configurations (lenses and mirrors) are performed and their suitability for integration into a compact placement head is evaluated. In parallel with the heating system, a dedicated four-degree-of-freedom tape winding machine is being developed to enable controlled placement on rotationally symmetric components as well as closed-section composite profiles. The system is intended for processing carbon fiber reinforced polypropylene and polyamide tapes.*

Keywords: **Automated Fiber Placement, Thermoplastic composites, Infrared heating, In-situ consolidation, Tape winding**

1. Introduction

Long fiber-reinforced thermoplastic (TP) polymer composites are gaining importance across aerospace, automotive and energy sectors due to their high specific strength, short consolidation cycles, weldability, and potential for recycling (Boon et al., 2021). Unlike thermoset-based composites that require lengthy autoclave curing, thermoplastic matrices can be processed by local melting and consolidation under heat and pressure, enabling single-step manufacturing without post-curing (Yassin and Hojjati, 2018). Additional advantages include virtually unlimited shelf life of the prepreg material and inherent resistance to most solvents and chemicals.

Automated Fiber Placement (AFP) and thermoplastic tape winding are computer-aided manufacturing processes for automated lamination of TP composites. In AFP, a prepreg tape is deposited onto a tool surface by a placement head mounted on a robotic manipulator. The tape and the substrate are simultaneously heated at the nip point, while a consolidation roller applies pressure to achieve in-situ consolidation (ISC). AFP is predominantly used in aerospace for large, complex structures (Lukaszewicz et al., 2012). When the same principle is applied to rotational parts — tubes, pressure vessels, drive shafts — the process is commonly referred to as thermoplastic tape winding (TTW). TTW is distinguished from classical filament winding by the use of fully impregnated prepreg tapes and ISC rather than wet winding with subsequent curing (Yassin and Hojjati, 2018). A key advantage of TTW is that the continuous nature of the winding process eliminates the need for tape cutting between courses, simplifying head design and increasing process efficiency for axisymmetric geometries.

The quality of in-situ consolidated parts depends critically on the thermal history at the nip point. The tape must be heated above the melting temperature of the semi-crystalline matrix to enable intimate contact and molecular diffusion between layers. Insufficient heating leads to poor interlaminar bonding, while excessive temperatures cause thermal degradation of the polymer (Stokes-Griffin and Compston, 2015). The achievable placement speed is therefore directly limited by the power density and controllability of the heat source. Common heat sources for ISC include hot-gas torches, diode lasers, xenon flash lamps,

[1] Ing. Václav Vomáčko, Ph.D.: VUTS, a.s., Svárovská 619 1, 460 01 Liberec; CZ, vaclav.vomacko@vuts.cz
[2] Ing. Vojtěch Miller: Technical University of Liberec, Faculty of Mechanical Engineering, Studentská 1402/2, 461 17 Liberec; CZ, vojtech.miller@tul.cz

ISSN: 1805-8256, doi: 10.21495/em2026-145

and infrared heaters (Yassin and Hojjati, 2018; Calawa and Nancarrow, 2007). Hot-gas torches offer low capital cost but suffer from poor energy efficiency, slow thermal response, and difficulty in confining the heated zone. Diode lasers provide high power density, precise beam shaping, and fast response, making them the dominant choice for high-performance applications in the aerospace industry, but their capital cost remains a significant barrier to wider adoption. Standard infrared heaters are the most affordable option; however, their extended radiating area and limited focusing capability result in insufficient power density at the nip point for practical placement speeds (Calawa and Nancarrow, 2007). This motivates the development of optimized IR heating systems that could bridge the gap between cost and performance. The goal is to concentrate the radiation from a low-cost IR source onto the nip point area using a system of optical elements, achieving the power density needed for ISC while keeping investment costs at a fraction of laser-based systems.

2. IR heating – optical simulation study

To evaluate the feasibility of focused IR heating, ray-tracing simulations were performed in Zemax OpticStudio. A medium-wave flat-panel ceramic IR emitter was used as the source model. The key metric was the irradiance distribution on a target area representative of the tape at the nip point. Several optical configurations were investigated. A dual-lens refractive system (Fig. 1a) and an off-axis parabolic mirror (Fig. 1b) were modeled. Both configurations demonstrated an increase in power density at the tape of approximately 10–15 % compared to the unfocused emitter; however, the resulting concentration remained below what is needed for practical winding speeds with thermoplastic matrices. In addition, both configurations presented practical limitations: the lens system suffered from broadband chromatic aberration, absorption losses at elevated temperatures, and difficulty fitting within the compact placement head envelope; the mirror offered better spectral efficiency but required a physically large reflector that obstructed the tape path. These results indicated that conventional focusing elements alone are insufficient, and further optimization of the heating system design is ongoing.

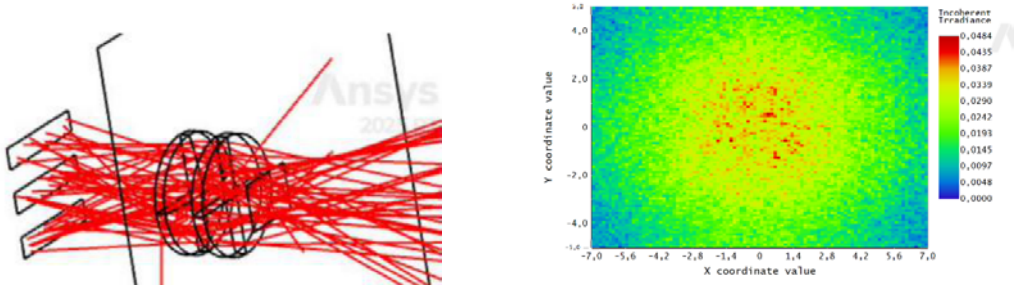

Fig. 1: Ray-tracing simulations of evaluated IR focusing configurations (Zemax OpticStudio): (a) refractive lens configuration, (b) intensity distribution on the tape.

3. Tape winding machine design

A dedicated tape winding test bench has been designed as a self-contained station for manufacturing rotationally symmetric TP composite parts such as tubes and cylindrical shells (Fig. 2). Four-degree-of-freedom configuration was selected: mandrel rotation, horizontal and vertical traverse of the placement head, and head rotation about a vertical axis. The station accommodates mandrels of 30–300 mm diameter and 300–1,500 mm length, with tape placement angles from 0° (axial placement) to ±90° (hoop winding) relative to the mandrel axis.

The machine frame is constructed from aluminum profiles and supports a precision-machined base plate carrying the mandrel drive and support system. The mandrel is held between a three-jaw chuck and a tailstock with a pneumatic quill that accommodates thermal expansion during processing. The mandrel rotation is driven by a servo motor through a gearbox to provide sufficient torque across the full range of winding speeds. The placement head integrates a tape unwinding and feeding mechanism with servo-driven rollers and controlled spool braking, a pneumatic consolidation roller, and the IR heating assembly. The entire head is mounted on a servo-driven vertical linear guide for automatic adaptation to varying mandrel

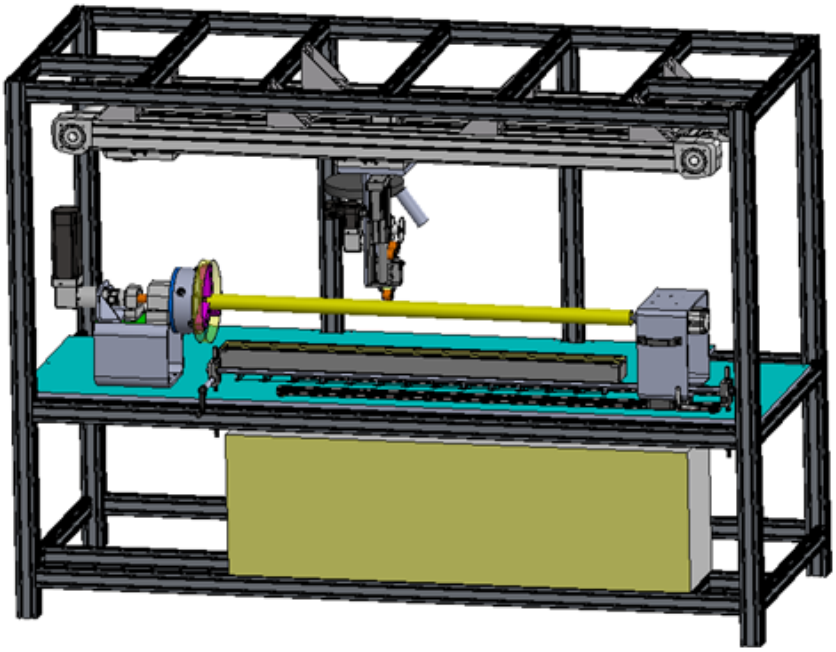

Fig. 2: 3D model of the tape winding test bench for thermoplastic composite manufacturing with IR heating.

diameters and for production of slightly tapered geometries. The working space is enclosed by transparent polycarbonate safety panels with interlocked doors.

Similar to the heated build plate used in fused filament fabrication, the mandrel is heated to maintain an elevated substrate temperature during winding. This is particularly important for semi-crystalline thermoplastic matrices, where controlled cooling influences the degree of crystallinity and consequently the mechanical properties of the final laminate (James and Black, 1996). Temperature monitoring is performed by a non-contact IR pyrometer integrated into the placement head, providing real-time feedback for closed-loop power regulation of the heating system.

4. Target applications and materials

The machine is designed to produce rotationally symmetric parts (tubes, cylindrical shells, conical sections) as well as open profiles, with a maximum part length of 1,500 mm. While the primary focus is on thermoplastic tape winding with in-situ consolidation, the machine architecture is also compatible with thermoset prepreg tapes. The initial target thermoplastic materials are carbon fiber reinforced polypropylene (CF-PP) tapes and carbon fiber reinforced polyamide (CF-PA6, CF-PA12) tapes. These materials are increasingly relevant for automotive, sporting goods and industrial applications where good mechanical properties, chemical resistance, and short cycle times are required (Boon et al., 2021).

5. Conclusion

An automated tape winding machine with a novel infrared heating system for in-situ consolidation of thermoplastic composites is under development. The optical simulation study confirmed that conventional focusing elements (lenses, mirrors) can increase the IR power density at the tape surface compared to an unfocused emitter, but the achievable concentration remains below the threshold required for practical winding speeds with thermoplastic matrices. The project is therefore pursuing an alternative optical delivery concept that promises significantly higher energy concentration at the nip point. The four-degree-of-freedom test bench provides the flexibility needed for a wide range of laminate geometries on rotationally symmetric and profiled parts.

Acknowledgments

This work is co-financed with the state support of the Technology Agency of the Czech Republic within the SIGMA Programme, project No. TQ15000291.

References

Boon, Y. D., Joshi, S. C., and Bhudolia, S. K. (2021) Review: Filament winding and automated fiber placement with in situ consolidation for fiber reinforced thermoplastic polymer composites. *Polymers*, 13, 12, pp. 1951.

Calawa, R. and Nancarrow, J. (2007) Medium wave infrared heater for high-speed fiber placement. In *SAE Technical Paper*. pp. 2007–01–3843.

James, D. L. and Black, W. Z. (1996) Thermal analysis of continuous filament-wound composites. *Journal of Thermoplastic Composite Materials*, 9, 1, pp. 54–75.

Lukaszewicz, D. H.-J. A., Ward, C., and Potter, K. D. (2012) The engineering aspects of automated prepreg layup: History, present and future. *Composites Part B: Engineering*, 43, 3, pp. 997–1009.

Stokes-Griffin, C. M. and Compston, P. (2015) The effect of processing temperature and placement rate on the short beam strength of carbon fibre–peek manufactured using a laser tape placement process. *Composites Part A: Applied Science and Manufacturing*, 78, pp. 274–283.

Yassin, K. and Hojjati, M. (2018) Processing of thermoplastic matrix composites through automated fiber placement and tape laying methods. *Journal of Thermoplastic Composite Materials*, 31, 12, pp. 1676–1725.

32nd International Conference
ENGINEERING MECHANICS 2026
Medlov, Czech Republic, May 11 – 13, 2026

BONE REMODELLING AROUND IMPLANT – TIME EFFECTIVE ALGORITHM

Votava T.[1], Marcián P.[2], Košková O.[3], Fuis V.[4], Wolff J.[5]

Abstract: *Numerical simulation of bone remodelling around implants is computationally demanding, especially for models based on high-resolution micro-CT data. Traditional approaches either reduce model resolution, which limits accuracy at the microstructural level, or employ voxel-based models that significantly increase computational cost due to stress concentration effects. This study presents a hybrid computational approach that combines an irregular finite element mesh for stress–strain analysis with a regular mesh for efficient stimulus calculation. Stress and strain energy density values are transferred between the two domains using transformation matrices. Bone remodelling is simulated using the adapted Huiskes–Weinans. The method was demonstrated on a two-dimensional model of trabecular and cortical bone surrounding a cranial fixator screw. Results show that the proposed approach significantly reduces computational time while preserving biologically relevant stimulus evaluation and expected remodelling behaviour. The method provides an efficient and accurate alternative for large-scale bone remodelling simulations.*

Keywords: Bone remodelling, Implant, FFT, Micro-CT

1. Introduction

Solving bone modelling/remodelling simulations around an implant using Finite element method (FEM) is a time-consuming issue. Bone remodelling process is described by a differential equation, which is solved in a discretized form using an iterative method. To obtain the final state, thousands of iterations must be performed. For large computational models, especially those based on micro-CT data, this may require months of computation (due to large number of nodes).

There are several ways to reduce computational time. One option is to decrease the resolution of the computational model, which is typically derived from CT images. Although this approach cannot capture the final distribution at the microstructural level, it significantly reduces the time required to solve the stress–strain state. However, this simplification complicates bone remodelling simulations. The mechanical stimulus, defined as a weighted sum of strain energy density sensed by osteocytes (Weinans 1992), is evaluated at computational nodes that generally do not coincide with the actual locations of osteocytes. As a result, stimulus evaluation becomes more complex and may lead to increased computational time.

[1] Ing. Tomáš Votava, Dis.: Institute of Solid Mechanics, Mechatronics and Biomechanics, Brno University of Technology, Technická 2896/2; 616 69, Brno; CZ, 200956@vutbr.cz

[2] Ing. Petr Marcián, PhD.: Institute of Solid Mechanics, Mechatronics and Biomechanics, Brno University of Technology, Technická 2896/2; 616 69, Brno; CZ, macian@fme.vutbr.cz

[3] Olga Košková, MD, PhD, Department of Burns and Plastic Surgery, University Hospital Brno and Faculty of Medicine, Masaryk university, Jihlavská 20, 625 00, Brno; CZ, koskova.olga@fnbrno.cz

[4] Assoc. Prof. Vladimír Fuis, PhD.: Centre of Mechatronics – Institute of Thermomechanics of the Czech Academy of Sciences – branch Brno and Faculty of Mechanical Engineering, Brno University of Technology, Technická 2896/2; 616 69, Brno; CZ, fuis@fme.vutbr.cz

[5] Prof. Jan Wolff, PhD Klinik für Kiefer- und Gesichtschirurgie, Campus Lübeck, Ratzeburger Allee 160/Haus D3, 23538 Lübeck, Germany, Jan.Wolff@uksh.de

ISSN: 1805-8256, doi: 10.21495/em2026-149

Another option is to use a voxelized computational model. However, the stair-step approximation of the geometry inherent to voxel-based models introduces sharp geometric discontinuities at voxel boundaries, leading to stress singularities. Consequently, small element and voxel sizes are required to mitigate these artificial singularities, which again results in increased computational time.

Both approaches have advantages and disadvantages, as described above. The idea of this study is to combine these two approaches. For solving stress strain states irregular mesh (obtained from segmented CT or micro-CT) was used. Strain energy density from irregular mesh was transformed using interpolation to regular mesh to calculate stimulus. Stimulus is than transformed with inverse function to irregular mesh where bone density increment via nodes was calculated.

2. Methods

For simulation micro-CT image from *os occipitale* was used. The solution was divided into two domains. The first domain consists of a finite element mesh, which is used to solve the stress–strain states. The second domain is a regular mesh used for stimulus calculation. The workflow of the bone remodelling simulation is shown in Fig. 1.

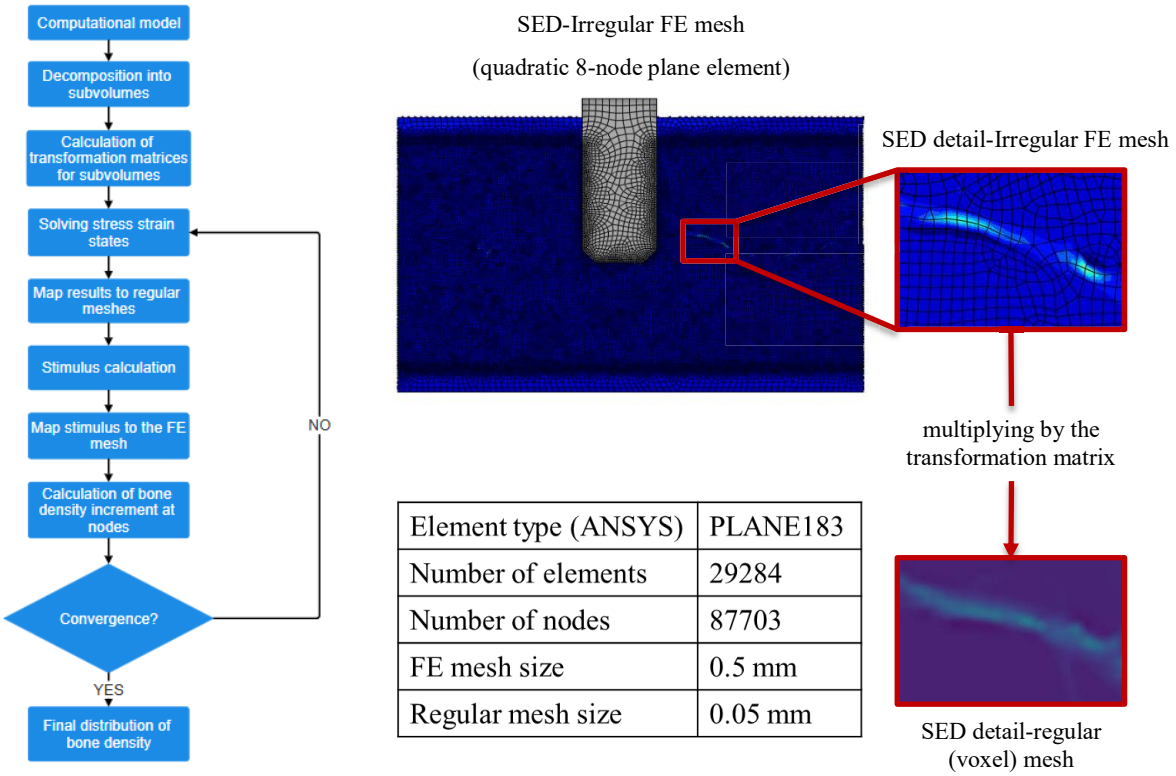

Element type (ANSYS)	PLANE183
Number of elements	29284
Number of nodes	87703
FE mesh size	0.5 mm
Regular mesh size	0.05 mm

Fig. 1: Bone remodelling flowchart (left) and demonstration of interpolated SED values (right).

For solving stress strain states software Ansys (ANSYS Academic Research Mechanical, Release 23.2; Swanson Analysis Systems Inc) was used. The finite element mesh can be divided into smaller subvolumes, which reduces the computation time required for the transformation matrices. The resolution of the regular mesh should be equal to or greater than the mean osteocyte distance. At the same time, the resolution of the regular mesh should at least correspond to the resolution of the CT images used for segmentation. Values in the regular mesh elements are obtained by interpolation of nearby values from the irregular finite element mesh. The relationships between quantities in the finite element mesh and the regular mesh are represented by transformation matrices.

2.1. Model of geometry

For testing purposes, a two-dimensional analysis of remodelling around a cranial fixator screw was performed. The geometric model consists of trabecular bone, cortical bone, and the screw (Fig. 2). The trabecular bone was created by segmentation of micro-CT images (voxel size 25 µm × 25 µm × 25 µm). The cortical bone and the screw were additionally modelled using CAD software. Their representation is

schematic only: the cortical bone has a uniform thickness, and the screw is modelled without threads. For discretization quadratic 8-node node plane element (in Ansys PLANE183) was used. The finite element mesh is available at the link: 10.5281/zenodo.19550154.

2.2. Boundary conditions

The computational model is fixed on both sides. To simulate typical loading conditions of the screw, a force perpendicular to the axial direction of the screw was applied (Fig. 2). The force magnitude was set to 100 N, as the analysis is qualitative and the main purpose of the simulation is to test the proposed

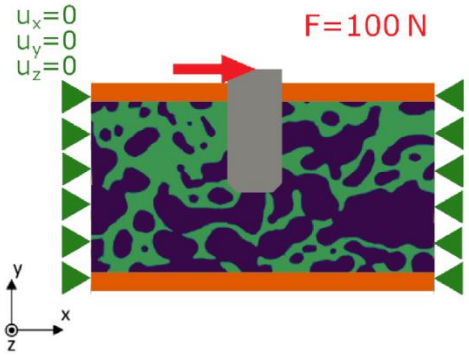

Fig. 2: Model of geometry and boundary condition.

method.

2.3. Model of material

For the purposes of this study, the implant, trabecular bone, and cortical bone were assumed to be homogeneous, isotropic, and linearly elastic materials. The implant material is characterized by a Young's modulus of $E = 110$ GPa and a Poisson's ratio of $\mu = 0.3$ [–]. Cortical bone is represented by a Young's modulus of $E = 15$ GPa and a Poisson's ratio of $\mu = 0.3$ [–] (Rho, 1993). The Young's modulus of trabecular bone is assumed to be dependent on bone density according to the following relationship (Marcián, 2021):

$$E = 13.636\left(\frac{1000\cdot\rho+3295.6}{0.221}\cdot 2.11\cdot 10^{-4} - 3.3\right) \text{[GPa]} \quad (1)$$

where ρ $\left[\frac{g}{cm^3}\right]$ is bone density. The Poisson's ratio of trabecular bone was assumed to be a constant value of μ*=0.3 [-]* (Rho 1993).

2.4. Bone remodelling algorithm

The strain energy density (SED) at the nodes of the finite element mesh is multiplied by a transformation matrix to obtain interpolated values on the regular grid. For micro-level remodelling simulations, the Huiskes–Weinans algorithm (Weinans, 1992) was adopted, with mechanical stimulus, defined as:

$$P(\mathrm{x}) = \sum_{i=1}^{n} U_i \cdot \exp\left(-\frac{d(\mathrm{x})}{d_0}\right) \quad (2)$$

where U_i is the strain energy density of each sensor cell, d is the distance of the sensor cell from the actor cell and $d_0 = 0.1\,mm$ (Isaakson 2009) is the distance from the sensor cell for which the stimulus is reduced to 37%. This equation represents a discrete form of convolution that is easy to compute on a regular mesh. To ensure bone growth only at the interface between bone tissue and the intertrabecular space, the matrix representing the regular mesh was multiplied by a mask matrix representing trabecular bone and dilated. The stimulus in the regular mesh was then multiplied by the inverse transformation matrix to obtain the stimulus at the nodes of the finite element mesh, which was subsequently used to calculate the bone density increment according to the following equation:

$$\frac{\Delta\rho}{\Delta t} = \begin{cases} A(P(\mathrm{x}) - U_{ref}(1+s)) & \text{if } P(\mathrm{x}) \geq U_{ref}(1+s) \\ 0 & \text{if } U_{ref}(1-s) < P(\mathrm{x}) < U_{ref}(1+s) \\ A(P(\mathrm{x}) - U_{ref}(1-s)) & \text{if } P(\mathrm{x}) \leq U_{ref}(1+s) \end{cases} \quad (3)$$

where U_{ref} is the reference stimulus, s is the remodeling equilibrium zone half-width and A is a time constant. Since analysis is qualitative U_{ref} and A were obtained through sensitivity analysis.

3. Results

For demonstration purposes, 1000 iterations were performed. Final distribution after 1000 iteration is shown in Fig. 3.

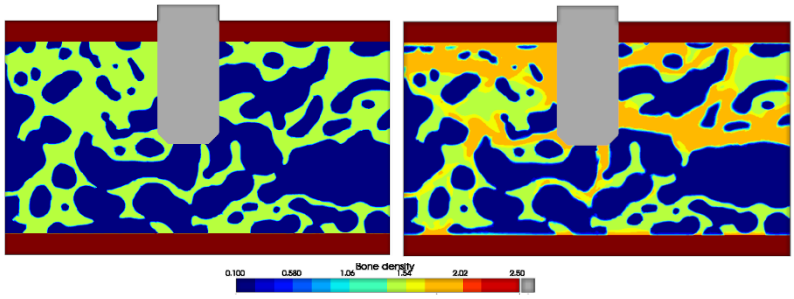

Fig. 3: Initial (left picture) and final distribution (right picture) of bone density.

In Fig. 4 is demonstrated initial border of bone tissue – bone marrow interface mapped on final distribution. In detail is evident that expected behaviour including changes in bone density and trabecular thickness was achieved.

4. Discussion

From Fig. 3 it is evident that the trabecular interface is not as smooth as expected. This is caused by irregularities in the finite element mesh, which represent the main disadvantage of the proposed approach. Another limitation is the interpolation itself: in the case of a coarse finite element mesh, peak SED values may not be captured, and interpolation cannot compensate for this error.

The advantage of this method is precise stimulus calculation. For irregular meshes, the stimulus in the presented form (a weighted sum of SED from osteocytes within a given area) is a challenging problem; moreover, the more irregular the mesh, the less accurate the resulting sum becomes. This indicates that the proposed approach better respects the underlying biological behaviour of bone tissue.

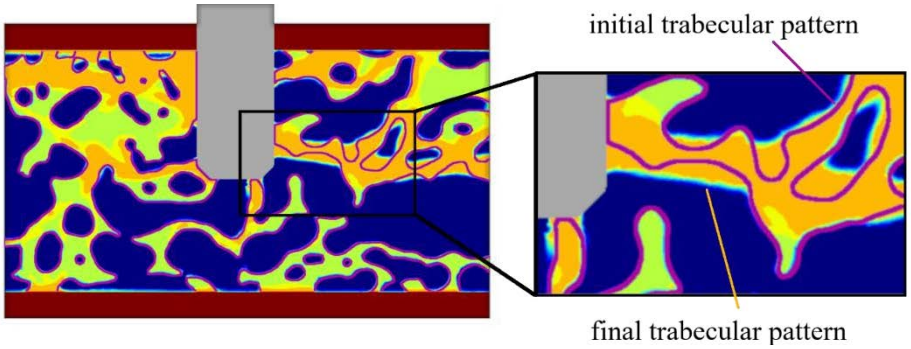

Fig. 4: Final distribution of bone density with initial bone tissue/marrow interface.

Acknowledgement

This publication was supported by the project "Mechanical Engineering of Biological and Bio-inspired Systems", funded as project No. CZ.02.01.01/00/22_008/0004634 by Programme Johannes Amos Commenius, call Excellent Research. The research was supported by the specific research FSI-S-26-8981 and institutional support RVO: 61388998.

References

Marcián, P. et al., 2021. On the limits of finite element models created from (micro)CT datasets and used in studies of bone-implant-related biomechanical problems. *Journal of the Mechanical Behavior of Biomedical Materials*, 117(5), p.104393.

Isaksson, H. et al., 2008. Remodeling of fracture callus in mice is consistent with mechanical loading and bone remodeling theory. *Journal of Orthopaedic Research*, 27(5), pp.664-672.

Rho, J.Y., Ashman, R.B. & Turner, C.H., 1993. Young's modulus of trabecular and cortical bone material: Ultrasonic and microtensile measurements. *Journal of Biomechanics*, 26(2), pp.111-119.

Weinans, H., Huiskes, R. & Grootenboer, H.J., 1992. The behavior of adaptive bone-remodeling simulation models. *Journal of Biomechanics*, 25(12), pp.1425-1441.

32nd International Conference
ENGINEERING MECHANICS 2026
Medlov, Czech Republic, May 11 – 13, 2026

INDEXING GEARBOX CAROUSEL HYBRID DISC MANUFACTURING

Zbončák R.[1]

Abstract: *The paper focuses on the manufacturing of a hybrid carousel disc for an indexing gearbox, developed to reduce the mechanism mass and improve its dynamic performance. It describes the manufacturing chain, including composite material definition, the design and fabrication of a mould from tooling board, and compression moulding technology. Furthermore, the study analyses technological aspects of machining abrasive GFRP/CFRP materials, including the selection of cutting conditions and tools, and the integration of steel inserts, which requires precise surface preparation and verification of adhesive bond quality. The work refers to FEA results for mass moment of inertia and natural frequencies as the basis for validating the proposed manufacturing solution. The presented know-how demonstrates the technological feasibility of the hybrid concept and provides a foundation for subsequent operational testing and patent-protected implementation.*

Keywords: Indexing gearbox, Carousel disc, Compression moulding, Short-fibres composite, Hybrid structure

1. Introduction

Hybrid structures are widely used in composite engineering to achieve the required mechanical properties (stiffness and strength) and/or dynamic performance. This approach enables the combination of the toughness of metals with the high specific stiffness and fatigue resistance of fiber-reinforced polymers (FRP). In general, a hybrid design is most beneficial when the global requirements favor a composite solution (e.g., stiffness, dynamics, fatigue resistance), while local functional requirements call for metallic features (e.g., dimensional accuracy, bearing and contact surfaces, etc.). Typical applications include rotating joints and structural ‘nodes’, where cyclic contact and wear occur; such conditions can be critical for the metal–composite interface and may govern the service life of the structure.

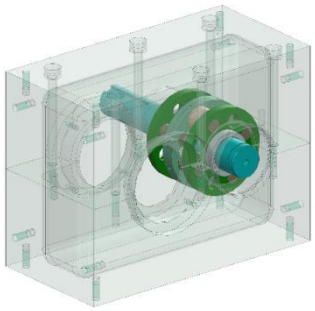

Fig. 1: Original ‘steel’ carousel assembly in indexing gearbox housing.

Hybrid structures offer lower mass, higher specific stiffness and strength, improved dynamic behavior (vibration response and damping), and enhanced fatigue resistance and damage tolerance. However, the interface between dissimilar materials is a key risk area, particularly with respect to galvanic corrosion in the presence of carbon fibers, mismatched coefficients of thermal expansion, and environmental effects (salts, moisture, temperature, UV exposure, and chemicals). These issues impose stringent requirements not only on the overall hybrid design but also on manufacturing discipline, especially at the material

[1] Ing. Radek Zbončák, MBA: VÚTS a. s., Svárovská 619; 460 01, Liberec; CZ, radek.zboncak@vuts.cz

ISSN: 1805-8256, doi: 10.21495/em2026-153

interface. The joints should be designed to be loaded predominantly in shear. Prior to bonding, the metal surface must be roughened and thoroughly degreased, and mechanical locking/fastening is also commonly employed to enhance joint reliability in hybrid assemblies.

In the case of the carousel disc of the indexing gearbox, whose CAD model is shown in Figure 1, the cam-induced loading is favorable for the use of a hybrid structure. The material interface is loaded predominantly in compression, acting exclusively in the direction normal to the bonded surface. The use of a composite is also well suited to the cyclic loading conditions of the mechanism.

2. Composite material

The elastic properties of a short-fiber composite can be analytically predicted using the Fox–Krenchel model, which is a modification of the Rule of Mixtures (RoM) model for continuous fibers:

$$E_L = E_m \cdot V_m + \eta_l \cdot \eta_{o,E,L} \cdot E_f \cdot V_f \tag{1}$$

$$\frac{1}{E_T} = \frac{V_m}{E_m} + \frac{V_f}{\eta_l \cdot \eta_{o,E,T} \cdot E_f} \tag{2}$$

$$\frac{1}{G_{LT}} = \frac{V_m}{G_m} + \frac{V_f}{\eta_l \cdot \eta_{o,G} \cdot G_f} \tag{3}$$

$$\nu_{LT} = \nu_m \cdot V_m + \eta_l \cdot \eta_{o,\nu} \cdot \nu_f \cdot V_f \tag{4}$$

where the analytical Cox shear-lag model describes the transfer of load from the matrix to a short fiber through interfacial shear:

$$\eta_l = 1 - \frac{\tanh\left(\frac{\beta l}{2}\right)}{\frac{\beta l}{2}} \tag{5}$$

$$\beta = \sqrt{\frac{2 \cdot G_m}{E_f \cdot r^2 \cdot \ln\left(\frac{R}{r}\right)}} \tag{6}$$

$$\mathrm{R} = \frac{r}{\sqrt{V_f}} \tag{7}$$

The Krenchel efficiency factor is the product of the fiber length efficiency factor and the fiber orientation efficiency factor:

$$\eta = \eta_l \cdot \eta_o \tag{8}$$

where individual efficiency factors are:

$$\eta_{o,E,L} = \cos^4(\theta) \tag{9}$$

$$\eta_{o,E,T} = \sin^4(\theta) \tag{10}$$

$$\eta_{o,G} = \cos^2(\theta) \cdot \sin^2(\theta) \tag{11}$$

$$\eta_{o,\nu} = \cos^2(\theta) \tag{12}$$

The disc composite is designed using short carbon fibers and an epoxy resin with a fiber volume ratio of 55 %. Alternatively, short glass fibers may also be used. These elastic properties are used for material definition in finite-element simulations.

3. Compression moulding

The suitable manufacturing technology for this application is compression molding. This process uses compression of long fibers (up to 20 mm long) impregnated with epoxy resin in closed mold. Hybrid disc is designed for standard modulus carbon fibers – virgin carbon chopped tow of consistent length of 12 mm. (Easy Composites, 2026) The first prototypes are made of chopped glass fiber GRC Concrete ZR 12 mm. (Synthetika, 2026) Epoxy resin LH 385 with hardener H 286 is used as a matrix. (Havel-

Composites s r. o., 2026) Its viscosity is 400–800 mPas/25°C and pot life is 90 min. Mold is machined of EdaBoard EP 978 with density of 680 kg/m^3. (Ebalta, 2026) Mold surface is treated with a liquid Sealer 02, which creates smooth and glossy surface.

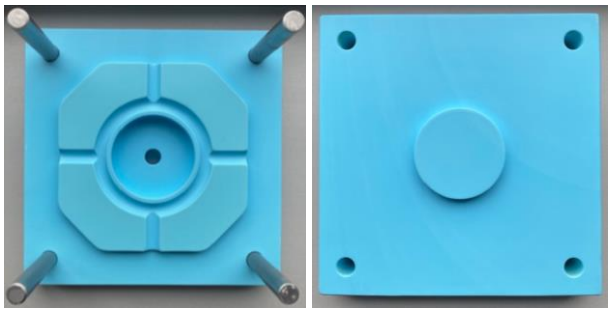

Fig. 2: Mold.

A single mold enables production of discs in the low tens, if the mold's surface is properly coated with a released agent after each use. Used released agent is CR1 Easy Release. The pressure to close the mold is First set of composite disc prototypes show fiber volume ratio of 51–59 %, which corresponds with suggested fiber volume ratio of 55 %.

4. Machining of composite

Machining is technologically demanding primarily due to the pronounced abrasiveness of glass fibres and the heterogeneous microstructure of the material. During drilling and milling, typical damage mechanisms include entry/exit delamination, fibre pull-out, local matrix peeling, and burr formation, while edge quality strongly depends on fibre orientation and local fibre concentration. From the standpoint of process parameters, it is critical to limit axial forces (especially in drilling) through appropriate tool geometry, feed optimization, and the use of backing support or double-sided clamping to reduce exit delamination; at the same time, rapid cutting-edge wear must be expected, so PCD/diamond-coated tools or cemented carbide with a wear-resistant coating are preferred. Thermal effects are significant for the epoxy matrix. Local overheating can lead to matrix degradation and reduced hole tolerance. Therefore, cutting conditions should be controlled to minimize friction and heat accumulation Because GFRP machining generates fine dust and fibrous particles, effective extraction and occupational hygiene measures are essential.

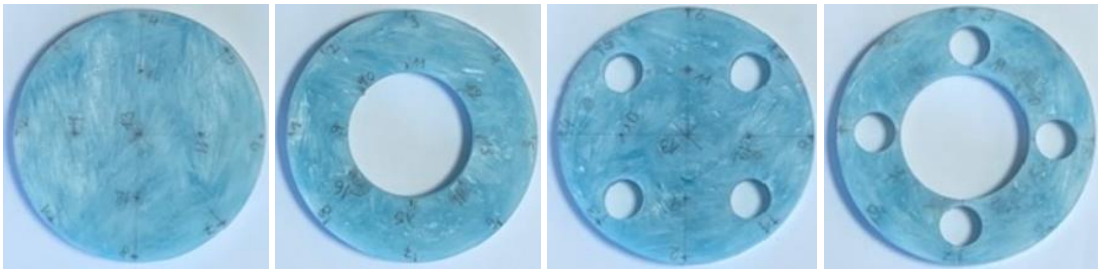

Fig. 3: Machined composite body of hybrid disc.

In this case, the composite was machined on an SLV EDU universal 3-axis milling machine with accuracy of 0.04 mm. The spindle speed ranged from 100 to 24 000 rpm. Cylindrical cutter Fraisa AX-NV3 (diameter 4 mm) was used. The feed rate was 1 500–2 000 mm/min with a material removal of 0.4 mm. It was demonstrated that, in the critical region between the flange and the insert, machining did not damage the thin laminate wall (1 mm). The machined composite surface was smooth, with no significant edge damage at the hole perimeters.

5. Inserts

Inserts are used to carry localized contact loads and to ensure dimensional accuracy. Joint reliability is governed by the adhesion and cohesion of the bonded interface: after drilling, the composite hole is lightly roughened and thoroughly degreased, while the steel insert is activated by grinding, degreasing, and, where appropriate, by applying a primer. A toughened epoxy adhesive with a controlled bond-line

thickness is used to minimize stress peaks and to promote predominantly shear load transfer. It is critical to prevent air entrapment during insertion, to maintain coaxiality of the insert with the subsequent drilling operation, and to control the curing cycle, since mismatched thermal expansion and environmental effects (moisture) can degrade the interface over time and trigger local debonding.

Fig. 4: GFRP with bonded-in steel drill bushings.

6. Disc performance

The mass of the original steel disc is 0.19 kg, whereas the mass of the redesigned hybrid disc is 0.08 kg. The mass moment of inertia of the original disc about the axis of rotation in the mechanism is 188 kg·mm², while that of the hybrid disc is 61 kg·mm². Table 1 summarizes the natural frequencies of both disc variants.

Tab. 1: Natural frequencies of steel and hybrid disc (V_f = 55 %).

	Steel	**E-glass**	**Carbon**
1st mode	4 161 Hz	3 782 Hz	5 586 Hz
2nd mode	5 197 Hz	4 115 Hz	6 229 Hz
3rd mode	9 550 Hz	7 794 Hz	10 200 Hz
4th mode	12 980 Hz	9 137 Hz	14 430 Hz

7. Conclusions

The theoretical FEA results (Ch. 6), together with the validated manufacturing process, provide a strong basis for successful implementation of the proposed concept. After the hybrid carbon-fiber discs are manufactured, the carousel will be tested on a rig simulating real operating conditions to verify the mechanical and dynamic performance as well as the service life. The above-described solution is protected by several patents. The polygonal joint itself is protected by Patent CZ 306709, and the entire hybrid disc solution is protected by Patent CZ 310532 B6. Technology and application of the hybrid disc are under utility model no. CZ 38182 U1 protection.

Acknowledgement

This publication was supported by the Czech Ministry of Industry and Trade in the framework of the institutional support for long-term conceptual development of research organization - recipient VÚTS, a. s.

References

EASY-COMPOSITES. Virgin Carbon Fibre Chopped Tow. Online. Easy Composites. 2026. Available from: https://www.easycomposites.eu/virgin-chopped-carbon-fibre-tow. [cit. 2026-01-16].

SYNTETIKA. Chopped Glass Fibre GRC Concrete ZR. Online. Synthetika. 2026. Available from: https://synthetikaeu.com/en_US/p/Chopped-glass-fibre-GRC-Concrete-Zr-12mm-1000g/1701?currency=CZK. [cit. 2026-01-16].

HAVEL-COMPOSITES. Epoxy resin LH 385. Online. (in Czech) Havel-Composites s r. o. 2026. Available from: https://www.havel-composites.com/cs/produkty/epoxidova-pryskyrice-lh-385. [cit. 2026-01-16].

EBALTA. Edaboard 978. Online. KTK Blansko s r. o. Ebalta. 2026. Available from: https://ebalta.cz/produkt/ebaboard. [cit. 2026-01-16].